UNIVERSIDAD CARLOS III DE MADRID

ESCUELA POLITÉCNICA SUPERIOR

Mechanical Behavior of Hybrid 3D Woven Composites

Doctoral Thesis

RAÚL MUÑOZ SÁNCHEZ

2014

Departamento de Ciencia e Ingeniería de Materiales e Ingeniería Química

Escuela Politécnica Superior

Mechanical Behavior of Hybrid 3D Woven Composites

Raúl Muñoz Sánchez

Advisors:

Dr. Carlos González Martínez

Dr. Javier Llorca Martínez

2014

*A mis padres, por una vida entera
dedicada a su familia y a la educación*

*"Un científico es alguien que usa pócimas
y arregla cosas."*

Nicolás Muñoz (4 años)

Agradecimientos

En primer lugar, agradezco profundamente a mis directores de tesis, los profesores Carlos González y Javier Llorca, tanto su dedicación como todas las enseñanzas personales y científicas que han sabido transmitirme durante estos años. Sería imposible no sentirme en deuda con ellos después de recibir tanta generosidad.

Agradezco también al Departamento de Ciencia de Materiales de la Universidad Politécnica de Madrid y, concretamente, al profesor Francisco Gálvez, por el soporte prestado en la realización de los ensayos mecánicos.

Gracias a todos los compañeros del Instituto IMDEA Materiales que han contribuido directamente al desarrollo de esta tesis. En primer lugar, a Paqui, por su ayuda con los impactos de alta velocidad, así como por su apoyo personal y los innumerables momentos que hemos pasado frente al ordenador; a los únicos representantes del hemisferio sur, Rocío Seltzer y Fede, por su amistad y por su ayuda con la torre de caída y el tomógrafo; a Quim, por su estoicidad y por desvelarme los secretos de "l'infusió" y del C-scan; a Vanesa y Juan Carlos, por su continua ayuda en el laboratorio y los buenos momentos que hemos pasado juntos; a José Luis, por su corte elegante; a Juan Pedro, por sus valiosos conocimientos acerca de los polímeros; a Silvia, Eva y Nathamar, por instruirme en el apasionante mundo del pulido y, finalmente, a R. Muñoz, mi *alter ego*, por hornear mis muestras y ser esa fuente inagotable de simpatía.

También merecen mi reconocimiento más sincero todos aquellos compañeros para los que Achilles es algo más que un héroe griego, entre los que destacaría a Sergio Sádaba, por caerse de pequeño en una marmita llena de ecuaciones y tener siempre una solución a mano; a Enrique, por ayudarme con los bugs de Linux; a Antoine, por pelearse con el cluster e iniciarme en el mundo del linux y a Ana, por matar sus cálculos sin rechistar, así como a mis ilustres compañeros de departamento por su agradable compañía.

Sin el cariño y la amistad de Teresa, Sergio Arias, Jon, Inés, Carmen, Paloma, Laura, Nacho, Torralba, Saeid y tantísimos otros compañeros de IMDEA que omitiré por brevedad, esta tesis no habría tenido este sabor tan dulce.

Y como de bien nacido es ser agradecido, no quiero olvidarme de algunos de esos compañeros o profesores que han marcado mi trayectoria profesional: desde aquel magnífico profesor de Física, D. José María Fraile, hasta Juan Carlos Pérez Cerdán y mis inicios en el mundo de la simulación con Cosmos, pasando por Ana Alonso, José Félix, Elvio, Manuel Doblaré y Begoña Calvo.

Por supuesto, no puede faltar en este apartado toda mi familia, a quien tanto le debo, y especialmente mi madre, a la que siento enormemente no poder mostrarle esta dedicatoria.

Finalmente, quiero agradecer de todo corazón a Yolanda su sacrificio personal, su cariño y su apoyo incondicional durante todo este tiempo. Sin ella, esta tesis nunca habría sido posible.

En Madrid, a 12 de Junio de 2014

Resumen

En la actualidad, el uso de materiales compuestos unidireccionales está muy extendido en el sector aeronáutico debido a sus excelentes propiedades mecánicas en el plano, su elevada resistencia a la corrosión, su estabilidad dimensional y su resistencia a fatiga. Sin embargo, su aplicación frente a cargas de impacto presenta el inconveniente de su baja resistencia a la delaminación y tolerancia al daño. La ausencia de refuerzo en la dirección del espesor los hace especialmente vulnerables frente a cargas fuera del plano del laminado, como los impactos de hielo o de fragmentos de pala que puede sufrir la piel del fuselaje de un avión durante su vida en servicio.

Una alternativa para mejorar la resistencia a la delaminación y la tolerancia al daño es usar como refuerzo telas con un patrón de entrelazado en tres dimensiones, como los tejidos ortogonales 3D, en los que los hilos horizontales (trama y urdimbre) se entrecruzan con mazos de fibras orientados en la dirección del espesor. Además, es posible emplear distintos tipos de fibras y combinarlas en distintas proporciones, es decir, *hibridizar* el refuerzo con el fin de optimizar sus propiedades mecánicas. Una vez tejidas, las preformas se impregnan de resina mediante Vacuum Assisted Resin Transfer Moulding (VARTM), con el consiguiente ahorro en los costes de producción en comparación con los laminados procesados en autoclave.

A pesar de las potenciales ventajas de los materiales compuestos híbridos con refuerzo ortogonal en 3D, su uso está todavía poco extendido debido a la falta de datos experimentales y de modelos que permitan predecir de forma fiable su comportamiento mecánico.

En esta tesis se analiza el comportamiento mecánico de un material compuesto formado por un refuerzo ortogonal en 3D de fibras de carbono, de vidrio S2 y de polietileno, e impregnado en una matriz de tipo polimérica termoestable (epoxi-viniléster). El comportamiento de este material se ha estudiado frente a solicitaciones de tracción, compresión, cortadura, e impactos de alta y de baja velocidad. Se ha analizado también el comportamiento mecánico de los mazos de fibras, así como la sensibilidad a la presencia de agujeros y la resistencia residual después de impacto. El estudio incluye una extensa campaña de inspección de los mecanismos de rotura, llevada a cabo mediante tomografía de rayos X, microscopía

óptica, microscopía electrónica y ultrasonidos, que ha permitido conocer la influencia de los procesos de daño en las propiedades macroscópicas del material compuesto.

También se ha investigado el efecto de la hibridación en los casos de carga fuera del plano del laminado: torre de caída, impacto balístico mediante cañón de gas y flexión de viga corta apoyada en tres puntos. Para ello, se impacta o se indenta alternativamente el material compuesto 3D en la cara más rica en fibra de vidrio o en la cara más rica en fibra de carbono. En el caso de la flexión en tres puntos, se incluye también un estudio comparativo del efecto de los refuerzos de polietileno.

El estudio se acompaña de una serie de modelos analíticos que permiten predecir, entre otros, la sensibilidad a la entalla a tracción y compresión, la carga inicial a la que se produce la delaminación o la curva de impacto balístico del material.

Finalmente, se proponen dos modelos numéricos, ambos formulados en la mesoescala y basados en la mecánica del daño continuo, para simular la respuesta del material frente a impacto de alta y de baja velocidad. El primero ofrece una buena correlación con los resultados experimentales, especialmente para el caso de impactos mediante torre de caída; el segundo es especialmente adecuado para reproducir la curva balística del material y capturar los mecanismos de fallo correspondientes, y se basa en el uso de elementos cohesivos y en la superposición de mallas no conformes mediante la técnica de *elementos embebidos*.

Abstract

Unidirectional fiber-reinforced composites are widely used in the aerospace industry due to their excellent in-plane mechanical properties, high corrosion resistance, dimensional stability and fatigue life. Nevertheless, they exhibit poor delamination resistance and damage tolerance, particularly under impact. The lack of reinforcement in the through-thickness direction makes them particularly vulnerable to out-of-plane threats caused by foreign objects, such as ice slabs or open-rotor blade fragments impacting on skin fuselages.

A cost-effective alternative is the use of 3D woven orthogonal reinforcements, in which delamination resistance and damage tolerance are improved by weaving a yarn in the through-thickness direction. This technique allows the combination of several fiber types (hybridization) and enables the optimization of the composite properties by varying the fiber content. Preforms may be infused by using out-of-autoclave processing techniques, such as Vacuum Assisted Resin Transfer Molding (VARTM), leading to considerable cost savings, as opposed to autoclave consolidation.

Despite of the potential of these materials, the use of hybrid 3D woven composites is limited by the lack of experimental data and reliable models able to predict the mechanical response of the material.

This work analyzes the mechanical behavior of a hybrid 3D woven orthogonal composite made up of a thermoset polymeric matrix (epoxy-vinylester) reinforced with carbon and glass fibers, as well as with polyethylene z-yarns in the through-thickness direction.

The mechanical behavior of the material was studied under tension, compression and shear, as well as under high- and low-velocity impact. The mechanical behavior of the yarns, the notch-sensitivity of the composite and its residual strength after impact were also measured. The study includes an extensive inspection campaign carried out by means of X-ray computer tomography, optical and electron microscopy, as well as ultrasounds. These results provide a critical information about the failure micromechanisms involved in the damage process, which helps to explain the macroscopic properties of the composite.

The influence of hybridization was also discussed under out-of-plane loading, such as drop-weight tests, ballistic impacts and short beam tests. To this end, the hybrid 3D

composite was alternatively impacted on the carbon or the glass faces. Regarding the short beam tests, the influence of the z-yarns was also discussed in detail.

A set of analytical models was also included to predict the notch-sensitivity in tension and compression, the delamination load threshold and the ballistic curve of the composite material.

Finally, two mesoscale finite element models were formulated within the continuum damage mechanics framework to simulate the response of the material under high- and low-velocity impact. The first one shows a good correlation with experimental results, especially during low-velocity impact, whereas the second one is suited to predict the ballistic curve and the failure mechanisms during high-velocity impact. The latter is based on the combination of cohesive elements and a mesh superposition technique called *embedded element.*

Contents

Contents

Contents

CHAPTER 1

Introduction

Fiber Reinforced Polymers

A *composite material* or simply *composite*, from Latin *composĭtus*, is a complex material made up of at least two constituents, macroscopically distinct and not soluble in each other. The component that provides strength and stiffness is called reinforcement and can be in the form of particles, short fibers, whiskers or long fibers; whereas the matrix is the component in which the reinforcement is embedded. The main role of the matrix is to protect the reinforcement against chemical attacks and to ensure the load transfer.

Composites can be grouped into three categories depending upon the matrix: metal-matrix composites (MMCs), ceramic-matrix composites (CMCs) and polymer-matrix composites (PMCs). While the MMCs and CMCs are suited for applications in which hardness, high-temperature, thermal stability or corrosion resistance are critical, their use is limited by the high manufacturing costs, Mortensen (2006). The most widely used composites are those based on a polymeric matrix reinforced with carbon and/or glass fibers.

Polymeric matrices can be divided into thermoplastics (polyethylene, polypropylene, polystyrene, polyvinylchloride) and thermosets (epoxy, vinylester, phenolic, bismaleimide, unsaturated polyester), Pascault *et al.* (2002). Thermoset polymers are stiffer, harder, more brittle and cheaper than thermoplastics, but less tougher, damage-tolerant and unable to be reshaped and melted. Regarding the reinforcement, long fibers provide excellent mechanical properties compared to the bulk material due to the chain orientation of the molecules and

Figure 1.1: Unidirectional prepreg tape (courtesy of Zoltek)

the small diameter, which reduces the presence of flaws. Examples of common fibers include glass, carbon, aramid, boron, silicon carbide and polyethylene. The length of the fiber ensures the load transfer in shear from matrix to the embedded fiber.

There is a large variety of fiber reinforced polymer (FRPs) composites. The most widely used are the unidirectional prepreg tapes (Figure 1.1) in which flat laminae are bonded by the resin. The anisotropy of each ply is overcome by stacking several layers oriented at various angles. This enables designers to tailor the properties of the material for different applications.

FRPs composed of carbon, glass or aramid fibers and epoxy matrices stand out among the most successful structural materials. They exhibit excellent in-plane mechanical properties, fatigue life, corrosion resistance and dimensional stability, so their use has increased significantly over the past years (Figure 1.2). Currently, they are in many industrial applications, in aerospace industry, sports, energy generation, automotive, etc.

However, unidirectional prepreg tapes suffer from two important disadvantages:

- Impact damage typically gives rise to delamination, which is difficult to detect and reduces the residual strength. The damage tolerance of these materials is low compared against aluminium alloys and steels, limiting their applicability in structures susceptible to be impacted.

- Prepregs are consolidated in autoclave at high temperatures, which significantly increases the manufacturing costs.

Delamination occurs at the interfaces between plies with different orientation when the interlaminar shear strength is exceeded. This is mainly due to the elastic mismatch
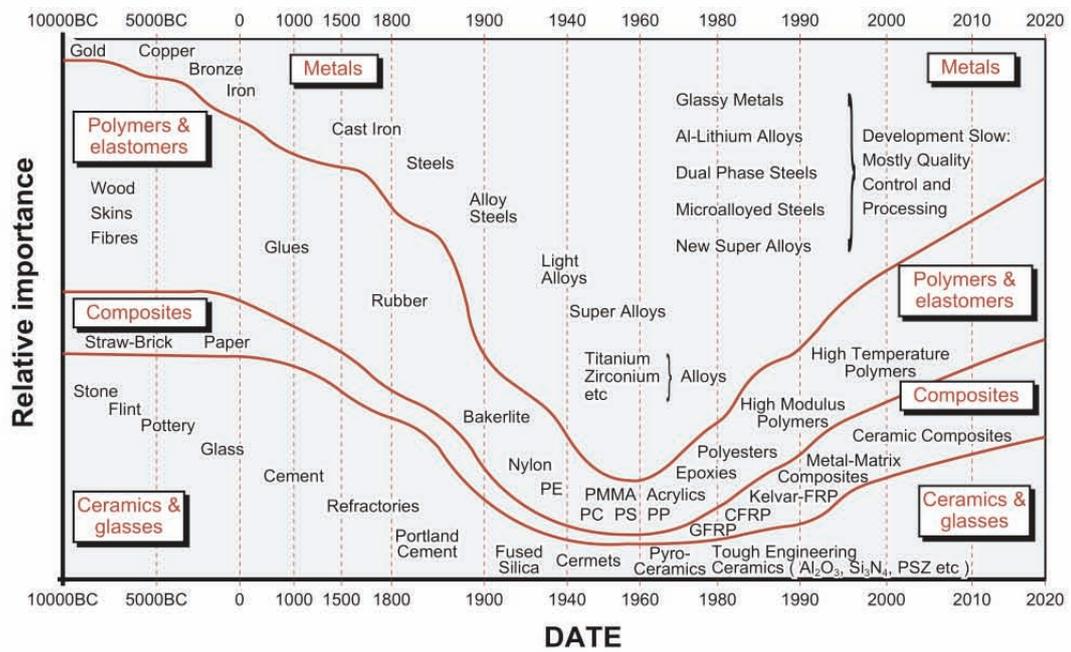
Figure 1.2: Evolution of the use of composites and other materials, Ashby (2005)
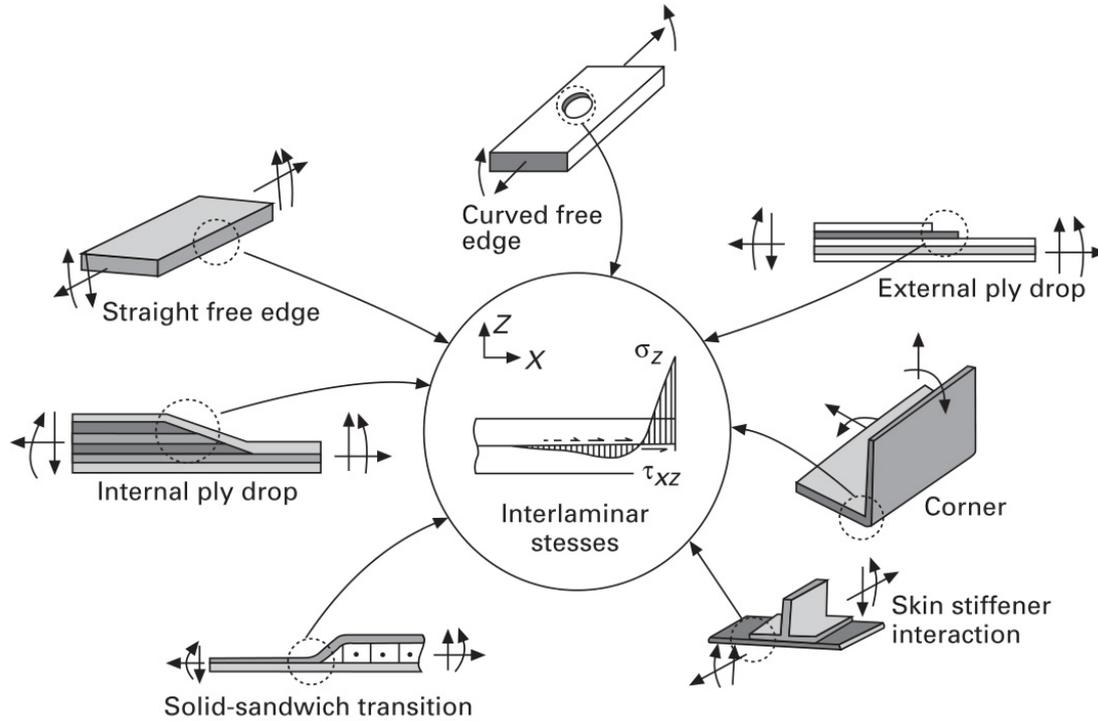
Figure 1.3: Delamination sources in composites, Sridharan (2008)

between adjacent ply elastic constants, but there are other sources of delamination, such as free edges, ply drops and bending (see Figure 1.3). To improve delamination resistance and fracture toughness, several methods have been suggested, including z-pinning, resin toughening, sizing of fibres to increase the interfacial adhesion strength with the resin matrix, Lee *et al.* (2002) and interleaving:

- Z-pinning consists on embedding small pins into composites to create a through-thickness reinforcement. Although in-plane shear strength, interlaminar fracture toughness and impact damage resistance can be improved, the damage induced during manufacturing and the distortion of the fibers around the z-pins reduces the in-plane properties and fatigue life of z-pinned composites, Chang *et al.* (2006).

- Toughening of thermoset resin systems can be improved by using modifiers, such as rubber or thermoplastic particles, but at the expense of the mechanical properties. This is especially critical at high-temperature, where thermo-oxidation takes place at the fiber/matrix interphase, causing the embrittlement of the composite, Haque *et al.* (2014).

4

- Continuous fibers are usually coated with a thin layer of sizing[1], Mortensen (2006), to prevent abrasion from manufacturing and to strengthen the interface bond, Marston et al. (1997). Note that chemical reactions and intermolecular forces that enable bonds are only possible when the matrix is capable of wetting the fibres, Tsu-Wei (1992), which in turns depends upon the relationship between the surface tension of the adhesive and the solid phase, Mazumdar (2002).

- Interleaving is done by inserting a thermoplastic resin film between adjacent layers of 2D textile preforms. This method signicantly improves the fracture toughness in mode I, but reduces the in-plane compression strength and presents some difficulties during resin impregnation, Rudov-clark (2007).

A cost-effective alternative to improve delamination resistance is the use 2D woven composites processed by out-of-autoclave techniques, such as Resin Transfer Moulding (RTM) or Vacuum Assisted Resin Transfer Moulding (VARTM). These materials have traditionally shown better fracture toughness and damage resistance than unidirectional prepreg tapes due to the higher friction caused by the waviness of the yarns. However, crimping usually penalizes the in-plane properties, so multiaxial fabrics (also known as non-crimp fabrics [NCFs]) can be used instead. They also exhibit higher damage tolerance compared to their unidirectional counterparts, Bibo et al. (1997), but lower in-plane properties, as well as a modest improvement of the out-of-plane response due to the lack of reinforcement in the thickness direction.

3D woven composites

VARTM technique allows the usage 2D preforms, such as plain weave, twill or satin (Figure 1.4) and also three-dimensional fiber architectures. A significant enhancement of the impact response and damage tolerance is achieved when 3D textile manufacturing techniques, such as braiding, knitting, stitching and through-the-thickness weaving, are applied to create 3D fiber reinforcement architectures (Figure 1.5). 3D weaving is the most widely used among these techniques because of its versatility (the weave pattern and the amount of binder yarns can be controlled), ability to create complex shapes (Figure 1.6), lower cost and simplicity. Mouritz et al. (1999a) reported that braiding machines are slow,

---

[1]Sizing of carbon fibers is typically done with uncured epoxy resin.

|		
(a) Plain weave	(b) Twill	(c) Satin
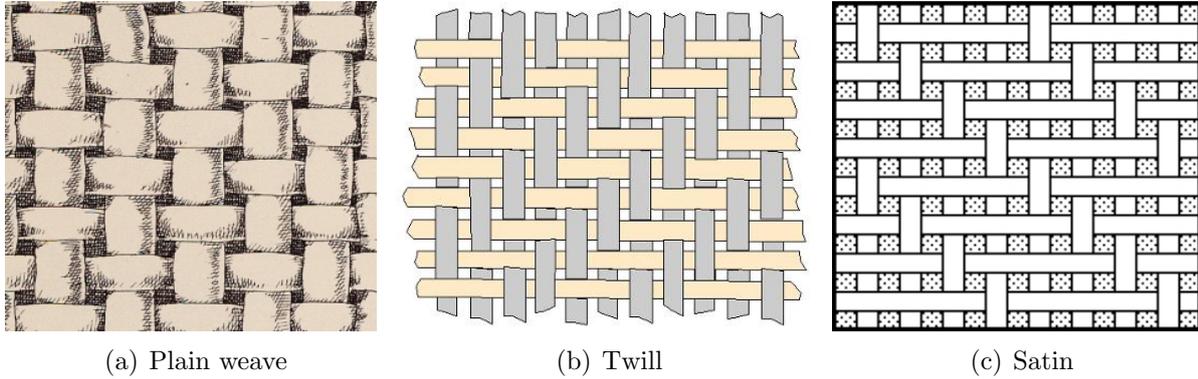
Figure 1.4: Common weaving patterns of 2D preforms

expensive and only capable of producing narrow preforms; stitching is limited by the size of the sewing machine and environmental effects, and thick preforms cannot be made by knitting.

There are several fibre architectures of solid 3D woven composites, namely multilayer, orthogonal and angle interlock, Hou (2008). The orthogonal is the simplest one and it consists of inserting two sets of orthogonal yarns alternatively in the direction of the loom (warp or stuffer) and perpendicularly (weft or filler), Figure 1.7. Another yarn, also known as z-yarn, warp weaver, z-binder or simply binders, is interlaced in the through-thickness direction running from the top to the bottom layer. Note that there is always one more fill layer than warp layer.

The complex distribution of fibers in 3D woven composites ensures a superior impact resistance and fracture toughness over traditional composites, Mouritz *et al.* (1999b). The outstanding impact response and damage tolerance of 3D woven composites has already been reported by several authors: Tanzawa *et al.* (1999) carried out double cantilever beam tests and demonstrated that G_{Ic} increases with the density of binders, but decreases with pre-straining; Pankow *et al.* (2011) evaluated the flexural response of 3D woven textile composite panels using the End Notch Flexure test and proved the effectiveness of the binder in reducing or suppressing delamination; Potluri *et al.* (2012) compared different 3D woven architectures (orthogonal, angle interlocked, layer-to-layer and modified layer-to-layer structures) with unidirectional and 2D laminates, and concluded that the 3D architecture makes the composite more damage-tolerant. The effect of the z-binder on the in-plane and out-of-plane properties of 3D woven composites at different strain rates

(a) 3D woven

(b) Warp-Knitted

(c) Braiding process

(d) Stitching process
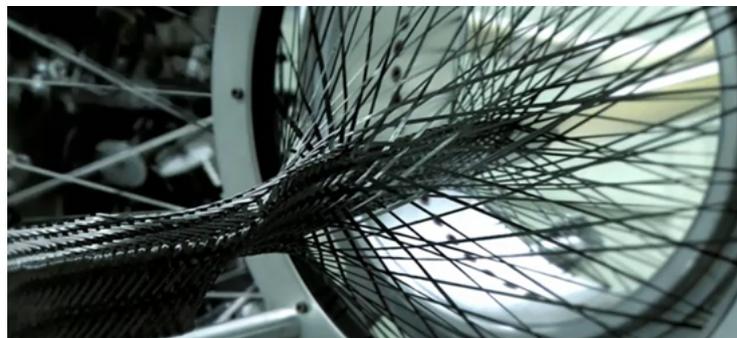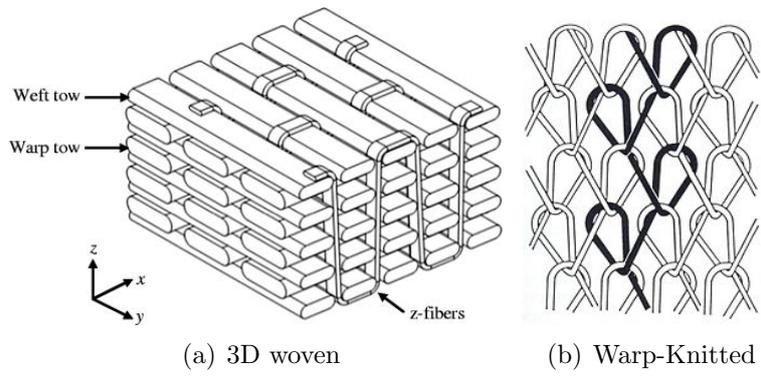
Figure 1.5: Common 3D textile techniques: weaving, warp-knitting, braiding and stitching.
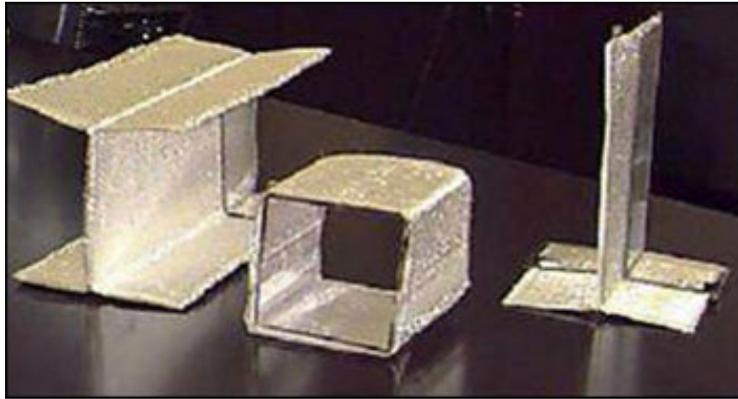
Figure 1.6: Examples of near-net-shape preforms manufactured by 3D textile techniques (3TEX, Inc)
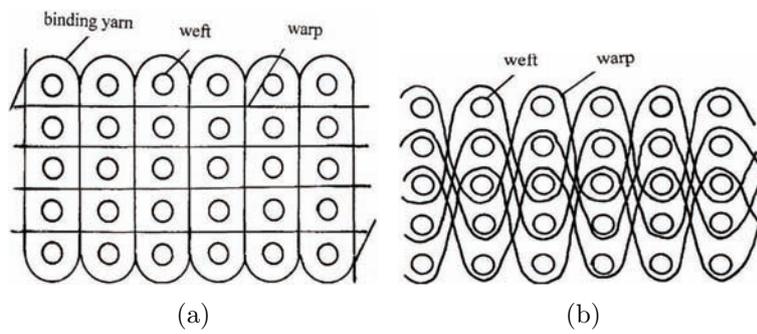

Figure 1.7: 3D woven structures: (a) orthogonal and (b) angle interlock, Gu & Zhili (2002)

was studied by Gerlach *et al.* (2012). Experimental tests conducted by Seltzer *et al.* (2013) revealed also that 3D woven architecture offer superior impact resistance and energy absorption capabilities than the 2D counterparts when subjected to drop-weight tests. This study demonstrated that state-of-the art 3D characterization techniques, such as X-ray microtomography (XCT), are extremely useful to understand the initiation and progression of damage in these materials in which failure processes are inherently 3D. Eventually, Grogan *et al.* (2007) reported higher ballistic limit of 3D composites as compared with 2D materials.

Regarding the in-plane response and the failure mechanisms involved, Cox *et al.* (1994b) and Cox (1996) showed that 3D woven composites presented higher failure strains than conventional multiaxial laminates, together with lower notch sensitivity and higher work of fracture. Following this pioneer work, there were many papers available in the literature on the mechanical response of 3D composites, but detailed studies focussing on the comprehensive assessment of the dominant damage micromechanisms in different 3D fiber preforms have appeared recently. For instance, Bogdanovich *et al.* (2013) and Ivanov *et al.* (2009) carried out a comprehensive experimental analysis of the elastic constants and damage micromechanisms of 3D non-crimp orthogonal woven composites loaded in tension. They showed that non-crimp 3D orthogonal woven composites have significantly higher in-plane strengths, failure strains and damage initiation thresholds than the 2D woven laminated counterparts.

Manufacturing of 3D woven composites

Three-dimensional woven fabrics are mainly produced by the multiple warp weaving method, as described in Tong *et al.* (2012). The process is highly automatized, reducing manufacturing costs and enabling large-scale production. Once the preform is ready, it is processed by either RTM or VARTM. The latter is cheaper and easier to handle, since one half of the mould is replaced by a membrane. As shown in Figure 1.8, the preform is placed into a one-sided mold covered with a plastic bag and, after sealing the bag, vacuum is created to draw the resin into the fabric, Mazumdar (2002). Finally, the resin is cured *in situ* or in autoclave. It should noted that resin infusion techniques increase the conformability and the possibility of producing near-net-shapes, which in turn reduces
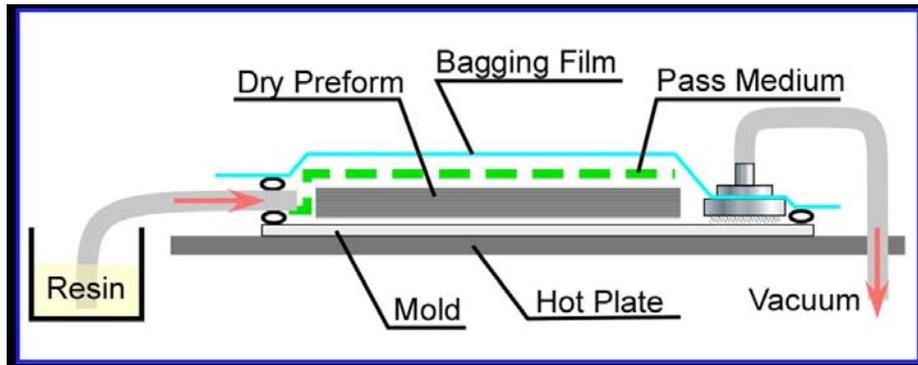
Figure 1.8: Schematic Vacuum Assisted Resin Transfer Molding Technique

the amount of joining elements. They are particularly suitable for low to medium volume production rates.

However, there are various important aspects regarding the manufacturing of 3D woven composites not discussed so far:

- The proper impregnation of fibers during processing is a main concern in liquid molding techniques. The permeability K of the fabric varies with the interlacement, Padaki N V (2010). The presence of the z-yarn increases the interlacement, but it also promotes the flow of resin in the through-thickness direction, so it remains unclear how permeability is affected by the 3D reinforcement, Zeng *et al.* (2014). Permeability depends also upon the volumetric fraction of fibers, which in turn depends on the compaction, i.e., the ability of the fabric to form doubly-curved surfaces, which is usually lower than in 2D fabrics, Zeng *et al.* (2014). The problem can be modeled by using Computation Fluid Dynamic (CFD) simulations in which the flow at the resin channels is modeled as Navier-Stokes fluid and yarns are considered as porous media governed by Darcy's law, Zeng *et al.* (2014), Stig & Hallström (2012), Desplentere *et al.* (2005), and Drach *et al.* (2014).

- Voids created during manufacturing may affect the mechanical properties of the final composite, Hernández *et al.* (2013).

- As shown in Figure 1.9, the binder induces some waviness (crimping) in the longitudinal yarns. This also may appear as a result of compaction. The fill yarns are typically more affected by crimping than the warp yarns due to two main reasons: warp stuffers are kept in tension during the weaving process, Gerlach *et al.* (2012);

10

z-yarns are only in contact with the fill yarns. Crimping penalizes the mechanical properties of the material, particularly in compression, Mahadik & Hallett (2011), Stig & Hallström (2013) and Ferreira *et al.* (2014).

- Abrasion and damage takes place in the warp yarns during manufacturing. Lee *et al.* (2002) quantified the influence of weaving on the mechanical properties of carbon and glass yarns and concluded that stiffness is not affected, whereas tensile strength is significantly reduced, particulary in glass yarns. Rudov-Clark *et al.* (2003) reported strength reductions of 30% to 50% in the warp yarns woven in a Jacquard loom (Figure 1.10).

Hybrid 3D woven composites

The mechanical properties of the 3D composites can be further enhanced by using two or more fiber types. Hybridization has consistently demonstrated better damage tolerance under impact, reduced notch-sensitivity and improved fracture toughness than their carbon-fiber counterparts, Aveston & Kelly (2013); Hanomsilp & Hogg (2003); Naik *et al.* (2001); Hosur *et al.* (2005); Sevkat *et al.* (2009); Enfedaque *et al.* (2010); González *et al.* (2014); Sayer & Bektas (2010). Dai & Jr (2014) analyzed the fatigue life of a hybrid composite and concluded that carbon has a positive effect on the tensile-tensile cyclic loading, but it reduces lifetime in compression-compression cycles. The flexural response of carbon-glass hybrid composites was also measured by Dong *et al.* (2012), showing that hybridization may improve flexural strength in $3.2 - 8.0\%$. Hybridization of aramid and E-glass fibers showed that strength increases with strain-rate, Gu *et al.* (2007).

Applicability of hybrid 3D woven composites

3D woven composites are particularly suitable for applications in which high energy absorption capabilities, low areal density and cost-effective materials are required, such as impact protection of primary structures in aerospace industry.
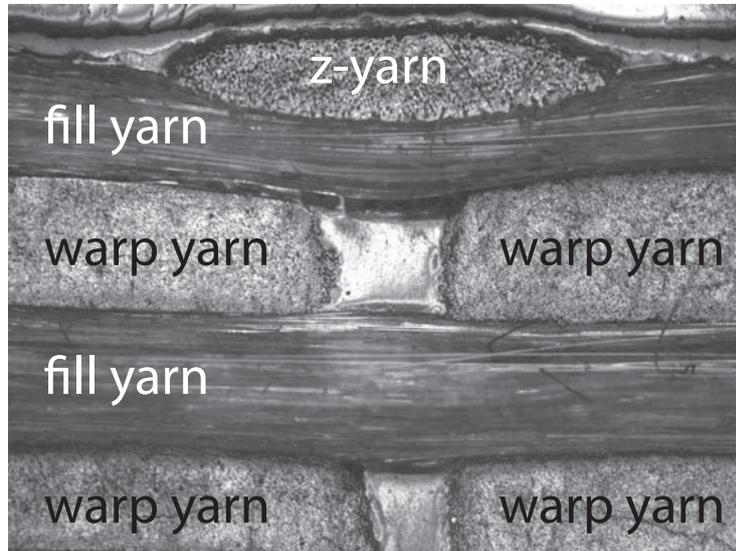
(a)

(b)

Figure 1.9: (a) Micrograph and (b) XCT image showing how the z-yarn causes crimping on the fill yarns of a hybrid 3D woven composite.

(a)

(b)
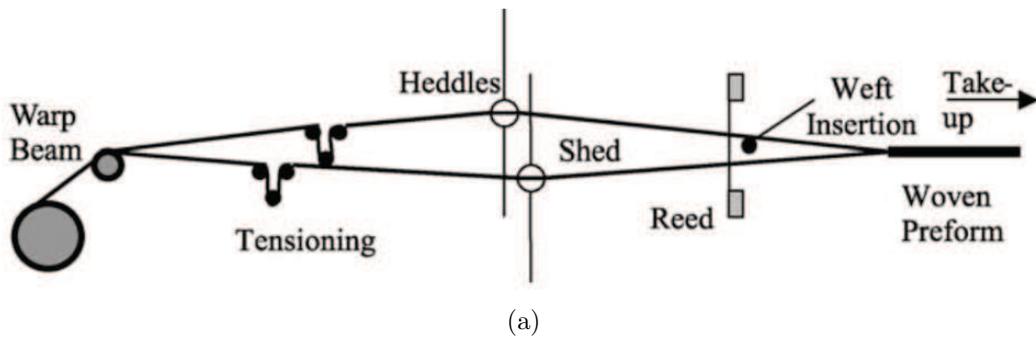
Figure 1.10: (a) Jacquard loom, Rudov-Clark *et al.* (2003) and (b) warp supply (University of Manchester) for 3D weaving.

1.1 Objectives

Despite of the potential advantages of hybrid 3D composites, there are only few studies devoted to analyze the mechanical response of these materials (Mahmood *et al.* (2013), Böhm *et al.* (2011), Jr & Dai (2013)). The huge variety and the complexity of the 3D fiber architecture makes the prediction of mechanical properties of 3D composites a challenging task, as their deformation and failure mechanisms are very complex and can show large differences as a function of the loading conditions and of the 3D fiber preform, especially when several fiber types are combined in a single material. In general, it can be concluded that the use of hybrid 3D woven composites is limited by the lack of experimental data, analytical models and affordable numerical strategies.

This work provides a comprehensive study of the mechanical response of a hybrid 3D orthogonal woven composite subjected to quasi-static and impact loads. The work studies in detail the influence of the through-thickness reinforcement and of hybridization on the mechanical response of a composite made up of epoxy-vinylester resin reinforced with glass, carbon and polyethylene fibers. To this end, experimental tests were combined with analytical models and an extensive damage inspection campaign. The information extracted from experimental tests was used to validate a numerical model, which accounts not only for the interply and intraply failure mechanisms, but also for the effect of the z-yarn. Unlike most of the models available in the literature, which are based on micromechanical approaches and the use of representative volume elements, this model can be used to reproduce complex loading states, such as impact, with an affordable computational cost.

Outline

This thesis dissertation is divided into two parts. The first part addresses the quasi-static response of the hybrid 3D orthogonal woven composite under tension, compression and shear (Chapters 3, 4 and 5), whereas the second part analyzes the damage tolerance (Chapter 6) and the mechanical response of the material under low- and high-velocity impact (Chapter 7). The material and the X-Ray tomography technique are previously described in Chapter 2.

It is worth noting that the quasi-static part includes also fibre yarn tensile tests, load-unload tensile test of coupons, as well as open-hole coupon tests in tension and compression.

Moreover, the influence of the z-yarns on the out-of-plane shear response of the composite material is studied in Chapter 5.

CHAPTER 2

Materials and Experimental Techniques

2.1 Material description

A composite panel was manufactured by vacuum infusion of an epoxy-vinylester resin (Derakane 8084) into a hybrid 3D orthogonal woven composite. Both the dry perform and composite panel were provided by 3TEX, Inc. (Cary, North Carolina, USA) with the commercial name p3w-d00001-hx21 (Figure 2.1). The preform was manufactured by using the 3WEAVE® technique, Mansour H. Mohamed & Mahmoud M. Salama (2001), Yushanov *et al.* (1999). This technique is characterized by the simultaneous insertion of all of the fill-directional yarns by special system of rapiers moved between the layers of warp directional yarns in each cycle of weaving operation; the use of special multi-harness system for through-thickness yarn insertion enabling to produce certain complex shapes and various hybrid fiber architectures; gentleness of the weaving method to all fibers, owed to a relatively low machine speed, and especially gentle treatment of warp-directional fibers which do not go through harness frames, Bogdanovich (2007).

The preform was non-symmetric and consisted of three warp (0) and four fill (90) fiber layers stacked as a cross-ply laminate $[90_c,0_c,90_{c/s2},0_{s2},90_{s2},0_{s2},90_{s2}]$. The diagram of the 3D

(a) carbon face   (b) glass face
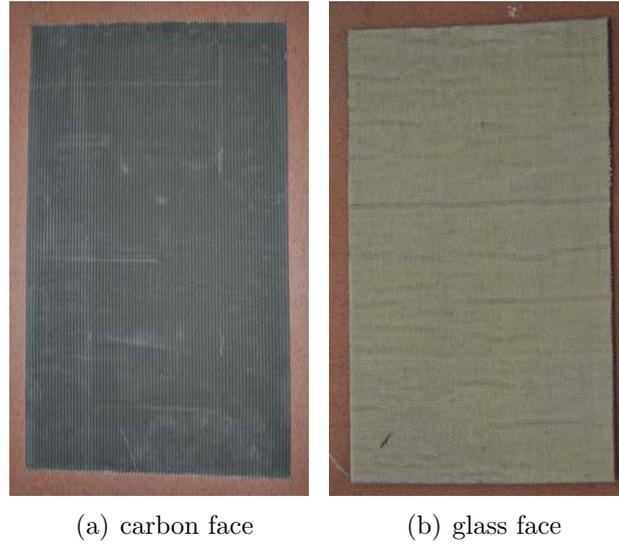
Figure 2.1: Flat infused panel of the hybrid 3D woven composite.

preform is shown in Figure 2.2(a). The fibers in the inner layers were distributed in yarns rectangular in shape, whereas the shape was elliptical in the outer layers (Figure 2.2(b)). The top four layers were made up of S2 glass fibers and the bottom 2 layers of AS4C carbon fibers. The hybrid layer (containing glass and carbon fibers) oriented in the fill direction was located between the glass and the carbon layers. Each tow of this layer contained both AS4C and S2 glass fibers, which were not intermingled but separated in two different zones of the tow (i.e. one half of the tow was formed by carbon fibers and the other half by glass fibers). It should also be noticed that every other tow was missing in the carbon layer oriented in the warp direction. In addition, the composite panel was reinforced in the through-thickness direction by z-yarn binders made up of ultra-high molecular weight polyethylene (PE) fiber (Dyneema SK75) that went from top to bottom layers in the warp direction. Note that consecutive z-yarns were *out of phase*. The diameter of the glass, carbon and dyneema fibers were 9 μm, 6.9 μm and 21 μm, respectively.

The nominal thickness of the dry fabric was 3.02 mm and its areal density was 4.24 kg/m^2. The nominal thickness of the composite was 4.1 mm, with an areal density of 6.44 kg/m^2. The overall fiber volume fraction in the composite was 47%. The areal density of the individual plies and the fiber density were provided by the manufacturer (Table 2.1). These data were used to obtain the volume fraction of each type of fiber in each direction (warp or fill), as shown in Table 2.2. In addition, the matrix volume fraction was

18

(a)

carbon yarn

hybrid yarn

glass yarn

glass yarn

z-yarn

z-yarn

warp direction

2 mm
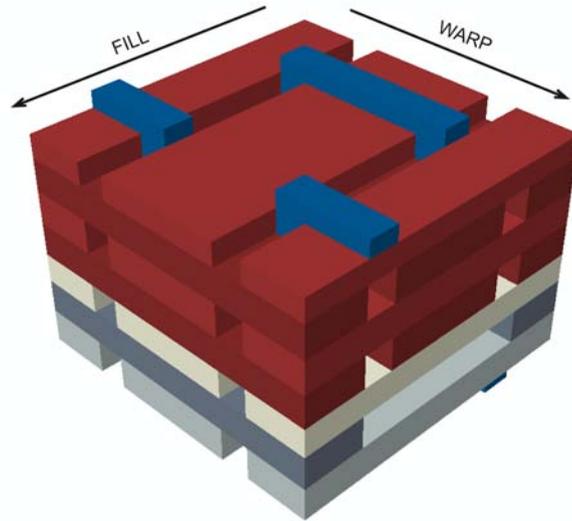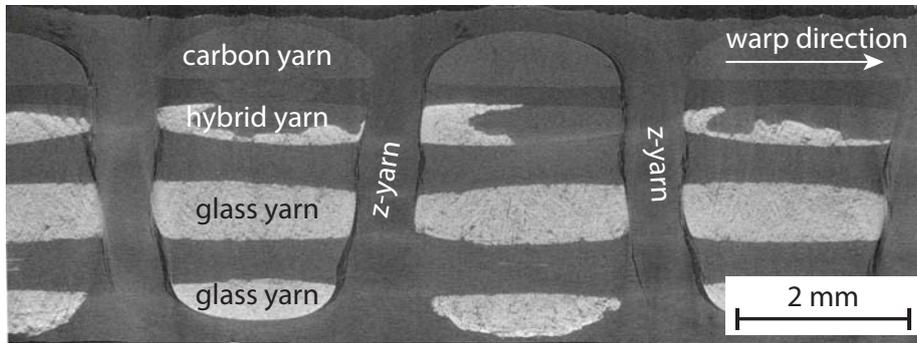
(b)

Figure 2.2: (a) Schematic of the unit cell of the hybrid 3D woven fiber preform. Carbon fiber bundles are shown in grey (dark grey for the warp direction and light grey for the fill), hybrid bundles in white and glass fiber bundles in red (dark red in the warp direction and light red in the fill direction). PE z-yarn binders in the warp direction are plotted in navy blue. (b) XCT tomography of the internal structure of the material.

determined from the matrix density and the weight of the composite panel before and after infiltration. This is also given in Table 2.2.

The local volume fraction V_f of fibers within the yarns was measured by optical microscopy, whereas the volume fraction of yarns within each ply V_g was measured by using XCT. Values varied in both cases from approximately 0.62 to 0.70, which led to a global volume fraction of fibers within each lamina $V_0 = V_f V_g = 0.43 - 0.50$.

layer	fibre	areal density g/m^2	yarn spacing $yarn/mm$
7 fill	Agy S2-glass	427.2	0.3228
6 warp	Agy S2-glass	779.8	0.3937
5 fill	Agy S2-glass	854.4	0.3228
4 warp	Agy S2-glass	779.8	0.3937
3 fill	S2-glass / carbon	213.6 / 261.1	0.3228
2 warp	AS4C carbon	315.3	0.3937
1 fill	AS4C carbon	518.8	0.3228
warp weaver	Polyethylene SK75	74.6	0.3937

Table 2.1: Details of the dry fabric provided by 3TEX, Inc.

Material	ρ (g/cm^3)	warp (%)	fill (%)	total (%)
Glass S2	2.48	15.4	14.7	30.1
Carbon AS4C	1.78	4.3	10.7	15.0
Polyethylene SK75	0.97	1.9	—	1.9
Total fibers		21.6	25.4	47
Matrix	1.02			53

Table 2.2: Density (ρ) and volume fraction of matrix and fibers as a function of fiber type and orientation within the hybrid composite.

2.2   Experimental techniques

To measure strains during the mechanical tests, both extensometry and digital image correlation (DIC) were used. The latter is a non-contacting optical technique to measure the displacement field on the surface of a specimen at different stages during deformation. The full strain field on the surface can be obtained afterwards as the derivative of the displacement field. The foundation of the technique is very simple: the displacement field is computed by tracking the distribution of grey intensity on the specimen surface in images acquired at different stages upon loading, Canal *et al.* (2012a).

The microstructure of the material was inspected by using several techniques, namely optical microscopy, scanning electron microscopy (SEM), C-scan ultrasounds and X-Ray computed tomography (XCT). Optical microscopy is easy-to-use, cost-effective and can be used for any material, whereas SEM provides an excellent resolution. However, such techniques only provide information of a specific section and, moreover, damage can be introduced during sample preparation. C-scan is widely used in aerospace industry to measure delamination in composites, but is unable to determine the shape of the flaws nor distinguish between failure modes. XCT is particularly powerful, because it enables the visualization of a 3D image so that the reconstructed volume can be cut by any plane; it is also a non-destructive technique which ensures that the sample is free of damage. The technique is further described below.

X-ray computed tomography

XCT is a non-destructive imaging technique in which the 3D view of an object can be reconstructed from several X-ray images collected at different angles. X-rays are generated by the acceleration of electrons towards a target material, normally made of a heavy element, such us tungsten or molybdenum. The electrons are extracted from a tungsten filament (cathode) with a V-shape when a high voltage is applied to it (Figure 2.3). The accelerated electrons travel inside a vacuum tube towards the anode and then to the end of the tube where they crash against the target, which is positioned in between the X-ray source and the detector. The interactions of the electron beam with the atoms of the target material produce the X-ray spectrum that is used for the tomographic scan. X-rays traveling through the sample are attenuated depending on the absorption coefficient of the
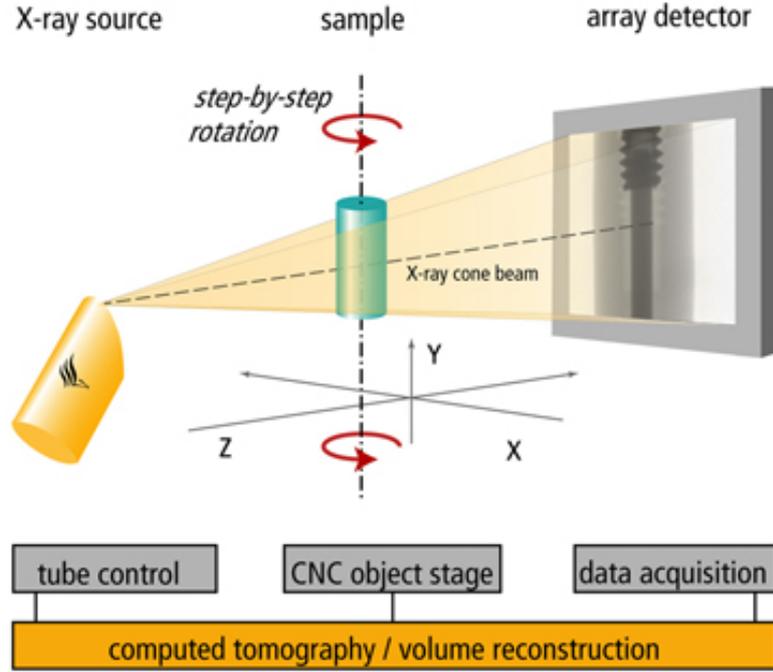
Figure 2.3: Scheme of working principle of an open X-ray tube with a transmission target.

material and the energy of the incident X-ray beam reaching the detector which records a radiography.

The sample can be modeled as a two or three-dimensional distribution of the X-ray attenuation coefficient, $\mu(x,y)$, which is a property that characterizes the ability of the material to absorb X-ray from the beam source. The radiation intensity I transmitted through a layer of material, Figure 2.4, is related to the incident intensity I_0 according to Lambert-Beer's law, equation 2.1. This equation relates the total attenuation p(t) (ratio of transmitted to incident intensity of radiation) through the X-ray absorption coefficient of the material, $\mu(x,y)$:

$$p(t) = ln\frac{I}{I_0} = \exp\left[\int_\Gamma \mu(x,y)ds\right] \tag{2.1}$$

where the line integral represents the total attenuation suffered by the X-ray beam traveling along a straight path s(x,y) through the cross-section of the object and t the distance from each ray of parallel beam to the center of rotation, Figure 2.4.
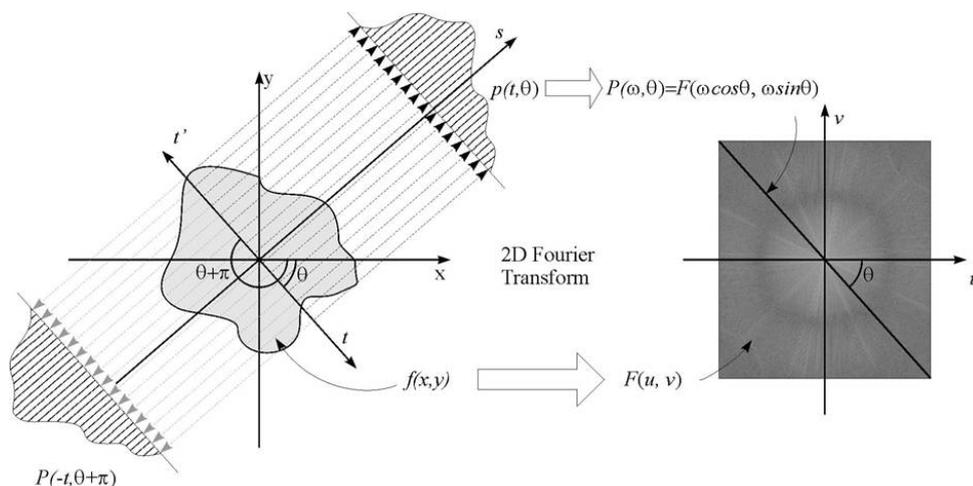
Figure 2.4: Principle of tomography and illustration of the Fourier slice theorem

The procedure for the reconstruction of a sample volume from the radiographies collected at different angles θ of rotation is summarized briefly, and explained on a parallel beam configuration for simplicity. During radiography collection, sample rotates around the z-axis (perpendicular to the paper). The cross-section of the sample is described by the function $f(x, y)$. The X-ray beam is assumed to be formed by parallel rays. When each ray passes through the sample, part of the radiation is absorbed and the attenuated intensity, $p(t, \theta)$, is collected in the detector. The attenuation will depend on the absorption coefficient of the material crossed and on the length of the path s through the sample.

Once the different projections are recorded for a set of rotation angles, the next step is to obtain the tomographic reconstruction of the original object. The object is reconstructed by means of the projection-slice theorem, Herman (1980), Kak & Slaney (1987). This theorem establishes that the reconstruction of the object $f(x, y)$ is possible from the X-ray attenuation projections acquired at infinite rotation angles, $p(t, \theta)$. This function $p(t, \theta)$ is also known as the Radon transform. The projection-slice theorem states that it is possible reconstruct the cross-section of the object by f(x,y) finding the inverse Radon function of $p(\omega, \theta)$ (Fourier inverse transform). By stacking up a series of cross-sections a volume of the object is obtained. Unfortunately, the inverse Radon transform is extremely unstable with respect to noisy data. In practice, a stabilized and discretized version of the inverse Radon transform (known as the Filtered Back Projection algorithm) Herman (1980), Kak & Slaney (1987) is used. The idea of the back projection is to assign to each point of the object the average intensity of all the projections that pass through that point. The

back projected image is, however, a blurred version of the original object. To overcome this effect, the reconstructed object is filtered using a high pass filter. Finally, the object is reconstructed by means of specific interpolation techniques. All the samples studied in this work were reconstructed using the algorithm based on the filtered back-projection procedure.

CHAPTER 3

Tensile Behaviour

The main goal of this chapter is to present a detailed analysis of the mechanical response and failure micromechanisms in tension of the hybrid 3D orthogonal woven composite. Plain and open-hole composite coupons were tested in tension until failure in the fill and warp directions. The macroscopic evolution of damage in the composite coupons was assessed by means of periodic unloading-reloading (to obtain the elastic modulus and the residual strain), whereas the microscopic mechanisms were established by means of X-ray computed microtomography. To this end, specimens were periodically removed from the mechanical testing machine and infiltrated with ZnI-containing liquid to assess the main damage modes as a function of the applied strain. Damage inspection was completed with the examination of post-mortem specimens by means of optical microscopy, scanning electron microscopy and XCT. In addition, fiber tows were extracted from the dry fabric, impregnated with the matrix and tested in tension. The experimental observations and the predictions of an isostrain model were used to understand the key factors controlling the elastic modulus, strength and notch sensitivity of hybrid 3D woven composites in tension. In addition, an analytical model based on Finite Fracture Mechanics was used to predict the notch behavior. All this information provides a comprehensive picture of the effect of fiber hybridization, 3D fiber architecture, crimping and damage on the mechanical behavior of hybrid 3D woven composites in tension.

3.1 Fiber yarns

3.1.1 Experimental techniques

In addition to the composite specimens, the mechanical properties of the different fiber yarns were also measured following the recommendations of the ASTM D4018 (1999).

Individual tows of carbon, glass and polyethylene were carefully extracted from the dry fabric to avoid damage. They were impregnated with Derakane 8084 epoxy-vinylester resin and cured at room temperature, following the instructions of the resin manufacturer, with a gelification time of 30 min. The procedure is illustrated in Figure 3.1. The linear density of the fiber tows before and after impregnation was measured. Cu tabs were glued to the impregnated tows, leading to a free length of 150 mm. They were tested in tension until failure under stroke control at 5 mm/min. Load and strain were continuously recorded during the test, the latter with an extensometer.

Thermo-gravimetric analyses of the impregnated carbon and glass yarns were conducted in a TGA Q50 Thermal Analyser (TA Instruments). All experiments were carried out in air with a purge rate of 60 ml/min and a heating rate of 10°C/min up to 1000°C. The sample weight was approximately 10 mg and 18 mg for carbon and glass fiber tows, respectively. The fiber weight fractions were 64% and 69% for carbon and glass fibers, respectively, which led to fiber volume fractions of 50.5% and 48%. This methodology could not be used to obtain the fiber volume fraction in the PE fiber yarns because of the low melting point of the fibers.

Six tows were tested in tension until failure for each fiber type. The average stress in the fibers is plotted as a function of the applied strain in Figure 3.2 for the carbon (AS4C), glass (S2) and polyethylene (SK75) fibers. The matrix contribution was neglected in the stress analysis and the average stress in the carbon and glass fibers was computed from the applied load P, the tow cross-section and the fiber volume fraction, as determined by the thermo-gravimetric analysis. In the case of the PE yarns, the average fiber stress was computed as $P\rho_f/\lambda_y$, where ρ_f stands for the fiber density and λ_y is the linear density of the dry yarn.

(a) Applying moulding release agent

(b) Stirring

(c) Pouring

(d) Tool
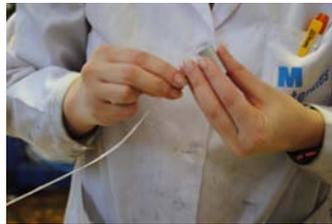
(e) Threading

(f) Impregnating

(g) Draining

(h) Sliding and tightening
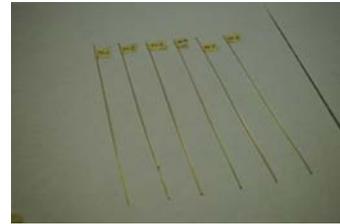
(i) Specimens without tabs

(j) Tabbing
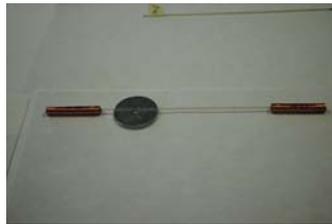
(k) Centering tabs
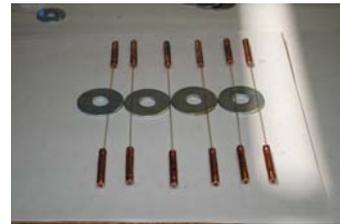
(l) Final specimens

**Figure 3.1:** Yarn impregnation procedure
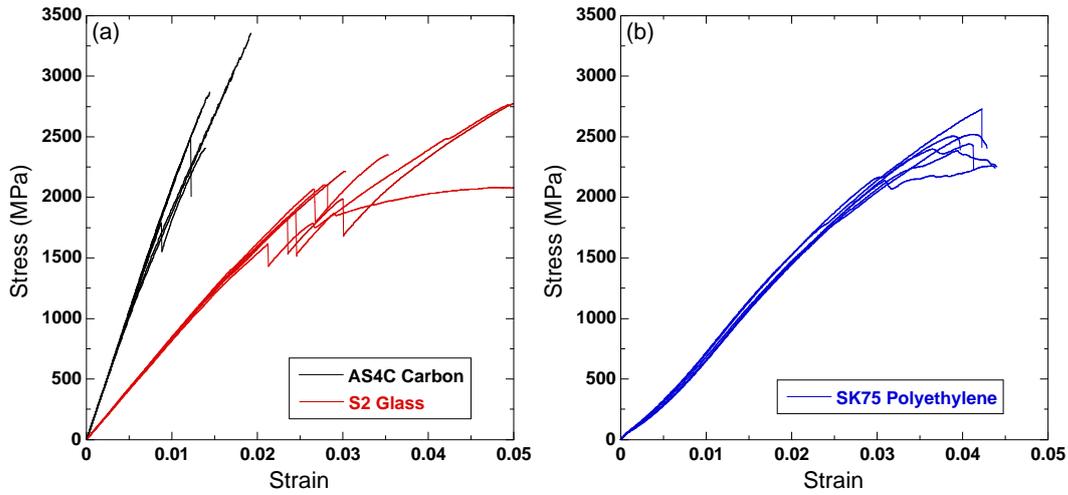
Figure 3.2: Stress-strain curves of the fiber tows. (a) Carbon and glass fiber tows (b) Polyethylene fiber yarns

3.1.2   Results and discussion

The carbon tows (Figure 3.2a) presented a linear elastic behavior up to 0.5% strain. Beyond this point, three specimens showed a slight reduction in stiffness, whereas two maintained the initial modulus until failure. One specimen presented evidence of damage (sudden stress drop) before final failure. All of them failed in a brittle fashion when the strain was in the range 1.2% - 1.9 %. Evidence of carbon stiffening was not found in these tests. The glass fiber tows (Figure 3.2a) also presented a linear elastic behavior up to 1.6%. The elastic modulus decreased with the applied strain beyond this point and damage prior to failure was observed in most of the yarns for applied strains in the range 2% to 3%. Final fracture occurred in a brittle fashion, as in the case of the carbon fiber tows, although at higher strains (in the range 3% to 5%). The PE fiber yarns (Figure 3.2b) showed a more ductile behavior and the stress-strain curves were non-linear in the whole range of deformation. The elastic modulus increased up to 1.0-1.5% strain and then decreased up to failure, which occurred at an applied strain in the range 4.0%-4.3%. It should be noted that the scatter in the stress-strain curves of the PE yarns was very small. The average elastic modulus, failure strain and tensile strength of the fiber tows, together with the corresponding standard deviations, are summarized in Table 3.1.

28

Table 3.1: Elastic modulus, tensile strength and fracture strain of the fibers within the fiber yarns

Fiber type	Elastic modulus (GPa)	Tensile strength (GPa)	Failure strain (%)
Glass S2	82 ± 1	2.4 ± 0.3	4.0 ± 1.0
Carbon AS4C	207 ± 2	2.8 ± 0.4	1.5 ± 0.2
Polyethylene SK75	85 ± 1	2.5 ± 0.2	4.1 ± 0.2

3.2   Tensile properties of plain coupons

3.2.1   Experimental techniques

Rectangular specimens of $250 \times 25 \times 4.1$ mm^3 were machined from the plate with the longest dimension aligned in either the warp or the fill direction for the mechanical tests. Glass fiber tabs of 50 mm in length were glued to the specimens, leading to a free length of 150 mm. They were tested in tension in an electromechanical universal testing machine (Instron 3384) following the recommendations of the ASTM D3039 (2000). Tests were carried out under stroke control at 2 mm/min and the load was continuously measured during the test with a load cell of 150 KN. Since composite is non-symmetric (and coupling between bending and extension might occur), the longitudinal strain was recorded on both faces of the specimen using an extensometer of 50 mm gage length on one face and digital image correlation (Vic2D) on the other. Periodic unloading-reloading was carried out in one test in each direction (warp or fill) to estimate the stiffness degradation as a function the applied strain.

XCT of the specimens was performed with a Nanotom 160NF (Phoenix) at 70-90 KV and 120-180 μA using a W target. 1800 radiographs were acquired for each tomogram with an exposure time of 1000 ms. The reconstructed volumes presented a resolution of 13-15 μm/voxel. Emphasis was placed on the qualitative assessment of the main damage mechanism in each material as a function of applied strain rather than in the quantification of specific damage modes (delaminated surface, volume of cracked tows, fraction of broken fibers, etc.).

The damage micromechanisms in the composite specimens tested in tension in the warp and fill directions were analyzed as a function of the applied strain by means of XCT. To
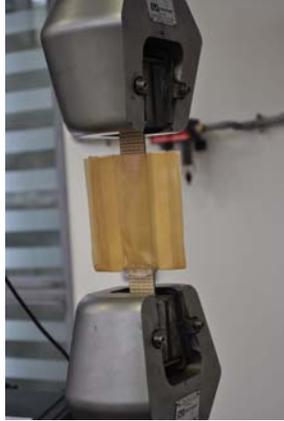
Figure 3.3: Specimen immersion in dye penetrant liquid prior to testing.

this end, tow coupons in each direction were deformed up to pre-defined strains. The tests were stopped and the specimens were immersed in a liquid for 2 hours while holding the displacement constant to facilitate the penetration of the liquid into the cracks (see Figure 3.3). The liquid was composed of 60 g of ZnI in 10 ml of water, 10 ml of ethanol and 10 ml of Kodak Photo-Flo 200. The specimens were removed from the machine and inspected by XCT as detailed below. Previous investigations have demonstrated that the immersion in this liquid does not modify the damage mechanisms in composites Sket *et al.* (2014).

Finally, post-mortem specimens were inspected by using three different techniques: optical microscopy, scanning electron microscopy and XCT:

- *Optical microscopy.* An optical microscope (Olympus BX-51) was used to inspect four sections located parallel and perpendicular to the load in the warp and fill directions. Samples were previously grounded and polished according to the standard procedure.

- *Scanning electron microscopy* (EVO MA15, Zeiss) was used to inspect transverse sections of post-mortem samples loaded in either warp or fill direction. A cutting yarn machine was used, so that no polishing was required. Specimens were sputter-coated with gold during 60s with a current of 20 mA (Quorum, Q150T ES).

- Four post-mortem specimens were cut at an increasing distance to the failure section. Samples were cut perpendicular to the loading axis to obtain high resolution images (4-5 μm) while keeping the region of interest free of damage. The sample was examined by XCT without dye penetrant.

3.2.2 Results and discussion

Three tensile tests were carried out in the fill and warp directions. The corresponding stress-strain curves are plotted in Figures 3.4a and 3.4b. The strains were measured by conventional extensometry on the glass face of the coupon and by digital image correlation on the carbon face. They are plotted in Figure 3.4c for two representative tests in the fill and warp direction. The differences in the strain between both faces were negligible, indicating that the extension-bending coupling induced by the asymmetry of the composite did not play a significant role in the tensile behavior,[1] at least until the fracture of the carbon fibers.

The stress-strain curves in the fill direction (Figure 3.4a) presented a linear-elastic behavior up to a strain in the range 1.2% to 1.6%, which is similar to the failure strain of the carbon fiber tows (Figure 3.2a). There was a sudden drop in the load bearing capacity of the composite but the load increased slightly with further strain until catastrophic failure, which occurred at an applied strain below 2.5%. The initial part of the stress-strain curve was also linear in the warp direction (Figure 3.4b), but a slight non-linearity was detected before the load peak, which occurred when the applied strain was in the range 1.3% to 1.7%, as in the fill direction. Nevertheless, the load bearing capacity of the composite increased with further straining and the maximum strength was attained for applied strains in the range 2.1% to 3.1%, just before the coupon failed catastrophically. This failure strain is compatible with the development of damage in the glass fiber tows.

Thus, composite coupons loaded in tension along the fill and warp direction presented two peaks. The maximum strength along the fill direction was attained in the first peak and was controlled by the fracture of the AS4C carbon fiber yarns. The maximum strength in the warp direction was attained in the second peak and was controlled by the fracture of the S2 glass fiber tows. It should be noted that the main differences in the composite architecture between the fill and warp directions were the presence of an extra hybrid ply with the fibers oriented in the fill direction and that the PE z-yarn binders were oriented along the warp direction.

---

[1]Despite of the non-symmetry of the laminate, the coupling bending-extension within the elastic regime is almost negligible. The higher stiffness of the carbon layers is balanced with a higher number of glass layers. The value of the matrix B is presented in the Appendix A.
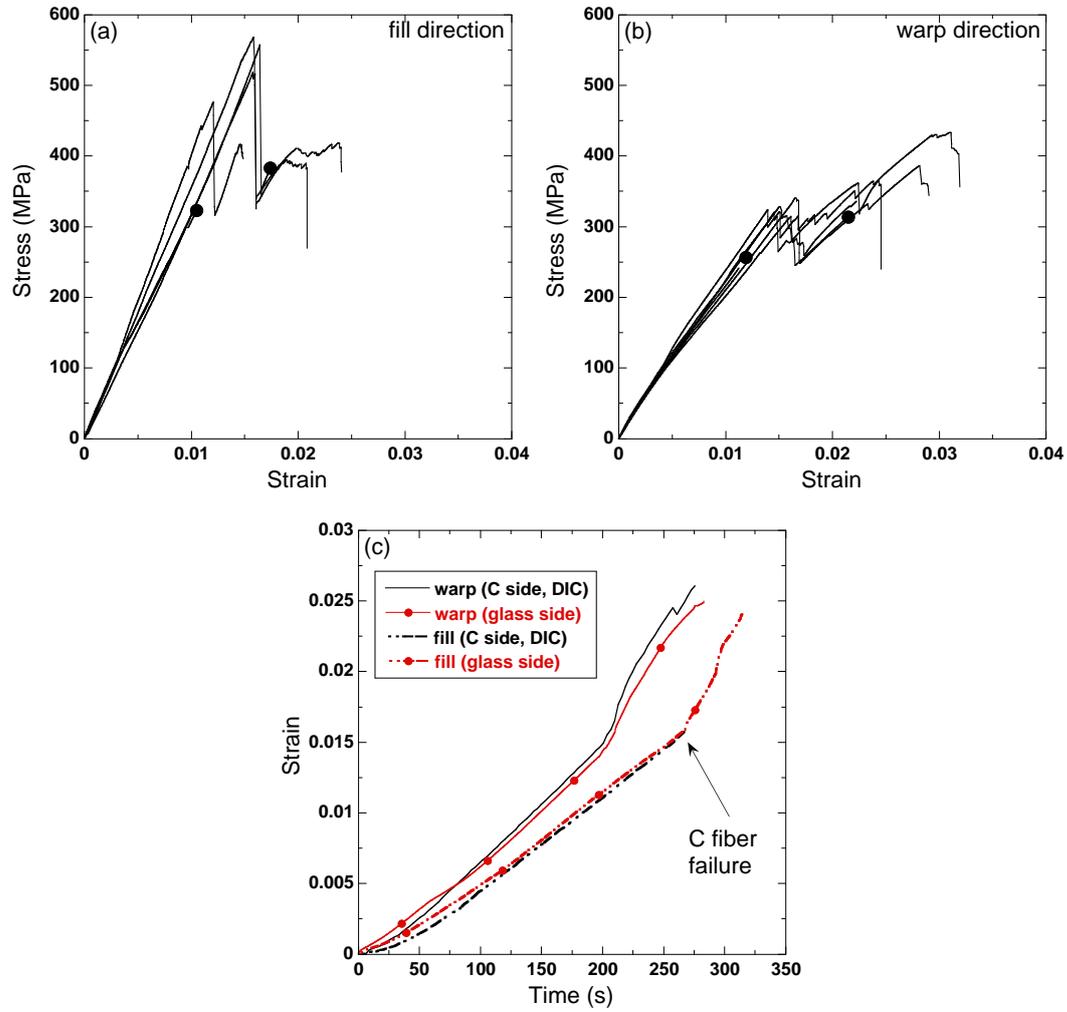
Figure 3.4: Stress-strain curves of the plain composite coupons. (a) Fill direction. (b) Warp direction. The solid circles in the curves indicate the instants in which the test was stopped and the coupons were examined by means of XCT. (c) Tensile strains measured by conventional extensometry on the glass face and by digital image correlation on the carbon face for two representative tests in the fill and warp direction, respectively.

32
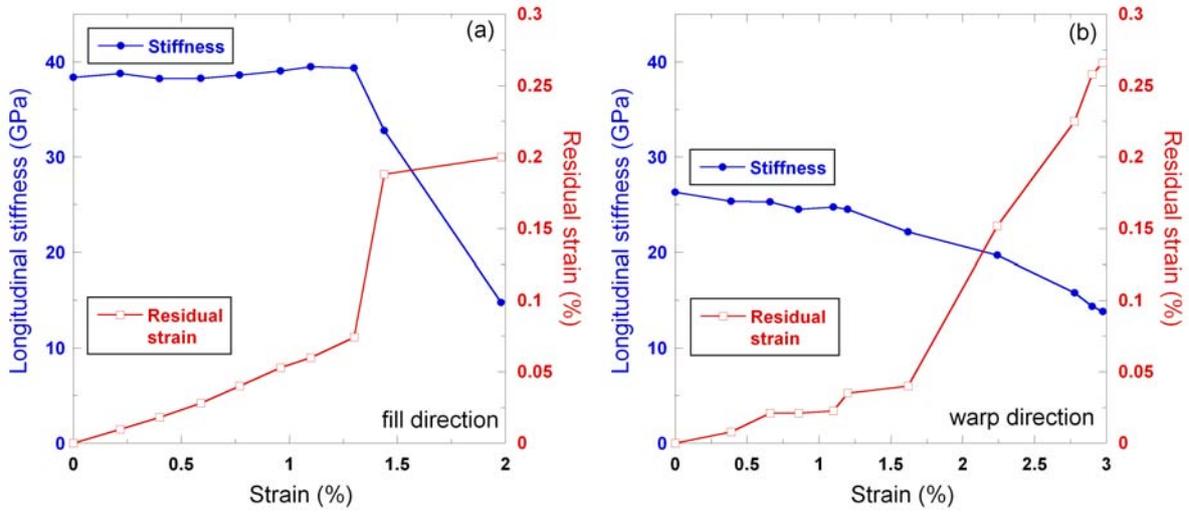
Figure 3.5: Evolution of the elastic modulus and of the residual strain (at zero load) with the applied strain. (a) Fill direction. (b) Warp direction.

The evolution of the stiffness as a function of the applied strain was obtained from the tests in which the coupon was periodically unloaded and reloaded. It is plotted in Figures 3.5a and 3.5b for the coupons deformed in the fill and warp directions, respectively. The stiffness was obtained from the slope of the stress-strain curve at the beginning of the unloading cycle, from the initial unloading point up to the point at which the load has decreased by 20%. The residual strain (understood as the longitudinal strain at zero load at the end of the unloading part of the cycle) is also plotted in these figures. In the case of the coupons deformed in the fill direction (Figure 3.5a), the stiffness remained constant (or even increased slightly) up to the onset of carbon fiber failure (1.3%-1.4%), even though the continuous increment of the residual strain in this range indicated the development of irreversible damage mechanisms in this region. It should be noted that the PE z-yarn oriented in the warp direction induced fiber crimping in the fill tows and the straightening of the carbon and glass fiber tows upon deformation could compensate the reduction in stiffness due to damage, leading to this plateau in the longitudinal stiffness. Fracture of the carbon fiber yarns led to a dramatic reduction in stiffness prior to failure while the permanent strain increased accordingly. In the coupons oriented along the warp direction (Figure 3.5b), stiffening of the coupon due to the straightening of glass and carbon fiber yarns was not significant and a continuous reduction in stiffness was observed from the beginning of the test, together with an increase in the residual strain. Both (reduction in

stiffness and increase in residual strain) were enhanced after fracture of the carbon fiber tows.

3.2.3 Damage and failure micromechanisms

Loading along the fill direction

XCT provides unique information regarding the microscopic damage and failure micromechanisms which develop during deformation of the complex 3D microstructure of the hybrid composite material. XCT was carried out in one coupon deformed in the fill direction and deformed up to strains of 1.05% and 1.74% (marked with solid circles in Figure 3a). The first analysis occurred in the linear region of the stress-strain curve, before carbon fiber breakage took place. Two cross-sections of the investigated volume parallel to the loading axis are shown in Figure 3.6. Bright regions in the tomograms correspond to cracks (or pores), whose contrast was enhanced by the presence of ZnI. The two carbon layers running in the fill and warp directions are at the top in Figure 3.6a. The missing yarn every other yarn in the warp direction is clearly visible in the same figure. The four glass fiber layers are at the bottom and the hybrid layer (light grey/dark grey contrast) is in between. The resin-rich area due to the missing yarn enhanced crimping of the adjacent carbon and carbon/glass yarns in the fill directions, leading to delamination of the fill tows from the matrix (marked with arrows). These delamination cracks propagated along the tows and notice that delamination was asymmetric: only the upper or the lower tow boundary was delaminated from the matrix. In addition, tensile transverse cracks were observed in the fiber tows oriented in the warp direction (perpendicular to the tensile loading). These cracks propagated through the matrix (and along the interface) within the fiber tows. The parallel cross-section in Figure 3.6b depicted the same failure mechanisms (namely, delamination of the carbon and hybrid fill tows from the matrix near the missing warp tows and tensile cracking of the warp tows) but it is worth noting that the PE z-yarns arrested the propagation of the delamination cracks. In addition, delamination of PE z-yarns was also evident (marked with arrows).
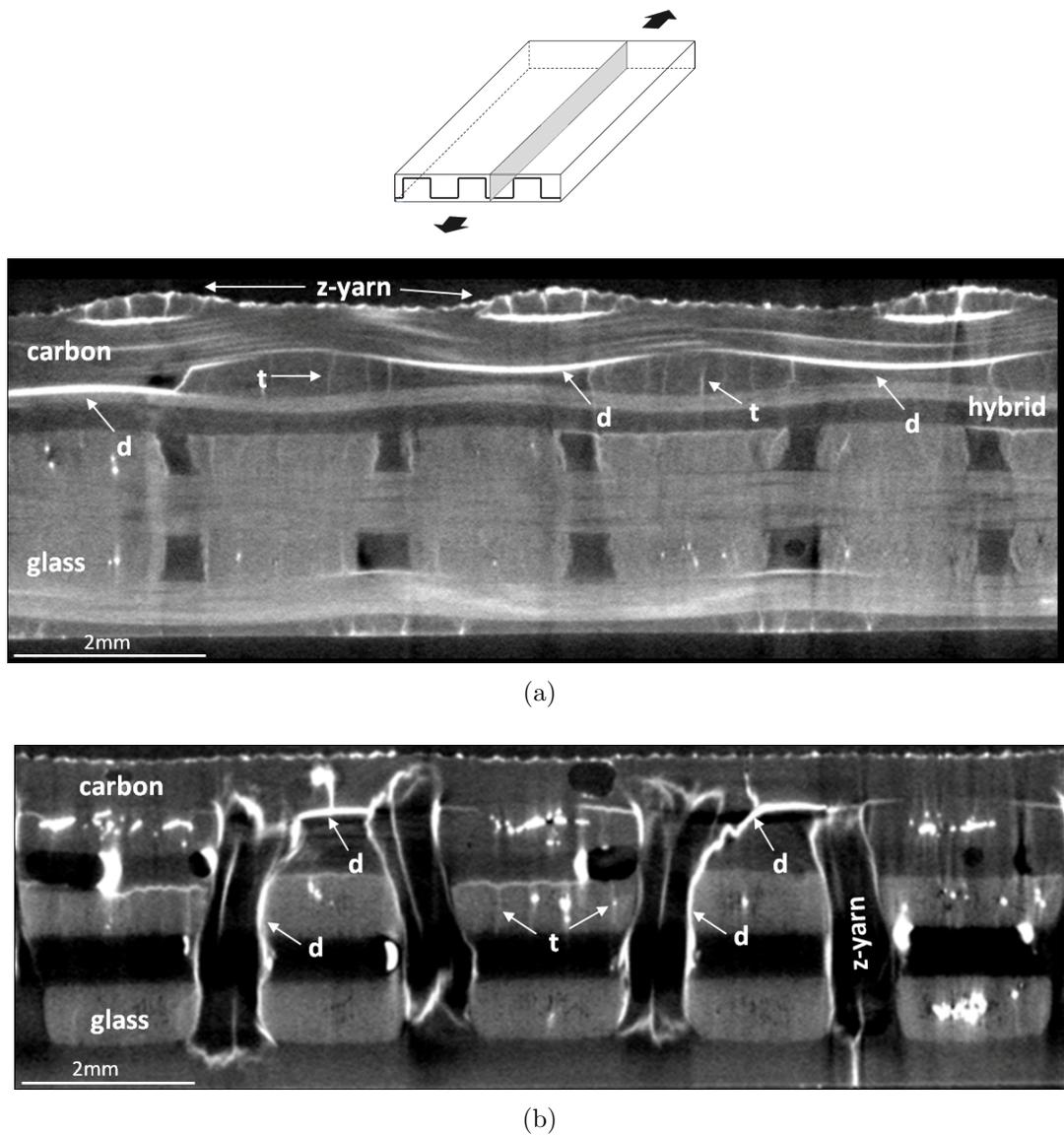
Figure 3.6: Tomograms of the coupon loaded in the fill direction up to 1.05% strain (a) Longitudinal section parallel to the (horizontal) loading axis. (b) Another longitudinal section parallel to the (horizontal) loading axis which contains the PE z-yarns. Glass fiber tows appear light grey, carbon fibers, PE z-yarns and matrix appear dark grey and white regions correspond to cracks infiltrated by ZnI. Arrows indicate the different damage mechanisms: **d** stands for delamination cracks from the fiber tows and z-yarns and **t** indicates transverse tensile cracks within the fiber tows.

Further information about the damage mechanisms was obtained from the cross-sections perpendicular to the loading axis, which are shown in Figure 3.7. The delamination cracks at the boundary of the carbon and glass fiber tows (already shown in Figure 3.6a) are also visible in these tomograms, together with delamination cracks at the boundary of PE z-yarns (Figure 3.7a). In addition, cracking within the fiber tows parallel to the loading axis (marked with arrows) was found (Figures 3.7a and 3.7b). Their number was higher in the fiber tows surrounded by the PE z-yarns (Figure 3.7a), in which cracks oriented in the horizontal and vertical direction are seen. The cracks parallel to the loading axis within the fiber tows could not be attributed to the far-field tensile stress field, but to the longitudinal shear stresses that develop within the tow as a result of asymmetric tow delamination from the matrix, i.e. the upper boundary of the tow delaminates from the matrix and deforms along the loading direction while the lower boundary remains adhered to the matrix (or *viceversa*).

The second XCT inspection of the specimen loaded in the fill direction was carried out at 1.74% strain after fracture of the carbon fiber tows. The tomograms in the longitudinal sections parallel to the loading axis are shown in Figure 3.8. Fracture of the carbon fiber tows is clearly visible in the upper region of the specimen, as well as extensive delamination of the fiber tows from the matrix (Figure 3.8a). In addition, delamination cracks propagated from one layer to another through the warp tows. The parallel section containing the PE z-yarns (Figure 3.8b) shows that they were able to arrest the longitudinal delamination cracks. In addition to these failure mechanisms, tensile cracks within the warp were found in both longitudinal sections. The inspection of the composite sections perpendicular to the loading axis (Figure 3.9) showed that fracture of the carbon tows enhanced the development of the delamination cracks at the boundary of all the fiber tows (carbon, glass and PE). As a result, the number of shear cracks parallel to the loading axis also increased and multiple shear cracks were visible within many glass fiber tows (Figure 3.9b).

The third inspection of the specimen loaded in the fill direction was carried out at $\varepsilon \approx 2.0\%$ after failure of the specimen. Optical microscopy was used for that purpose. As shown in Figure 3.10(a), extensive damage is observed in the carbon tows, whereas glass yarns remain intact at the section analysed. A closer examination (Figure 3.10(b)) revealed that damage actually initiated at the fiber-matrix interface.

(a)

(b)
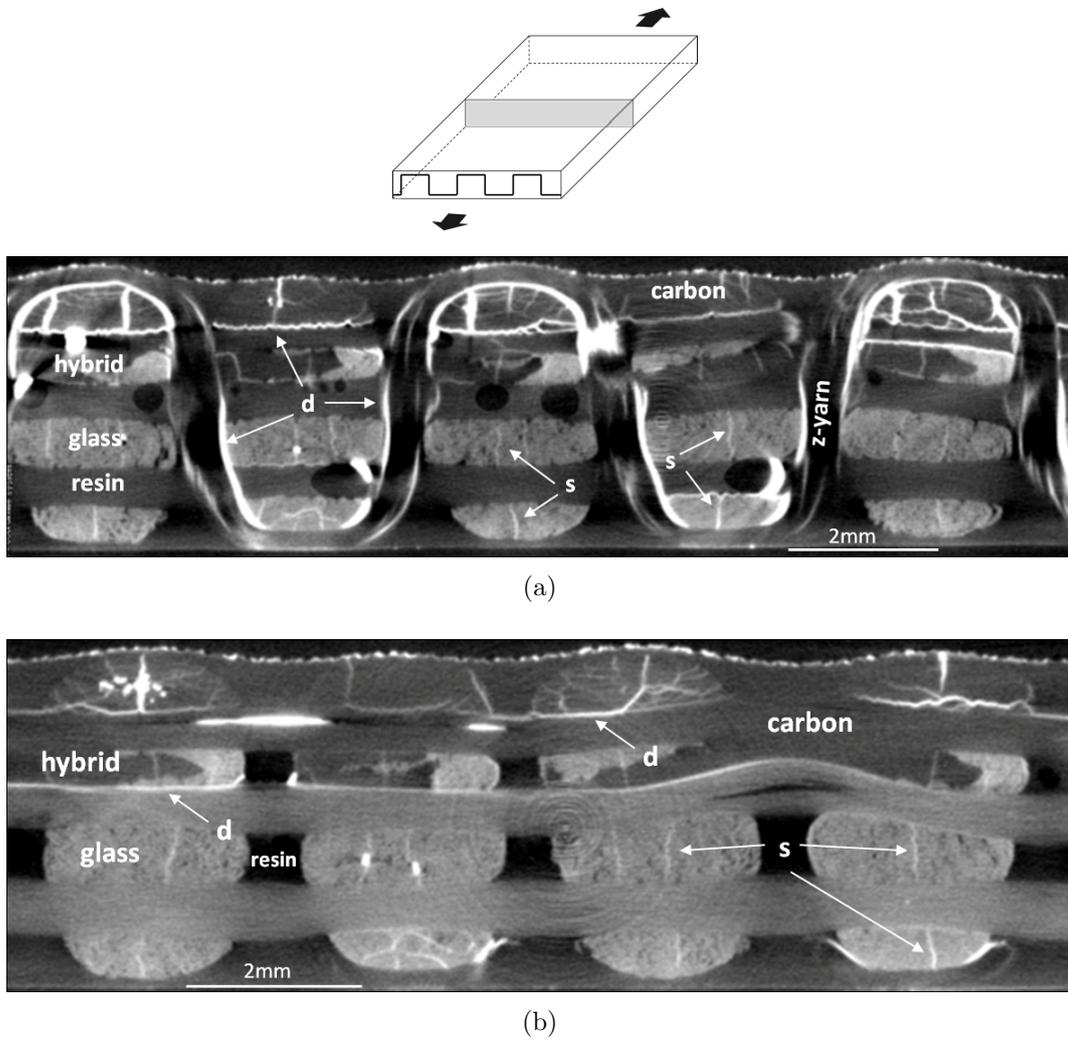
Figure 3.7: Tomograms of the coupon loaded in the fill direction up to 1.05% strain. (a) Transverse section perpendicular to the loading axis which contains the PE z-yarns. (b) Another transverse section perpendicular to the loading axis. Glass fiber tows appear light grey, carbon, PE fibers and matrix appear dark grey and white regions correspond to cracks infiltrated by ZnI. Arrows indicate the different damage mechanisms: **d** stands for delamination cracks from the fiber tows and z-yarns and **s** indicates shear cracks within the fiber tows.

(a)

(b)
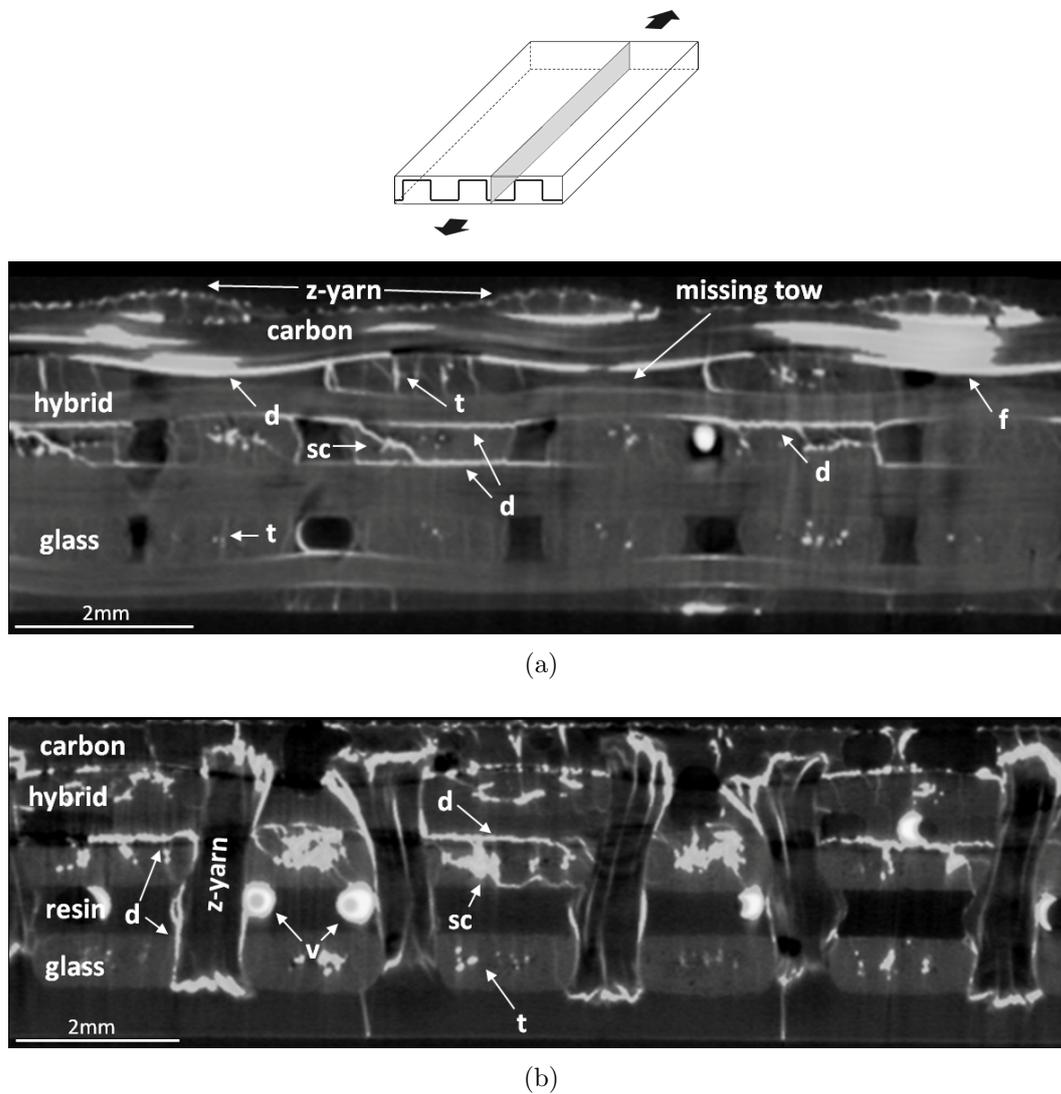
Figure 3.8: Tomograms of the coupon loaded in the fill direction up to 1.74% strain. (a) Longitudinal section parallel to the (horizontal) loading axis. (b) Another longitudinal section parallel to the (horizontal) loading axis which contains the PE z-yarns. Glass fiber yarns appear light grey, carbon fiber yarns and matrix appear dark grey and white regions correspond to cracks or voids infiltrated by ZnI. Arrows indicate the different damage mechanisms: **f** stands for the fracture of the carbon fiber tows, **t** tensile transverse cracks within the fiber tows, **d** delamination of the fiber tows, **sc** slanted translaminar cracks within the fiber tows created by propagation of delamination cracks through the tow and **v** voids.

(a)

(b)
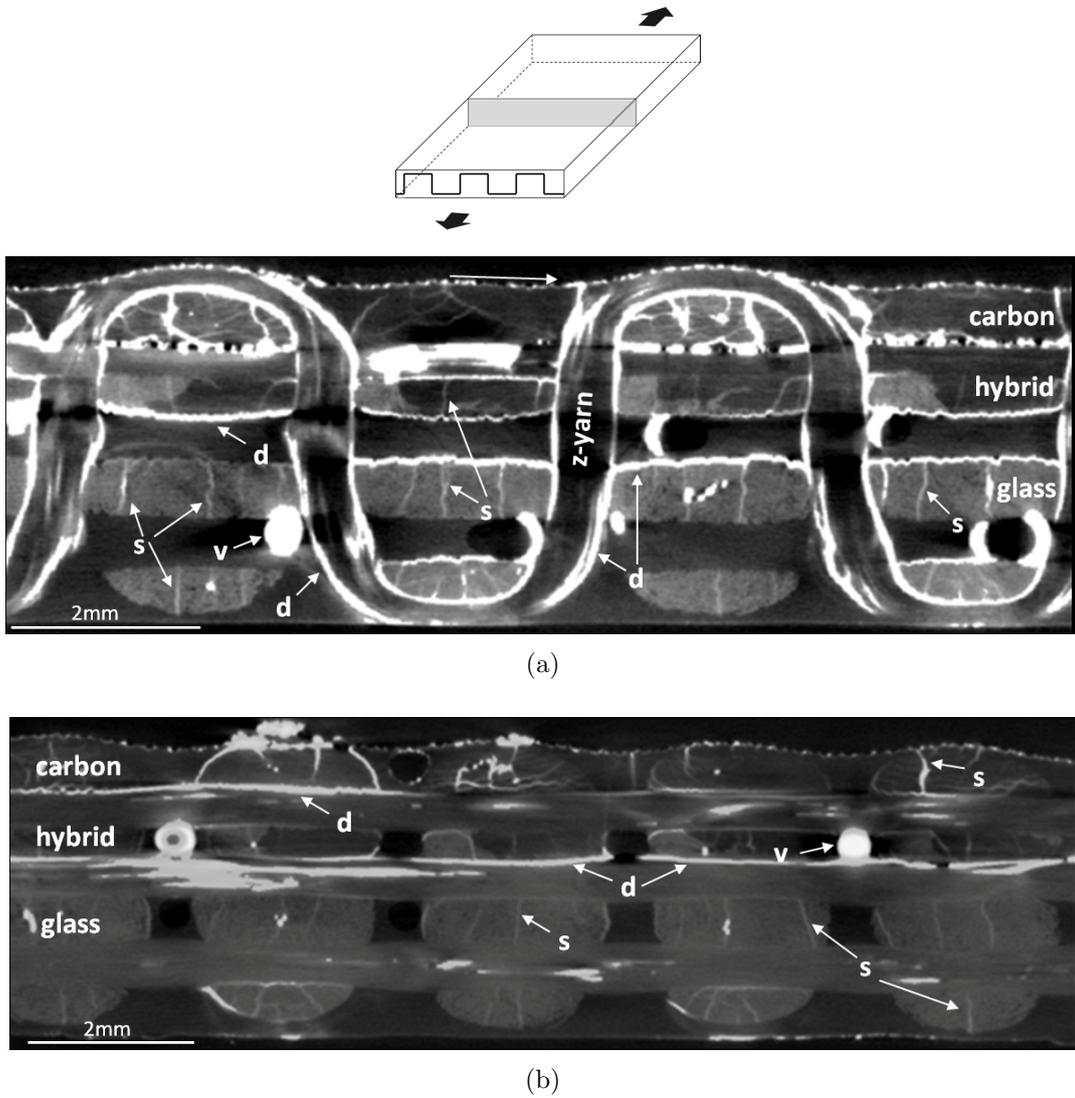
Figure 3.9: Tomograms of the coupon loaded in the fill direction up to 1.74% strain. (a) Transverse section perpendicular to the loading axis (b) Another transverse section perpendicular to the loading axis which contains the PE z-yarns. Glass fiber yarns appear light grey, carbon fiber yarns and matrix appear dark grey and white regions correspond to cracks or voids infiltrated by ZnI. Arrows indicate the different damage mechanisms: **t** tensile cracks within the fiber tows, **d** delamination of the fiber tows, **s** indicates shear cracks within the fiber tows, and **v** voids.
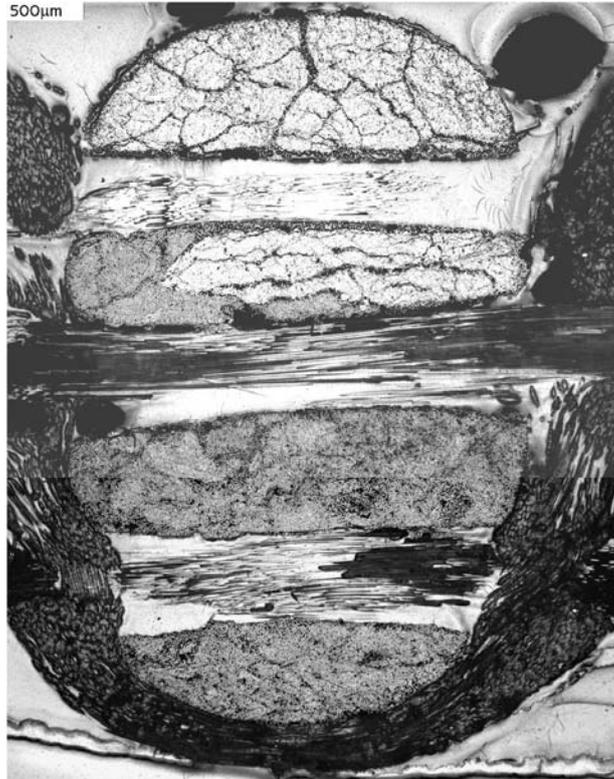
(a) Composition of two micrographs. The presence of cracks is much more evident in carbon and hybrid tows (top) than in glass yarns (bottom)
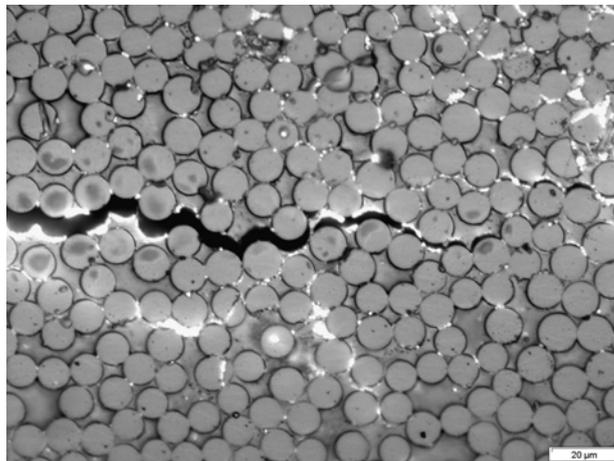
(b) Fiber-matrix debonding

Figure 3.10: Micrographs of the coupon loaded in the fill direction up to final failure. Transverse section perpendicular to the loading axis. Glass fiber yarns appear dark grey, carbon fiber yarns and matrix appear light grey.

Loading along the warp direction

XCT was carried out in one coupon deformed in the warp direction at strains of 1.19% and 2.15% (marked with solid circles in Figure 3.4b). The tomograms of cross-sections parallel and perpendicular to the loading axis deformed up to 1.19% are depicted in Figures 3.11 and 3.12, respectively. The main damage mechanisms observed in the longitudinal sections which did not contain PE z-yarns were fiber tow delamination and tensile transverse cracks within the fiber tows (Figure 3.11a). Delamination cracks were occasionally deflected into the fiber tows, propagated across the tow and led to another delamination crack at the opposite tow surface. The sections containing PE z-yarns also showed extensive delamination of the PE yarns from the matrix and carbon and glass fiber tows, while delamination cracks between matrix and carbon or glass were arrested by the z-yarns (Figure 3.11b).

The XCT of the sections perpendicular to the loading axis at 1.19% strain (Figure 3.12) showed the expected damage mechanisms: delamination cracks between the matrix and the fiber tows (PE, carbon and glass) as well as extensive shear cracks within the carbon and glass fiber tows induced by the asymmetric delamination of the fiber tows from the matrix.

XCT in the composite coupons loaded in the warp direction after the fracture of the carbon yarns are depicted in Figures 3.14 and 3.15. Figure 3.14 includes the cross-sections parallel to the loading axis, in which extensive tensile transverse cracks in the carbon tows appear as the main damage mechanism (Figure 3.14a). Delamination cracks at the fiber tow interfaces are visible but preferentially at the PE z-yarn boundaries (Figure 3.14b). They propagated into the carbon and glass fiber tows, leading to extensive intratow cracking. The cross sections perpendicular to the loading axis showed extensive damage in the carbon fiber tows (Figure 3.15), while shear cracking of the glass and hybrid fiber tows was visible throughout the section. Maximum shear crack density within the tows was found on the sections containing the PE z-yarns (Figure 3.15b) and it was triggered by the shear stresses within the tow promoted by the delamination of the z-yarns.

The third inspection of the specimen loaded in the warp direction was carried out at $\varepsilon \approx 2.8\%$ after failure of the specimen. Three different techniques were used for that

(a)

(b)
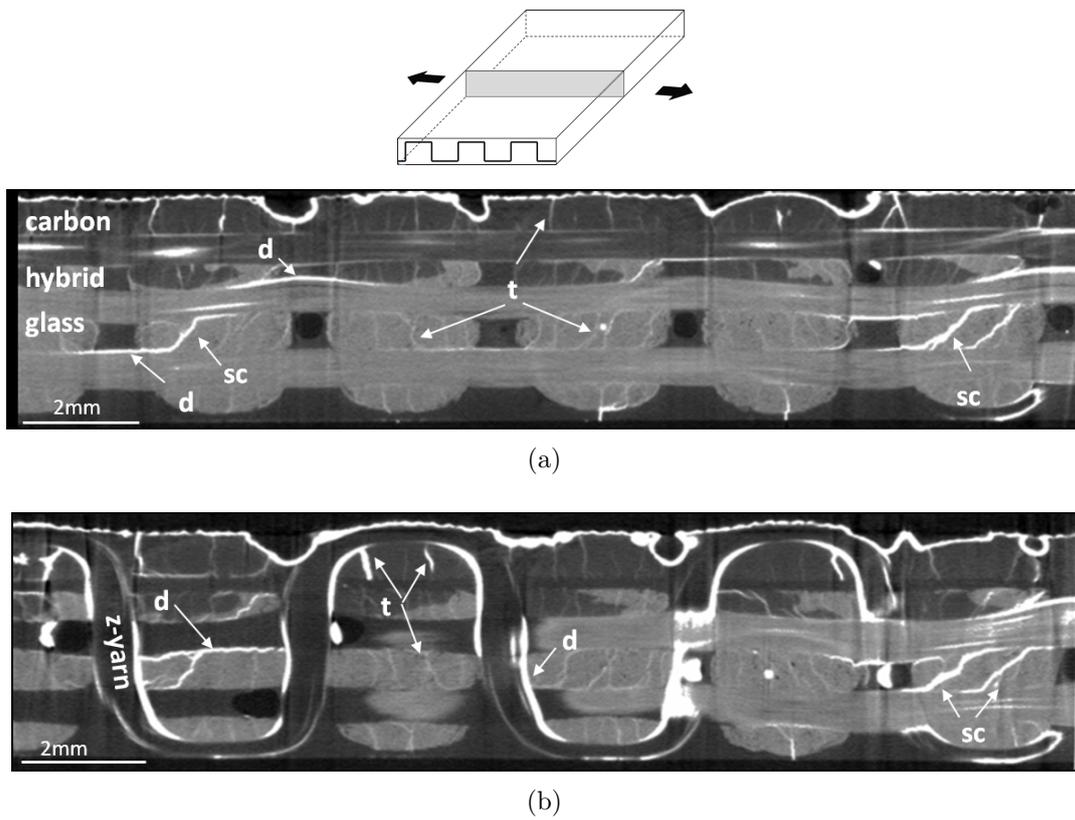
Figure 3.11: Tomograms of the coupon loaded in the warp direction up to 1.19% strain. (a) Longitudinal section parallel to the (horizontal) loading axis (b) Another longitudinal section parallel to the (horizontal) loading axis which contains the PE z-yarns. Glass fiber yarns appear light grey, carbon fiber yarns and matrix appear dark grey and white regions correspond to cracks infiltrated by ZnI. Arrows indicate the different damage mechanisms: **t** tensile transverse cracks within the fiber tows, **d** delamination of the fiber tows, **sc** slanted translaminar cracks within the fiber tows created by propagation of delamination cracks through the tow.

42
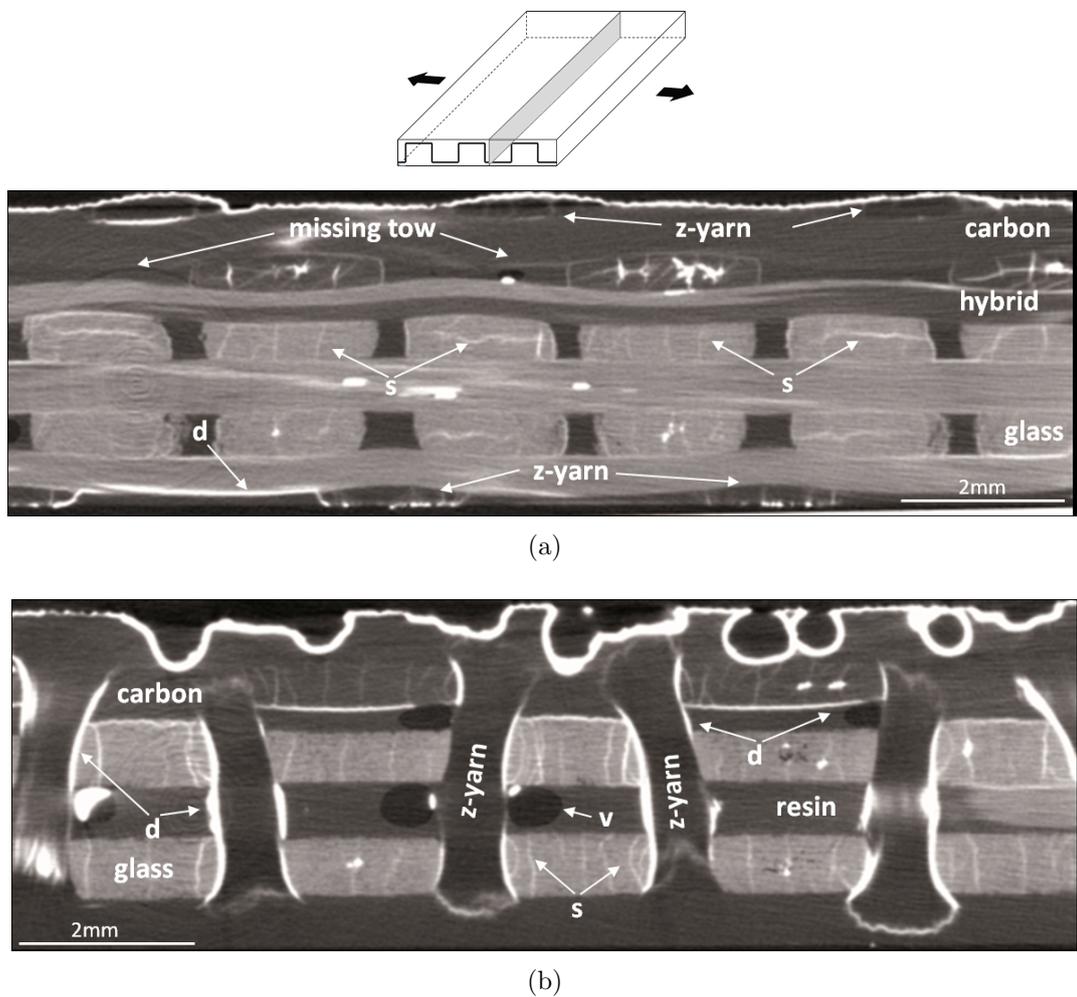
Figure 3.12: Tomograms of the coupon loaded in the warp direction up to 1.19% strain. (a) Transverse section perpendicular to the loading axis (b) Another transverse section perpendicular to the loading axis which contains the PE z-yarns. Glass fiber yarns appear light grey, carbon fiber yarns and matrix appear dark grey and white regions correspond to cracks infiltrated by ZnI. Arrows indicate the different damage mechanisms: **s** shear cracks within the fiber tows, **d** delamination of the fiber tows, and **v** indicated voids (which appear black).
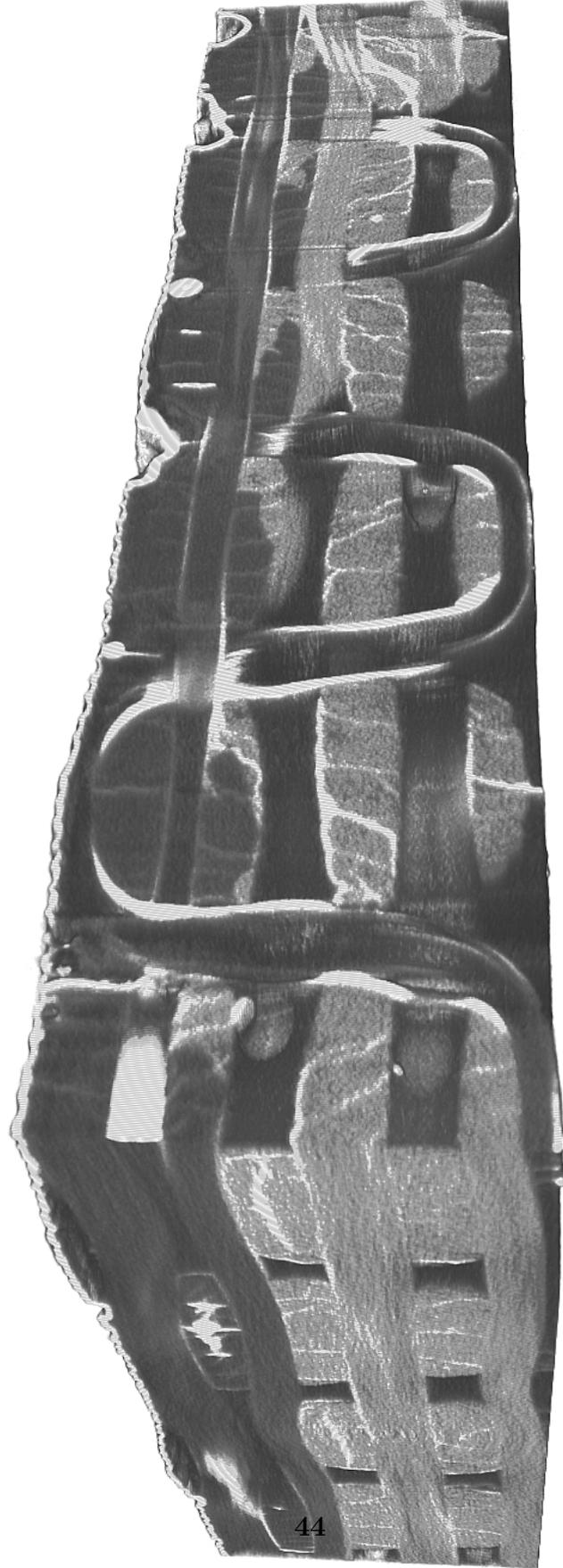
Figure 3.13: Hybrid 3D woven composite loaded in the warp direction. Isometric view.
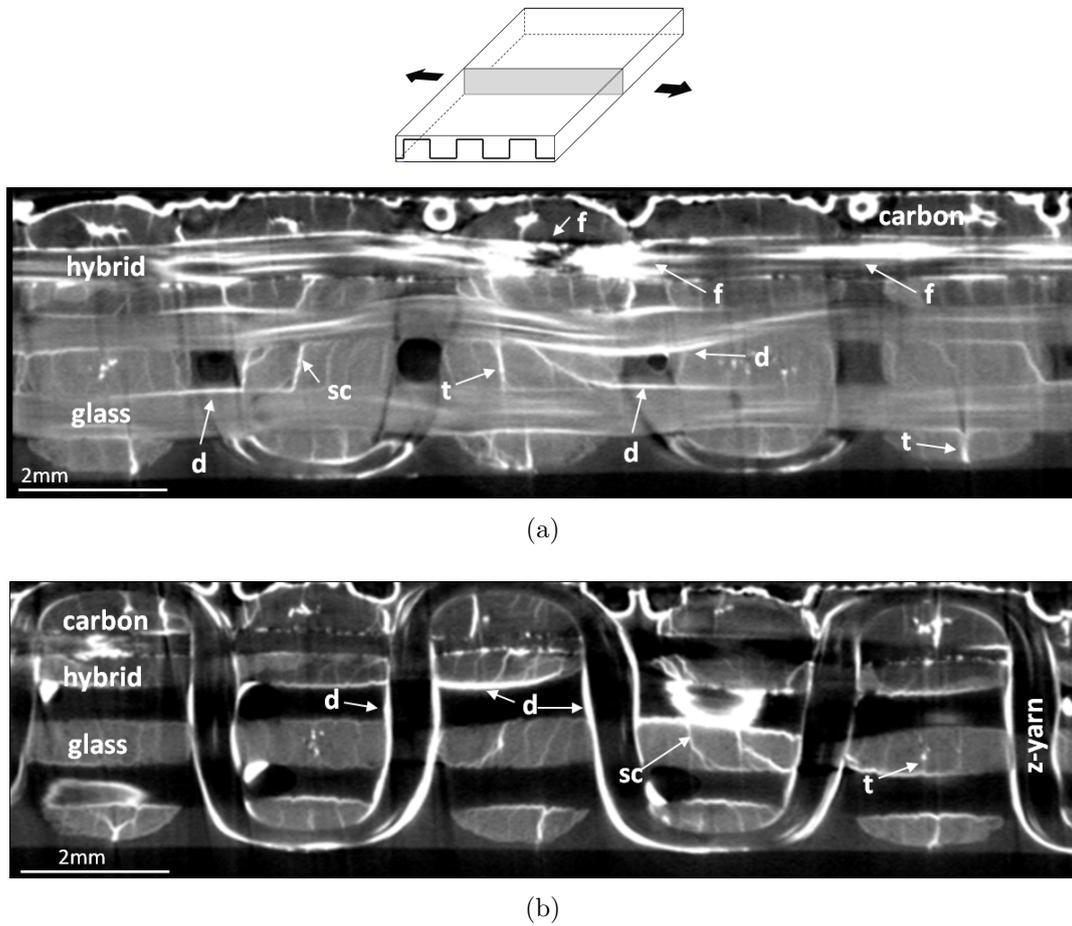
Figure 3.14: Tomograms of the coupon loaded in the warp direction up to 2.15% strain. (a) Longitudinal section parallel to the (horizontal) loading axis. (b) Another longitudinal section parallel to the (horizontal) loading axis which contains the PE z-yarns. Glass fiber yarns appear light grey, carbon fiber yarns and matrix appear dark grey and white regions correspond to cracks infiltrated by ZnI. Arrows indicate the different damage mechanisms: **f** stands for the fracture of the carbon fiber tows, **t** tensile transverse cracks within the fiber tows, **d** delamination of the fiber tows, **sc** slanted translaminar cracks within the fiber tows created by propagation of delamination cracks through the tow.
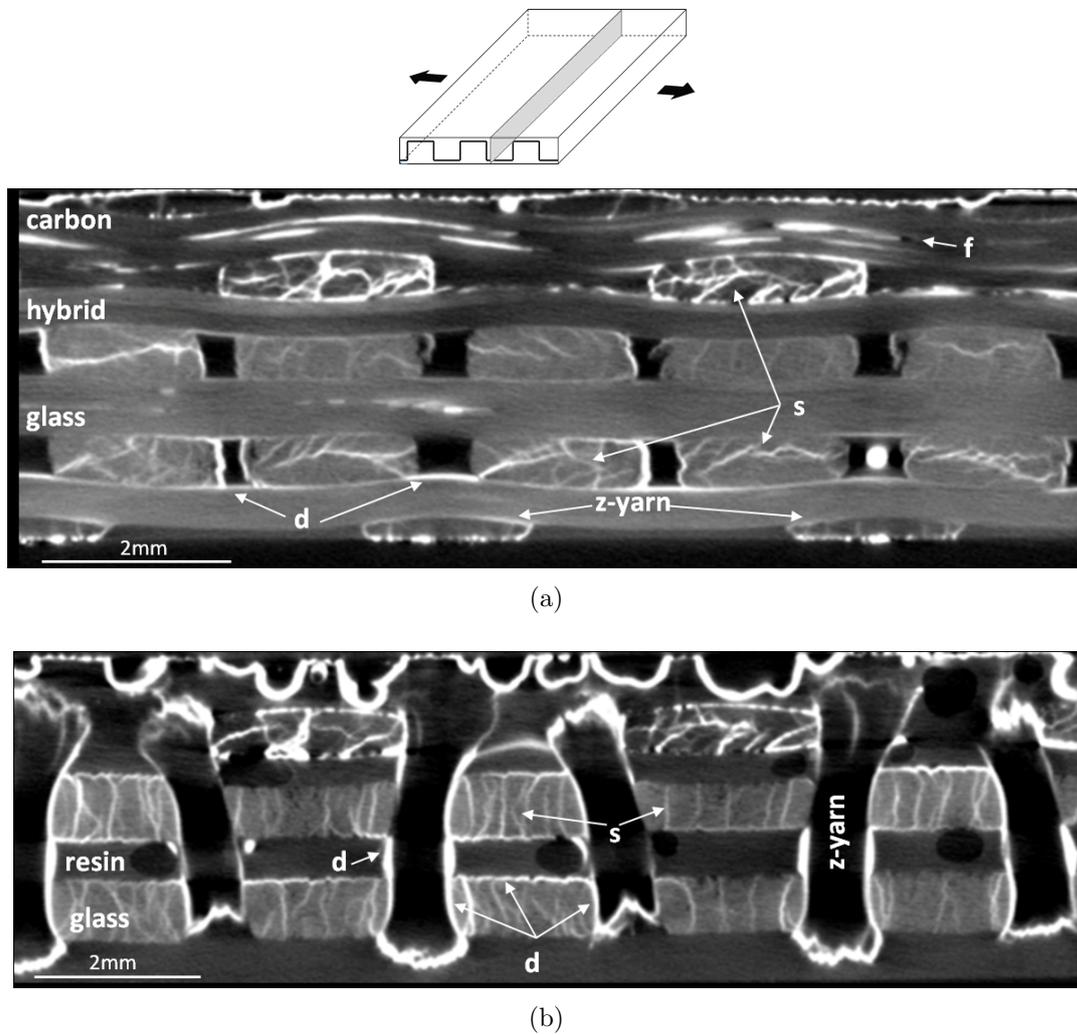
Figure 3.15: Tomograms of the coupon loaded in the warp direction up to 2.15% strain. (a) Transverse section perpendicular to the loading axis (b) Another transverse section perpendicular to the loading axis which contains the PE z-yarns. Glass fiber yarns appear light grey, carbon fiber yarns and matrix appear dark grey and white regions correspond to cracks infiltrated by ZnI. Arrows indicate the different damage mechanisms: **f** stands for the fracture of the carbon fiber tows, **s** shear cracks within the fiber tows, and **d** delamination of the fiber tows.

purpose: optical microscopy, scanning electron microscopy (SEM) and XCT (without dye penetrant). Significant differences were found between in-plane and out-of-plane loading.

In-plane loading. As shown in Figure 3.16, transverse tensile stresses led to three failure modes: translaminar cracks propagating from one yarn to another across the matrix, debonding at the yarn-matrix interface and transverse cracking within the yarn (bottom). The presence of such damage mechanisms reduces the stiffness of the material in the warp direction. Furthermore, it is apparent from Figure 3.17 that they are somehow related to delamination. However, it remains unknown whether delamination or transverse cracking occurs first.

Out-of-plane loading. Tensile loading not only caused fiber breakage at planes normal to the loading direction, but also other important failure micromechanisms due to the presence of in-plane shear stresses. Longitudinal shear stresses may arise at any plane parallel to the loading direction, which in turn may generate cracks either within the yarn (Figure 3.18(c)) or at yarn-matrix interfaces. The latter is very common in non-crimp fabrics due to the heterogeneity of the material and the large size of resin pockets (Figure 3.18(b)). Moreover, interfaces between orthogonal yarns are also a common source of cracks. A yarn being pulled-out is shown in Figure 3.19. The top interface is already debonded, whereas cracks initiate at the center of the yarn and at the bottom interface.
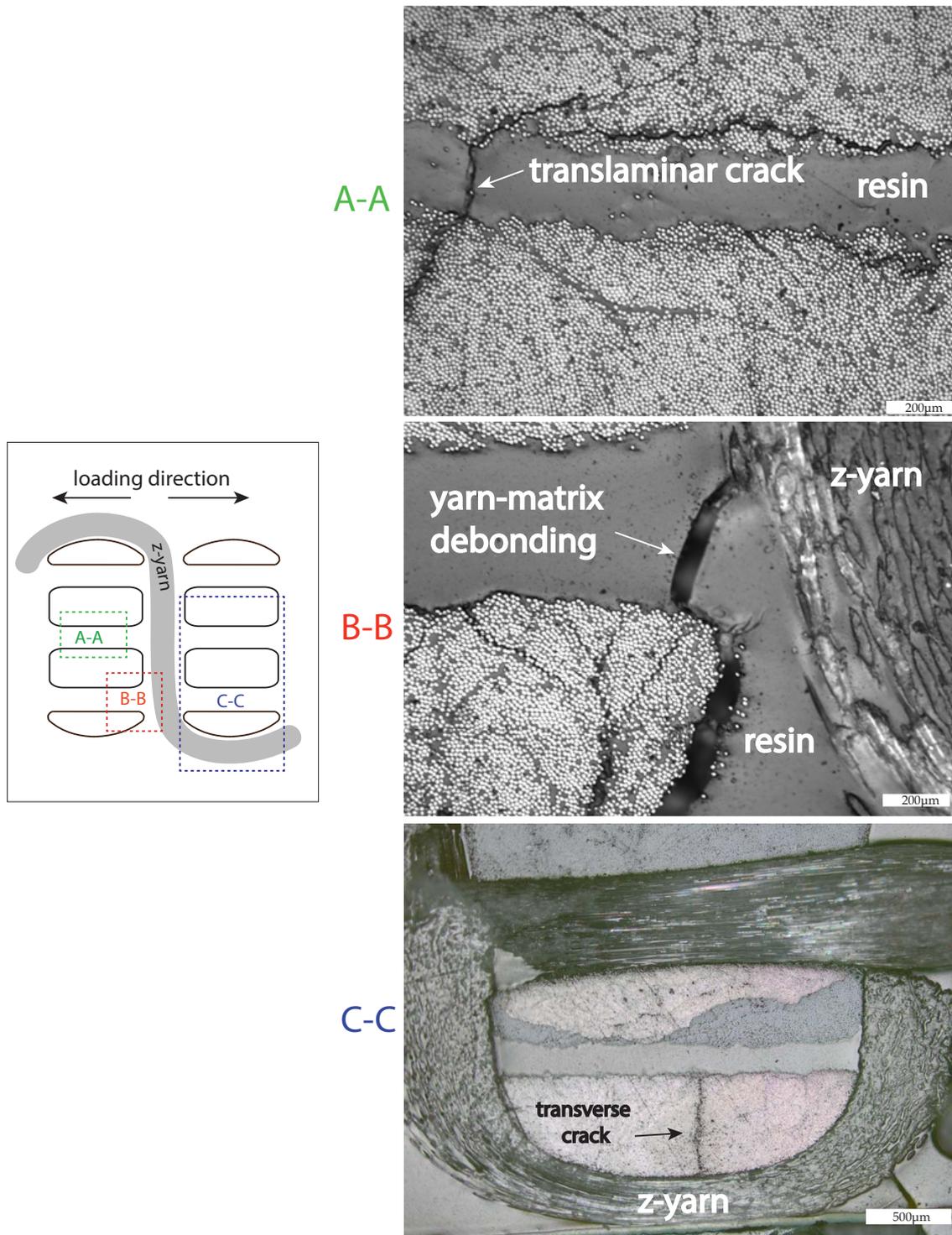
Figure 3.16: Cracks appearing while in-plane loading in a section parallel to the warp direction (optical microscopy).
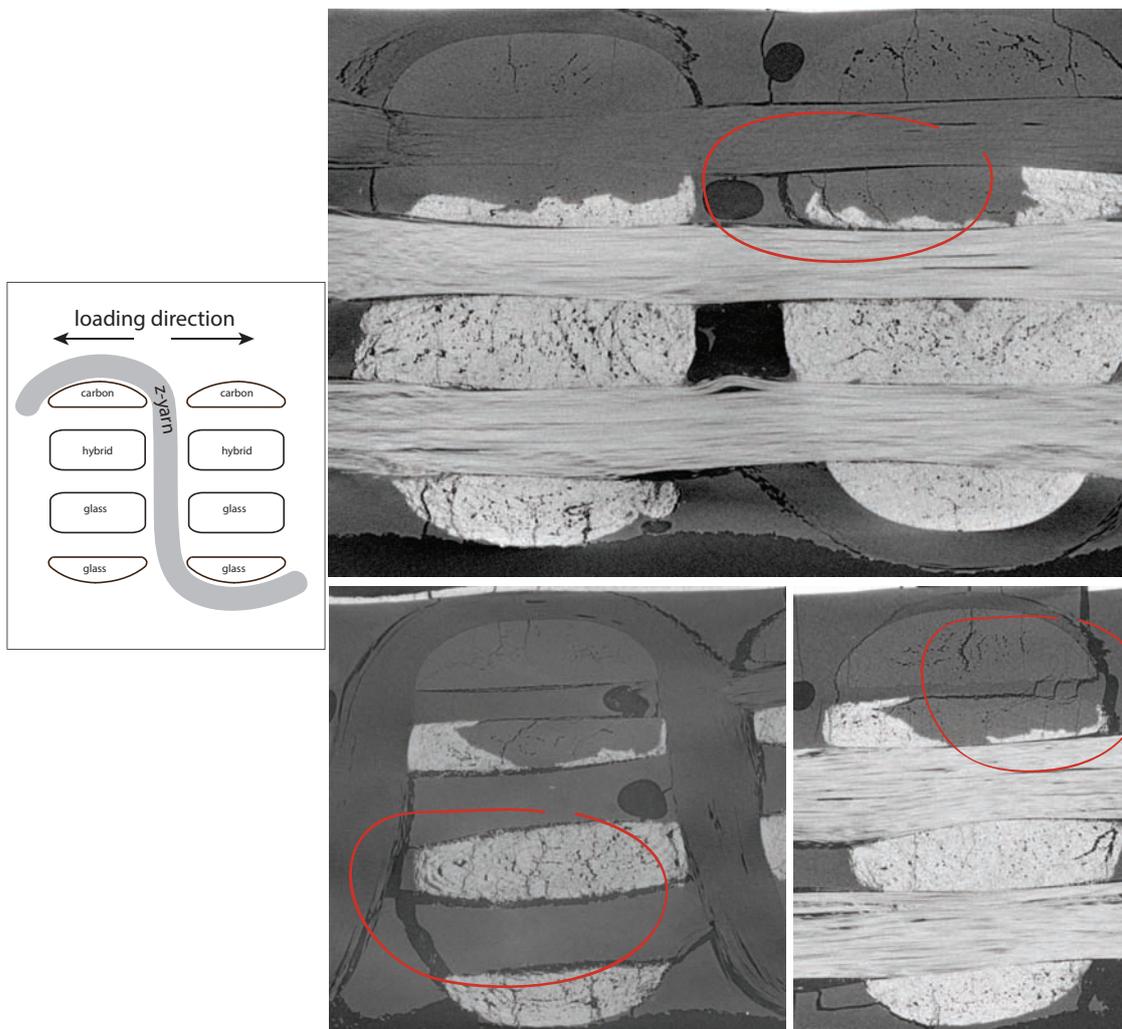
Figure 3.17: XCT post-mortem images. In-plane loading. From top to bottom and left to right: coupling transverse cracking and delamination, delamination and translaminar cracking.
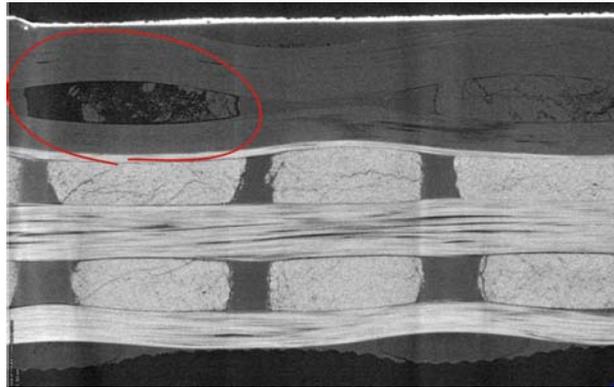
(a) Fiber breakage
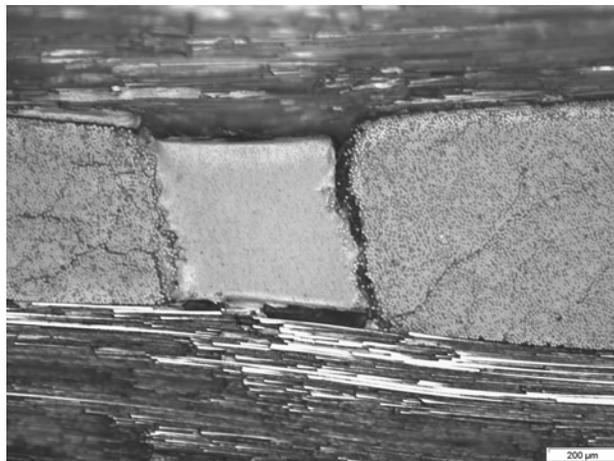
(b) Delamination at resin pocket between two longitudinal and two transverse yarns

(c) Extensive cracking at carbon tow (top) caused by longitudinal shear stresses

Figure 3.18: Micrographs of the coupon loaded in the warp direction up to failure. Transverse section perpendicular to the loading axis. Failure modes observed were (a) fiber breakage, (b) yarn debonding and delamination in resin rich areas and (c) intratow cracks.

50
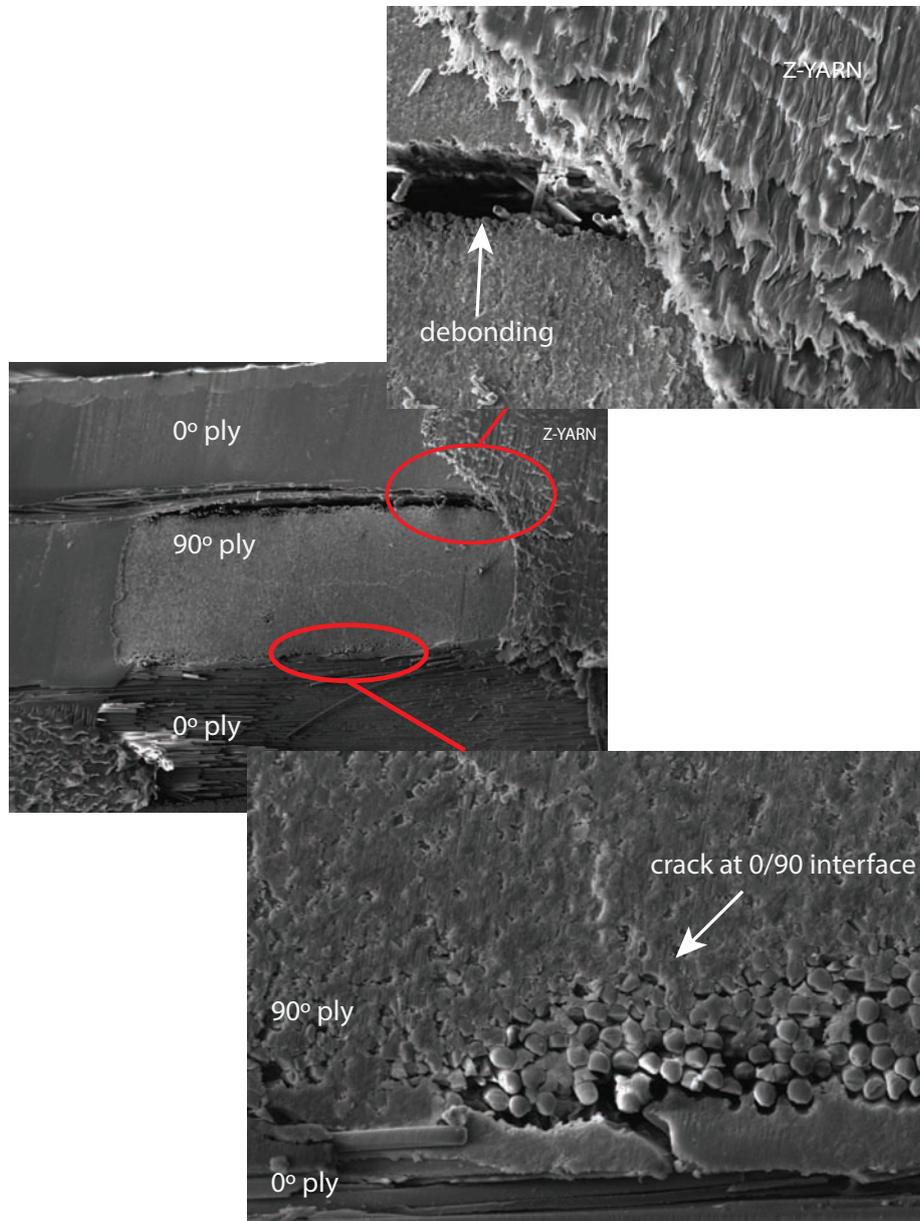
Figure 3.19: Micrographs (SEM) of the coupon loaded in the warp direction up to failure. Transverse section perpendicular to the loading axis. Cracks generated by in-plane shear stresses. Debonding of yarn-matrix at the top interface and crack initiation at the bottom interface.

3.3 Tensile properties of open-hole coupons

3.3.1 Experimental techniques

Testing conditions of open-hole coupons were similar to those presented in section 3.2.1. Thirteen rectangular specimens of $250 \times 25 \times 4.1$ mm^3 were machined from the plate with the longest dimension aligned in either the warp or the fill direction for the mechanical tests. Glass fiber tabs of 50 mm in length were glued to the specimens, leading to a free length of 150 mm (see Figure 3.20). They were tested in tension in an electromechanical universal testing machine (Instron 3384) following the recommendations of the ASTM D5766 (1995) for rectangular coupons with a central hole of 4.1 mm and 11 mm diameter. Tests were carried out under stroke control at 2 mm/min and the load was continuously measured during the test with a load cell of 150 KN. Since composite is non-symmetric (and coupling between bending and extension might occur), the longitudinal strain was recorded on both faces of the specimen using an extensometer of 50 mm gage length on one face and digital image correlation (Vic2D) on the other.

3.3.2 Results and discussion

The tensile stress-strain curves of the open-hole tests are plotted in Figures 3.21a and 3.21b for coupons with a central hole of 4.1 mm and 11 mm diameter, respectively. These curves present similarities and differences with those measured in plain coupons (Figure 3.4). The maximum strength was also attained at lower strains when the composite was loaded in the fill direction and was dictated by the fracture of the carbon fibers. The coupons loaded in the warp direction attained the maximum strength at higher strains after the failure of carbon fibers. Nevertheless, as shown in Figures 3.22(a) and 3.22(b), damage in the ligament induced by the presence of the hole promotes transverse cracking and leads to a non-linear stress-strain curve even in the samples loaded in the fill direction. The non-linearity increased with the hole diameter. Final failure occurs when cracks initiate at the hole edges (Figures 3.22 and 3.23). Moreover, the specimen failure after the peak strength was gradual, particularly in the specimens with large holes (Figure 3.21b). This behavior is indicative of a ductile failure mechanism in which the material in the ligament failed progressively as the applied strain increased.
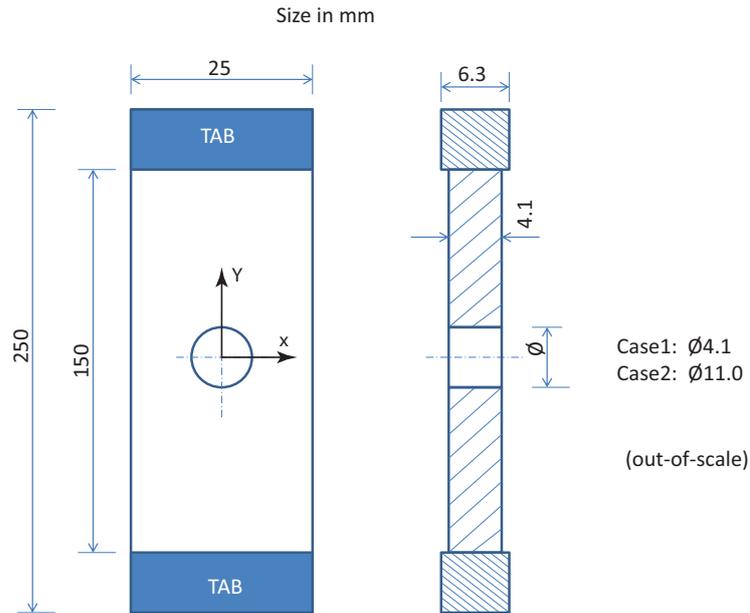
Figure 3.20: Drawing of the open-hole specimen.

It is worth mentioning that significant bending occurred in specimens with the smallest diameter because of the non-symmetry of the laminate (Figures 3.24(a) and 3.24(b)). In contrast, this was not observed in specimens with the largest hole.

The notch sensitivity of the hybrid 3D woven composite in the fill and warp directions is shown in Fig 3.21c, in which the failure stress (normalized by the average failure stress of the plain coupon) is plotted as a function of the hole diameter (divided by the coupon width). The experimental results for the open hole tests with different hole diameter are very close to the straight line which indicates that failure strength was proportional to the ligament width (particularly in the fill direction) and thus that the stress concentration induced by the circular hole did not influence the failure strength. Reduced notch sensitivity in carbon/epoxy 3D woven composites was already reported by Cox *et al.* (1994b) and Cox (1996). It was partly attributed to the presence of geometrical flaws that were broadly distributed in strength and space; and partly to the coarseness of the reinforcing yarns, which led to extensive debonding and reduced stress intensification around sites of failure. Nevertheless, the hybrid 3D woven composites presented better notch insensitivity, indicating that hybridization with glass and PE fibers improves the damage tolerance.
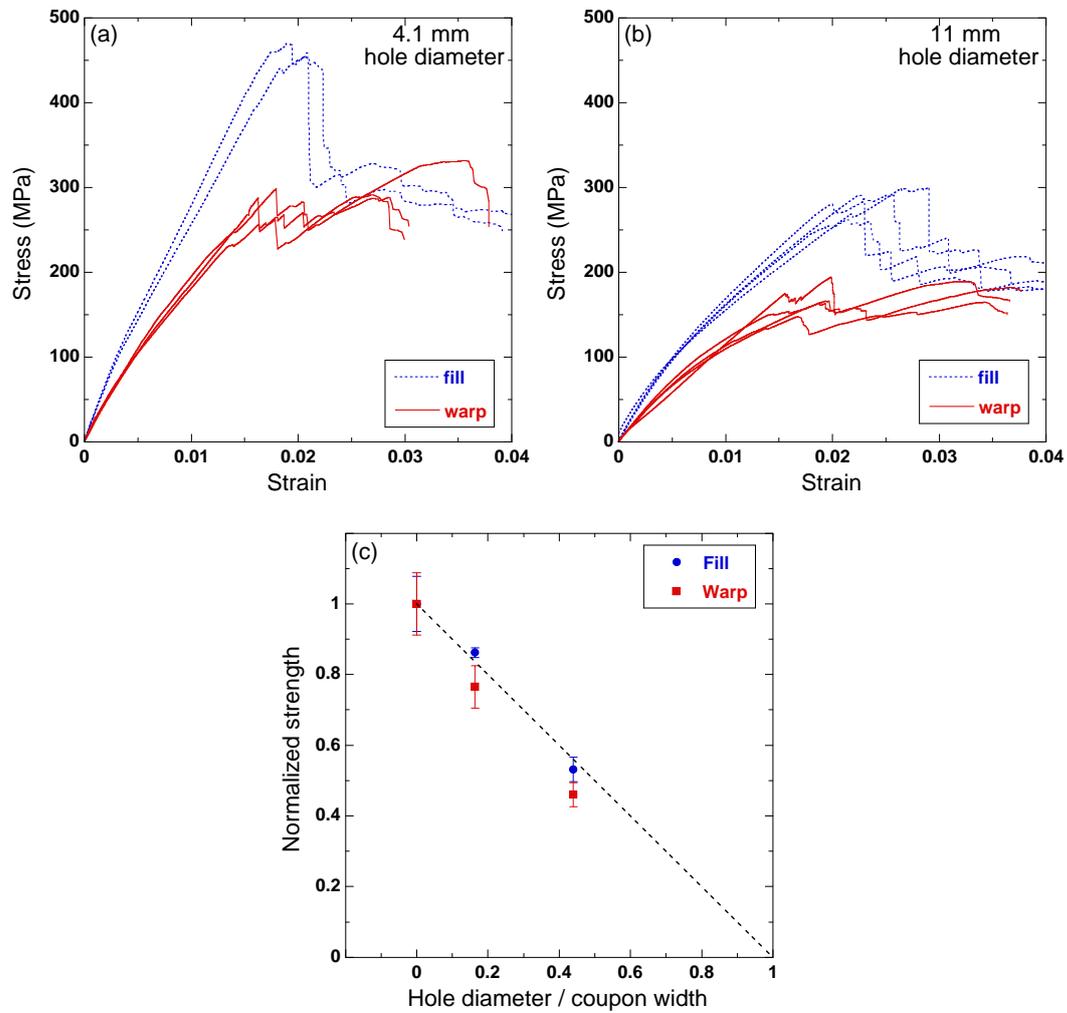
Figure 3.21: Stress-strain curves of the open-hole composite coupons in the fill and warp direction. (a) 4.1 mm diameter hole. (b) 11 mm diameter hole. (c) Notch-sensitivity of the hybrid 3D woven composite. The notch-insensitive behavior is given by the dashed straight line.
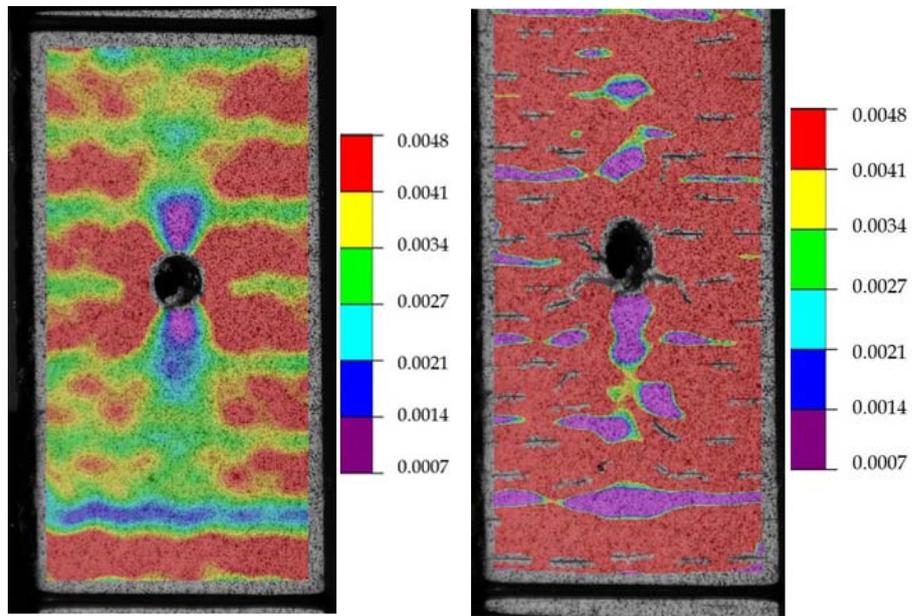
(a) Strain concentration around the hole at $\varepsilon_y = 0.007$

(b) Crack onset at hole edge and extensive transverse cracking at $\varepsilon_y = 0.034$

(c) Final failure of the specimen immediately after crack onset at hole edge at $\varepsilon_y = 0.035$

Figure 3.22: Contour plot of the nominal strain in vertical direction within a rectangular region at the center of the specimen loaded in the warp direction. Hole diameter, 4.1mm.

(a) Strain concentration around the hole at $\varepsilon_y = 0.012$

(b) Crack onset at hole edges at $\varepsilon_y = 0.015$

(c) Failure of the carbon layers at $\varepsilon_y = 0.02$
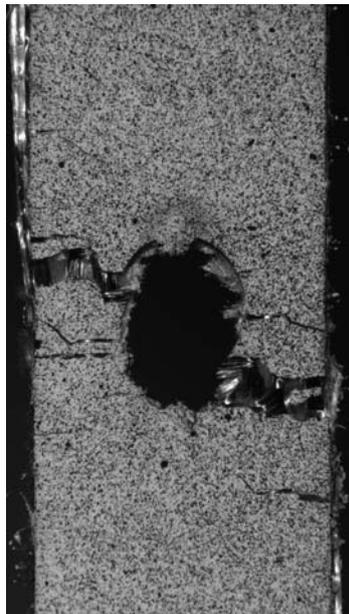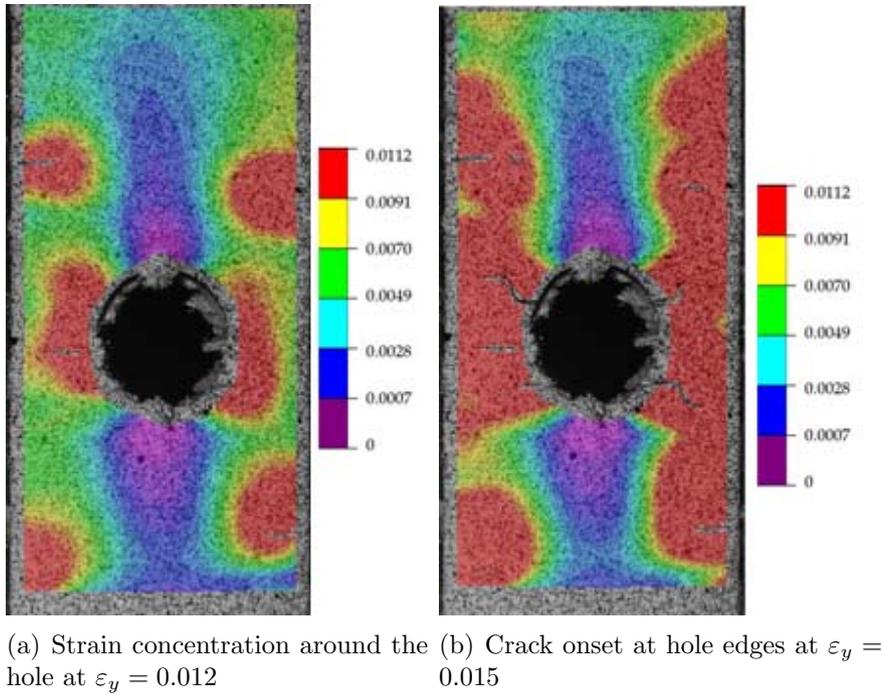
Figure 3.23: Contour plot of the nominal strain in vertical direction within a rectangular region at the center of the specimen loaded in the warp direction. Hole diameter, 11mm.
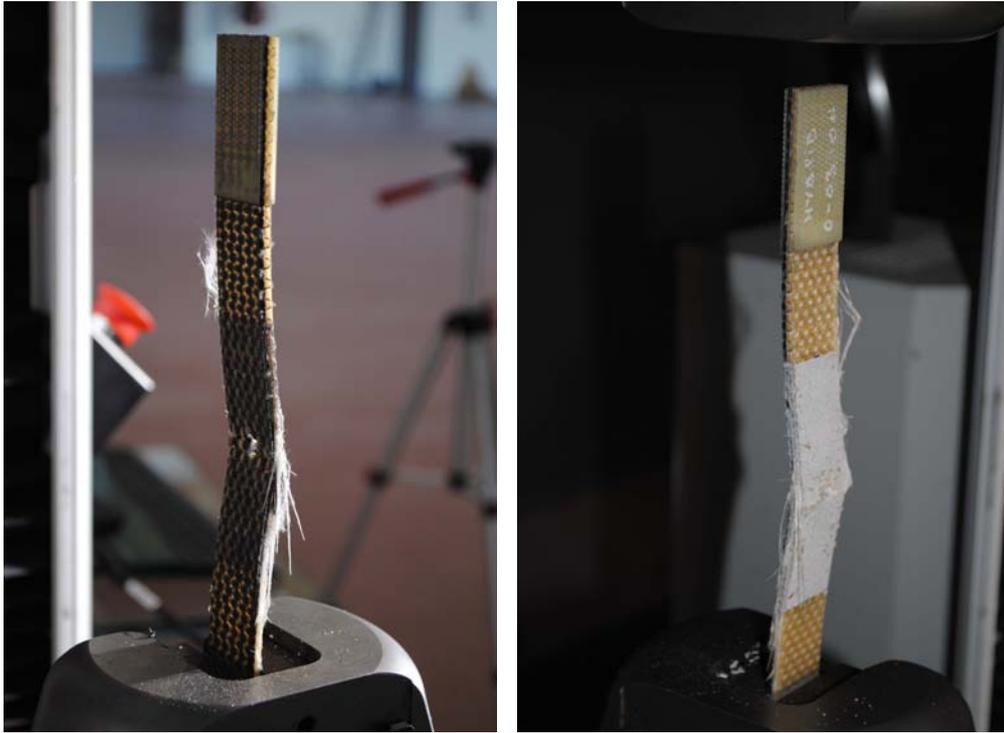
(a) Carbon side   (b) Glass side

Figure 3.24: Bending of open-hole specimen (diameter 4.1mm) tested in tension in the warp direction. (a) Carbon and (b) glass faces.

3.4 Modeling

3.4.1 Prediction of the tensile properties of the coupon

Although XCT analyses showed the development of different damage mechanisms upon tensile deformation, the tensile strength of the composite coupons seemed to be controlled by the fracture of the fiber yarns in the loading direction. Previous investigations of the tensile behavior of 3D woven composites were conducted by Cox *et al.* (1994b), showing that the tensile strength can be estimated fairly well from the stress carried by the individual tows oriented in the loading direction assuming an isostrain approach. According to this hypothesis, the composite mechanical behavior in the fill and warp directions should be predicted from the experimental values of the fiber elastic modulus and failure strain obtained from the fiber tow tests using a simple model based on the rule of mixtures. The composite elastic modulus in the fill (E^f) and warp (E^w) directions could be expressed as

$$E^f = E_c f_c^f + E_{s2} f_{s2}^f + E_m(1 - f_c^f - f_{s2}^f) \tag{3.1}$$

$$E^w = E_c f_c^w + E_{s2} f_{s2}^w + E_{pe} f_{pe}^w/2 + E_m(1 - f_c^w - f_{s2}^w - f_{pe}^w/2) \tag{3.2}$$

where E_c, E_{s2} and E_{pe} stand for the elastic moduli of the fibers (Table 3.1), f_c^f, f_{s2}^f are the carbon and glass fiber volume fractions in the fill direction (Table 2.2), and f_c^w, f_{s2}^w and f_{pe}^w the carbon, glass and PE fiber volume fractions in the warp direction (Table 2.2), respectively. This model assumes that the contribution to the elastic modulus of the fiber yarns perpendicular to either the fill or the warp direction is given by the matrix modulus, E_m, which was taken as 2.9 GPa, according to the manufacturer. In addition, only one half of the volume fraction of the PE fibers was considered to compute the elastic modulus in the warp direction because of the shape of the PE z-yarns. The model predictions are compared with the experimental data in Table 3.2, showing excellent agreement and supporting the use of the isostrain approach to model the elastic deformation in tension of hybrid 3D woven composites.

Table 3.2: Experimental results and model predictions for the elastic modulus and tensile strength of the hybrid 3D woven composite in the fill and warp directions

orientation	Elastic Modulus		Tensile strength	
	Experiments (GPa)	Model (GPa)	Experiments (MPa)	Model (MPa)
Fill	38.4 ± 1.6	38	531 ± 42	545
Warp	24.6 ± 0.7	24.6	395 ± 35	612

The prediction of the tensile strength in the fill direction, X^f, was carried out using the same model under the assumption that the composite behavior is linear until fracture. Thus,

$$X^f = E^f \varepsilon_c \tag{3.3}$$

where ε_c is the failure strain of the carbon fiber tows (Table 3.1). In the case of the warp direction, the tensile strength was attained at the fracture of the glass fibers after the carbon fiber yarns were broken. Neglecting the contribution of the carbon fiber yarns to the elastic modulus, the composite tensile strength in the warp direction, X^w can be computed as

$$X^w = \left[E_{s2} f_{s2}^w + E_{pe} f_{pe}^w / 2 + E_m (1 - f_c^w - f_{s2}^w - f_{pe}^w / 2) \right] \varepsilon_{s2} \tag{3.4}$$

where ε_{s2} stands for the fracture strain of the glass fiber tows. The model predictions are compared with the experimental results in Table 3.2. The model predictions in the fill direction are very accurate, as this is the result of the linear behavior of the composite until the fracture of the carbon fiber tows (Figure 3.4a). However, the model overestimated the composite strength in the warp direction because the failure strain of the composite ($2.8 \pm 0.3\%$) was much lower than the failure strain of the glass fiber bundles ($4.0 \pm 1\%$), which controlled the composite strength in this orientation. In fact, if the failure strain of the S2 glass fiber yarns, ε_{s2} in equation 3.4 is substituted by the failure strain of the coupon in the warp direction (2.8%), the isostrain model prediction for the composite strength in the warp direction drops to 428 MPa, close to the experimental results. The early fracture of the glass fiber bundles was very probably promoted by the bending stresses induced in the asymmetric hybrid laminate after the failure of the carbon fibers and the

stress concentration in the vicinity of failed tows. This mechanisms limited the maximum loading bearing capability of the hybrid composite.

3.4.2 Prediction of the notched response

Several analytical models have been suggested in the literature to predict the open-hole tensile strength of composite laminates. The most widely used are the *point stress* Whitney & Nuismer (1974) and the *average stress* methods. The point stress criterion assumes that failure takes place when the stress at a given distance from the notch tip (the characteristic distance) reaches the unnotched strength of the laminate, whereas the average stress criterion predicts failure when the average stress over a characteristic distance is equal to the unnotched strength of the laminate, Camanho *et al.* (2012). Unfortunately, these models rely on the characteristic length, which is not a material property and depends on various factors such as hole size and stacking sequence, Hodge *et al.* (2011). More recently, Camanho *et al.* (2012) have proposed a model based on the Finite Fracture Mechanics (FFM) which overcomes this problem. The model is able to predict the notched strength of a composite laminate for a range of diameters by imposing simultaneously a stress-based criterion and an energy-based criterion over a certain distance. Mathematically, this is expressed as

$$\frac{1}{l} \int_{R}^{R+l} \sigma_y(x,0)dx = X_T^L \tag{3.5}$$

$$\frac{1}{l} \int_{R}^{R+l} \mathcal{K}_I^2(a)da = \mathcal{K}_{Ic}^2 \tag{3.6}$$

where R stands for the radius of the hole, a the crack length, l the crack length at failure, $\mathcal{K}_I$ the stress intensity factor, $\mathcal{K}_{Ic}$ the fracture toughness, X_T^L the unnotched strength and $\sigma_y(x,0)$ the stress distribution along the x-axis at the center of the specimen, Figure 3.20.

The main advantage of this model is that it is based on the ply elastic properties, the unnotched strength and the fracture toughness of the laminate. More details can be found in the Appendix B.

Table 3.3: Experimental results and model predictions for the open-hole tensile strength of the hybrid 3D woven composite with a hole of 11mm in the fill and warp directions.

	X_L^T (MPa)	$\sigma_{4.1}^\infty$ Exp. (MPa)	$\mathcal{K}_{Ic}$ (MPa$\sqrt{\text{m}}$)	σ_{11}^∞ Exp. (MPa)	σ_{11}^∞ Model (MPa)	Error (%)
Fill	531.2	458.0	66.0	325.0	323.2	0.56
Warp	394.9	302.2	32.5	181.8	193.0	5.81

The model has been applied to estimate the fracture toughness of the laminate in the warp and fill directions. To this end, the experimental results from the unnotched strength X_L^T and the notched strength σ^∞ of the 4.1 mm diameter specimen were used together with the ply elastic properties. Once the fracture toughness is known, the model can also be applied to predict the notched strength for other hole diameters. This exercise was carried out with the experimental results from hole tests for a 11 mm specimen in the warp and fill directions. The predictions were in good agreement with the experiments. The values obtained for $\mathcal{K}_{Ic}$ in the warp and fill directions were 32.5 MPa$\sqrt{m}$ and 66 MPa$\sqrt{m}$, respectively, (Table 3.3). These values are in agreement with those presented by Arteiro *et al.* (2013a), Camanho & Catalanotti (2011) and Arteiro *et al.* (2013b). The higher discrepancy observed in the warp direction is likely due to the presence of damage mechanisms which were not accounted for in the model, such as delamination. In addition, the model is not designed for 3D composites and it provides better results for quasi-isotropic laminates than for cross-ply materials.

Once the fracture toughness $\mathcal{K}_{Ic}$ is known, the critical energy release rate $\mathcal{G}_{Ic}^l$ can be readily obtained by using equations B.9 and B.10. This leads to $G_{Ic}^{\text{warp}} = 94 \frac{KJ}{m^2}$ and $G_{Ic}^{\text{fill}} = 332 \frac{KJ}{m^2}$. While the values in the warp direction are in agreement with those reported by Pinho *et al.* (2006), the critical energy release rate in fill direction seems to be too high.

3.5   Concluding remarks

The analysis of the deformation and failure micromechanisms of a hybrid 3D woven composite in tension showed that the elastic deformation was controlled by the elastic modulus and volume fraction of fiber yarns oriented in the loading direction. Due to the complex 3D architecture, damage developed at low strains in the form of debonding of

the fiber tows (longitudinal and z-yarns) as well as of tensile and shear cracking of the fiber tows. Tow debonding was arrested by the z-yarns, whereas tensile transverse cracks were concentrated within fiber tows perpendicular to the loading axis. Shear cracking of the fiber tows was due to asymmetric debonding of the fiber tows from the surrounding material and developed in longitudinal and transversal tows. Nevertheless, the influence of these damage mechanisms in the elastic modulus was limited and, depending on the architecture, was balanced by the straightening of the fiber tows upon tensile straining. Thus, the elastic moduli in both fill and warp directions was accurately predicted by an isostrain model using the actual properties of the fiber tows within the composite.

Elastic deformation stopped abruptly when the applied strain reached $\approx 1.5\%$ due to the brittle failure of the carbon fiber tows. This first peak in the stress-strain curve could be adequately predicted by the isostrain model and bending stresses (induced by the non-symmetric laminate) did not influence the mechanical response. Nevertheless, fracture of the carbon yarns did not lead to the laminate fracture because the laminate was held together by the PE z-yarns while the glass fiber tows continued supporting the applied load. This led to another peak in the stress-strain curve, which was controlled by the fracture of the glass fiber tows. Whether or not the second peak was higher than the first one depended on the volume fraction of carbon and glass fibers oriented in the loading direction. It should be noted that the strain at which this second peak was attained (2-3%) was significantly lower than the failure strain of the glass fiber tows ($\approx 4\%$). This is likely due to the combining effect of two factors: the development of bending stresses in the damaged coupon and the stress concentration in the vicinity of failed tows.

It is also worth noting that the PE z-yarns will lead to through-thickness compression of the laminate as it stretches along the the warp direction. This will enhance friction between warp tows, improving the shear load transfer between tows and increasing the probability that significant loads can be sustained by the warp tows even after some of them (primarily carbon, but increasingly glass too as the strain increases) have failed. This enhanced friction is a major potential source of damage tolerance and energy absorption McGlockton *et al.* (2003). Thus, the full contribution of the glass fibers to the composite strength was not employed but their presence increased the fracture strain and the energy dissipated during fracture. Thus, hybridization of the 3D woven composite led to a notch-insensitive behavior as demonstrated by open-hole tests.

CHAPTER 4

Compressive Behavior

The in-plane compressive strength of composites is lower than the in-plane tensile strength. This is particularly critical in 3D composites, in which stress concentration near tabs, yarn crimping and 3D weaving may reduce the compressive strength, Cox *et al.* (1994b), Kuo *et al.* (2007), Mahadik & Hallett (2011), Yudhanto *et al.* (2013), Edgren *et al.* (2008). Thus compressive strength is a limiting design factor of structural components manufactured with 3D composites, especially in the presence of notches or when the material has been previously damaged.

This chapter is devoted to study the mechanical response in compression of unnotched and notched specimens. To this end, an experimental campaign was carried out including plain and open-hole tests. Damage was inspected in post-mortem specimens by means of XCT and SEM to ascertain the deformation and damage mechanisms of the composite and the role played by the z-yarns. Finally, the fracture toughness of the specimens was estimated by means of two analytical models.

4.1 In-plane compressive properties of plain coupons

This section presents the compressive behavior of plain coupons of the hybrid 3D woven composite.

Figure 4.1: Compression test specimen.

4.1.1 Experimental techniques

Ten rectangular specimens of $140 \times 25 \times 4.1$ mm^3 were machined from the plate with the longest dimension aligned in either the warp or fill direction. Glass fiber tabs of 65 mm in length were glued to the specimens, leading to a free length of 10 mm (Figures 4.1 and 4.2). Such small distance prevents specimens from buckling, but may induce some stress concentration. Specimens were tested in uniaxial compression in an electromechanical universal testing machine (Instron 3384) following the recommendations of the ASTM 3410 (1995) and using the well-known IITRI fixture (Figure 4.3). Tests were carried out under stroke control at 1.5 mm/min and the load was continuously monitored during the test with a load cell of 150 KN. The longitudinal strain along the loading axis was measured with two standard resistive strain gages (350 Ω) attached to both surfaces of the specimen.

Specimens loaded in the warp direction were inspected by XCT with a Nanotom 160NF (Phoenix) at 90 KV and 110 mA using a W target. 1800 radiographs were acquired for each tomogram with an exposure time of 750 ms. The reconstructed volumes presented a resolution of 12.5 μm/voxel.

Scanning electron microscopy (EVO MA15, Zeiss) was used to inspect transverse sections of post-mortem samples loaded in the fill direction. Specimens were sputter-coated with gold during 60s with a current of 20 mA (Quorum, Q150T ES).
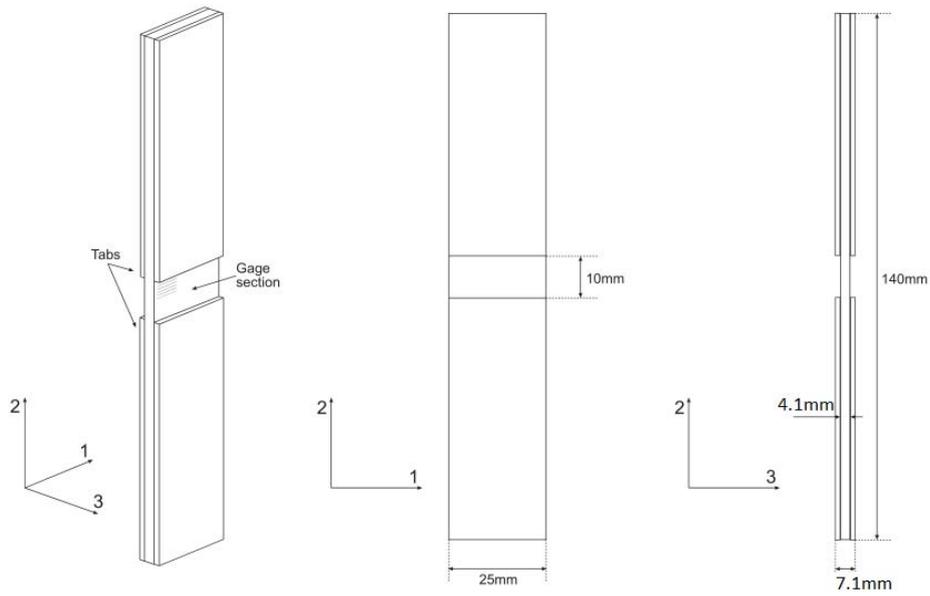
Figure 4.2: Schematic of compression specimen.
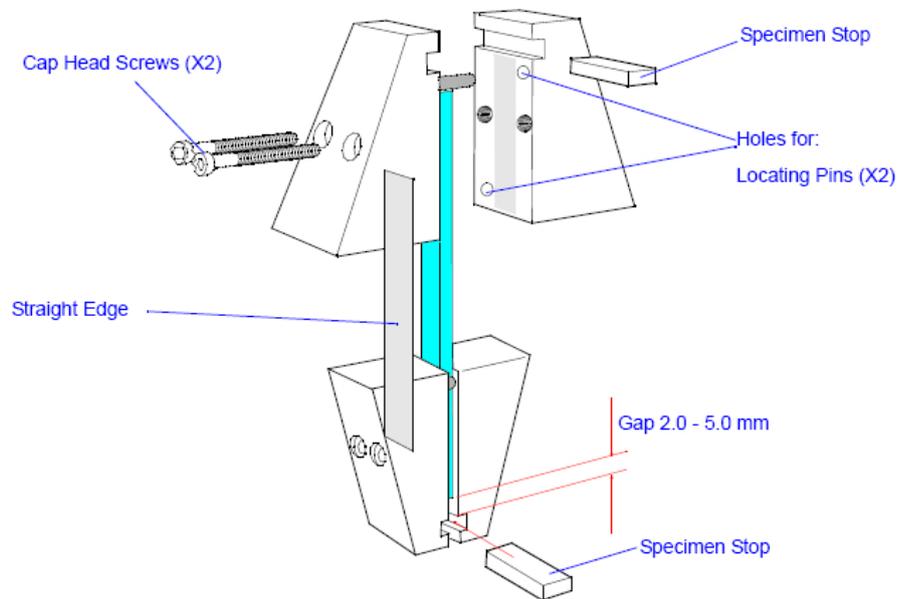
**Figure 4.3:** IITRI fixture (Instron). Plain compression set-up.
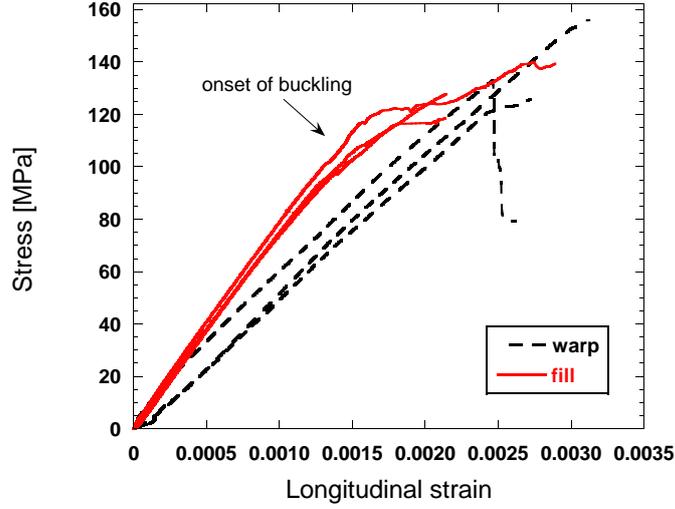
Figure 4.4: Stress-strain curves in plain compression

Table 4.1: Experimental results of elastic modulus and the compressive strength of the hybrid 3D woven composite in the fill and warp directions. The results obtained under tension are also included for comparison.

orientation	E_{11}^t(GPa)	E_{11}^c(GPa)	X^t (MPa)	X^c (MPa)
Fill	38.4 ± 1.6	73.9 ± 6.1	531 ± 42	132 ± 11.0
Warp	24.6 ± 0.7	55.3 ± 2.9	395 ± 35	132 ± 4.3

4.1.2 Results and discussion

The in-plane compressive stress-strain curves obtained in the warp and fill directions are plotted in Figure 4.4. The response in the warp direction was linear up to failure, whereas coupons loaded in the fill direction underwent a non-linear attenuation at $\varepsilon_{long} \approx 0.15\%$. A closer examination of strain gage readings, Figures 4.5(a) and 4.5(b), revealed that the onset of non-linearity coincides with the beginning of global buckling, which in turn reduces the ultimate strength X_{fill}^c. In fact, despite of the higher volume fraction of carbon fibers in the fill direction, the ultimate strength was almost identical in both directions (Table 4.1). It is worth noting that the ultimate strength was reached at very low strain levels ($\varepsilon \approx 0.2\% - 0.3\%$) in both cases.
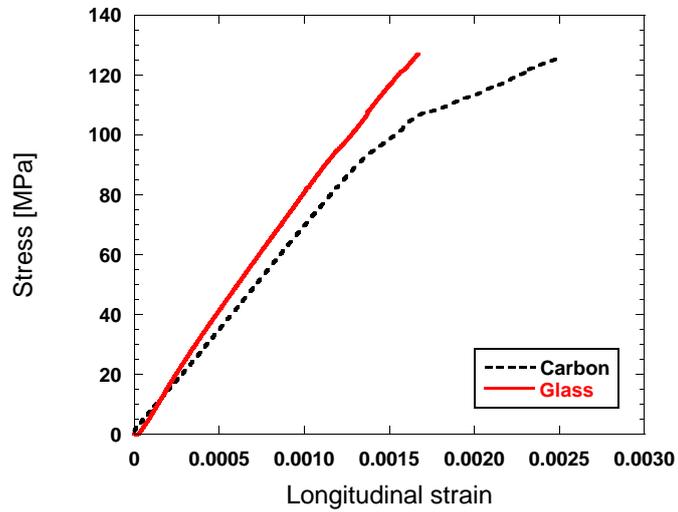
(a) fill direction
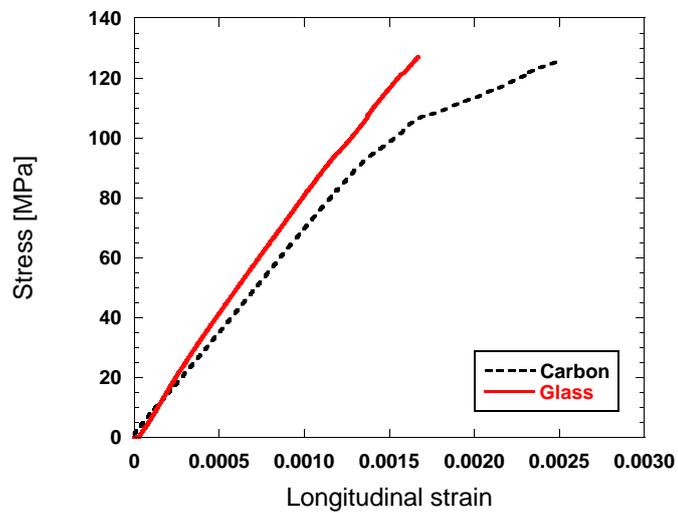
(b) warp direction

Figure 4.5: Compression tests of plain specimens. Comparison between readings of strain gages at carbon and glass faces when loading in the (a) fill and (b) warp directions.
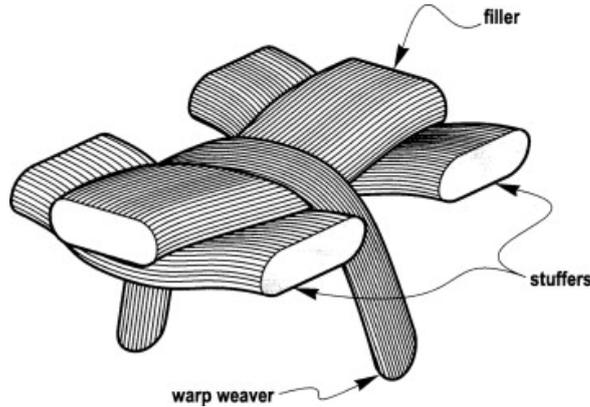
Figure 4.6: Crimping induced in the yarns due to the compressive force exerted by the z-yarns along the through-thickness direction. From Cox *et al.* (1994b).

Damage and failure micromechanisms

Fleck (1997) reported 6 different failure modes of polymer matrix composite under longitudinal compression: elastic microbuckling, plastic microbuckling, fiber failure, splitting, buckle delamination and shear band formation. The term *microbuckling* refers to the buckling underwent by the fibers due to the lack of support caused by the existence of voids or by the matrix non-linear behavior onset, which in turn can be due to either plastic yielding (ductile matrices) or microcracking (brittle matrices), Jelf & Fleck (1992). *Fiber failure* is related to the bending strength of fibers, whereas *splitting* refers to matrix cracking in the longitudinal direction. *Buckle delamination* is the buckling experienced by a new sublaminate generated after delamination. Finally, transverse cracking may occur by matrix yielding at a fracture angle α to the loading direction. XCT and SEM inspection of broken specimens revealed the presence of most of these failure modes, namely microbuckling, shear bands formation and buckle delamination.

The damage inspection of the broken specimens indicates that the different behavior observed in the warp and fill directions should be attributed to the presence of the z-yarn, which induces some waviness in the fill yarns (Figure 4.6) and switches the failure mode from *microbuckling* to *buckling delamination.* Microbuckling takes place in the warp direction due to matrix cracking in the transverse yarns and propagates across the thickness of the laminate (Figure 4.7). In contrast, matrix cracking in the fill direction causes delamination (Figure 4.8), giving rise to slender sublaminates that buckle earlier. This explains the reduction of strain-to-failure in the fill direction observed in Figure 4.4.

Initial state (undamaged) Matrix cracking Fiber microbuckling
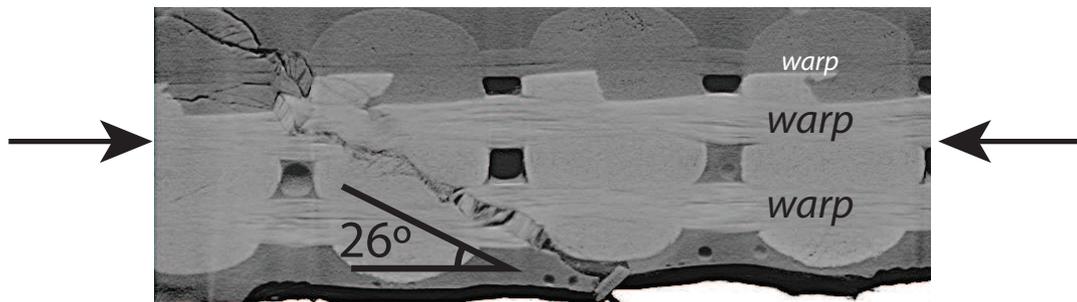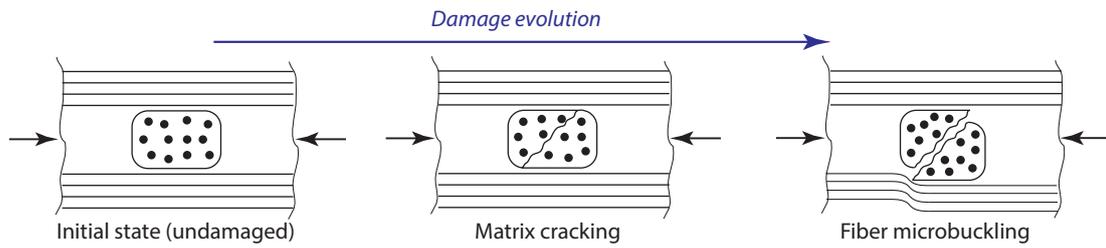
(a) Kink band propagation through-the-thickness in a section parallel to the warp direction of a plain compression specimen. The fracture plane is inclined at $\alpha \approx 26°$ with respect to the loading direction.
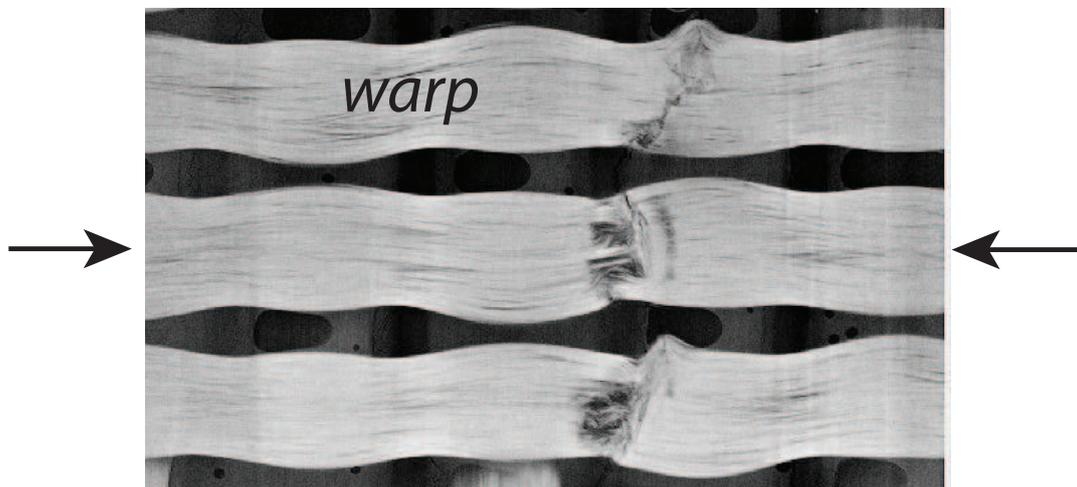
(b) Crimping, fiber misalignment and kink band generation in glass yarns after loading in compression in the direction of the longitudinal axis.

Figure 4.7: XCT images of specimens loaded in compression in warp direction after failure. Kink bands are not only generated across the thickness of the laminate (a), but also within the plane parallel to the midplane of the laminate (b).

69
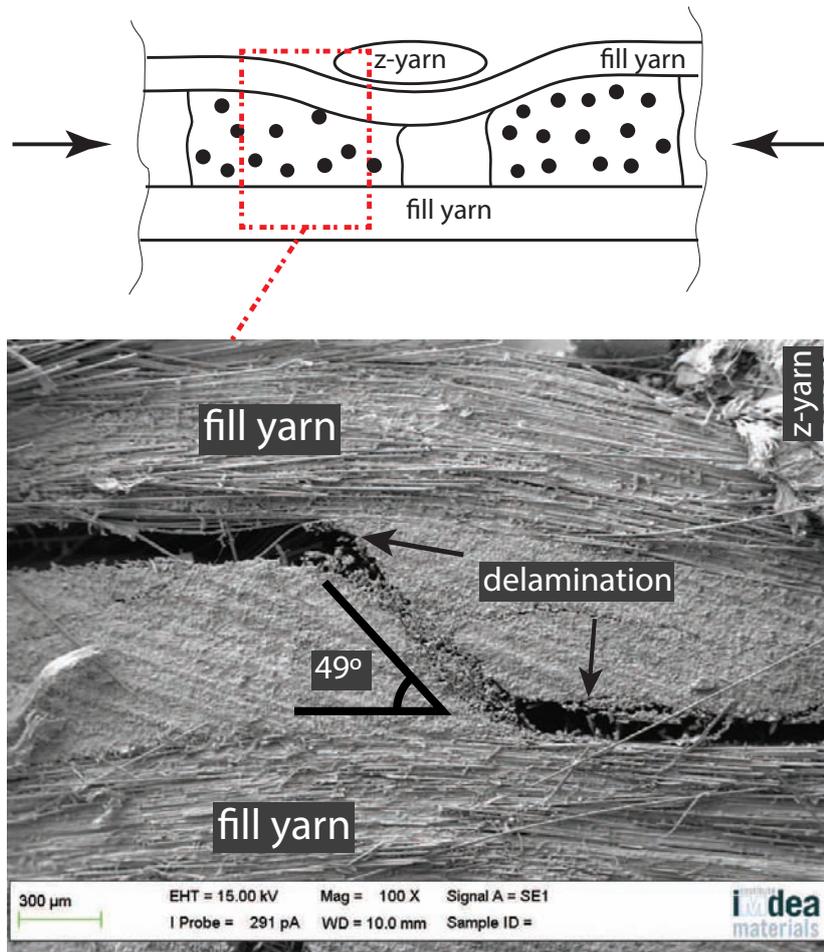
Figure 4.8: Debonding and transverse matrix cracking under in-plane compression loading in a section parallel to the loading direction (fill). The fracture angle α is higher than the angle of maximum shear stress (45°) due to the pressure-sensitivity of the epoxy-vinylester resin in compression.

In summary, it can be concluded that the response of plain specimens in compression is matrix-dominated. Damage always initiates by matrix cracking, regardless of the failure mode −fiber microbuckling or delamination− leading to a significant reduction 60% of the compressive strength as compared with the tensile strength (Table 4.1).
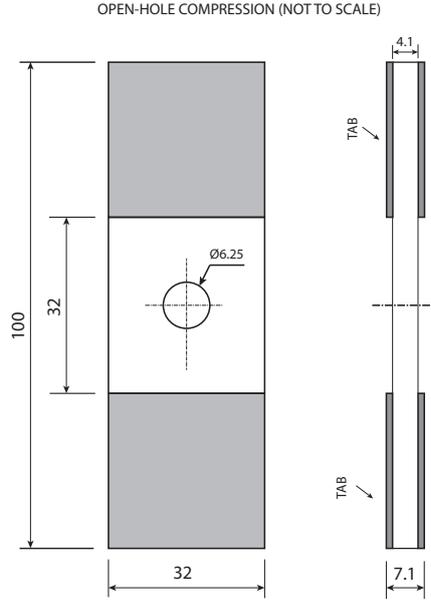
Figure 4.9: Schematic of open-hole specimen

4.2 In-plane compressive properties of open-hole coupons

4.2.1 Experimental techniques

Ten rectangular specimens of $100 \times 32 \times 4.1$ mm^3 were machined from the plate with the longest dimension aligned in either the warp or fill direction. A 6.25 mm diameter hole was drilled at the center of the specimen. Glass fiber tabs of 34 mm in length were glued to the specimens, leading to a free length of 32 mm (Figure 4.9). They were tested in uniaxial compression in an electromechanical universal testing machine (Instron 3384) following the recommendations of the AITM 1-0008 (2004). Tests were carried out under stroke control at 1.0 mm/min and the load was continuously monitored during the test with a load cell of 150 KN.

Specimens loaded in the warp direction were inspected by XCT with a Nanotom 160NF (Phoenix) at 90 KV and 120 μA using a W target. 1800 radiographs were acquired for each tomogram with an exposure time of 750 ms. The reconstructed volumes presented a resolution of 15.8 μm/voxel.
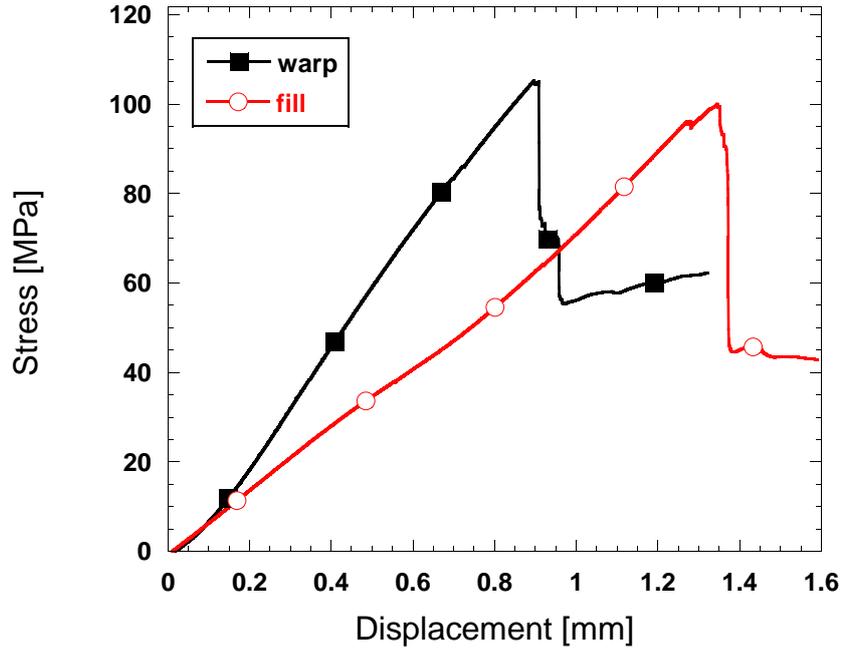
Figure 4.10: Stress-displacement curves of representative warp and fill open-hole specimens loaded in compression.

4.2.2 Results and discussion

As shown in Figure 4.10, the stress-displacements curves in the warp and fill directions were linear up to failure and the scatter was negligible. Despite of the higher carbon volume fraction in the fill direction, the notched strength was slightly higher in the warp direction (Table 4.2). This is likely due to the waviness induced by the z-yarns, which mainly affects the fill yarns located at the outermost layers.

Table 4.2: Experimental results of elastic modulus and ultimate stress in compression of the 3D hybrid woven composite in the fill and warp directions (open-hole specimen).

orientation	Ultimate compressive stress (MPa)
Fill	95.5 ± 8.5
Warp	101.72 ± 8.0

The material exhibited a notch-insensitive behavior. This is clearly illustrated in Figure 4.11, where the values of the compressive strength are close to the straight line that stands for notch-insensitivity.
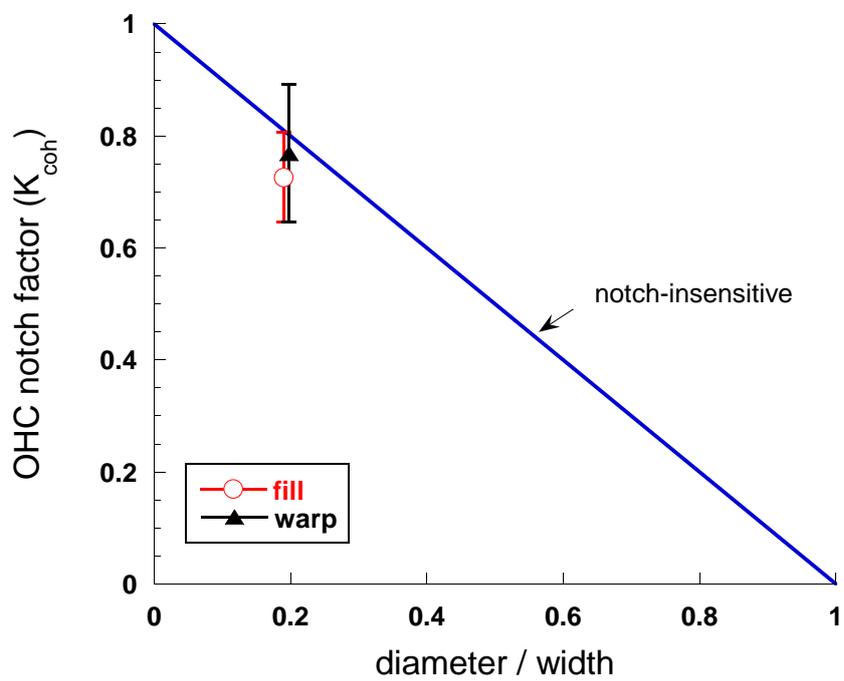
Figure 4.11: Notch sensitiveness in compression. Comparison between Plain and Open-hole tests. K_{coh} stands for the ratio between the notched and the unnotched strengths.
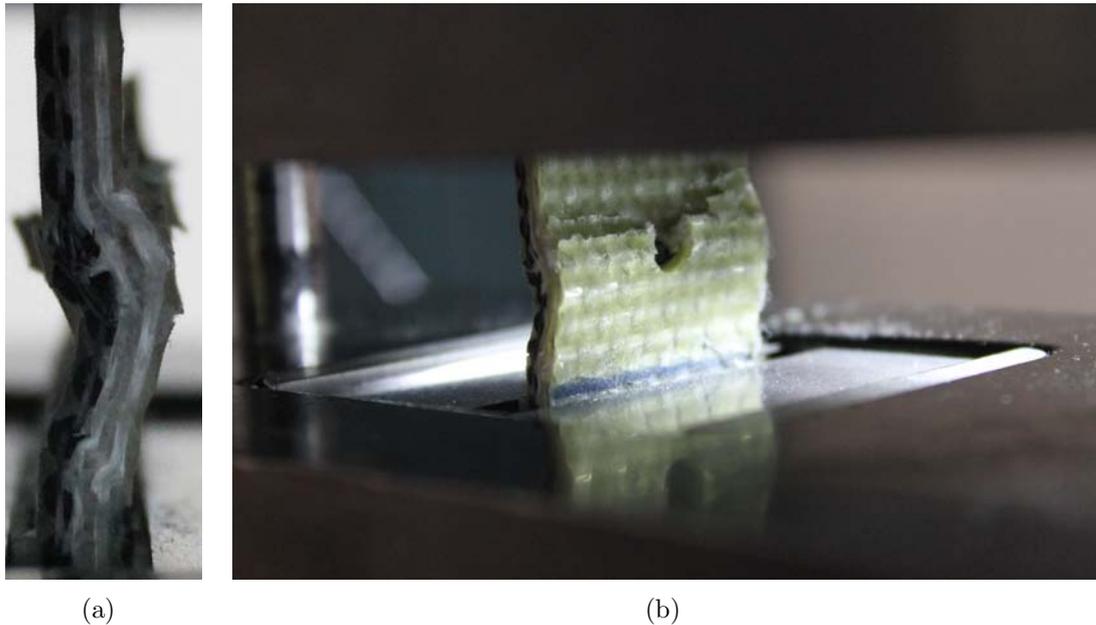
Figure 4.12: Open-hole specimen compressed in warp direction. (a) Lateral and (b) back views.

Damage and failure micromechanisms

Fiber microbuckling was clearly observed during open-hole compression tests (Figure 4.12). Further examination of broken specimens loaded in the warp direction by means of X-Ray microCT revealed the presence of matrix cracking along the z-yarn-matrix and the yarn-matrix interfaces of the carbon layer oriented in the fill direction, Figure 4.13. The crack path is perpendicular to the loading direction and propagates from the hole outwards. This is likely due to the stress concentration and the crimping induced in the fill yarns by the z-yarns. Matrix cracking reduces the support of the fibers and gives rise to fiber kinking of carbon tows oriented in the warp direction, Figure 4.14(a). Once kinking is triggered, it propagates downwards leading to the specimen failure.

It is worth noting that kinking did not initiate at the hole, as stated by other authors, but at certain distance from the hole. In fact, no evidence of stress concentration around the hole were found in glass layers. The only failure mode found in glass layers was microbuckling as a result of kink propagation from adjacent carbon layers, far away from the hole, Figure 4.14(b).
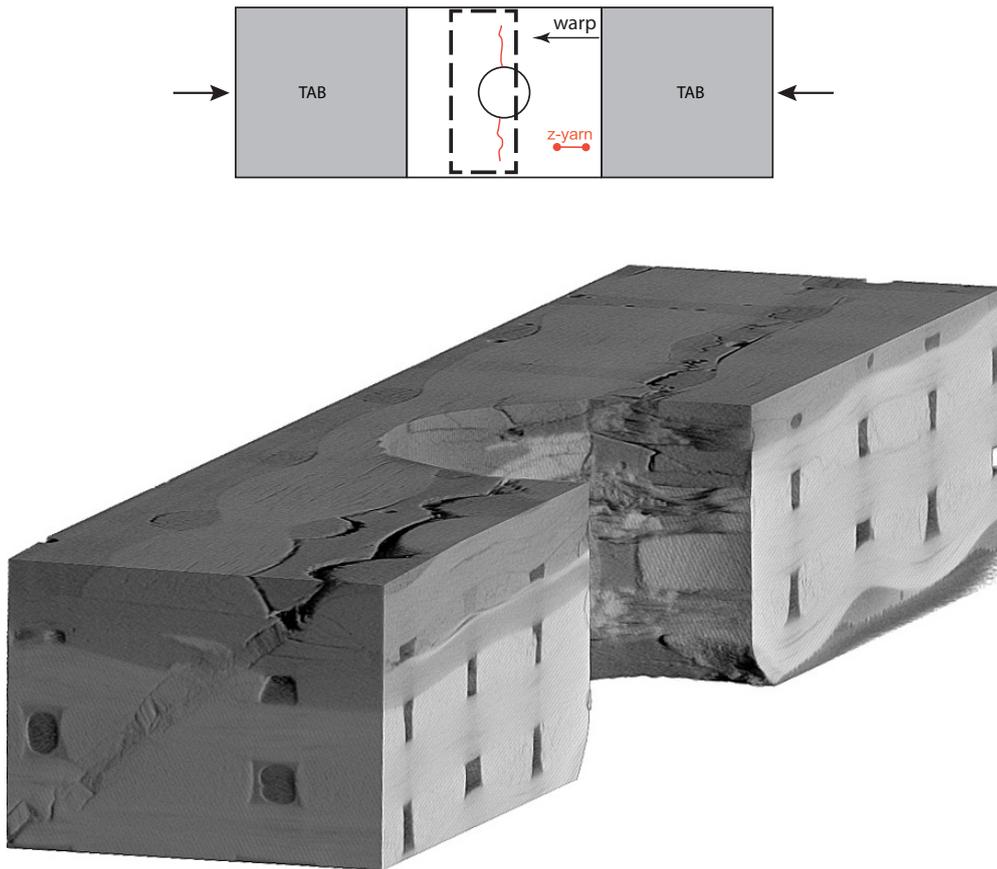
Figure 4.13: XCT image of a broken open-hole specimen loaded in compression in the warp direction. Onset of cracking by z-yarn-resin debonding at the top of the laminate (carbon layers) and subsequent propagation throughout the thickness.
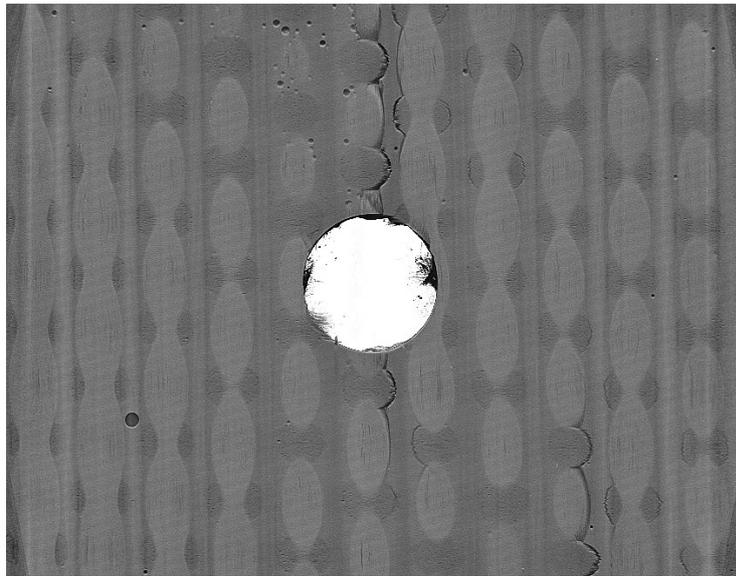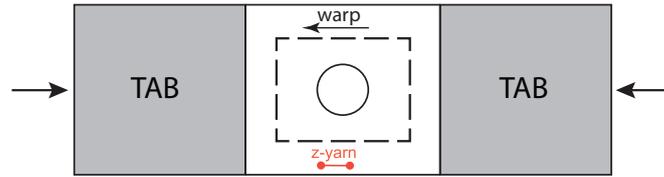
(a)
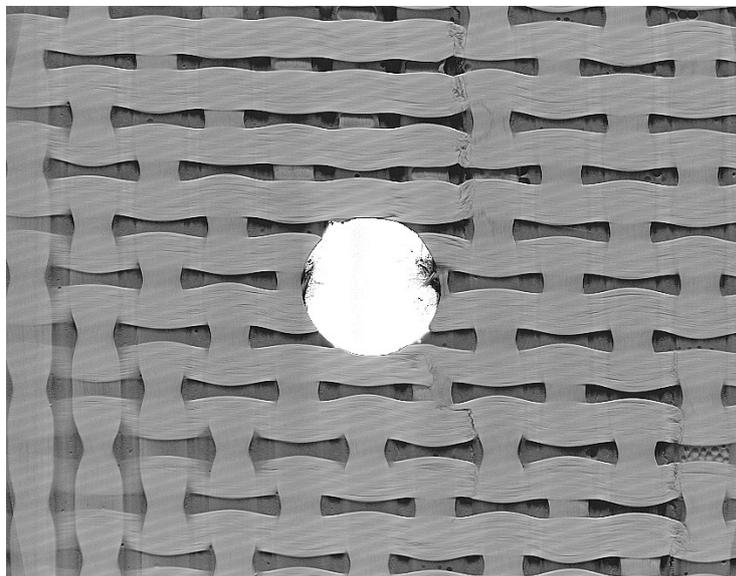
(b)

**Figure 4.14:** XCT images of a broken open-hole specimen loaded in compression in the warp direction. Onset of cracking around the hole in the carbon layer (a). Fiber microbuckling in the glass layer propagated from adjacent carbon layer (b).

4.3 Modeling

4.3.1 Prediction of the compressive properties of the coupon

Numerous phenomenological models have been developed in the past to predict the in-plane compressive properties of a composite laminate. It is commonly accepted that the response in compression of these materials is mainly controlled by the development of microbuckling and kinking. These phenomena are strongly dependent on the matrix properties: while soft resins may cause microbuckling, stiff resins typically lead to the formation of kink bands. Schultheisz & Waas (1996) state that microbuckling is expected to be controlled by the matrix stiffness in shear for high fiber volume fraction composites. Based on this idea, Rosen (1965) proposed one of the most widespread analytical models to predict the compressive strength of unnotched composite laminates. The model accounts for the resin properties, as well as for the characteristics of the fibers:

$$\sigma_{cr} = \frac{G_m}{1 - V_f} + \frac{\pi^2 E_f}{3} \left(\frac{d_f}{\lambda}\right)^2 V_f \tag{4.1}$$

where V_f stands for the fiber volume fraction, E_f and G_m for the longitudinal and shear stiffness of the fiber and matrix, respectively, d_f is the fiber diameter and λ is the buckling wavelength. This model typically overestimates the critical load σ_{cr}, so more theories have been suggested. Budiansky & Fleck (1993) proposed another model for conventional laminates:

$$\sigma = \frac{\tau_y \sqrt{1 + \frac{\sigma_{Ty}}{\tau_y^2} \tan^2 \beta}}{\phi_0 + \phi} \tag{4.2}$$

where τ_y and σ_{Ty} are the in-plane shear and transverse tensile yield strength of a unidirectional composite, respectively, ϕ_0 the fibre misalignment in the kink band, ϕ the additional fibre rotation in the kink band under a remote stress σ and β the band orientation angle, Figure 4.15. This equation is deduced by imposing the condition of static equilibrium of momentum between the moment generated by the misalignment of fibers and the moment exerted by the supporting transverse normal and shear stresses.
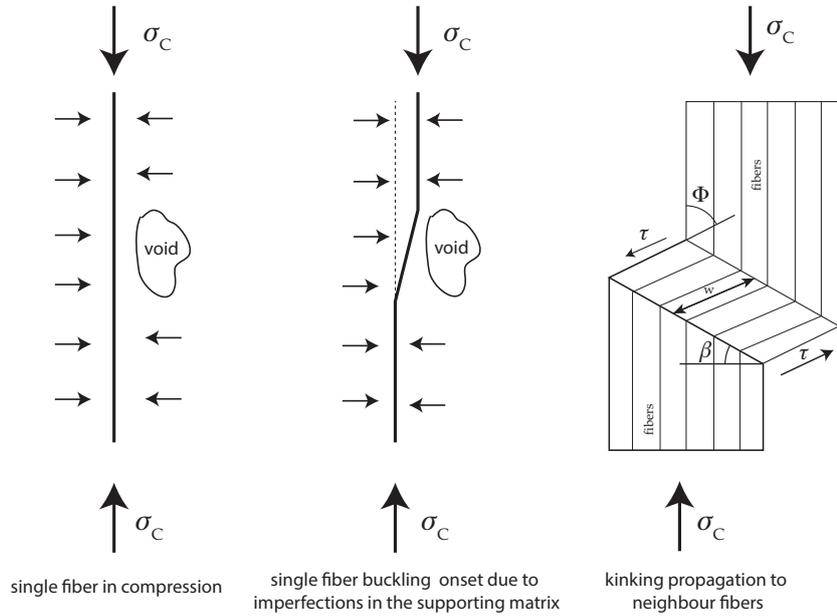
Figure 4.15: Fiber kinking schematic. While the load is aligned with the fiber direction, buckling is impeded by the constrain of the matrix. However, imperfections (misalignment, waviness, matrix cracking, plastic matrix, void), lead to fiber buckling. Then microbuckle propagates to neighbour fibers leading to the formation of a kink band.

However, the model is very sensitive to variations of β, which is not constant, as revealed by further examination of XCT images, so it is difficult to apply it to this case.

4.3.2 Prediction of the notched response

This section compares two analytical models to estimate the fracture toughness of the composite: the Finite Fracture Model described in Appendix B and already applied in chapter 3 to predict the fracture toughness in tension, and a model suggested by Soutis (2013) based on the crack cohesive zone initially suggested by Dugdale (1960). The former can be applied not only to predict the fracture toughness of laminates in tension, but also in compression, Erçin *et al.* (2013). The latter assumes that the stress distribution along the crack decreases linearly with the separation δ between the two crack surfaces. Accordingly, the area under the traction-separation $\sigma - \delta$ curve corresponds to the critical energy release rate G_c (Figure 4.16). Fiber kinking, matrix cracking and plasticity, as well as delamination are accounted for this model.

Table 4.3: Estimation of the critical energy release rate and the critical stress intensity factor of the hybrid 3D woven loaded in compression in the warp direction by using two different analytical models.

Model	G_c (KJ/m^2)	$\mathcal{K}_c$ (MPa$\sqrt{\text{m}}$)	E^* (GPa)
cohesive (Soutis)	21	23.8	27
finite fracture (Camanho)	7.3	13.5	27

$$G_c = 2 \int \sigma(\delta) d\delta = \sigma_{un} \delta_c = 21 \text{KJ/m}^2 \tag{4.3}$$

where σ_{un} is the unnotched strength of the laminate and δ_c is the kink band width measured experimentally[1] (Figure 4.17).

Results from both models are compared in Table 4.3, showing that the cohesive model predicts higher values of the fracture toughness than the Finite Fracture Mechanics model.

It should be noted that the conversion between G_c and $\mathcal{K}_c$ is established in terms of the relationship

$$G_c = \frac{\mathcal{K}_c^2}{E^*}$$

where

$$E^* = \frac{\sqrt{2 E_y E_x}}{\sqrt{\sqrt{\frac{E_y}{E_x}} + \frac{E_y}{2 G_{xy}} - \nu_{yx}}}$$

being E_x, E_y, G_{xy} and ν_{yx} the effective properties of the laminate.

---

[1]Note that this value can be also obtained from the expression proposed by Soutis & Curtis (2000) and using the exponent $n = 0.37$, as suggested by Edgren *et al.* (2008). This provides a very good approximation to the measured values of the kink band:

$$w = \frac{\pi d_f}{4} \left(\frac{V_f E_f}{2 \tau_y} \right)^n = \frac{\pi \cdot 6 \mu m}{4} \left(\frac{0.5 \cdot 230 \text{GPa}}{2 \cdot 30 \text{MPa}} \right)^{0.5} = 309 \mu m \tag{4.4}$$
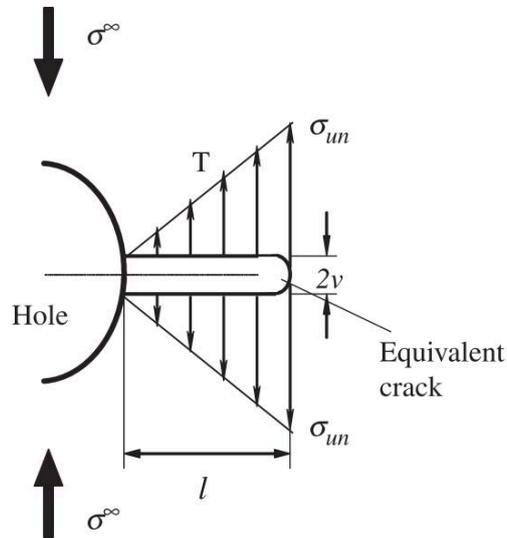
Figure 4.16: Basis of the cohesive model suggested by Soutis (2013). l is the length of the equivalent crack, T stands for the traction vector acting on the free surfaces, ν is the band width and σ_{un} is the unnotched strength.
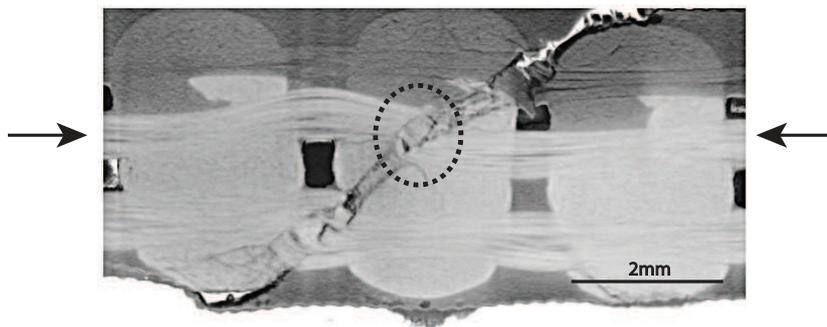
Figure 4.17: Kink band propagation through-the-thickness in an open-hole specimen. The kink band width was $\approx 320\mu m$.

4.4 Concluding remarks

The results presented above indicate that the hybrid 3D woven laminate exhibits a notch-insensitive behavior in compression. This is likely due to the fact that the response of both unnotched and notched coupons is controlled by one single failure mode: fiber kinking. Fiber kinking is triggered by matrix cracking, which in turn might be affected by the stress concentration around the hole. However, XCT inspection revealed that fiber kinking does not start specifically at the hole edges, so the stress concentration around the hole has only a limited influence on the fracture toughness.

Another important factor is the effect of the z-yarns, which increases the waviness of the fill yarns, reducing the stability and the compressive strength.

A couple of analytical models have been used to predict the fracture toughness of the composite. This is particularly useful for modelling purposes due to the complexity of the experimental determination of the fracture toughness of 3D woven composites. As expected, values found were significantly lower in compression than in tension.

CHAPTER 5

Shear Behavior

This chapter is devoted to examine the in-plane and the interlaminar shear response of the hybrid 3D woven composite. Shear stresses arise in the presence of riveted joints, at the interface between layers with different stiffness or under in-service operation conditions such as impact. So far, most of the authors have been concerned about the shear response of unidirectional composites, Van Paepegem *et al.* (2006), Totry *et al.* (2008), but there is a lack of information regarding other fiber architectures like 3D wovens. A comprehensive study of the deformation and fracture mechanisms obtained from in-plane shear and three-point bending tests is presented here to gain understanding in the shear response of 3D composites. The analysis is supported by a detailed XCT inspection of the deformation and failure mechanisms, as well as by a quantification of the fiber rotation.

5.1 In-plane shear behavior

The in-plane shear behavior of a unidirectional composite is typically non-linear. The linear elastic region is followed by a plateau –where matrix cracking occurs– and then by a strain hardening due to the fiber rotation towards the loading axis, Sket *et al.* (2014). Failure occurs at very large strains (often > 15%). Likewise, Bogdanovich *et al.* (2013), Gerlach *et al.* (2012), Tarnopol *et al.* (2000) Lomov *et al.* (2009) reported a non-linear behavior of 3D woven composites. The lack of reinforcement in the non-principal directions leads to weak shear planes whose behavior is controlled by the matrix properties which
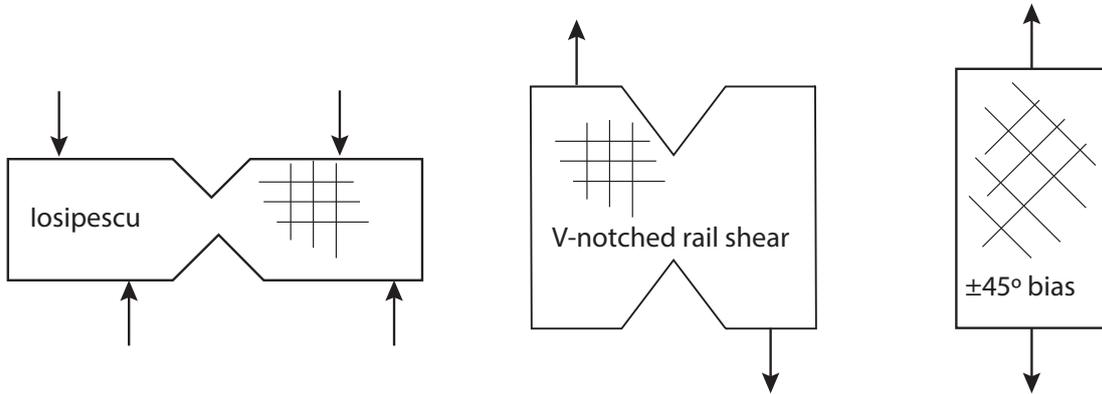
Figure 5.1: Schematic of in-plane shear test strategies. Two notches are machined in the Iosipescu (left) and the V-notched rail shear (center) specimens. The preparation of the Tensile Shear Test Method (right) is very simple and only requires a standard tensile test with the layers oriented at $[\pm 45°]$ to the loading axis.

could compromise the final performance of the material. Moreover, the role played by the binder and hybridization in the in-plane shear response are not well understood, so a deep analysis of the in-plane shear behavior and of the failure mechanisms of hybrid 3D woven composites is presented here.

The characterization of the in-plane shear response of a composite is not an easy task, particularly in highly anisotropic and heterogeneous laminates. The main problem is to achieve an uniform shear stress state in the specimen. To this end, several methods have been developed in the past, including the Iosipescu test (ASTM D5379 (2001)), the V-notched rail shear test (ASTM D7078 (1995)) and the tensile shear test (ASTM D3518 (2001)), Figure 5.1. The first two methods provide a quasi-uniform stress state in a small portion of the material at the ligament between two notches, but special fixtures are needed to achieve the simple shear stress state. The Tensile Shear Test (TST) method is likely the most commonly used in industry due to the simplicity (only requires a standard tensile test), although it is more difficult to analyze. It is carried out by means of a tensile test of a rectangular coupon until failure at a given velocity. To prevent damage from gripping, tabs are used at the ends of the specimen. The most relevant properties obtained from this test are the in-plane shear modulus G_{12} and the shear strength S. The method is typically applied to symmetric and balanced laminates with unidirectional plies oriented at $[\pm 45°]$.

Unfortunately, the 3D woven composite studied in this thesis is not covered by any of the standards mentioned above due to its non-symmetric structure and to the presence of the binder. However, unlike other preforms (e.g. 3D braided), 3D woven orthogonal composites do not include fibers inclined to the principal axes, so it can be assimilated to a standard cross-ply laminate. Z-yarns are parallel to the warp bundles, so the shear response of the material is still controlled by the matrix and the in-plane behavior of the material will not be strongly affected by the through-thickness reinforcement. Furthermore, stresses arising from coupling tension-bending due to the non-symmetric structure of the laminate are negligible within the range of validity of the standard.

Based on the previous considerations, it was decided that *a priori* this composite is a suitable candidate for the TST method, ASTM D3518 (2001).

5.1.1   Experimental techniques

Four specimens were machined for the tensile tests with an angle of $\pm 45°$ between fibers and the loading direction. Nominal dimensions were equal to those reported in Chapter 3: $250 \times 25 \times 4.1$mm^3. Glass fiber tabs of 50 mm in length were glued to the specimens, leading to a free length of 150 mm (Figure 5.2). They were tested in tension at room temperature using an electromechanical universal testing machine (Instron 3384) following the recommendations of the ASTM D3518 (2001), (Figure 5.3). Both resistive extensometry and Digital Image Correlation (DIC) were used –each in one face of the specimen– to measure the strain along the loading axis, whereas transversal strains were only measured by DIC. This method provides the full displacement field in one of the faces and, unlike strain gages, is not affected by fiber rotation or the roughness of the specimen. Three specimens were covered with a speckle pattern in the glass face and another one on the carbon face. Images obtained with the DIC system were captured every 5 seconds. Unfortunately, transverse strains were not measured for strains > 14% in all specimens, because the pattern was destroyed at such high deformation (Figure 5.3).

Tests were carried out under stroke control at 2 mm/min and the load was continuously measured during the test with a load cell of 150 KN. The in-plane shear stress-strain
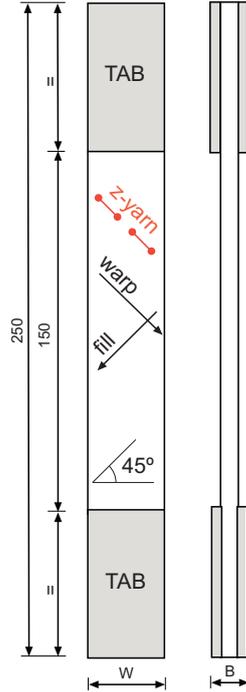
Figure 5.2: Schematic of the $\pm 45°$ specimen. Note the directions of the reinforcement and of the z-yarn.

response was obtained following the procedure described in the ASTM D3518 (2001). According to the standard, the in-plane ply shear stress τ_{12} is given by

$$\tau_{12} = \frac{\text{P}}{2\text{BW}} \tag{5.1}$$

where P is the applied load and B and W the specimen thickness and width, respectively (Figure 5.2). The corresponding shear strain γ_{12} is computed as

$$\gamma_{12} = \left|\varepsilon_{\text{longitudinal}}\right| + \left|\varepsilon_{\text{transverse}}\right|$$

where $\varepsilon_{longitudinal}$ stands for the average longitudinal strain from the two faces of the specimen. The in-plane shear modulus G_{12} was computed as the slope of the stress-strain curve between $\gamma_{12} = 1.5 \cdot 10^{-3}$ and $\gamma_{12} = 6.0 \cdot 10^{-3}$. The in-plane shear strength S was the stress at a shear strain of 5%, as recommended by the standard.

It is worth noting that equation 5.1 is deduced from the Classical Laminate Theory. Thus, the possible stresses induced by the unsymmetric lay-up configuration, the non-

(a) $\gamma_{12} = 0$ (b) $\gamma_{12} = 19\%$ (c) $\gamma_{12} = 43\%$, close to final failure
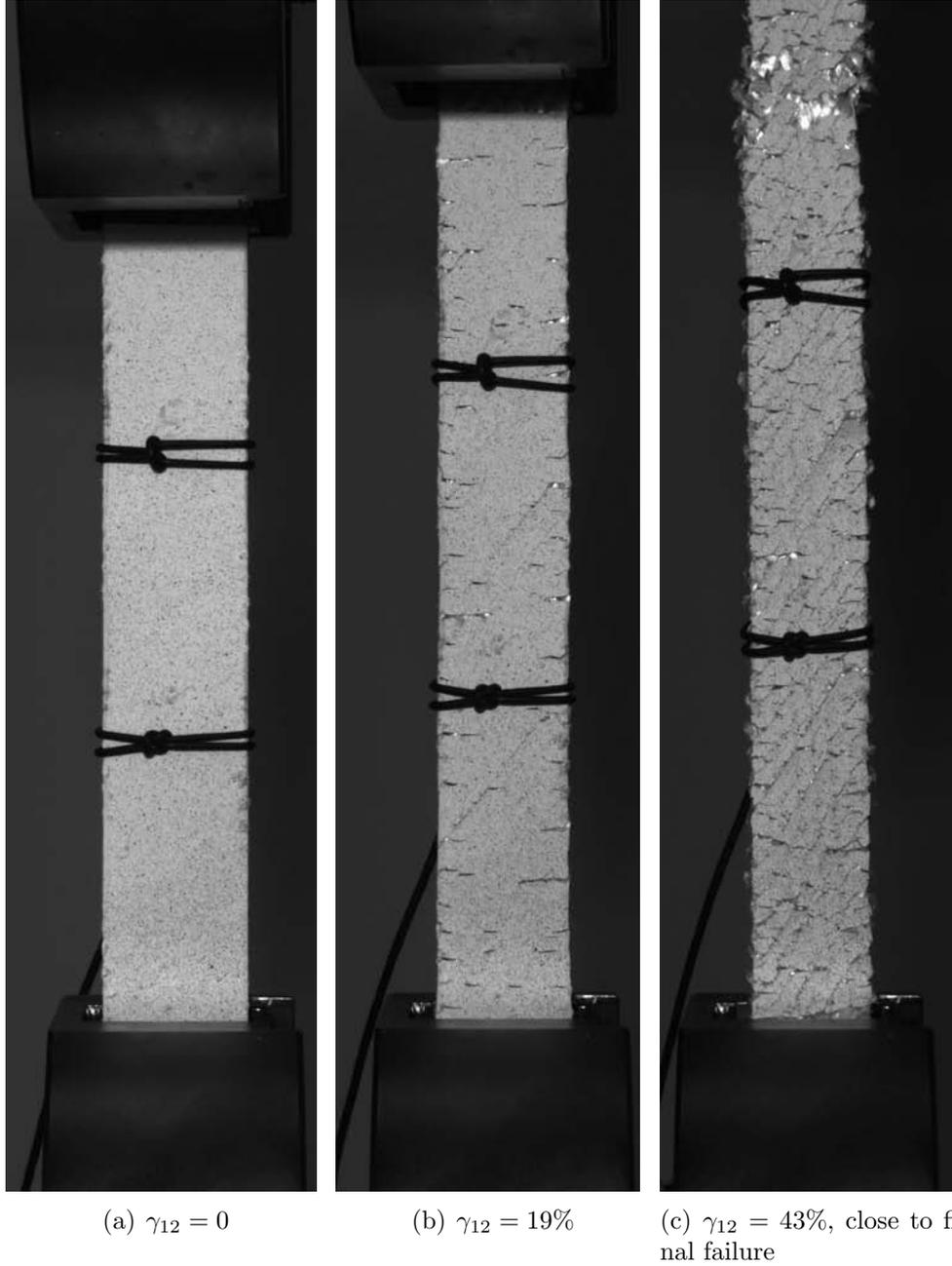
Figure 5.3: Tensile test of a hybrid 3D woven composite laminate with the fibers oriented at $[\pm 45°]$ from the loading direction. Extensive cracking appeared during deformation. Moreover, the shear bands along yarn directions are visible.

Figure 5.4: Angle between fibres measured after failure.

linear geometrical effects caused by fiber rotation, the net section reduction (necking) observed in the specimens and the out-of-plane stresses induced by the z-yarn crimping are not accounted for. While such effects are not relevant for small strains, they cannot be neglected at large deformations.

The angle θ between yarns was measured by optical methods to evaluate the influence of fiber rotation on the mechanical response. This was possible because fiber yarns became visible to the naked eye after the resin was damaged, Figure 5.4.

Finally, a post-mortem specimen was examined by XCT to ascertain the damage and failure micromechanisms. The region of interest was chosen near the failure section, at the center of the specimen. Measurements were performed with a Nanotom 160NF (Phoenix) at 110kV and 110 mA using a W target. 2300 radiographs were acquired for each tomogram with an exposure time of 500 ms. The reconstructed volumes presented a resolution of 11 μm/voxel.

5.1.2 Results and discussion

The stress-strain $\tau_{12} - \gamma_{12}$ curve of the hybrid 3D woven composite is plotted in Figure 5.5. The material exhibits a very ductile response enhanced by the cross-ply stacking sequence and the large size of the resin pockets. Three regimes are clearly distinguished:

Table 5.1: In-plane shear properties of the hybrid 3D woven composite

G_{12} (GPa)	τ_{12} at $\gamma = 5\%$ (MPa)	$\tau_{12}^{\text{apparent}}$ at $\gamma = 32\%$ (MPa)
3.4 ± 0.9	27.3 ± 2.0	43.8 ± 3.1

- ***region A-B***. The composite initially exhibits a linear elastic response up to $\gamma_{12} \approx$ 1.0%. The shear strength S and shear modulus G_{12} obtained within this regime are presented in Table 5.1.

- ***region B-C***. The material deforms with a low tangent shear modulus (30 MPa) up to $\gamma_{12} \approx 30\%$. Such strain hardening is likely due to the non-linear geometrical effect of fiber rotation, Wisnom (1995), Totry *et al.* (2010). As shown by DIC in Figure 5.5, shear bands develop in this regime.

- ***region C-D***. A moderate stiffening occurs from $\gamma_{12} \approx 30\%$ up to failure. The tangent shear modulus increases from 30 MPa to 60 MPa. A first examination of post-mortem specimens would suggest that this is only due to fiber rotation from 45° to 32°. However, a more thorough analysis revealed that fiber orientation took place at a constant rate (Figure 5.6) —kinematically imposed by the axial deformation— and does not justify this abrupt change. A possible explanation may be the fiber locking at ply level. As the composite is further stretched, yarns rotate until they come into contact and are unable to slip, enhancing the in-plane shear stiffness of the composite[1], Carvelli *et al.* (2012). This idea is supported by the fact that the insertion of the z-yarn between two consecutive warp yarns reduces the gap between them and thus facilitates locking. Moreover, no evidence of fiber breakage was found during the test.

Final failure occurs at $\gamma_{12}^{\text{ult}} = 42\%$ and $\tau_{12}^{\text{ult}} = 43$ MPa. The finite strains achieved in shear lead to a strain localization (necking) at the weakest section. At this point, small pieces of resin detach from the composite in a brittle manner and the load is fully transferred to a few dry bundles. This causes the immediate failure of the coupon. The failure section of two specimens is depicted in Figure 5.7.

---

[1]Even though fiber locking is typically observed in dry fabrics during picture frame shear tests, the high deformability and the large size of the yarns and the resin channels in this composite can justify this hypothesis.
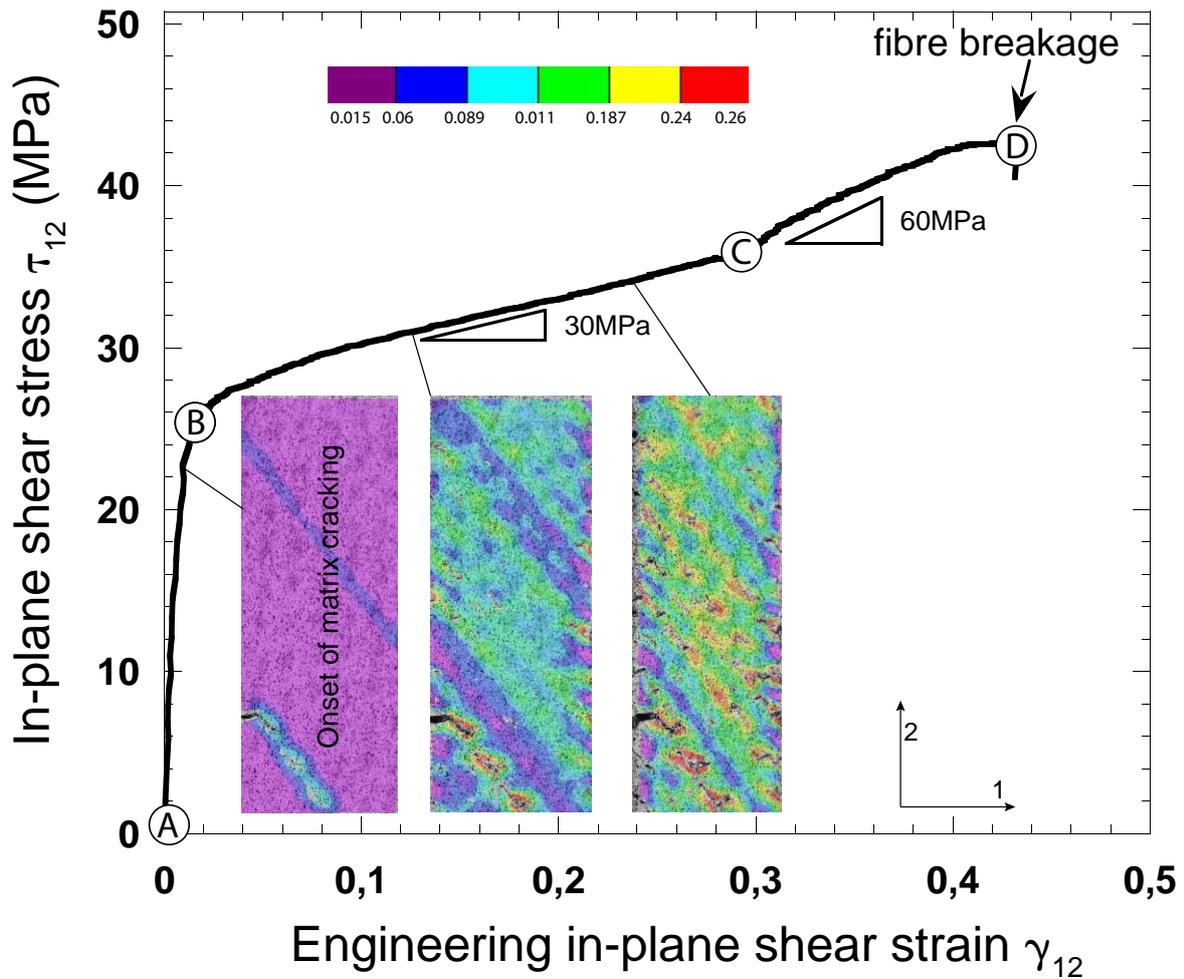
**Figure 5.5:** Engineering shear stress *vs* shear strain curves of the hybrid 3D woven composite. The contour plots of the Green-Lagrange strains measured in the loading direction by means of DIC are included, showing the progressive generation of shear bands.
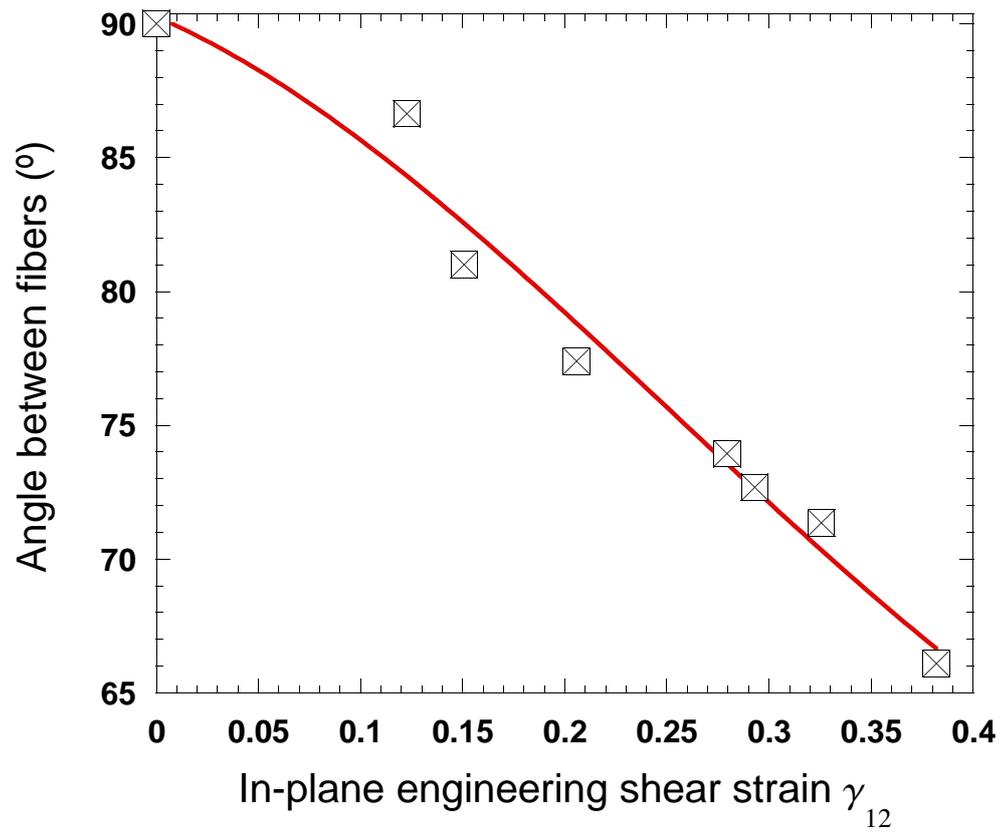
Figure 5.6: Evolution of angle between fibers.

(a) Carbon face
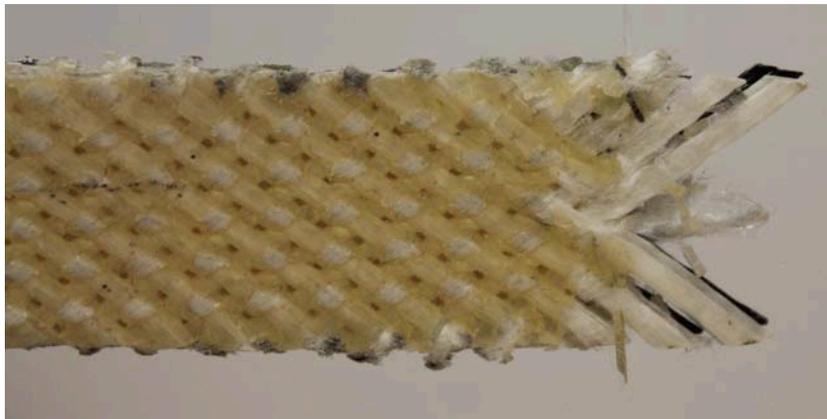
(b) Glass face

Figure 5.7: Fractured regions of two specimens tested in shear.

Damage mechanisms

The XCT inspection of one specimen tested in shear revealed the presence of multiple failure mechanisms at ply and laminate level:

- At ply level, the kinematic incompatibility between the fibers and the matrix gives rise to in-plane shear stresses. As a result, this generates shear bands parallel to the yarns and causes tow splitting and yarn-matrix debonding. As shown in Figures 5.8 and 5.9, these cracks run parallel to the yarns. These damage mechanisms would explain the transition to the non-linear deformation regime observed at point B of the shear stress-strain curve.

- At laminate level, fiber rotation in plies oriented at opposite angles gives rise to the so-called *scissoring effect* in which the $\pm 45°$ interface is subjected to in-plane shear forces. As depicted in Figure 5.10, this rotation causes shear cracking at the ligaments of resin located between two consecutive z-yarns as well as extensive yarn-matrix debonding. In unidirectional composites this effect is only constrained by the matrix between layers, typically leading to delamination and to a reduction in the shear strength. However, in 3D composites, the rotation of the fill yarns is constrained by the friction with the z-yarn. This causes a tightening of the z-yarn (Figure 5.11) and therefore a stress concentration that leads to extensive z-yarn-matrix debonding (Figures. 5.8 and 5.10).

Another interesting finding is the orientation of cracks within the fibre bundles. As shown in Figure 5.12, the fracture plane generated by tow splitting is inclined at certain angle α with respect to the vertical direction. This is likely due to the crimping induced by the binder in the carbon fill yarns, which causes a non-uniform distribution of the frictional forces acting over the yarn. This in turn leads to the generation of longitudinal shear stresses within the yarns during yarn pull-out. This is illustrated in Figure 5.13.

Nevertheless, recalling the results from tensile tests, cracks were oriented in either vertical or horizontal directions. This suggests that other factors than crimping might also affect the orientation of the fracture angle α during in-plane shear testing. A possible explanation could be the presence of transverse compressive stresses σ_{22} developed during the yarn rotation.
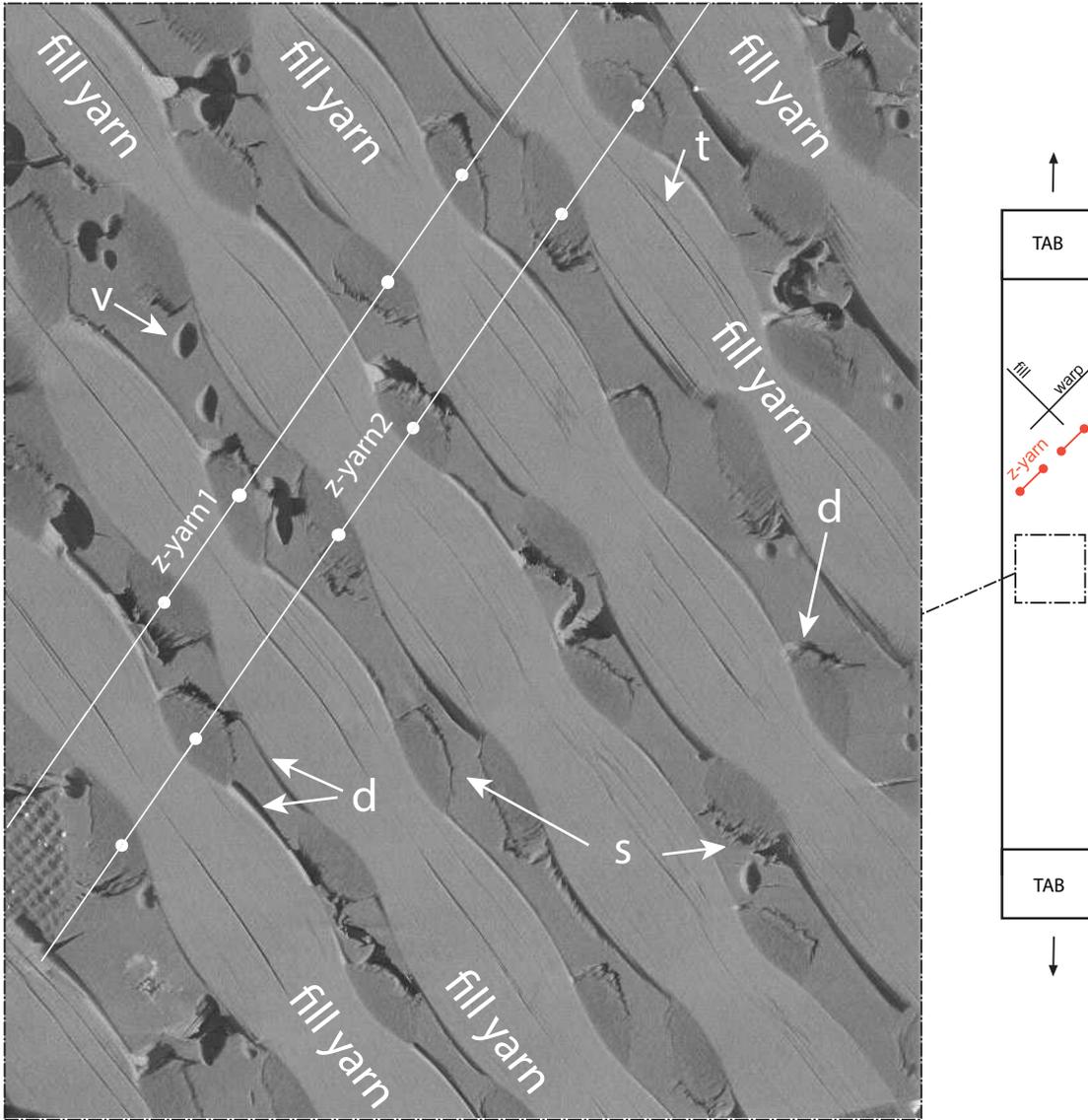
Figure 5.8: Section parallel to the outer surface of the laminate throughout the carbon fill layer. Carbon fiber yarns and matrix appear light grey. The orientation of two adjacent z-yarns (z-yarn1 and z-yarn2) is indicated with two parallel white lines. White filled dots indicate the location of the corresponding z-yarn cross sections, which appear dark grey. Arrows indicate the different damage mechanisms: d stands for debonding of the fiber tows or the z-yarns, t tow splitting within the fiber tows and s is shear at ligaments of resin constrained by two consecutive z-yarns. v indicates voids.
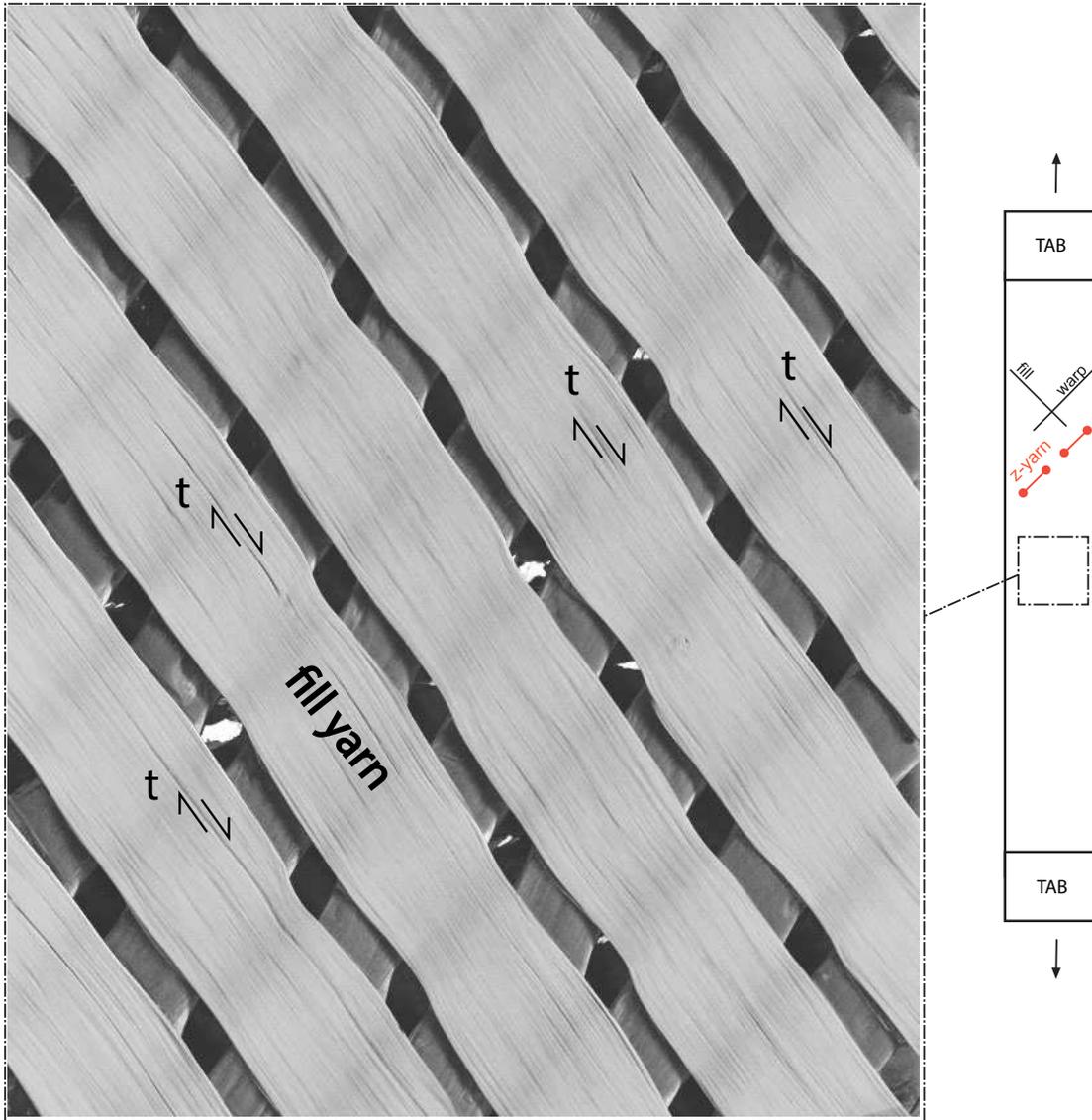
Figure 5.9: Section parallel to the outer surface of the laminate containing the fill glass layer. *t* stands for tow splitting.
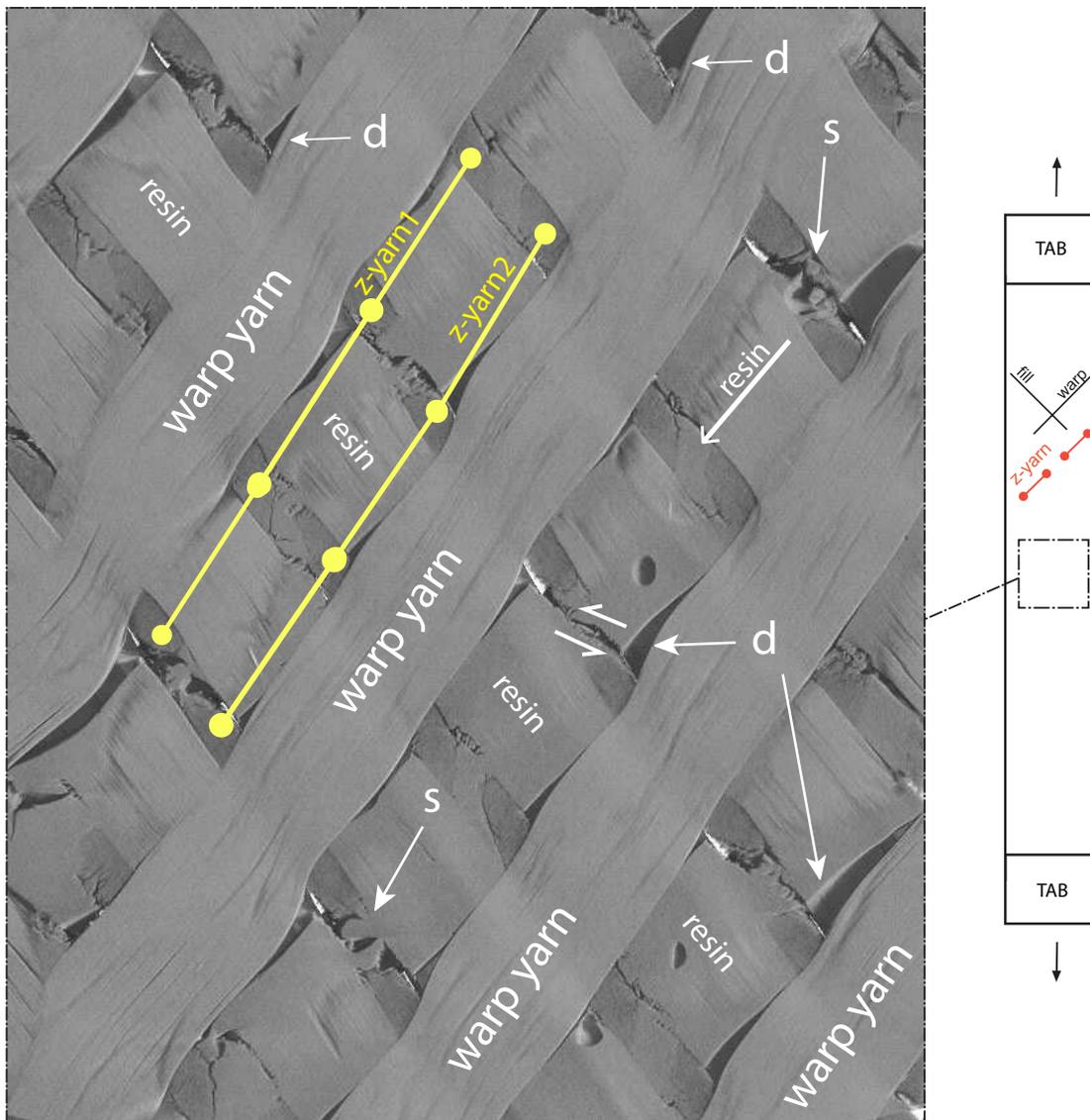
Figure 5.10: Section parallel to the outer surface of the laminate containing the carbon warp layer and the resin at the two carbon layers interface. Carbon fiber yarns and the matrix appear light grey. The orientation of two adjacent z-yarns (z-yarn1 and z-yarn2) is indicated with two parallel yellow lines. Yellow filled dots indicate the location of the corresponding z-yarn cross sections, which appear dark grey. Arrows indicate the different damage mechanisms: d stands for delamination of the fiber tows or the z-yarns, s is shear at ligaments of resin constrained by two consecutive z-yarns. Extensive shear cracking is visible at the ligaments of resin located between z-yarns. Yarn-matrix debonding is also clearly depicted.

before testing   after testing
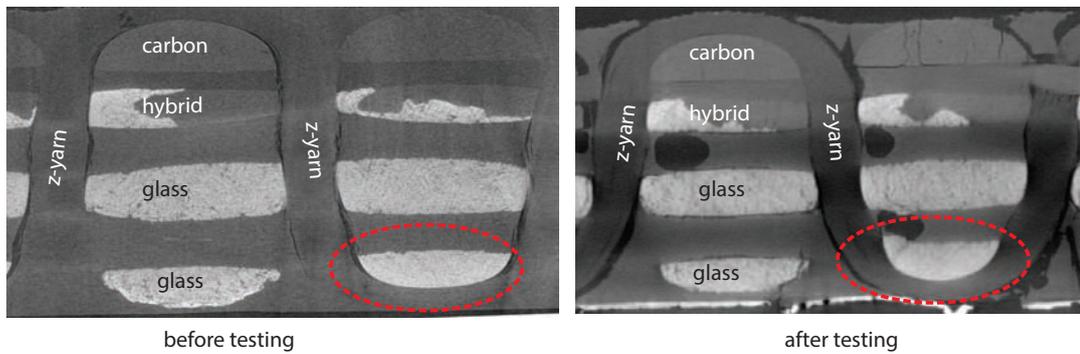
Figure 5.11: Comparison between XCT images before and after in-plane shear testing. The lateral forces exerted by the fill yarns during fiber scissoring cause a tightening of the z-yarn which in turn enhances the constrain on the bottom fill yarns.
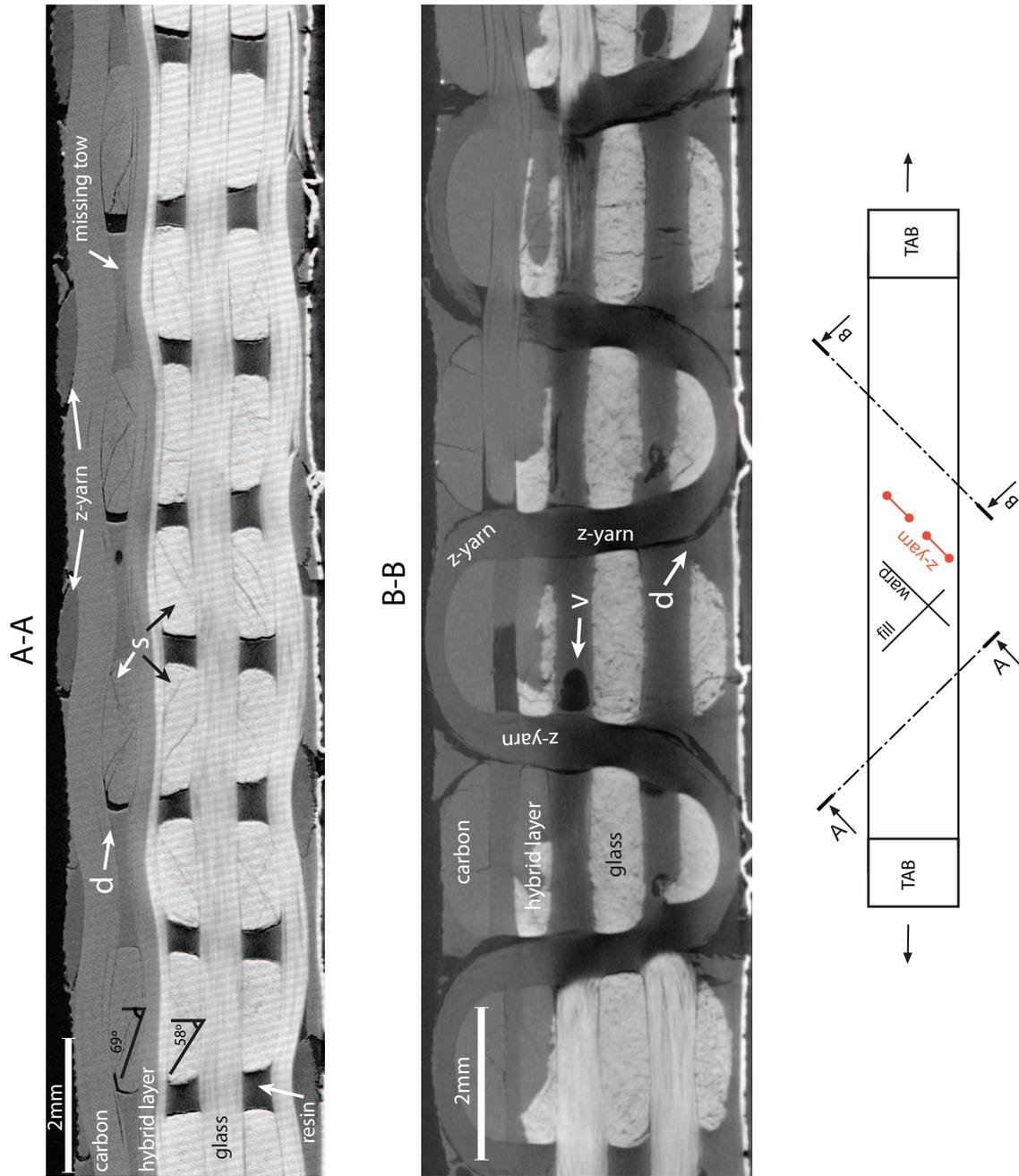
Figure 5.12: Cross section perpendicular to the warp and z-yarns (A-A) and cross section perpendicular to the fill yarns (B-B). Glass fiber yarns appear light grey, carbon fiber yarns appear dark grey, z-yarn and the matrix appear slightly darker than carbon yarns and the white region at the bottom correspond to DIC speckle pattern. Arrows indicate the different damage mechanisms: v indicates voids, d stands for debonding of the fiber tows or the z-yarns and s indicates shear cracking within the tow. The fracture angle in glass and carbon yarns were $\alpha_{glass} \approx 58°$ and $\alpha_{carbon} \approx 69°$, respectively.
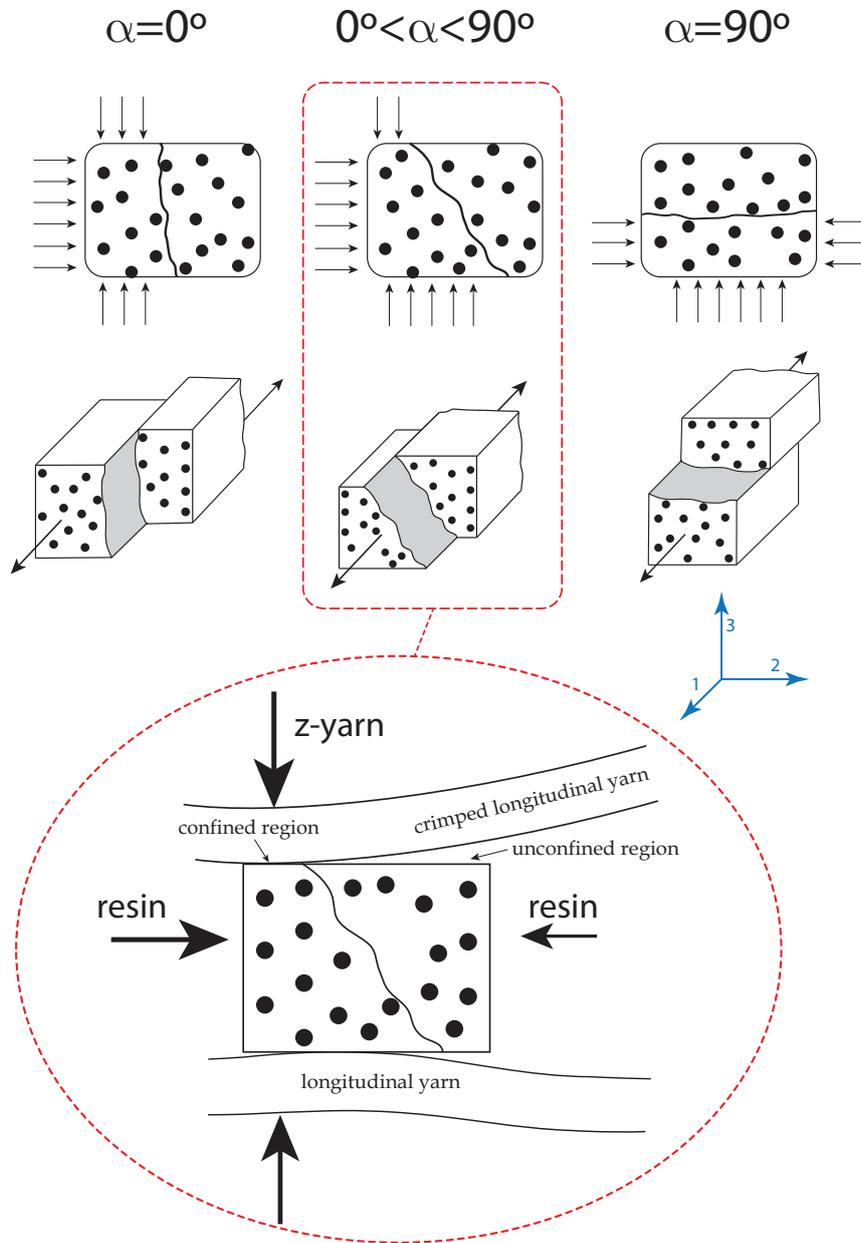
Figure 5.13: Influence of transverse compressive stresses on the orientation of the fracture planes developed during yarn pull-out. Heterogeneous distribution of frictional forces gives rise to different orientations of the fracture planes. Figures at the center illustrate how the waviness of the yarns causes a non-uniform distribution of transverse compressive stresses leading to an inclined crack. Note that the lateral confinement is not constant and can be enhanced during fiber rotation.

5.2 Interlaminar shear behavior

This section analyzes the influence of the 3D weaving and hybridization on the mechanical response of the hybrid 3D composite under interlaminar shear. To this end, short beams with and without binder were tested and inspected by means of XCT. The influence of hybridization was evaluated by indenting the laminate on the carbon and the glass faces.

This approach provides useful information (contact history, local deformations, interlaminar and out-of-plane shear stresses) for the analysis of impact on composite materials. In fact, the contact stresses developed during this test are similar to the localized stresses generated during impact, Walter *et al.* (2010).

5.2.1 Experimental techniques

Three-point bending tests on short beams with and without z-yarns were carried out to study the effect of the z-yarn reinforcement. To this end, a fiber preform was vacuum infused with an epoxy-vinylester resin (Derakane 8084) by vacuum assisted resin transfer moulding technique (VARTM), Figure 5.14(a). VARTM is similar to RTM, except that it uses a one-sided mold and vacuum is applied to the preform with a flexible bag to speed up the resin infiltration. In selected cases, z-yarns were taken out from the dry fabric prior to infusion, Figure 5.14(b). This was done very carefully by hand, removing the z-yarns with tweezers, so that no damage was introduced.

Tests were carried out at room temperature according to the ASTM D2344/D2344M (1999). Load was applied with an electromechanical universal testing machine (Instron 3384), under stroke control at 1 mm/min, through a roller at the midpoint of a short beam supported by two rollers. Load was monitored with a load cell of 150 KN. The nominal specimen size was $24.6 \times 8.2 \times 4.1$mm^3, whereas the diameter of the loading nose and of the rolling supports were 4.00 mm and 2.94 mm, respectively. The loading span was 16 mm. A schematic of the test is depicted in Figures 5.15 and 5.16.

Four sets of tests of 4 specimens each were conducted to analyze the influence of the z-yarn and the hybridization. Specimens were alternatively loaded on the carbon and the glass faces in specimens with and without z-yarn, as illustrated in Figure 5.17.

(a) Processing set-up during infusion by VARTM.

(b) Dry fabric without z-yarns (dark zone)

Figure 5.14: Preparation of specimens without z-yarns.

Two specimens loaded in the carbon face (with and without z-yarns) were inspected before testing and after failure by means of a Nanotom 160NF (Phoenix) at 90kV and 80 μA using a W target. 1800 radiographs were acquired for each tomogram with an exposure time of 500 ms. The reconstructed volumes presented a resolution of 6.6 μm/voxel.
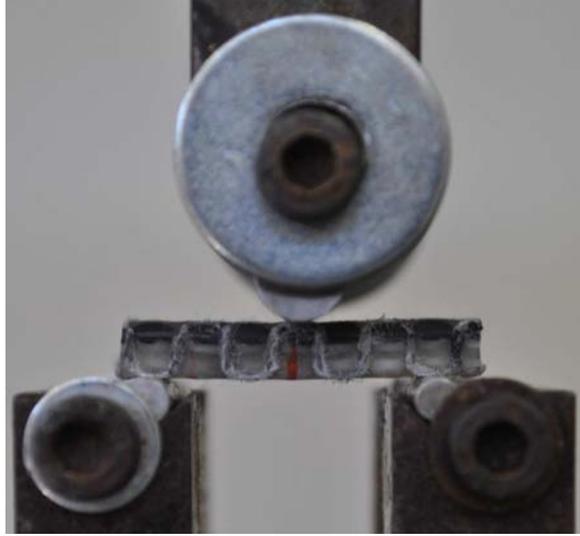
Figure 5.15: Photograph of the Short Beam Three-point bend test set-up.
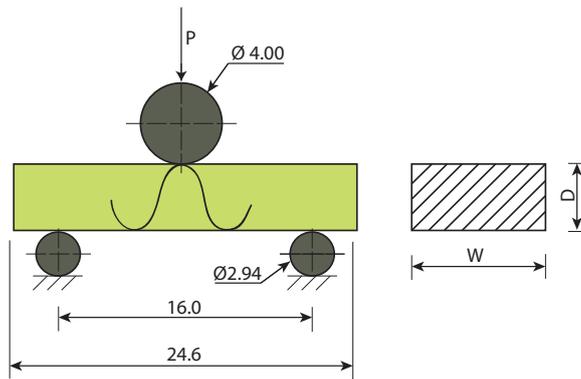
Figure 5.16: Short Beam Three-point bend test set-up schematic.

Assuming a rectangular cross section, the short beam shear strength S^{sbs} was calculated as

$$S^{sbs} = 0.75 \frac{P}{\text{DW}} \tag{5.2}$$

where P is the maximum load at the first peak of the load-displacement curve, W is the specimen width and D the specimen depth.

It is worth noting that this test addresses fiber-reinforced composite materials in which failure initiates at the midplane by shear. However, the presence of the z-yarns changes the failure mode of 3D composites, so failure takes place by crushing under the loading

nose. Consequently, S^{sbs} is only valid for comparative purposes and should be treated as an apparent value of the strength.

5.2.2 Results and discussion

A representative load-displacement curve of each load case (see Figure 5.17) is plotted in Figure 5.18. Significant differences were found depending upon the presence of the z-yarn and the loading face. The specimens without z-yarns initially exhibit a linear response up to the onset of failure (either by delamination at free edges or by out-of-plane shear cracking). Afterwards, they fail in a quasi-brittle manner after a displacement $\delta \approx 1 - 2$ mm. Scatter was negligible during the elastic regime, but significant differences were found afterwards. Regarding the specimens with z-yarns, they also initially exhibit a linear response, but this is followed by a non-linear deformation in which the composite undergoes a continuous hardening likely due to geometric non-linearities. These tests were ended before failure. Results were quite repetitive along the whole curve.

Influence of the z-yarns

As shown in Table 5.2, the presence of the z-yarn reduced S^{sbs} by 31% and 27% with respect to the materials without z-yarns when indenting in carbon and glass faces, respectively. The damage tolerance was, however, significantly enhanced by the z-yarns, which led to the development of a large variety of new energy dissipation mechanisms. Similar results have been reported in the literature. Walter *et al.* (2010) compared the monotonic and cyclic short beam test response of 3D and 2D composites, and concluded that 2D composites were stronger but less damage tolerant.

Influence of hybridization

The effect of hybridization mainly affects the onset of matrix cracking, but not the shape of the load-displacement curve. S^{sbs} was reduced when the load was applied on the carbon face by $\approx 14.8\%$ and 10.0% in specimens with and without z-yarns, respectively.
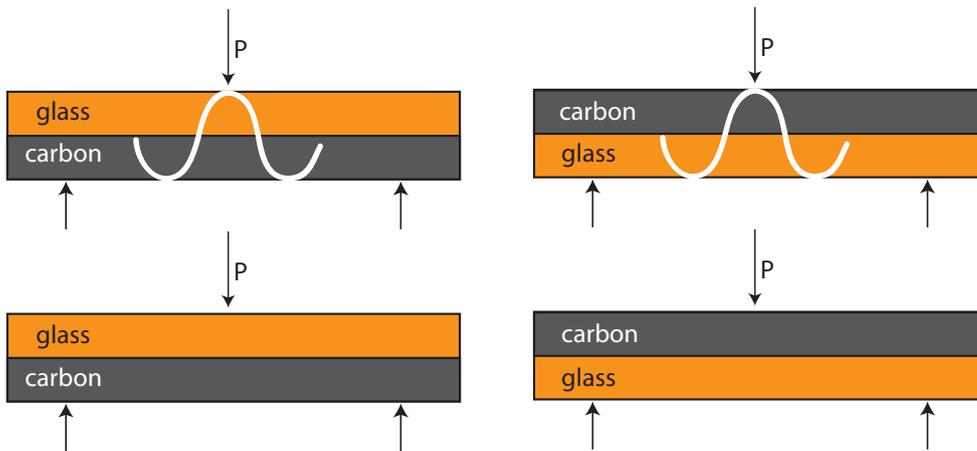
Figure 5.17: Load cases: coupons with and without binder indented on either the carbon or the glass face. Specimens are oriented with the largest dimension parallel to the warp yarns.
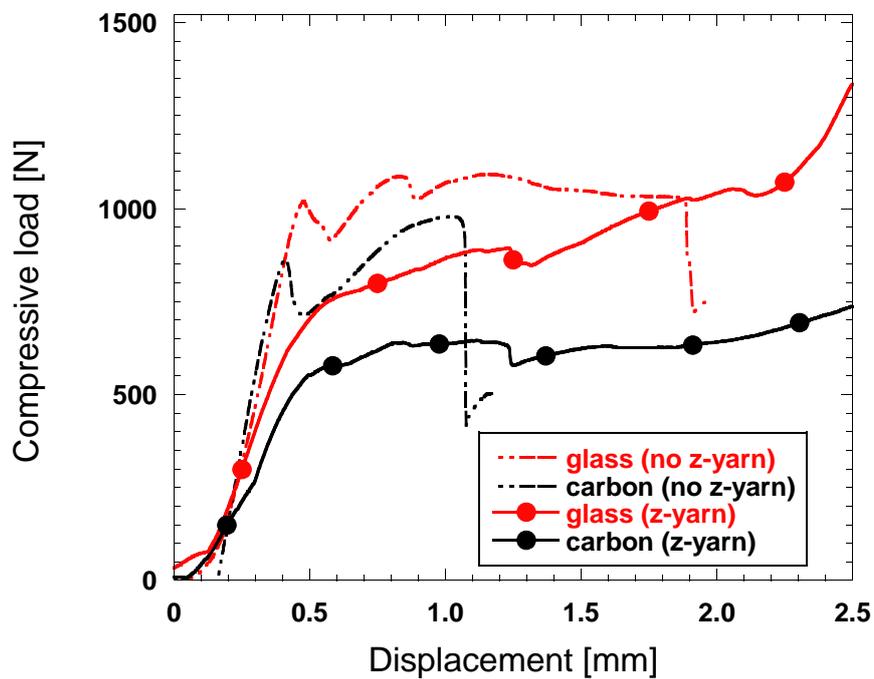

Figure 5.18: Representative load-displacement curves of the three-point bend test of a short beam under different conditions. See text for details.

Table 5.2: Apparent short-beam strength S^{sbs} (MPa)

| indented face	z-yarn	no z-yarn
carbon	13.8 ± 1.27	20.0 ± 1.42
glass	16.2 ± 0.97	22.2 ± 1.14

Damage inspection

The results reported above indicate that both hybridization and the presence of the z-yarns affect the mechanical behavior of the 3D composite. As discussed below, these differences are explained by the failure mechanisms involved in each loading case.

A sequence of snapshots were captured during the test[2], revealing that failure of specimens without z-yarns always initiates under the loading roller by transverse shear cracking. Afterwards, as depicted in Figures 5.19(a) and 5.19(b), cracks propagate and induce delamination at the midplane of the beam. XCT inspection of a tested specimen showed also the presence of out-of-plane compressive stresses and the generation of a pine tree damage pattern (Figure 5.20). It should be noted that transverse shear cracking was more evident when the load was applied on the carbon face due to the higher brittleness of the carbon fibers, which makes them more sensitive to contact stresses. This in turn might explain the lower values found of F^{sbs}_{carbon}.

XCT inspection of specimens with and without z-yarns revealed that the presence of the z-yarns increases the ductility of the composite (Figures 5.19 and 5.21). Since layers are held together by the z-yarns, specimens are forced to bend as a simply supported beam, undergoing large deformations and giving rise to multiple failure mechanisms. As the loading roller is progressively wrapped by the beam, the contact stress distribution changes and shifts the maximum pressure from the center to the edge of the contact zone, Abrate (1998). Compressive and tensile stresses caused by bending become more important than shear stresses and govern the response of the composite. Tensile stresses at the bottom layers give rise to z-yarn debonding (Figure 5.22(a)) or to transverse matrix cracking (Figure 5.22(b)), depending on the presence of the z-yarn on this specific section. Meanwhile, bending compressive stresses cause fiber kinking at the upper layers, whereas interlaminar shear stresses lead to delamination as well as tow splitting at intermediate layers.

---

[2]For sake of brevity only those obtained at $\delta \approx 2 - 2.5$ mm are depicted in Figure 5.19.
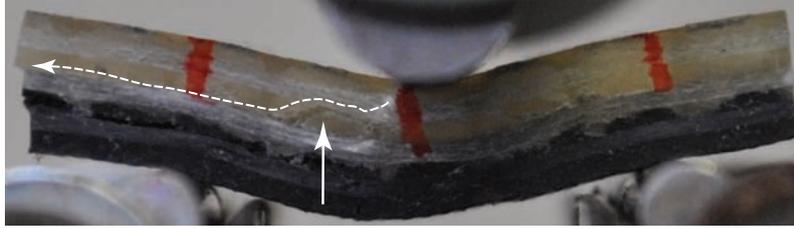
(a) Load applied on the glass face of a specimen without z-yarns. Dashed line indicates the crack propagation path. Transverse shear cracking initiates under the loading roller and induces delamination at the interface between two orthogonal glass layers.
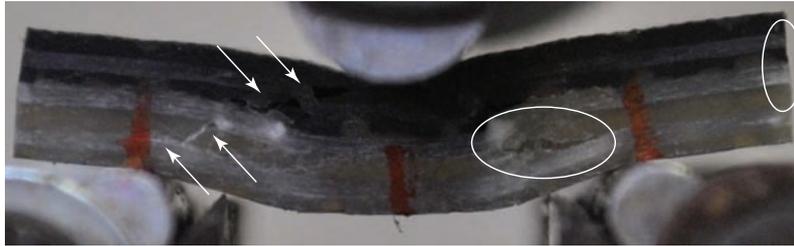
(b) Load applied on the carbon face of a specimen without z-yarns. Transverse shear cracks initiates under the loading roller and propagates across the thickness following a pine tree pattern. Compressive bending stresses cause fiber kinking in carbon layers.

(c) Load applied on the glass face of a specimen with z-yarns. No evidence of cracks were found at this deformation level.
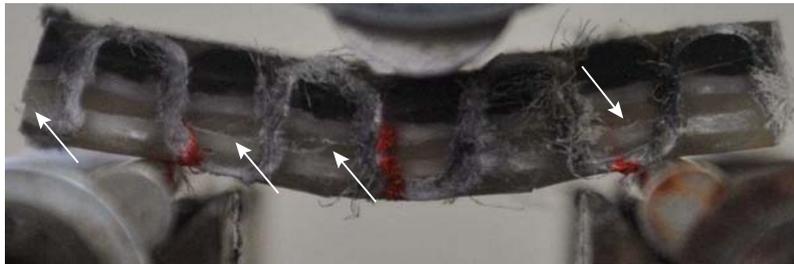
(d) Load applied on the carbon face of a specimen with z-yarns. Transverse shear cracking appears in glass layers in the region of influence of the loading roller and propagates outwards at the interface between two glass layers. Note that cracks remain closed because of the effect of the z-yarn.

Figure 5.19: Optical micrographs of Three-point Bend test of a short beam at $\delta \approx 2-2.5$ mm.
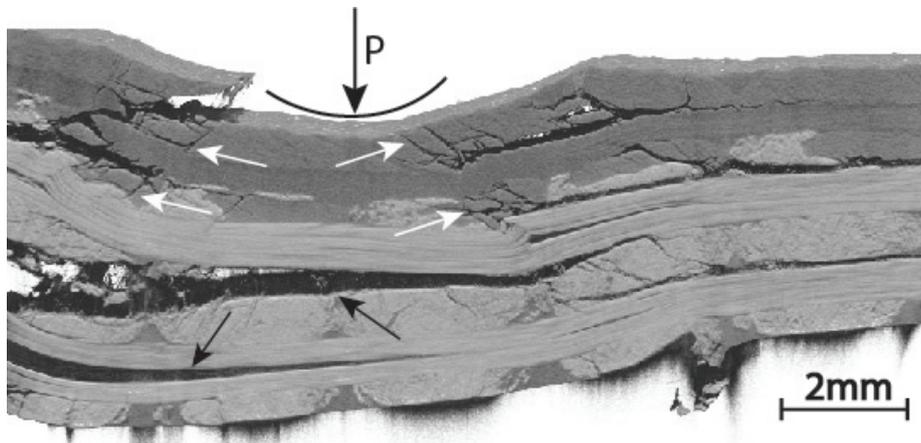
Figure 5.20: Delamination of a specimen without z-yarns loaded on the carbon face. White arrows indicate transverse shear cracking and black arrows interlaminar shear cracking.
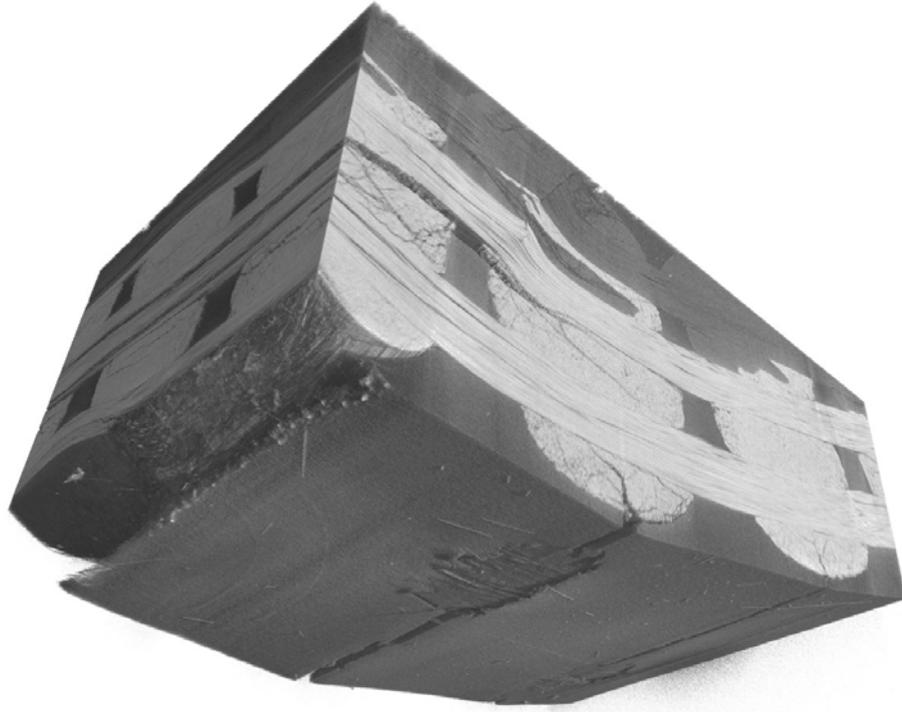
(a) With z-yarns
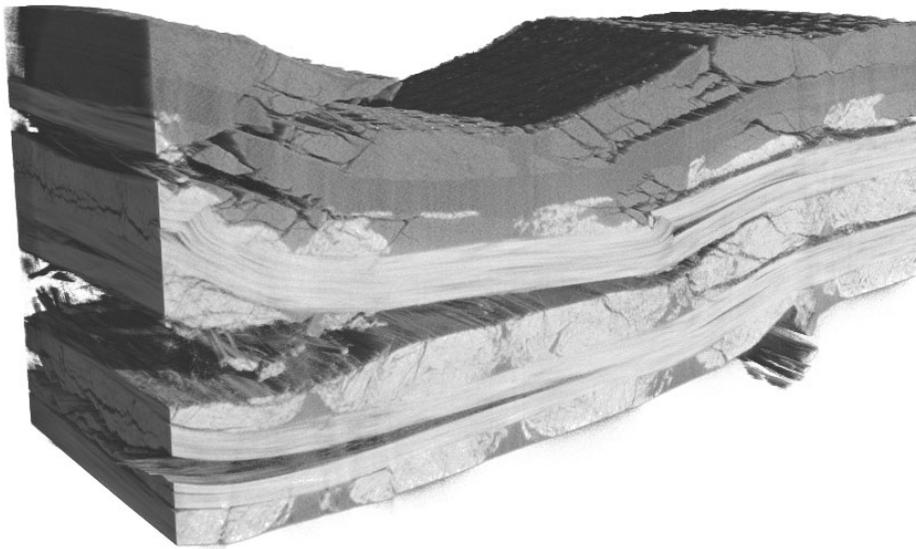
(b) Without z-yarns

Figure 5.21: Specimens loaded on the carbon face.
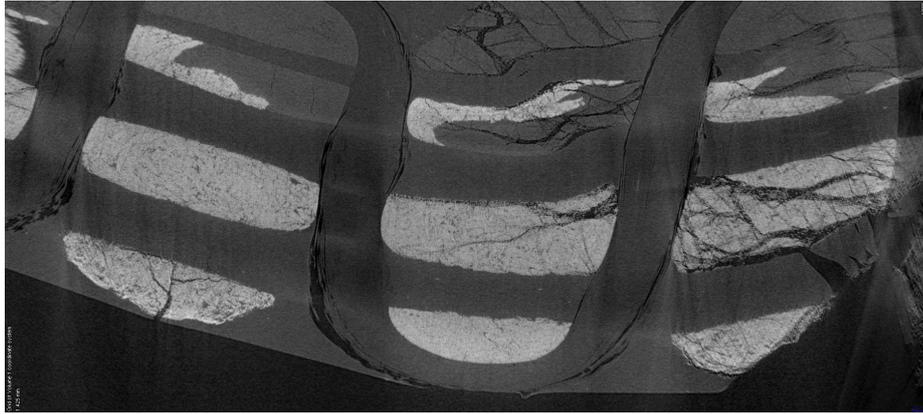
(a) Cross section containing the z-yarns.
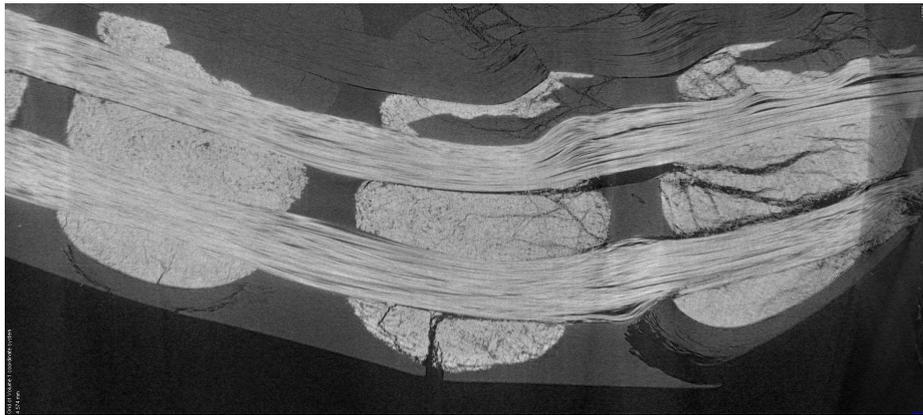
(b) Cross section not containing the z-yarns.

Figure 5.22: Cross sections parallel to the warp direction in a specimen with z-yarns after the Short Beam test. The specimen deforms in a ductile manner. Tensile bending stresses cause either (a) z-yarn debonding in sections containing the binder or (b) intra-yarn transverse cracking in sections without the z-yarns.

5.3 Concluding remarks

The in-plane shear behavior of the hybrid 3D woven was highly non-linear. The mechanical response is controlled by several phenomena, namely the onset of matrix cracking (either as tow splitting or at the yarn-matrix interfaces), fiber rotation and fiber locking. The presence of the z-yarns enhances the resistance of the composite to scissoring, but it is a source of stress concentrations.

Transverse shear stresses developed under the loading roller play a critical role during short beam tests, particularly when the load is applied on the carbon face due to the higher brittleness of carbon fibers. The presence of the z-yarn clearly enhances the ductility of the composite due to its ability to hold layers together and to generate other energy dissipation mechanisms. Specimens with z-yarns are mainly affected by in-plane tensile and compressive stresses generated during bending, rather than shear stresses.

CHAPTER 6

Damage Tolerance

Low-velocity impact events caused by foreign objects, such as a tool drop during mainte-
nance operations, are particularly critical in composites. They may cause damage difficult
to be detected, reducing significantly the compressive strength. This is one of the most
limiting factors in the widespread use of composites in aerospace.

This chapter is devoted to study the damage tolerance of the hybrid 3D woven com-
posites after a low-velocity impact event. The test is separated into two parts: firstly, the
damage inflicted into a specimen by an out-of-plane concentrated dynamic load is mea-
sured by means of C-scan inspection. Afterwards, the impacted coupons are tested in
compression to obtain the residual compressive strength. The influence of hybridization
on the compressive residual strength is also discussed.

6.1 Experimental techniques

6.1.1 Drop-weight

Drop-weight impact tests were conducted according to the Standard ASTM D7136/D7136M
(1995). Sixteen rectangular specimens of $150 \times 100 \times 4.1$ mm^3 were machined from the
composite plate with the longest dimension aligned in either the warp or fill direction for
the mechanical tests. Specimens were alternatively impacted on the carbon and glass faces,
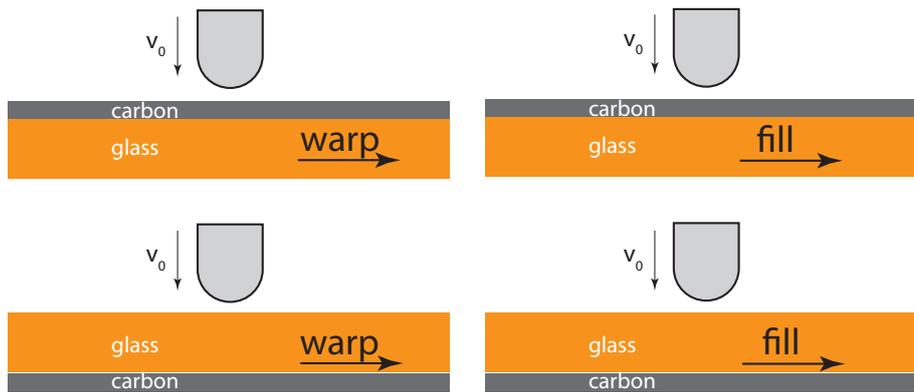
Figure 6.1: Four sets of tests were conducted: impact on the carbon face with the plate oriented in the warp and fill directions (top) and impact on the glass face with the plate oriented in the warp and fill directions (bottom).

and the plate was alternatively positioned with the longest side parallel to either the warp or the fill directions (Fig. 6.1).

Tests were carried out using an Instron Dynatup 8250 drop weight testing machine (Fig. 6.2). The specimens were simply supported by the fixture and hold at the corners with clamping tweezers, leading to a free impact area of 125×75 mm^2. Guiding pins were used to center the specimen. This configuration minimizes the fixture interferences with the impactor. Impacts events were performed by releasing the impactor with a selected mass from a chosen height, which dropped freely. The impact mass was set to 4.98 Kg and the drop height to 56 cm to achieve an impact energy of 27.47 J. A hemispherical-shaped steel tup of 12.7 mm diameter was used as impactor. The tup was instrumented with an accelerometer to measure the impact load, as well as the tup displacement and velocity.

6.1.2   Compression After Impact

The residual compressive strength after impact of the laminates was measured according to the ASTM D7137/D7137M (2005). To this end, the impacted coupons were subjected to in-plane compression to evaluate the residual compressive strength. Tests were carried out using an electromechanical universal testing machine (Instron 3384), Fig. 6.3. The fixture includes adjustable side plates to accommodate the thickness variations and to prevent specimens from buckling. The specimens were simply supported at the four edges, and the compressive load was applied directly to the top fixture plate by a platen installed in the

Figure 6.2: Drop-weight set-up. Detail of the coupon and the clamping tweezers.

(a) Front view   (b) Top view
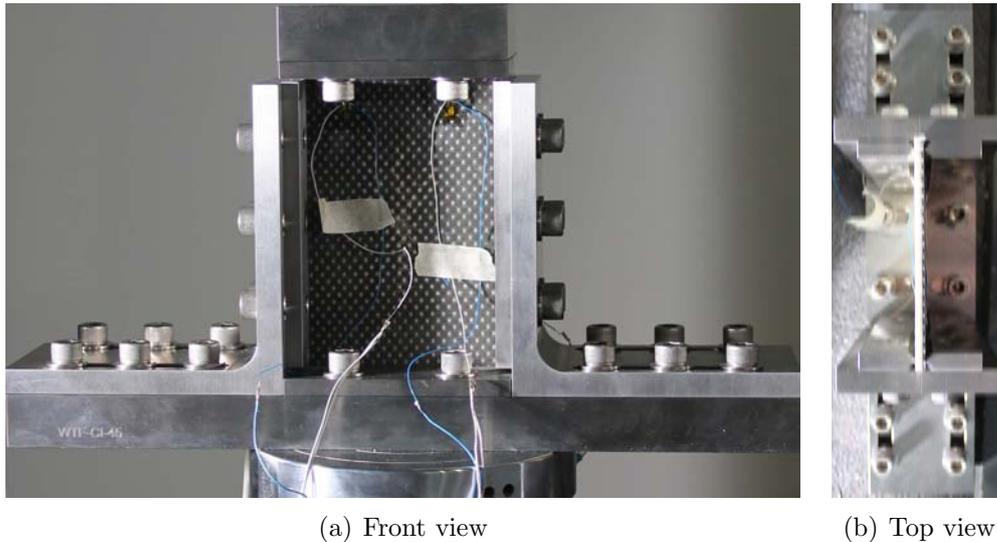
Figure 6.3: Compression after impact tool.

cross-head of the testing machine under displacement control at 1 mm/min. The load was continuously measured during the test with a 150 KN load cell. The instrumentation of the specimens included four back-to-back strain gages (350 Ω HBM) to detect any evidence of specimen bending during the test. Strain gages were located at 25 mm from top and lateral edges. The test starts with a pre-load of 450 N to ensure that all surfaces come in contact and also to align the plates.

6.2 Results and discussion

6.2.1 Drop-weight

Force-time curves of the impact tests are plotted in Fig. 6.4(a). After some initial oscillations –probably due to stress wave reflections– the behavior was linear up to the onset of instabilities, which corresponds to matrix cracking and some fiber breakage, Schoeppner & Abrate (2000). Such instabilities were more evident in specimens loaded on the glass face. Once the peak load was reached, the remaining elastic energy was recovered, so that the impactor rebounded with a residual velocity lower than the initial one (Fig. 6.4(b)). The total contact duration was $\approx$ 8 ms. It should be noted that results were very repetitive.
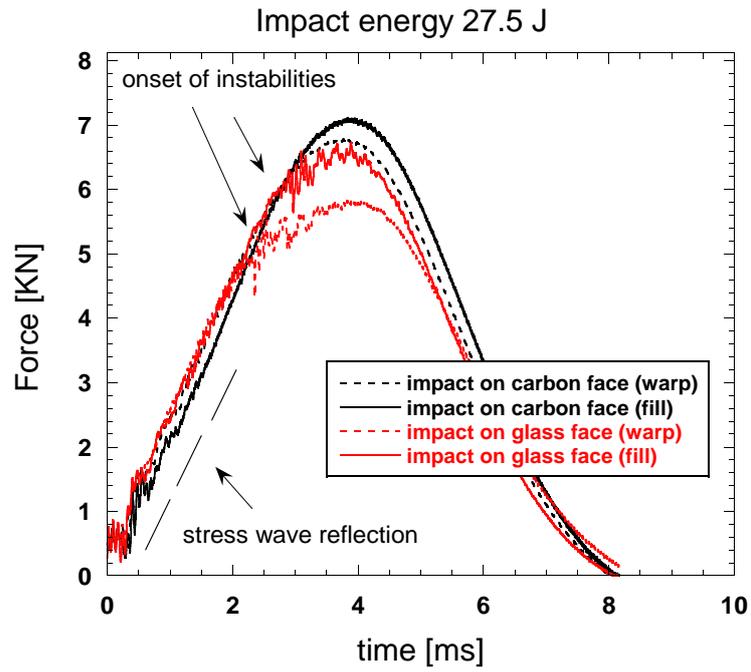
(a) Force-time curves
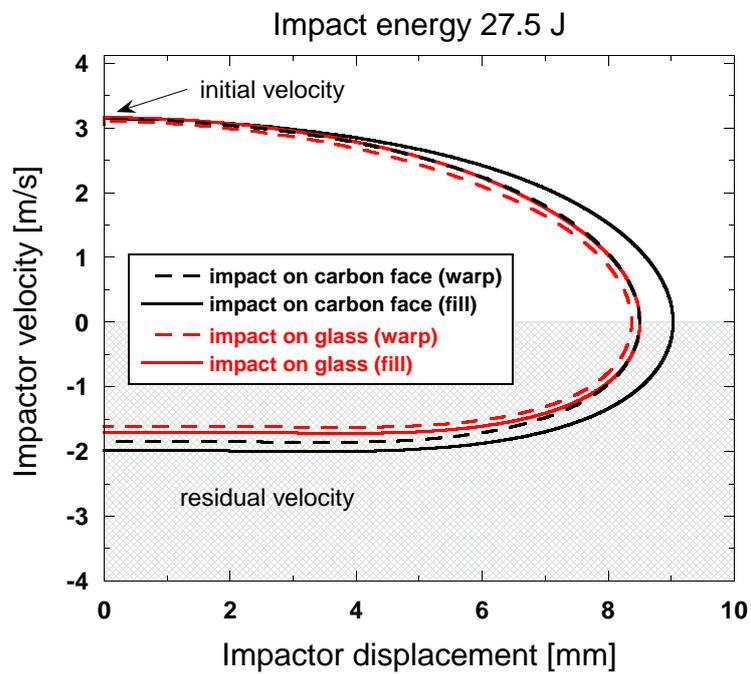
(b) Velocity-displacement curves

Figure 6.4: Results from the drop weight tests of rectangular specimens oriented either on the warp or fill directions and loaded alternatively on the carbon and the glass faces with an impact energy of 27.5J. (a) Force-time and (b) velocity-displacement curves.
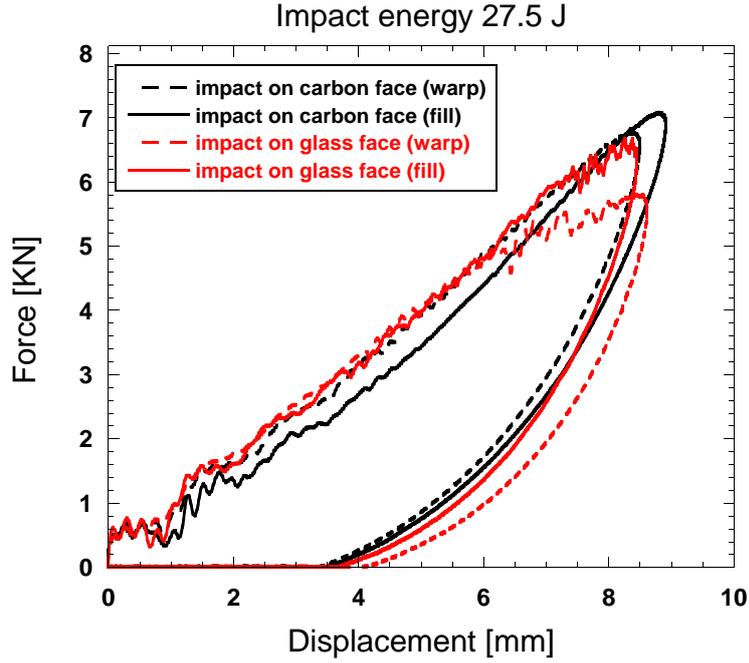
Figure 6.5: Results from the drop weight tests of rectangular specimens oriented either on the warp or fill directions and loaded alternatively on the carbon and the glass faces with an impact energy of 27.5J. Force-displacement curves.

Table 6.1: Stored elastic energy after drop weight impact of 27.5J on either the carbon or the glass face of rectangular coupons oriented in the fill and warp directions.

Stored elastic energy (%)	Carbon	Glass
Fill	40.3	29.7
Warp	35.0	28.1

The energy absorbed was calculated as the area under the force-displacement curves (Fig. 6.5). As shown in Table 6.1, approximately one third of the energy was stored as elastic energy, whereas the other two thirds were dissipated through damage, plasticity and plate vibrations. Comparison between curves plotted in Fig. 6.6 revealed that specimens impacted on the carbon face stored more elastic energy than those impacted on the glass face. Similarly, specimens oriented in the fill direction provided the best performance in terms of the peak force and the stored elastic energy as a result of the higher volume fraction of fibers oriented in this direction.

116
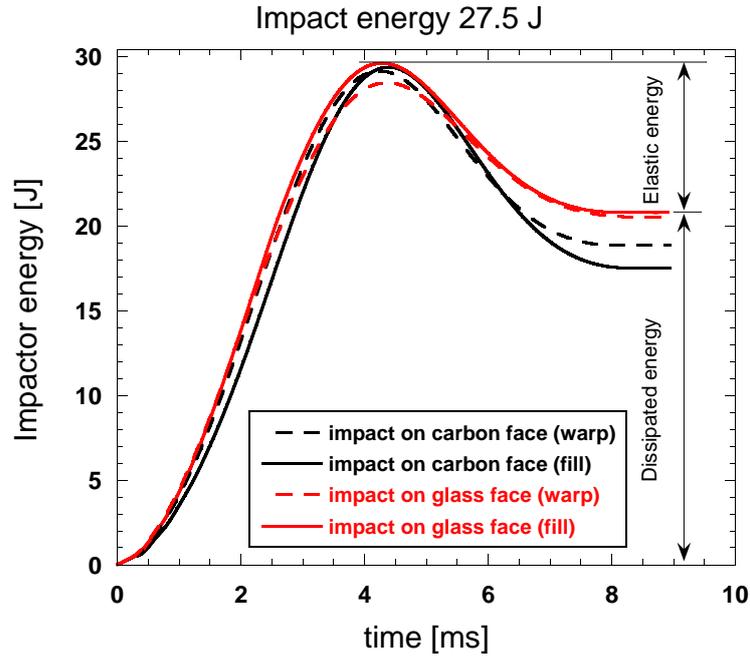
Figure 6.6: Results from the drop weight tests of rectangular specimens oriented either on the warp or fill directions and loaded alternatively on the carbon and the glass faces with an impact energy of 27.5J. Energy-time curves.

Table 6.2: Damaged area over the total area after drop weight impact test of 27.5J in several configurations.

Damaged area %	Carbon	Glass
Fill	5.7	6.4
Warp	12.8	16.2

C-scan inspection of impacted specimens revealed the presence of extensive damage (Fig. 6.7). As shown in Table 6.2, the extension of damage was slightly higher when the load was applied on the glass face and it was more spread when the plate was oriented in the warp direction. This explains the lower peak loads and the lower absorption capability of specimens oriented in the warp direction and impacted on the glass face.
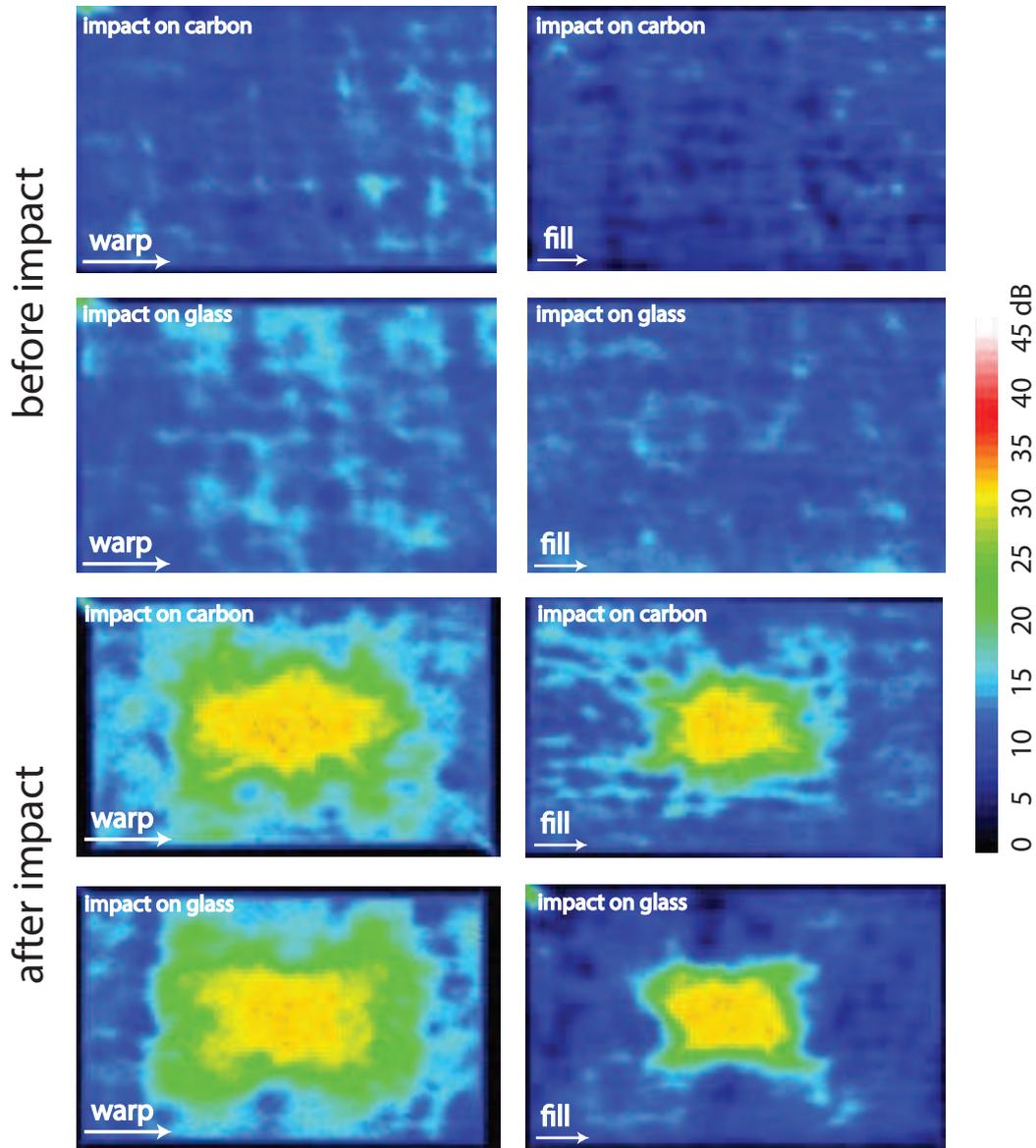
Figure 6.7: C-scan ultrasonic inspection with a 5Mhz transducer of rectangular specimens before (top) and after (bottom) drop weight impact of 27.5J. Contour plots show the presence of matrix cracking. Damaged area was significantly higher when the specimens were oriented in the warp direction (left) than in the fill (right). In contrast, minor differences were found when the load was applied either on the carbon or the glass face.
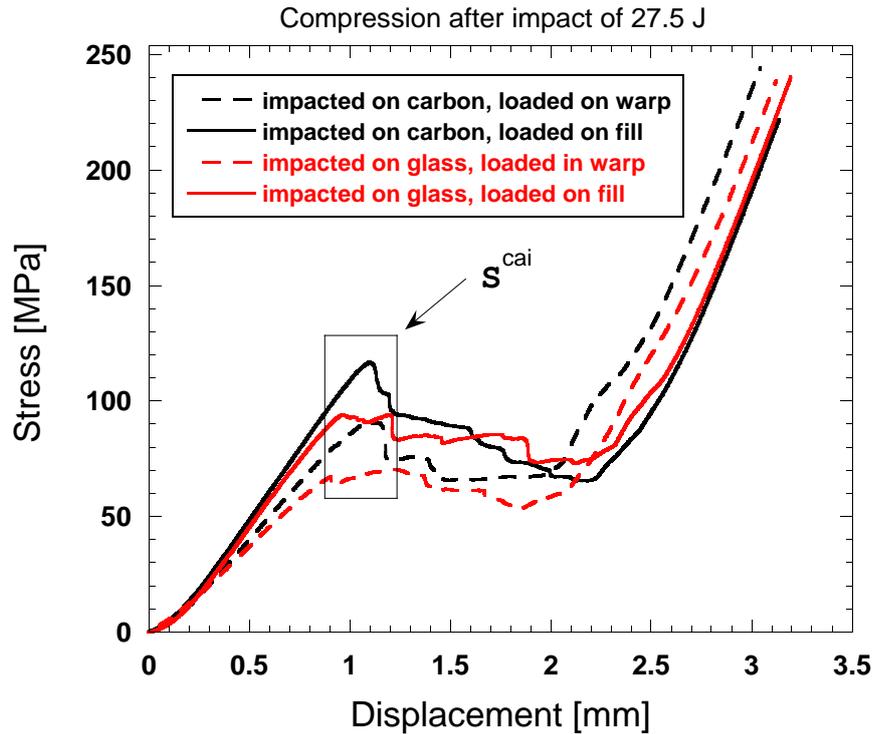
Figure 6.8: Stress-displacement curves in compression after impact. Comparison between warp and fill directions, as well as impact on carbon or glass sides.

6.2.2 Compression After Impact

Damaged coupons were tested in compression. As shown in Fig. 6.8, the initial response was linear up to $\delta \approx 1$mm. Further examination of strain gages readings revealed that bending takes place during this regime (Fig. 6.9). This was accompanied by a progressive increase of damage[1] until a plastic hinge developed at the center of the coupon (Fig. 6.10). This effect, which was already reported by Potluri *et al.* (2012), determines the onset of the non-linear behavior. Surprisingly, the laminate did not fail at this point. Instead, after a short plateau the load increased linearly with the deformation. The tests were stopped when the load reached 100 KN to prevent damage on the compression platens. This result highlights the high ductility and damage tolerance of this laminate.

Comparison of curves in Figure 6.8 showed that the best performance was achieved when the load was applied on the carbon face. This is readily explained by the lower damage inflicted during drop weight impact. Likewise, specimens with the fill yarns oriented along

---

[1]Cracking was clearly heard during the test.
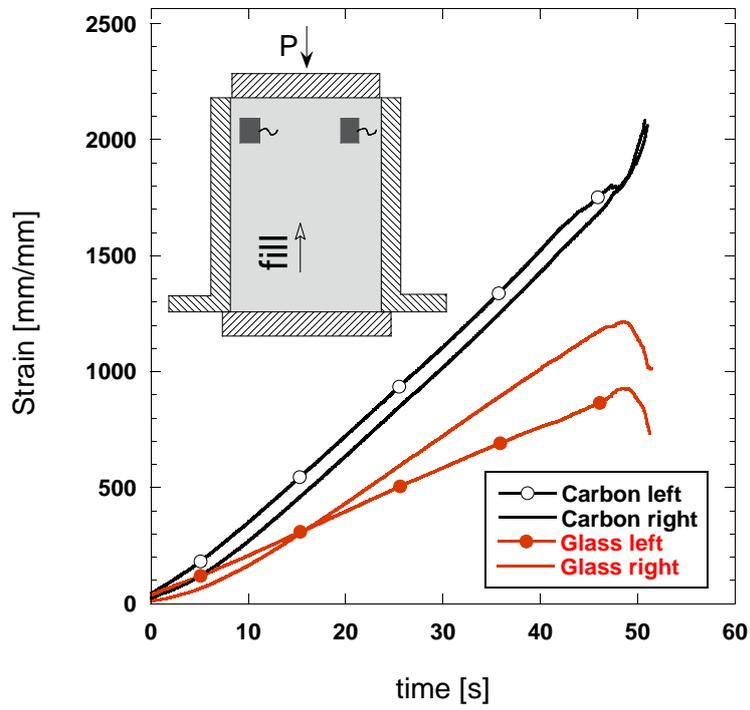
Figure 6.9: Strain gage readings during compression in the fill direction of a specimen previously impacted on the carbon side.
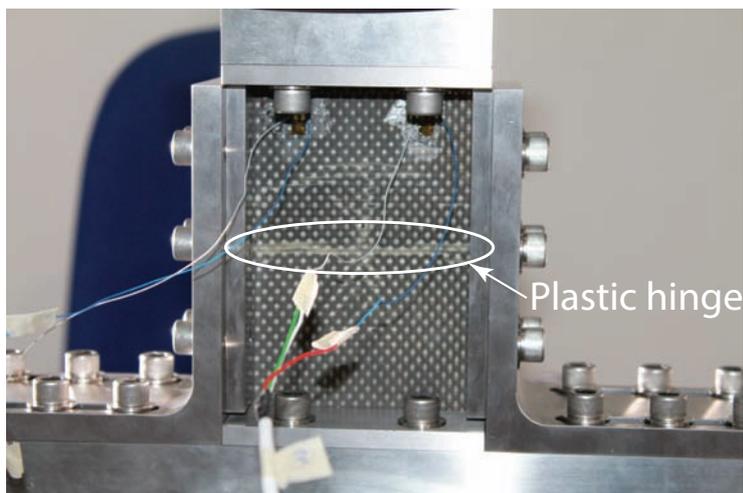
Figure 6.10: Plastic hinge at the center of a coupon during compression after impact testing.

Table 6.3: Experimental results of compressive strength after impact S^{cai} of the hybrid 3D woven composite. Influence of impacted side (carbon or glass) and fiber orientation (fill or warp)

orientation	S^{cai} (MPa)		E^{cai}(GPa)	
	Carbon	Glass	Carbon	Glass
Fill	103.0 ± 11.5	96.6 ± 4.6	80 ± 5.8	68 ± 5.6
Warp	88.1 ± 0.2	73.8 ± 13.5	53	57 ± 4.1
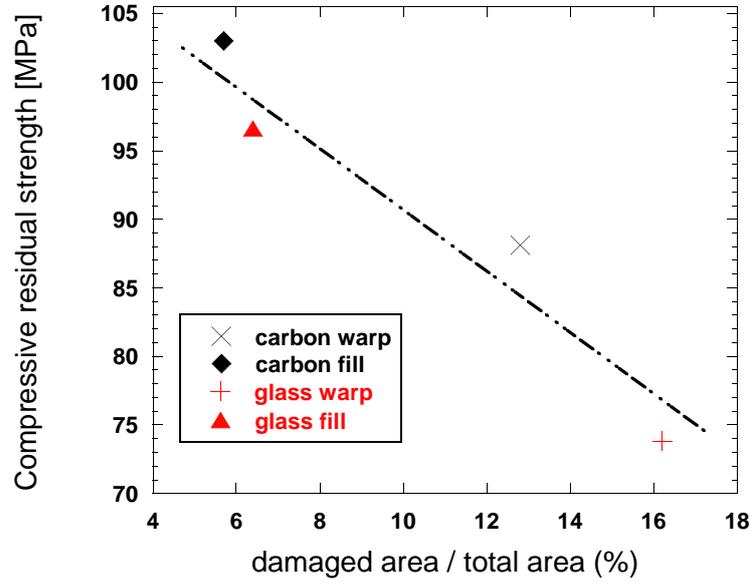
Figure 6.11: Relationship between damaged area and S^{cai}.

the longest side provided better damage tolerance than those oriented in the warp direction. This can be explained not only for the lower damage inflicted, but also for the higher number of layers oriented in the longitudinal direction. This is also reflected in the values of the ultimate stress S^{cai} presented in Table 6.3, which was calculated as:

$$S^{\mathrm{cai}} = \frac{P_{\max}}{A} \tag{6.1}$$

where $P_{\max}$ is the maximum load prior to failure and A is the initial cross sectional area.

Further analysis revealed that the size of the damaged area is inversely proportional to S^{cai} (Fig. 6.11).

6.3   Modeling

6.3.1   Delamination threshold

The threshold force P_c of delamination is particularly relevant for aircraft design purposes. Davies *et al.* (1994) formulated an analytical model based on fracture mechanics to determine this critical load:

$$P_c^2 = G_{IIc}\frac{8\pi^2 E t^3}{9(1-\nu^2)} \tag{6.2}$$

where G_{IIc} is the critical energy release rate in mode II, t is the laminate thickness, and E and ν are the effective in-plane stiffness and Poisson's ratio of the laminate, respectively.

Recalling that P_c can be readily deduced from the point of the drop weight load-time curve at which the instabilities start, this model can be used to obtain G_{IIc}, Irving & Cartie (2002). This value is particularly useful for modelling purposes. Applying eq. 6.2 to specimens loaded on the carbon side and oriented in the warp direction and substituting $P_c \approx 4900$N, $E = 27$GPa, $t = 4.1$mm, $\nu = 0.4$, then $G_{IIc} = 3800$N/m. This value is five times higher than that reported by Irving & Cartie (2002) for quasi-isotropic unidirectional laminates.

6.3.2   Residual strength

The *equivalent hole* method suggested by Edgren *et al.* (2008) was applied to predict the residual strength of the laminate. This approach assumes that the damaged area – based on an equivalent overlapping delamination criterion– is equivalent to a hole, so that the CAI coupon is considered as an open-hole specimen.

$$A_{\text{damaged}} \approx \pi \times \frac{D_{\text{equivalent}}^2}{4} \Rightarrow D_{\text{equivalent}} \approx \sqrt{\frac{4A_{\text{damaged}}}{\pi}} \tag{6.3}$$

To study the notch-sensitivity of the material in compression, a comparison was established between the strength of unnotched, open-hole and compression after impact coupons. No relevant differences were found between the warp and fill directions, neither in the car-
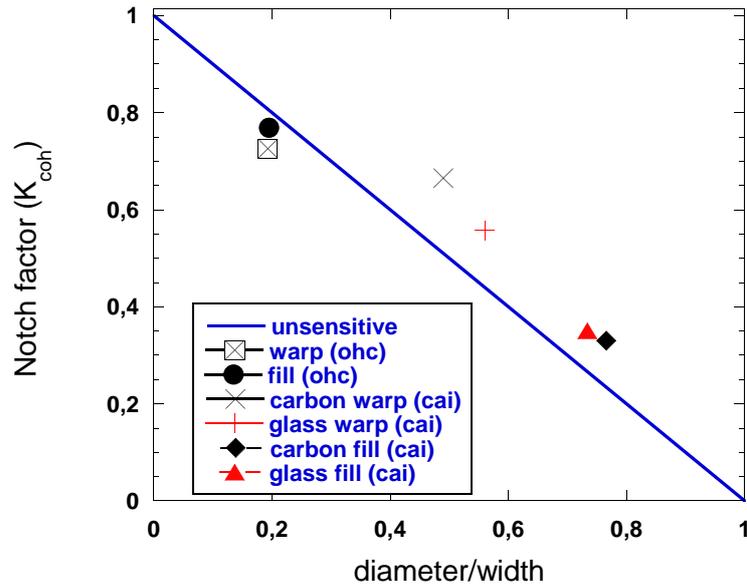
Figure 6.12: Notch sensitiveness in compression. Comparison between plain, open-hole and CAI tests. The latter is calculated as an equivalent hole diameter obtained from C-scan damage inspection. K_{coh} refers to the ratio unnotched / notched strength.

bon and glass faces. Fig. 6.12 reveals that the equivalent hole model slightly overpredicts the compressive residual strength of the hybrid 3D woven composite, as it was already reported by Edgren *et al.* (2008) for the case of unidirectional tapes. This can be readily explained by the fact that the damaged area was measured based on the matrix cracking detected by the C-scan, which is less critical than the presence of a cut-out. Moreover, the model does not account for geometrical effects that may trigger instabilities.

6.4   Concluding remarks

It can be concluded that the hybrid 3D woven laminate is highly damage-tolerant. Despite of the early onset of global buckling, it was able to withstand further loading. The through-thickness reinforcement seems to play a significant role, ensuring a load transfer from damaged to undamaged layers and reducing the splitting of the laminate into slender sublaminates.

Critical energy release rate in Mode II can be estimated from the threshold load of matrix cracking during drop weight impact. The application of an equivalent open-hole

model to predict the critical load provides also a reasonable estimation of the residual strength, although slightly overestimated.

As expected, the residual compressive strength was inversely proportional to the size of the damaged area. In that sense, hybridization can be used to improve the performance of a composite subjected to impact loads. The performance is higher when the plate is oriented in the fill direction and the load is applied on the carbon face. The latter is not in agreement with the results obtained from short beam tests. This can be readily explained by the different failure modes involved in the damage process.

CHAPTER 7

Impact Behavior

Composite materials used as primary structures in aerospace applications can be subjected to impact loading during in-service conditions. Damage in composites is not always visually detectable, as oppose to metals, in which impact events typically leave noticeable dents, Rhymer *et al.* (2012). Some examples of threats include hailstones, lightning strike, Muñoz *et al.* (2014), bird ingestion, runway debris during take off and landing, as well as tool drop during maintenance operations. Spacecraft, wind turbine and marine composite structures are also subjected to impact during operation.

In other cases, composite materials are not part of the primary structure, but are designed to protect critical components or the occupants of a vehicle against impacts, as it is the case of crushing boxes in automotive industry Johnson & David (2010). Thus, a good comprehension of the energy absorption capabilities and failure mechanisms of composite materials under impact is needed.

The ability of a composite structure to withstand impacts relies not only on the features of the plate itself (thickness, mass and material properties), but also on the mass, material properties, shape and velocity of the projectile. The impact regime is particularly relevant, so several attempts have been made to group impact regimes into a finite number of categories. According to Abrate (1998), high velocity impacts are those in which the ratio between the impact velocity and the through-thickness compressive wave velocity is larger

than the strain to failure in that direction. Tool drop during maintenance operations and take-off debris impact are, respectively, examples of low velocity and high velocity impacts.

This chapter analyzes the mechanical response and the energy absorption capability of the hybrid 3D woven composite in the low velocity and high velocity regimes. The influence of hybridization on the impact response is also discussed with the help of XCT images and finite element simulations.

7.1   Low velocity impact

7.1.1   Experimental techniques

The composite panels were machined into 145×145 mm^2 square plates and clamped by their corners on a hollow square section of 127×127 mm^2, Figure 7.1.

Four coupons were impacted with energies of 94 J and 162 J to study the response of the material under penetration and perforation, respectively[1]. The nominal impact velocity was set to 4 m/s. Each panel was tested on either the carbon fiber or the glass fiber rich faces (from now on, CF and GF, respectively) at the aforementioned impact energies. The four load cases are summarized in Figure 7.2. Note that results from drop-weight tests are typically very reproducible and exhibit very low scatter, as shown in Chapter 6 and as reported by Enfedaque *et al.* (2010), Sevkat *et al.* (2013), González *et al.* (2011) and Seltzer *et al.* (2013). In this case, the slope of the loading regime in the load-displacement curve is very similar in all cases, regardless of the impact energy.

The low velocity impact tests were carried out at room temperature and humidity using an Instron Dynatup 8250 drop-weight test rig equipped with a pair of rebound catchers to prevent multiple impacts on the tested specimens. The tup was hemispherical with a diameter of 12.7 mm and it was instrumented with an accelerometer. Force and time were recorded in a data acquisition system, from which velocity and displacement can be calculated by integrating the force history according to

---

[1]The term *penetration* refers to the case in which the projectile enters the target, whereas *perforation* means complete penetration through the target. Eventually, *embedment* refers to a penetration case in which the projectile remains attached to the target after the impact event, Anderson Jr. *et al.* (2003).
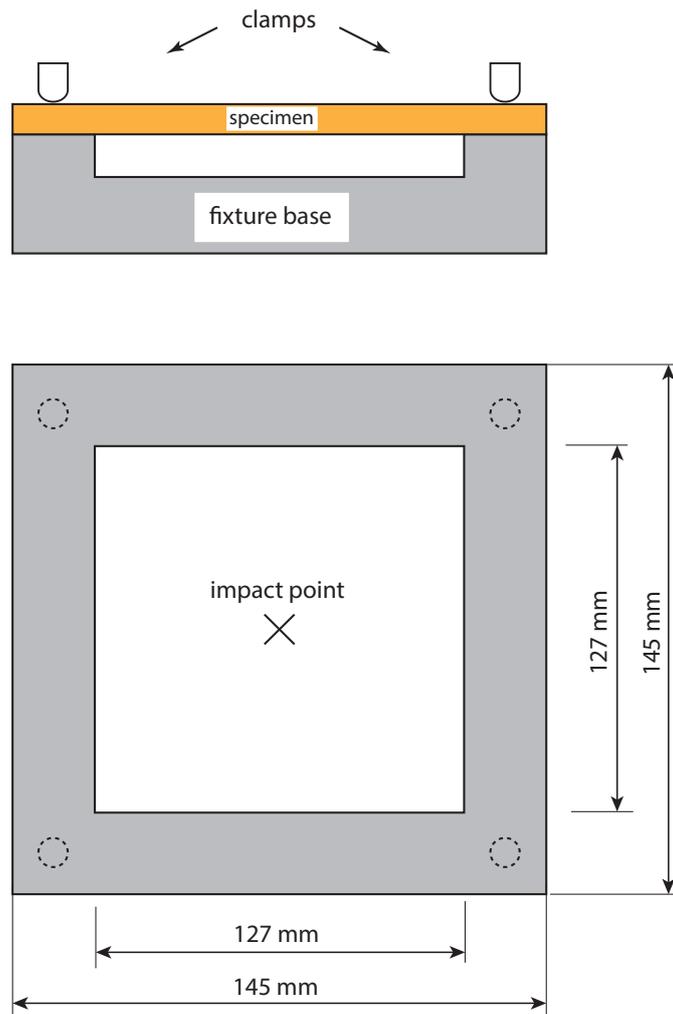
Figure 7.1: Schematic drop-weight impact set-up (not-to-scale).
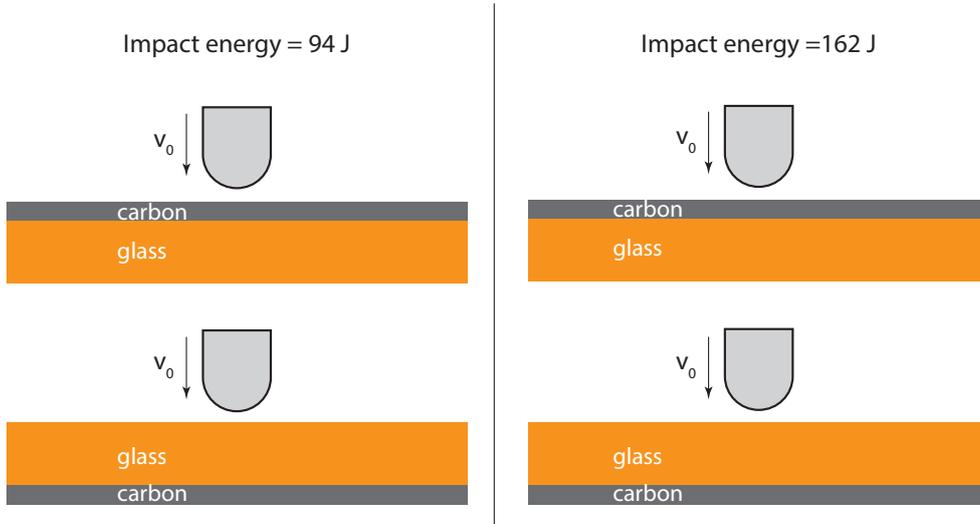
Figure 7.2: Schematic of the low velocity load cases: impact of 94 J on carbon and glass faces (left) and impact of 162 J on carbon and glass faces (right).

$$v(t) = v_i + gt - \int_0^t \frac{F(t)}{M_i} dt \tag{7.1}$$

$$w_i(t) = \int_0^t v(t)dt = v_i t + \frac{gt^2}{2} - \int_0^t \left(\int_0^t \frac{F(t)}{M_i} dt \right) dt \tag{7.2}$$

where v_i and w_i are, respectively, the initial velocity and the displacement of the impactor, g the acceleration of the gravity and M_i the mass of the impactor, González *et al.* (2011).

Two representative specimens were inspected after failure by means of a Nanotom 160 NF (Phoenix) XCT to obtain detailed information about the actual damage mechanisms through the thickness. X-Ray parameters of the W target were 90 KV and 140 μA. 1500 radiographies were acquired during the 360° rotation of the sample with an exposure time of 750 ms. The tomograms resolution was in the range 9-11 μm/voxel, depending on the specimen width.
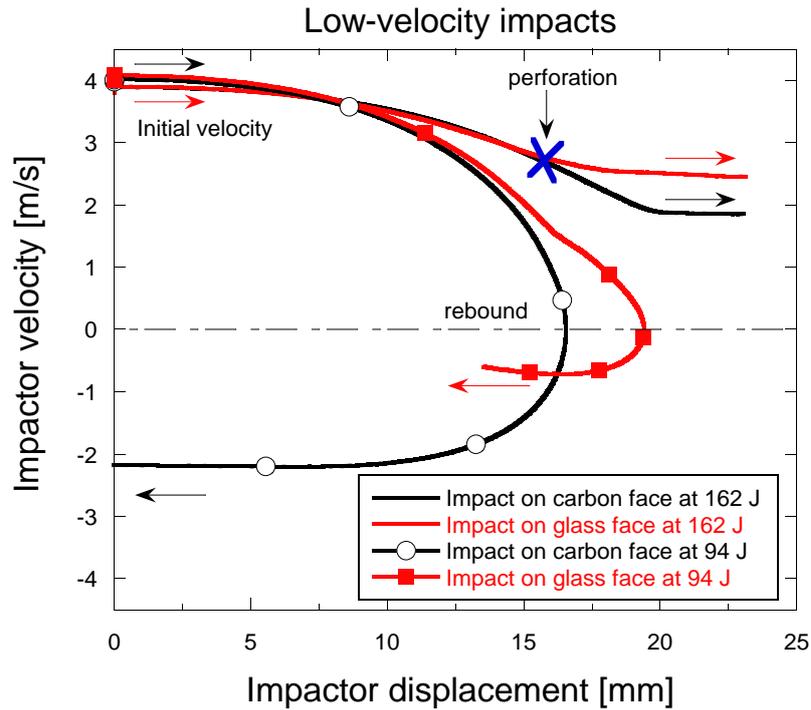
Figure 7.3: Velocity of the impactor as a function of impactor displacement. At low energy levels, the impactor rebounds with a residual velocity lower than the initial one when the displacement is close to 15-20 mm. At high impact energies, the impactor is able to perforate the plate and the velocity is always positive.

7.1.2 Results and discussion

Impact event

The impact event can be described in terms of the principle of energy conservation. As the impactor comes into contact with the target, a fraction of the initial kinetic energy of the impactor is gradually converted into elastic energy, Lopes *et al.* (2009b), whereas the remaining energy is dissipated in the form of plate vibrations, friction and fracture. The 94 J impact energy was not sufficiently high to cause perforation, so the energy stored by the plate was recovered and the impactor rebounded with a certain velocity, Figure 7.3. At 162 J, plate perforation occurred and all the elastic energy stored in the plate was dissipated. The impactor velocity was always positive. In both cases, the residual velocity was lower than the initial one due to energy spent during the impact.

Force histories of the 94 J and the 162 J impacts are plotted in Figure 7.4. The response was similar at both energy levels up to the peak load. As the impactor came in contact
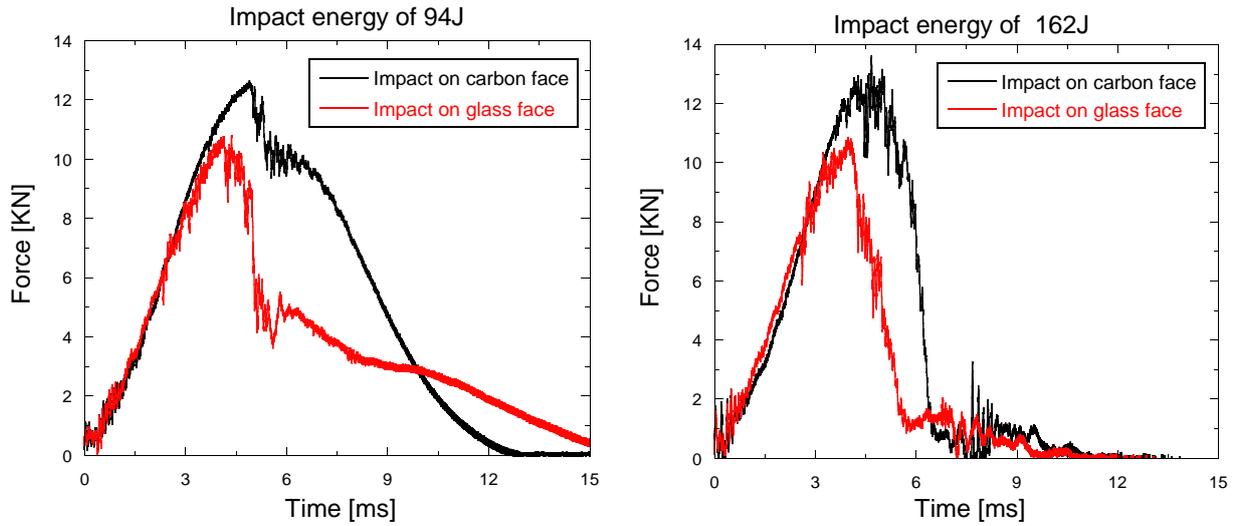
Figure 7.4: Force-time curves under low velocity impact without perforation (left) and with perforation (right).

with the target, some initial oscillations were followed by a gradual increase of the reacting force exerted by the plate. Once fibers started failing, the response became much more unstable and important differences arose between the impact energies considered. At 162 J, fiber breakage occurred in all layers and the force dropped off abruptly as a result of the perforation of the plate, while some fibers did not fail at 94 J, and the impactor was unable to fully penetrate the laminate. The presence of undamaged fibers ensured a smoother post-peak response at 94 J, so that the load decreased progressively until the impactor and the plate were no longer in contact. The contact duration was approximately equal to 12-15 ms at low energy levels and 6-7 ms at high energy levels. Further analysis also revealed that hybridization had a significant influence on the maximum load, which was higher when the impact was carried out on the carbon face.

It should be noted that some minor instabilities were also observed in coupons impacted on the glass face at ≈ 7 KN, regardless of the impact energy. This effect has been attributed to the onset of delamination in unidirectional composites, González *et al.* (2011). In the case of the hybrid 3D woven composite, it is likely due to matrix cracking, which had very limited influence on the mechanical behavior.

130

Table 7.1: Absorbed energy during low velocity impact tests.

	stored elastic energy (% of 94 J) (no perforation)	dissipated energy (% of 162 J) (perforation)
carbon face	30	79
glass face	3	65

Energy absorption and damage mechanisms

The quality of a bumper can be determined by the ability to absorb the kinetic energy of the impactor with the minimum damage or, if perforated, by the ability to absorb the maximum amount of energy. While the former can be evaluated by the elastic energy stored, the latter is measured by the energy dissipated, which corresponds to the area under the load-displacement curve. Note that the terms *absorbed energy* and *dissipated energy* are only equivalent when perforation occurs.

Figure 7.5 shows that coupons impacted on the CF absorbed more energy than those impacted on the GF, regardless of the impact energy. CF laminate stored more elastic energy than GF at 94 J, whereas CF laminate dissipated more energy than GF at 162 J. Quantitative results are found in Table 7.1.

The large energy absorption capability of 3D woven composites has already been reported by Seltzer *et al.* (2013) and is likely due to the presence of the z-yarns and the multiple failure mechanisms involved during impact, which facilitate the dissipation of energy. The large displacements reached by the impactor also revealed that the hybrid 3D composite was very ductile as compared with conventional CFRP laminates.

XCT inspection of coupons impacted on the glass face at 94 J showed that the deformation of the upper layers of the laminate (glass) was constrained by the presence of the carbon layers at the bottom, which have a lower failure strain. Once the carbon layers failed, the shear plug generated beneath the impactor was pushed outwards, Figure 7.6. This mechanism explains the sudden drop observed in the load-displacement curve of the GF 94 J case at a displacement of 17 mm, Figure 7.5. In contrast, upper layers are free to deform and the laminate bends smoothly when the ductile layers are located at the bottom (CF configuration), Figure 7.7. As the plate bends, the bottom layers of the laminate are subjected to membrane stresses, absorbing a higher amount of energy. This behavior explains the higher energy absorption capability of the CF configuration.
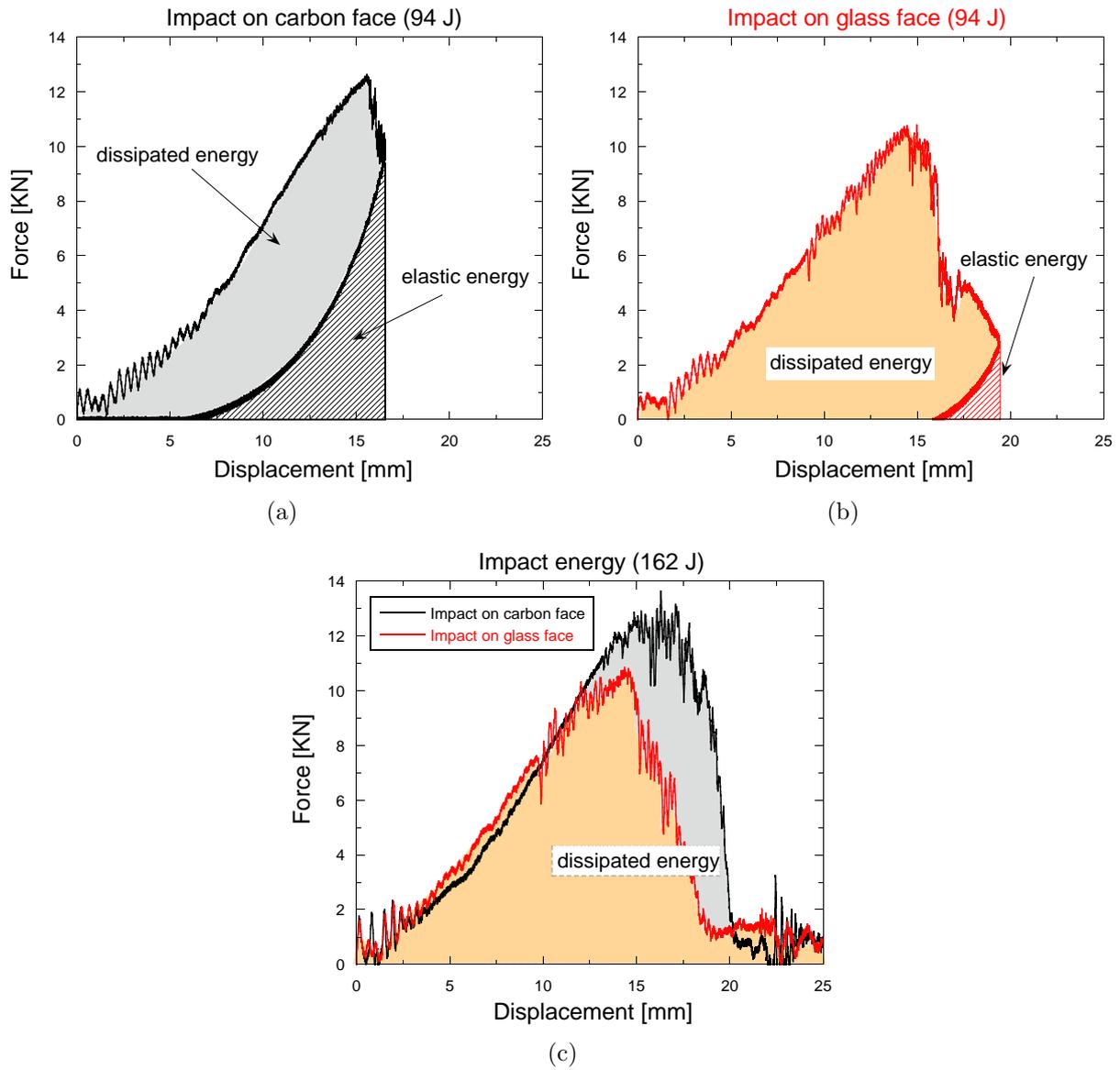
Figure 7.5: (a) and (b) Stored elastic energy and dissipated energy at 94 J. (c) dissipated energy at 162 J. Note that the GF configuration was almost perforated, so the amount of elastic energy stored was minimum.

The impact event was accompanied by multiple failure mechanisms common to both configurations: contact stresses under the impactor caused matrix crushing and shear cracking; yarns were dragged by the impactor, giving rise to tow splitting and also to some delamination at the cross-over sites; z-yarns readily debonded due to the poor adhesion of the polyethylene and, eventually, fiber kinking was also observed in the upper layers as a result of the in-plane compressive stresses developed while bending. More details about the influence of the fibre type and fibre architectures on the failure mechanisms of 3D composites can be found in Seltzer *et al.* (2013).
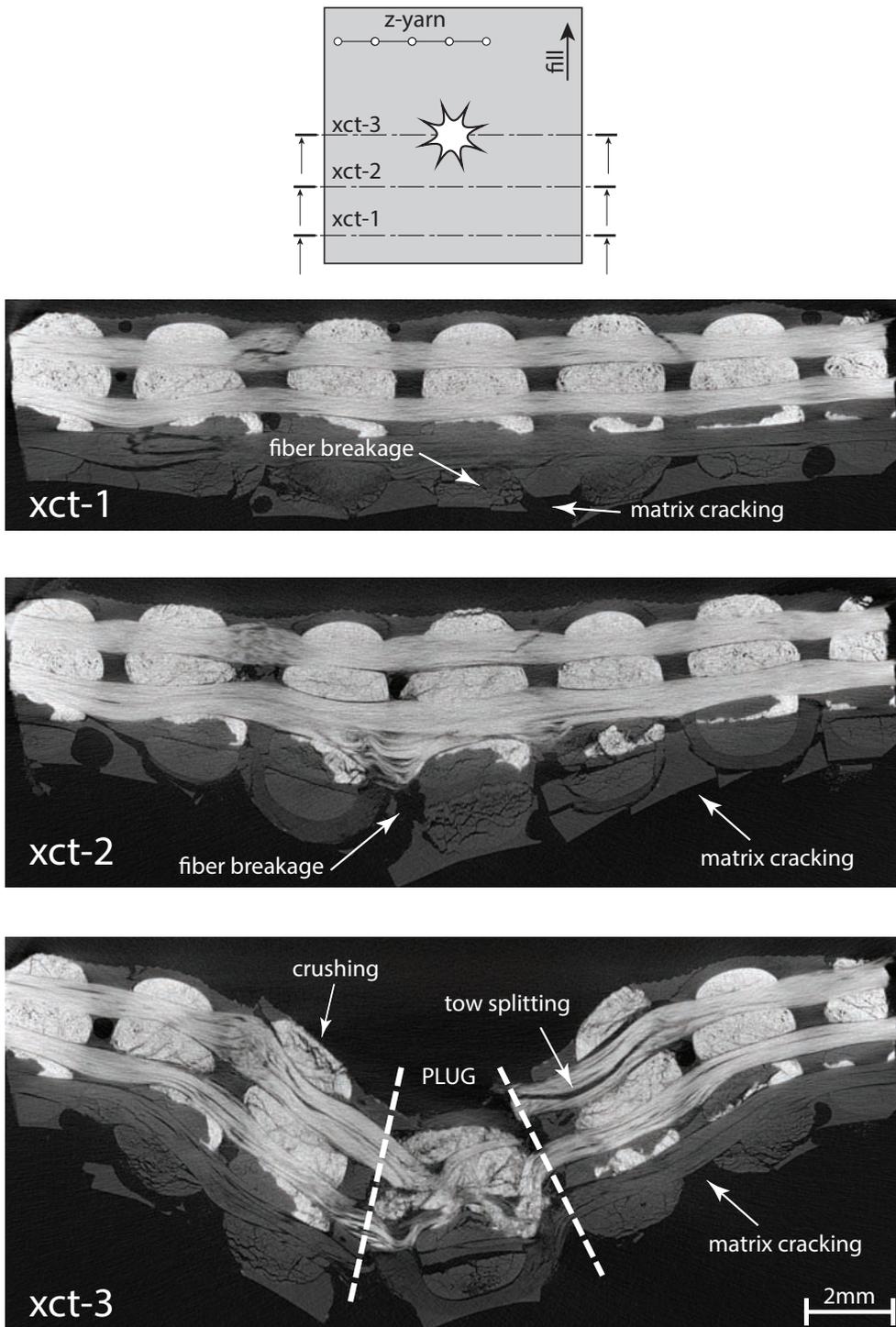
Figure 7.6: XCT cross-sections of the imprints left on the 3D hybrid GF configuration after impact at 94 J. The location of each tomogram is specified at the top. GF are in white, while CF, Dyneema and resin are grey. Impact caused large deformations at the center of the coupon, leading to extensive matrix cracking and fiber breakage at the warp and fill yarns located at the bottom of the laminate. This in turn triggered the formation of a plug which drags warp yarns, causing tow splitting and delamination. Crushing was also evident beneath the impactor.

134
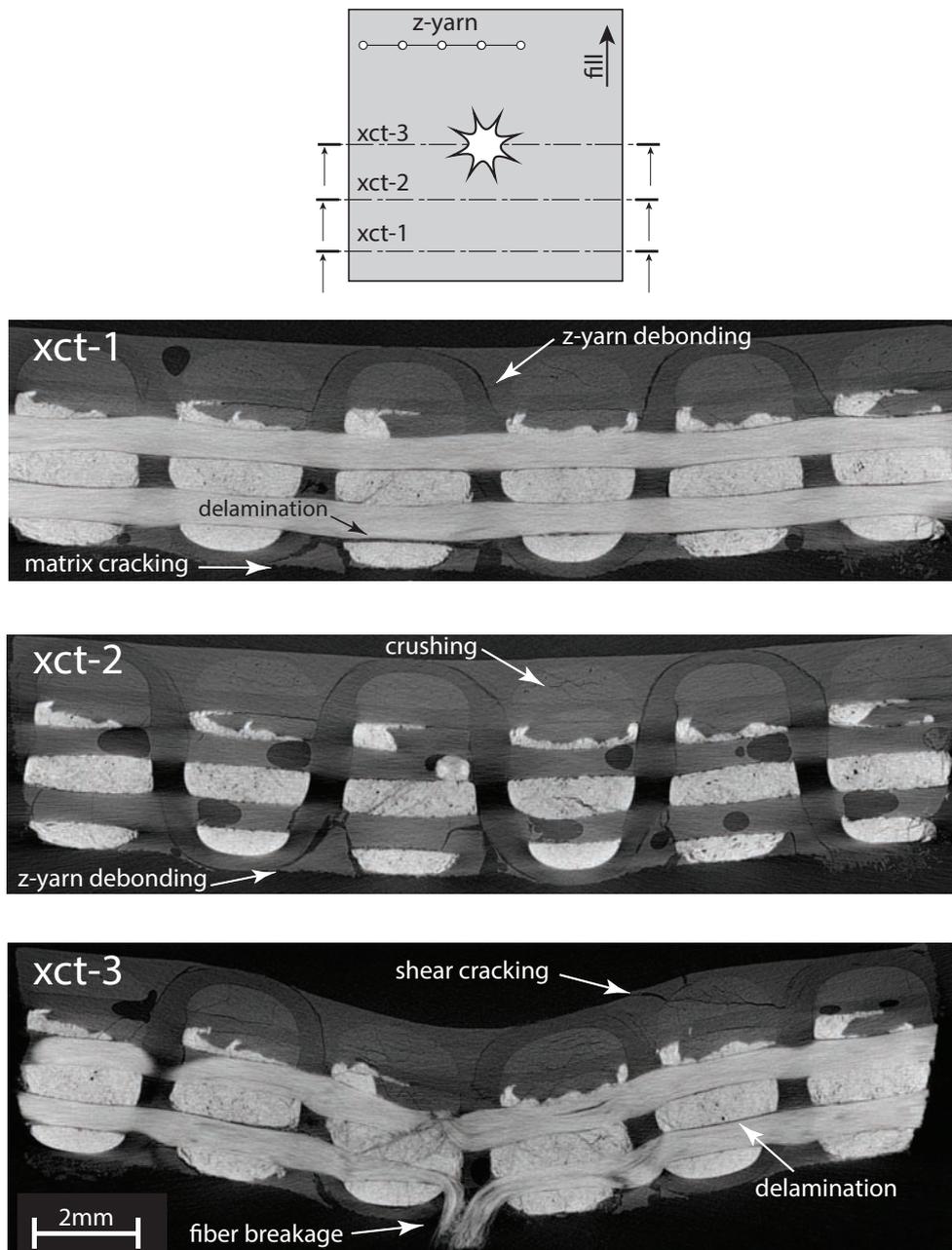
Figure 7.7: XCT cross-sections of the imprints left on the 3D hybrid CF configuration after impact at 94 J. The location of each tomogram is specified at the top. GF are in white, while CF, Dyneema and resin are grey. The deformation of the plate was lower and less concentrated than in the GF configuration. Fiber breakage was only evident at the warp yarns located at the bottom of the laminate. There was some shear cracking at the indented face as a result of the brittleness of the carbon fibers.

7.2 High velocity impact

7.2.1 Experimental techniques

Twenty square plates of 100×100 mm^2 were impacted on either the carbon or glass face with spherical[2] steel projectiles of 5.5 mm diameter (caliber 0.22") and 0.706 g. The projectiles were embedded in a sabot to fit on a 7.62 mm barrel and impelled at velocities ranging from 250 m/s up to 550 m/s (100J). To this end, a pneumatic launcher (SABRE A1 +) gas gun was used either with air or helium compressed up to 150 bars. Specimens were placed into the impact chamber and held with rubber strips to ensure that boundary conditions did not interfere with the results. The experimental set-up is depicted in Figure 7.8.

The energy absorption capability of the laminate was calculated as the difference between the initial and the residual kinetic energies of the projectile[3]. The initial V_i and residual velocities V_r were measured with a Phantom V12 high-speed video camera (Figure 7.8(a)). Images were recorded at a rate of 40,000 frames per second, with a resolution of 512×256 pixels and an exposure time of 23.45 μs.

Damage was inspected in all specimens before and after impact with ultrasounds (TecniTest TRITON 1500). Measurements were carried out at 30 mm/s, using a Sonatest SLG 5-102 transducer of 10 mm diameter with a central frequency of 5 MHz. The interval between levels was 1 dB and the resolution was set to 1 mm. The commercial software Visual Scan V-1.0 was used to visualize the results.

XCT inspection was conducted with the same equipment and procedure described in Section 7.1.1. X-ray voltage and intensity were set to 100 KV and 130 μA, respectively, whereas the exposure time was 1000 ms. The resolution of the tomographs was 9-11 μm/voxel.

---

[2]The spherical shape was selected to avoid effects of orientation.

[3]The kinetic energy of the ejected material was neglected. Total mass loss of each specimen was $\approx 0.1 - 0.3$ g.

(a) High-speed camera
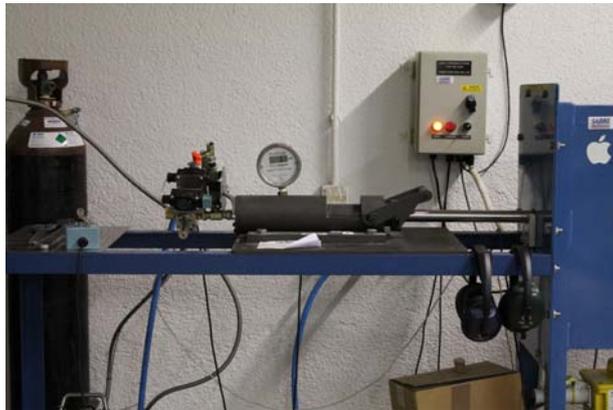
(b) Pneumatic launcher

(c) Chamber

Figure 7.8: High velocity impact experimental set-up

Table 7.2: Ballistic limit V_{50} of the hybrid 3D woven composite.

	V_{50} (m/s)
Impact on carbon face	359
Impact on glass face	326

7.2.2 Results and discussion

Ballistic limit and energy absorption

The ballistic limit V_{50} is the projectile velocity at which there is a 50% probability that the projectile is stopped by the plate, Rao *et al.* (2009). It was obtained as the average of the critical velocities V_0, which in turn were determined by applying the Jonas-Lambert expression for each shot:

$$V_0 = (V_i^n - V_r^n)^{\frac{1}{n}} \tag{7.3}$$

$$V_{50} = \sum_{i=1}^{k} (V_0)_i / k \tag{7.4}$$

where V_i and V_r are, respectively, the initial and the residual velocities of the projectile, k is the number of shots and $n = 2$ for composite materials impacted by spherical projectiles, Reid & Zhou (2000). As depicted in Figure 7.9, this expression correlates well with the experimental results, showing that V_{50} was a 10% higher in the specimens impacted on the carbon face (Table 7.5).

Further analysis also indicates that the hybrid 3D woven composite absorbed more energy when it was impacted on the carbon face. The absorbed energy is plotted in Figure 7.10 as a function of the initial kinetic energy. It shows that the energy absorbed is almost independent of the initial kinetic energy above a certain threshold.

Interestingly, the comparison between ballistic and drop-weight impacts revealed that, at the same energy level, the energy absorption of the composite decreases with the impact velocity. An impact of 94 J at 4 m/s was completely absorbed by the composite, whereas an impact of 92 J at 510 m/s fully penetrated the plate.
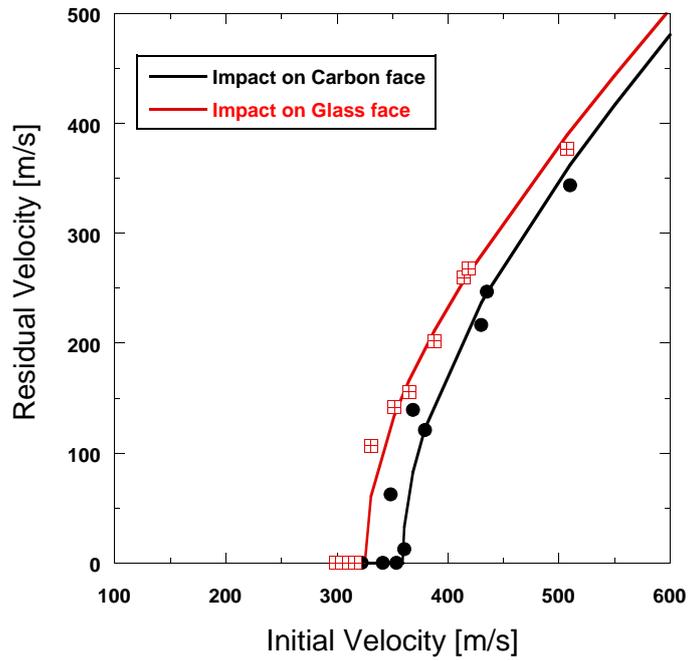
Figure 7.9: Experimental ballistic curves of the hybrid 3D woven composite.
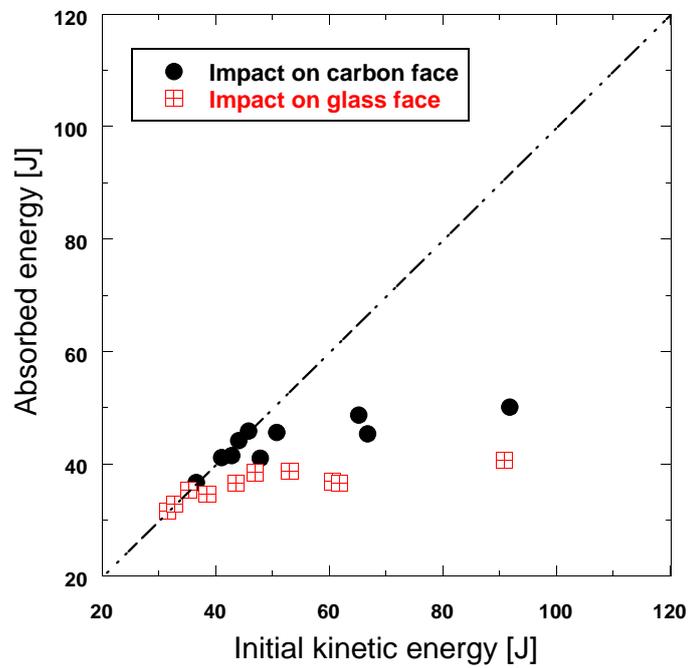
Figure 7.10: Specific absorbed energy during impact tests of the hybrid 3D woven composite.

(a) t=0 ps   (b) t=23 ps   (c) t=48 ps   (d) t=73 ps   (e) t=585 ps
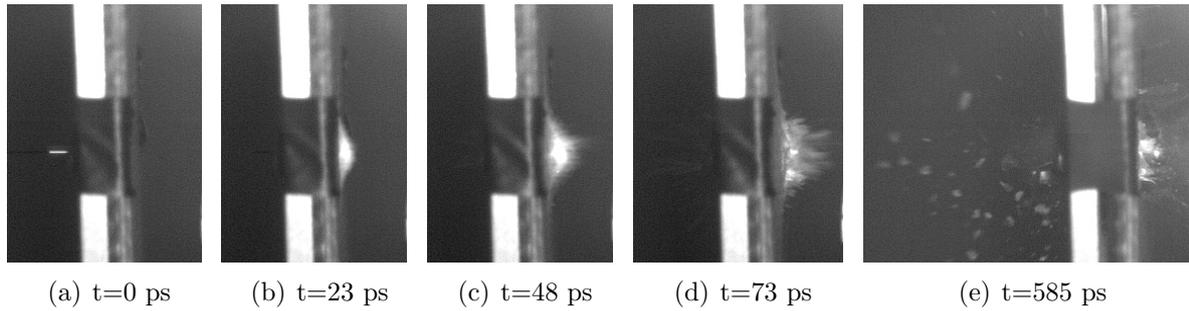
Figure 7.11: Sequence of events during a high velocity impact on the CF configuration.

Failure mechanisms

The impact event was similar in all cases. The plate was first indented and then perforated when the kinetic energy was sufficiently high. Otherwise, the projectile rebounded or it was embedded within the target. The impact event was very short and the main eigenmodes of the plate –global bending and twisting– were not excited until the projectile exited the target. In fact, boundary conditions did not affect the response of the plate. Figure 7.11 illustrates an example of an impact event. The projectile comes from the left side at 360 m/s and hits the carbon face. After some local deflection, the fiber strength is exceeded in all layers and the laminate is perforated, spreading out fragments of the material. Eventually, the projectile exits with a residual velocity V_r=12.5 m/s. The mechanical response was very localized. This is different from drop-weight tests, where global plate bending played a significant role.

Damage on the target was first caused by indentation. As the projectile comes in contact with the target, contact stresses develop under the impactor, giving rise to matrix cracking, z-yarn breakage and, more importantly, fiber tearing of some warp and weft yarns. The latter defines the perforation path and is caused by the transverse shear stresses. It should noted that fiber breakage was localized in few bundles, whereas matrix cracking was spread over a larger area. This is illustrated in Figure 7.12.

Indentation also led to extensive damage at the back face of the laminate due to the reflection of the compressive stress waves generated under the projectile as tensile stress waves. This phenomenon is called *spallation* and is due to the mismatch in mechanical impedances of the back layer and the air. Evidences of spallation were found in the hybrid 3D composite. Tensile out-of-plane stresses caused matrix cracking and the failure of a

140

Damage caused by indentation
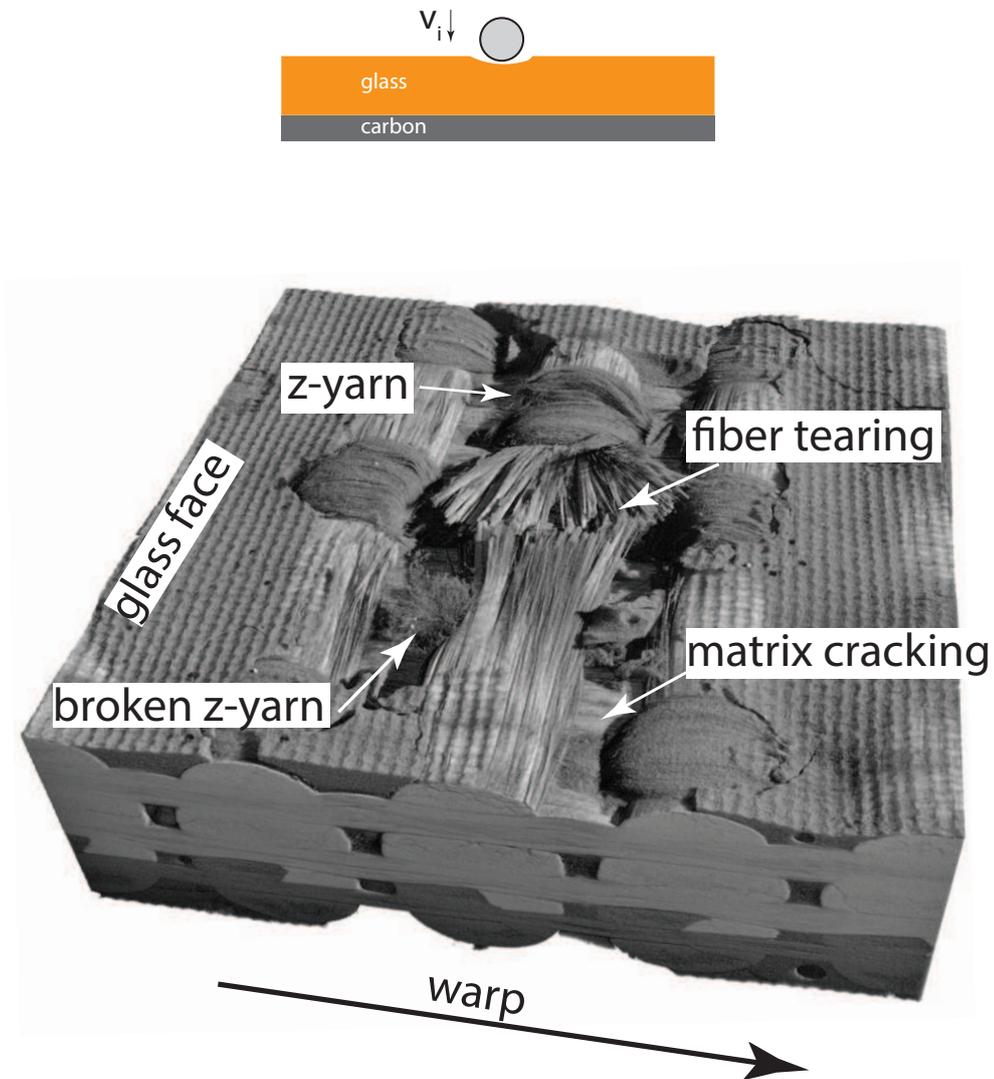
Figure 7.12: Tomogram of a coupon impacted on the glass face at $V_i = 299.3$ m/s and non-perforated (front view). Glass fibers are light grey, while carbon fibers, Dyneema and resin are dark grey. Indentation causes matrix cracking, fiber breakage of z-yarns and fiber tearing of glass yarns.
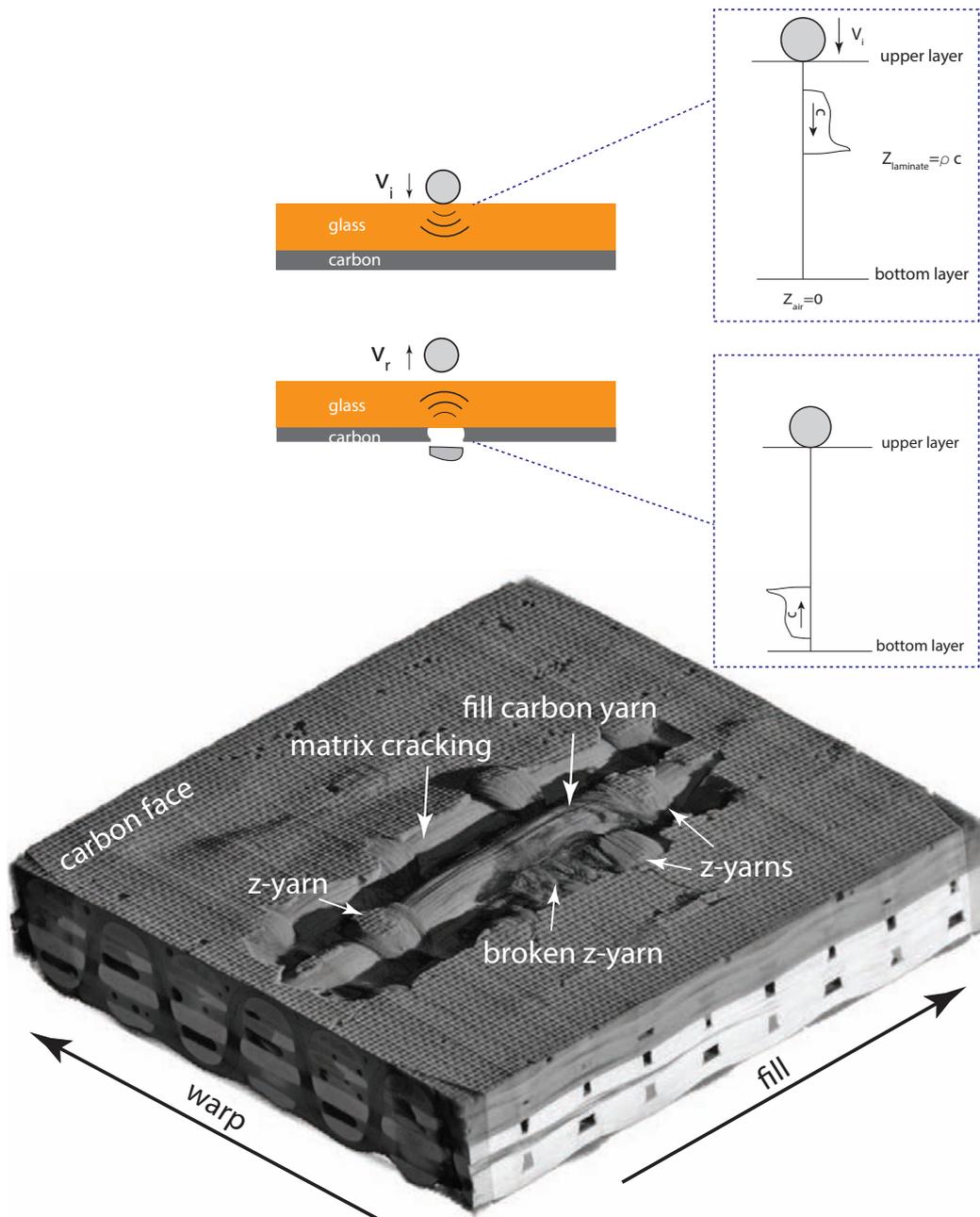
Figure 7.13: Tomogram of the back face of a coupon impacted at $V_i = 299.3$ on the glass face and non-perforated. Glass fibers are white, while carbon fibers, Dyneema and resin appear grey.

z-yarn at the back face of the laminate (Figure 7.13), but did not affect the fill yarns. Interestingly, the remaining z-yarns avoided the delamination commonly observed at the bottom layers of unidirectional tapes.
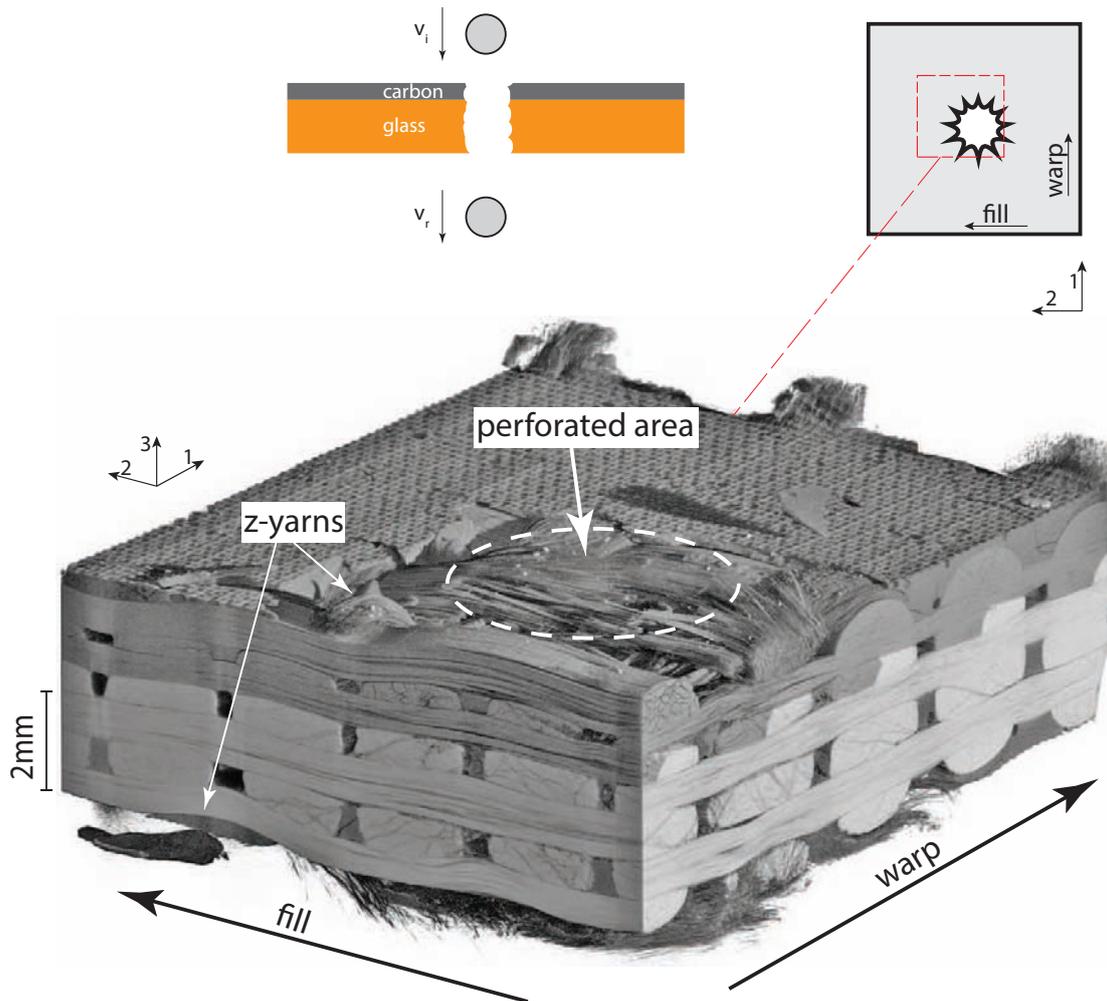
Figure 7.14: Tomogram of a coupon impacted on the carbon face and perforated ($V_i = 379.3$ m/s, $V_r = 121.10$ m/s). Glass fibers appear in white, while carbon fibers, Dyneema and resin are grey. Damage is localized in a small region and decreases rapidly from the center outwards. Crimping of the fill yarns is clearly induced by the binder.

Damage was localized in a small region around the impactor during ballistic impacts. This makes a significant difference with drop-weight tests, where damage was spread over a larger region. XCT inspection of a perforated specimen showed that matrix cracking and fiber breakage are more evident as the section is closer to the hole generated by the spherical projectile, Figure 7.14. Despite of the severity of the impact, intrayarn cracking only affects three or four yarns in each direction. The image also shows the crimping induced by the z-yarns on the outermost fill yarns.
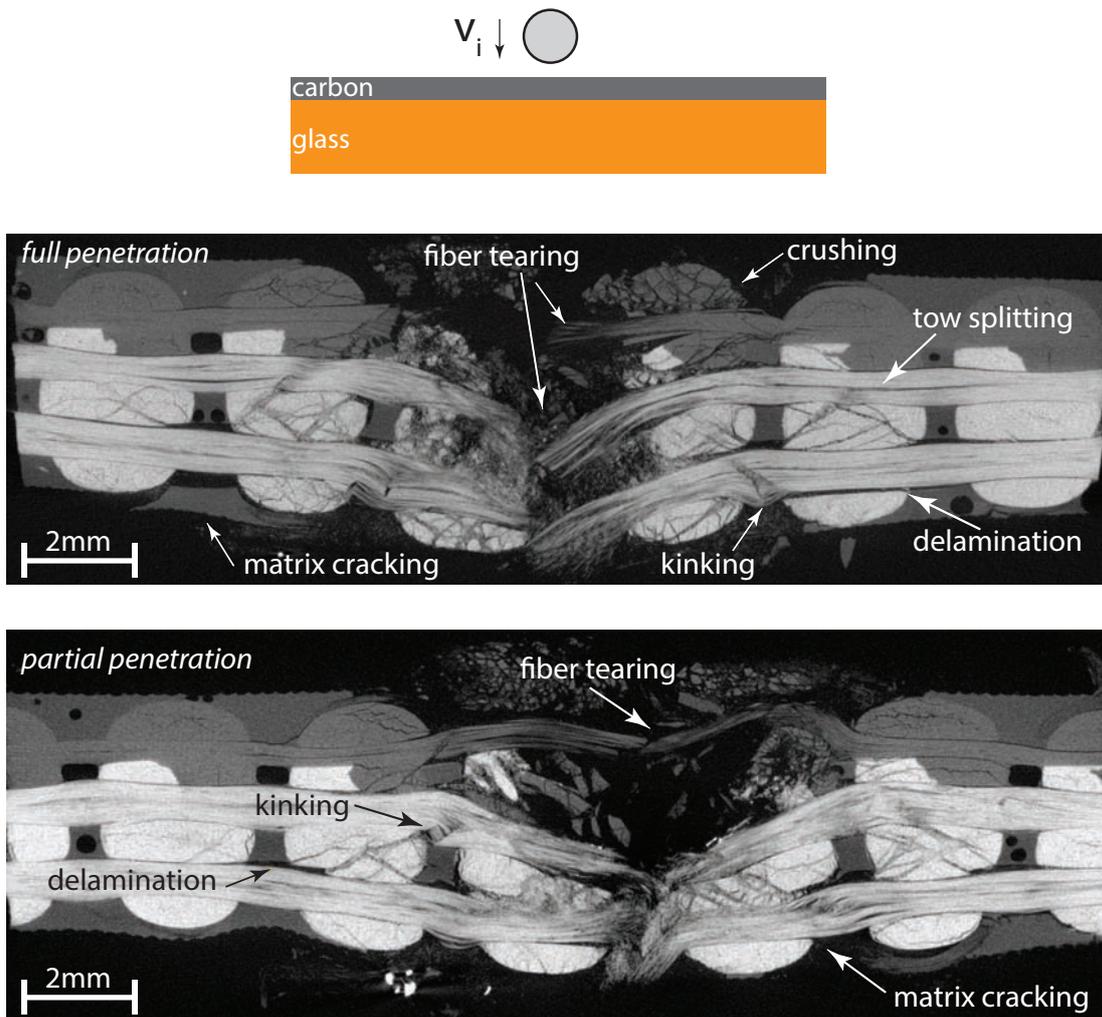
Figure 7.15: Tomograms of the damaged sections of two coupons impacted on the carbon face: perforated (V_i=360 m/s, V_r=12 m/s) (top) and non-perforated (V_i=341.5 m/s, V_r=0) (bottom). Sections are parallel to the warp direction. Glass fibers are white, while carbon fibers, Dyneema and resin are grey. The projectile induces transverse shear stresses giving rise to failure of the warp yarns. Note that even the warp yarns of the non-perforated coupon are also broken. Other minor failure modes are also depicted, namely matrix cracking, fiber kinking, crushing and delamination.

The failure mechanisms observed in perforated and non-perforated specimens were similar. As depicted in Figure 7.15, *fiber tearing* due to the out-of-plane shear stresses induced by the projectile is the most important failure mechanism. There is also extensive matrix cracking at the top and back faces as a result of indentation and spallation stresses, respectively. As the projectile drags the warp yarns, it leads to tow splitting and some delamination, whereas local bending observed in some glass yarns gives rise to fiber kinking.
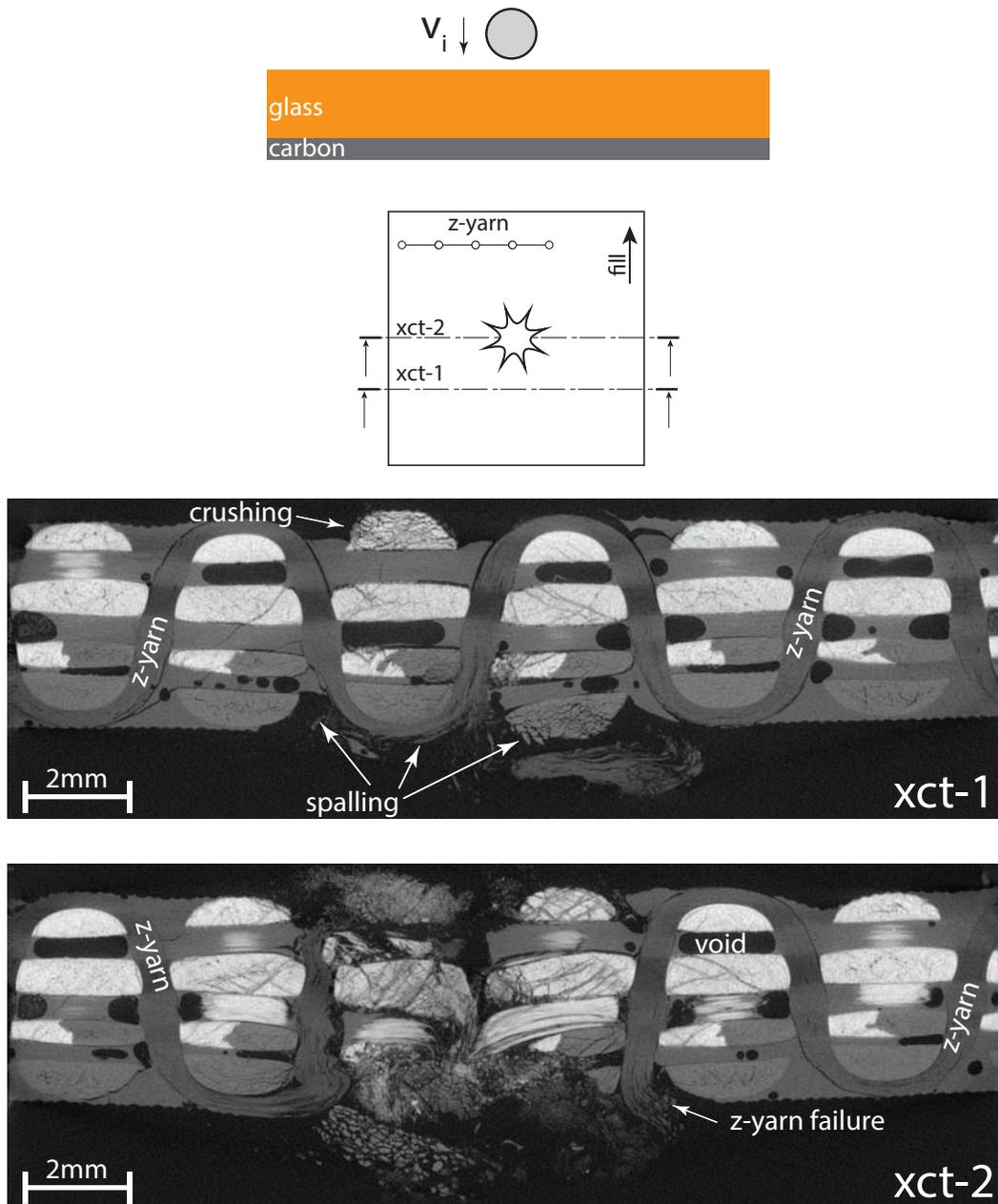
Figure 7.16: Tomograms of a coupon impacted on the glass face and perforated (V_i=351.8 m/s, V_r=141.7 m/s). Sections are parallel to the warp direction. Glass fibers appear white, while carbon fibers and Dyneema appear grey.

The z-yarns played an important role in the response of the composite. As illustrated in Figure 7.16, damage by crushing and spalling is more evident on the fill yarns not wrapped by the z-yarn. Moreover, the more damaged fill yarns are those where z-yarn breakage occurs. As expected, z-yarns hold layers together, significantly reducing the delamination.
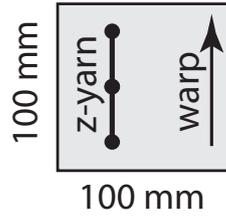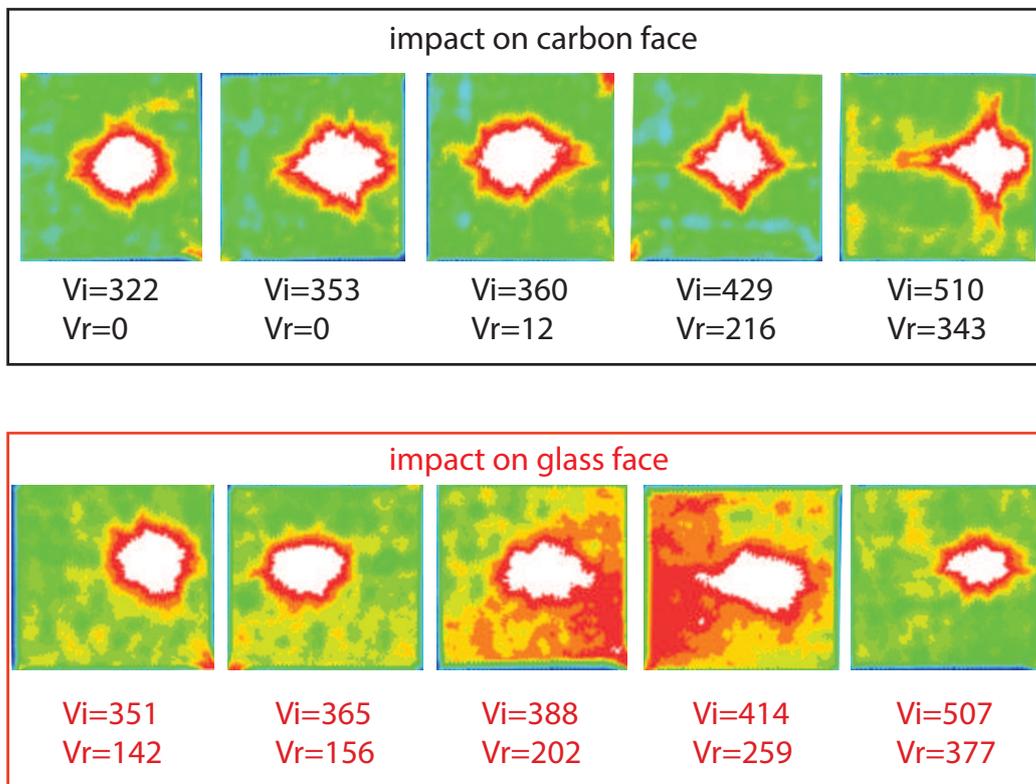
Figure 7.17: C-scan ultrasound inspection of specimens impacted on the carbon face (top) and on the glass face (bottom). Contour plots show the level of attenuation. Damage pattern has an approximately elliptical shape with the major axis oriented perpendicularly to the z-yarn direction.

C-scan inspection did not show significant differences between coupons impacted on the carbon and the glass faces. The size and shape of the damage patterns were similar and can be roughly approximated by an ellipse in which the major axis is oriented perpendicularly to the z-yarn, Figure 7.17.
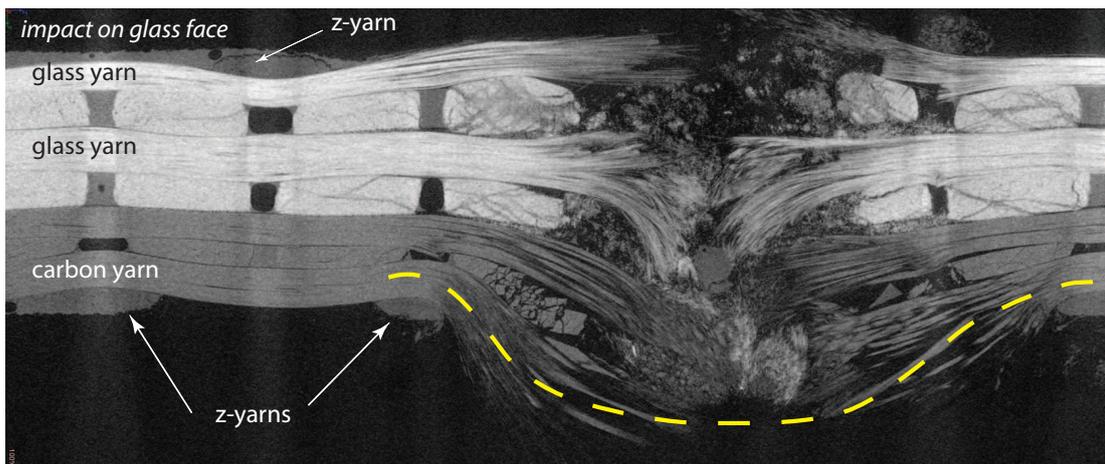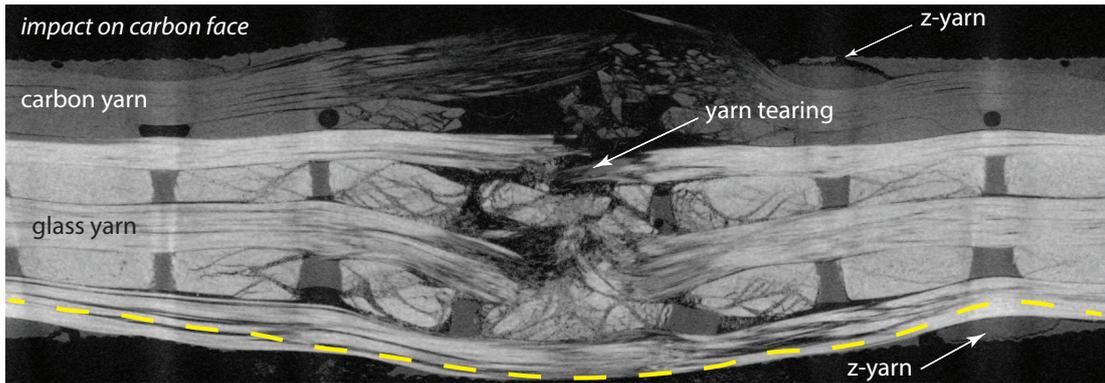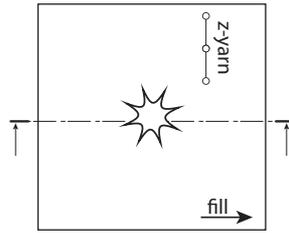
Figure 7.18: Tomograms parallel to the fill direction of specimens after full penetration. Glass fibers appear in white, while carbon fibers, Dyneema and resin are grey. Bending is and more localized in specimens impacted on the glass face (bottom).

Since C-scan inspection did not clarify the higher energy absorption capability and the higher ballistic limit measured on the CF configuration, several specimens impacted on the glass and carbon faces were further inspected by means of XCT. It was found that the fill yarns located at the top and intermediate layers failed in shear, whereas those located at the bottom failed in tension as a result of the membrane stresses (Figure 7.18). Since the energy dissipated during fiber failure is much higher in tension than in shear (tensile

strength and stiffness of yarns are usually much higher than the out-of-plane shear strength and stiffness for a similar failure strain), this suggests that bottom layers can absorb more energy than top layers during impact.

Whether a yarn fails in shear or in tension will depend on the deformability of the neighbor layers. As the confinement increases, the layer is more prone to fail by shear. For instance, the lowest ply of a laminate is never constrained by the neighbour layers, so it will be subjected to membrane stresses[4].

Figure 7.18 also showed that bending in the CF configuration was spread over a larger area than in the GF due to the higher failure strain of the glass fibers. This ensures not only a higher amount of fibers contributing to dissipate energy, Tabiei & Nilakantan (2008), but also a higher number of yarns which will fail in tension rather than in shear and, consequently, a higher energy absorption capability.

7.3 Numerical modeling

Drop-weight and high velocity experimental tests reported in this chapter were simulated by using a mesomechanical approach based on the finite element method. This allowed to study the failure mechanisms and the influence of the mechanical properties on the impact response of the composite.

7.3.1 Low velocity

Finite element model

The size of the laminate was 145×145 mm^2, whereas the test rig was modeled as a hollow square plate of 127×127 mm^2. The test rig was modeled as a rigid surface and the projectile was defined as a rigid body. The laminate was split into seven plies of the same thickness (0.586 mm). The shape of the impactor was hemispherical of 12.7 mm of diameter and 18.75 mm of height (Figure 7.19).

Each ply was modeled with linear solid elements (with either 6 or 8 nodes and reduced integration). Plies were connected each other by using conforming meshes. The mesh

---

[4]Note that the outermost layers of 3D woven composites are always oriented in the fill direction.
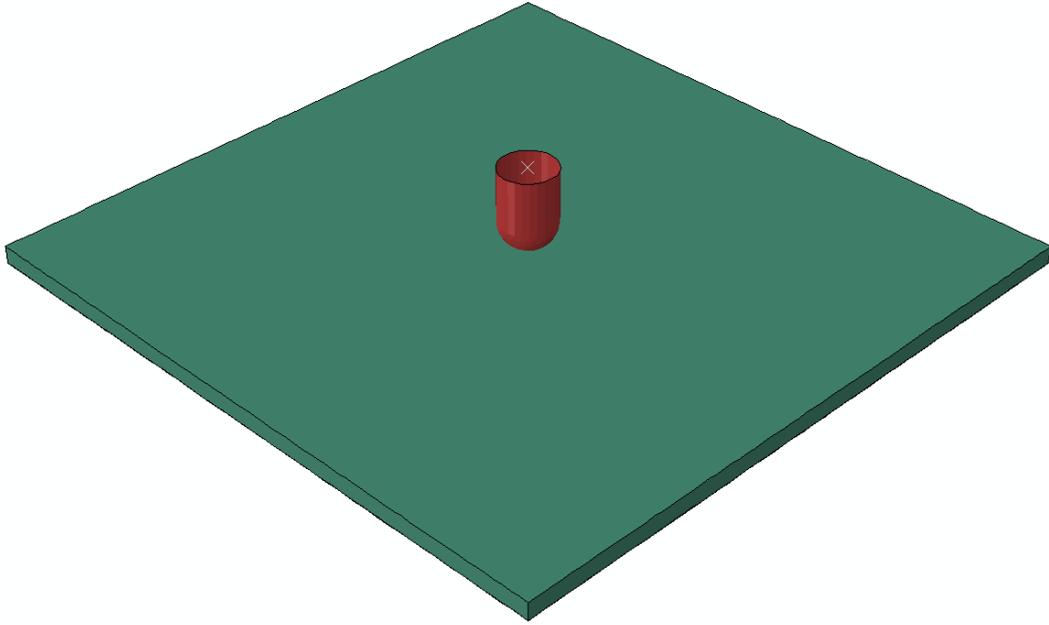
Figure 7.19: Drop-weight finite element model.

was refined at the impact region to capture stress gradients, leading to approximately 750 000 elements. A non-structured meshing strategy was followed to reduce the damage localization problems commonly observed in materials with softening Bažant (1998). This mesh also showed a lower hourglassing effect compared with a structured mesh.

The plies behaved as orthotropic solids in which the response is linear elastic up to the onset of the intralaminar damage by matrix or fiber failure. A continuum damage model based on the LaRCO4 failure criteria Dávila *et al.* (2005), Pinho *et al.* (2005), was implemented as a user subroutine VUMAT in Abaqus Explicit, Figure 7.20. The input parameters of the constitutive model are the elastic constants (E_1, E_2, E_3, ν_{12}, ν_{13}, ν_{23}, G_{12}, G_{13}, G_{23}), the strengths (X_T, X_C, Y_T, Y_C, S_L, Z_C) and the fracture energies corresponding to each failure mode (G_{1+}, G_{1-}, G_{2+}, G_{2-}, G_6 and G_{3-}). More details of the constitutive model are provided in Appendix C.

The elastic constants were already determined in Appendix A by applying the microme-chanical equations of C.C.Chamis (1984), except the stiffness in the through-thickness di-rection, which was defined arbitrarily as $E_3 = 7.5$ GPa. Chamis' equations were also applied to calculate the ply strengths (Table 7.3) from the fiber and matrix strengths pro-vided by the manufacturers, except the through-thickness strength, which was also defined arbitrarily as $Zc = 400$ MPa.

149
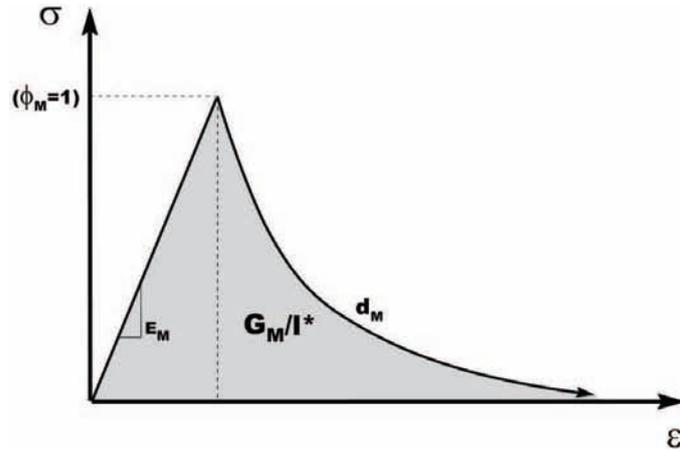
Figure 7.20: Parameters of the intraply damage constitutive model, Lopes *et al.* (2009a).

Table 7.3: Ply strength (MPa) estimated from the Chamis' model, C.C.Chamis (1984)).

	X_T	X_C	Y_T	Y_C	S_L	Z_C
Glass layers	2201	1980	68	109	40	400
Carbon layers	2206	1800	69	111	42	400
Hybrid layer	2237	1833	69	110	42	400

Table 7.4: Ply fracture toughness (N/mm) estimated from the elastic energy stored by each failure mode.

	G_{1+}	G_{1-}	G_{2+}	G_{2-}	G_6	G_{3-}
Glass layers	343	596	1	9	2	142
Carbon layers	127	94	1	8	1	153
Hybrid layer	207	280	1	8	1	149

The fracture energies G_M were first estimated as four times the elastic energy stored in each failure mode and then arbitrarily modified to fit the load-displacement curve of one impact, Table 7.4. These values were then used for the rest of the models. Note that these fracture energies were sufficiently high to avoid snap-back[5] of the elements, Maimí *et al.* (2007b).

---

[5]Snap-back occurs in brittle failures when the control of the load is lost, leading to an unstable solution that will dissipate more energy than it should, Bažant (1998), Carrara *et al.* (2011).

Regarding the boundary conditions, the laminate was simply supported on the test rig, so a normal contact was defined between them to avoid penetration. The test rig was completely constrained, so it was unable to translate or rotate. The impactor was modeled as a rigid body and enforced to move along vertical direction with a mass point of 11.72 kg (94 J) and 22.4 Kg (162 J) attached to it. Initial velocity of the impactor varied from 3.8 to 4.0 m/s. Since some elements may be removed during perforation, contact surfaces were defined in all layers.

Impacts were simulated with the explicit finite element code Abaqus Explicit. The explicit solver integrates the equations of motion by using an explicit central difference integration rule which satisfies the dynamic equilibrium at the beginning of an increment and calculates the kinematic state at the increment $i + 1$, Ridruejo *et al.* (2011). Unlike backward-Euler integration methods used in implicit codes, explicit integration leads to a conditionally stable problem in which the stability limit Δt depends on the size of the element and the sound speed of the material $c = \sqrt{\frac{E}{\rho}}$, Courant *et al.* (1967):

$$\Delta t = min \left[\frac{l}{c} \right] \tag{7.5}$$

where l is the characteristic length of an element. This implies that the computational cost increases with small elements of high stiffness and low density.

Accordingly, the use of small elements ensures a stable solution, but increases the computational cost. In particular, simulations took 100 hours running with 22 processors in double precision and parallelized using the domain decomposition method. The onset of damage clearly penalizes the critical stable time Δt and increases the computational cost. Although mass scaling can be used to increase Δt, this approach was disregarded as it affects the energy balance and distorts the results. Other numerical issues available in Abaqus Explicit like *distortion control*, which prevents solid elements from inverting, were not applied due to the non-negligible artificial energy introduced in the model.

Penetration modeling of continuum solids using finite element analysis requires an element erosion criteria to remove damaged elements with excessive deformation. The removal of an element generates traction-free surfaces and allows the penetrator to progress through the material, Gama & Gillespie (2011), and influences the response of the composite. In this case, elements were deleted after full degradation in tension in the fiber direction or

in compression in the out-of-plane direction. Fiber breakage and crushing are controlled by the damage variables d_{1+} and d_{3-}, as explained in Appendix C. Actually, to avoid the distortion of elements and to reduce the computational cost of the simulations without affecting the results, failure cut-offs were defined at $d_1 = 0.7$ and $d_3 = 0.9$, before complete degradation occurs. Fiber breakage releases a large amount of energy during failure, whereas crushing is especially critical in high velocity impacts, where indentation and shear plugging play a critical role.

Numerical results

A good agreement was found between experiments and simulations. As shown in the load-displacement curves depicted in Figure 7.21, the finite element simulations were able to capture the differences between the CF and the GF configurations, as well as the energy required to perforate the laminate. Correlation was better in specimens impacted on the carbon face. The stiffness of the GF configuration was overestimated, probably due to the modeling strategy, which does not account for delamination. In contrast, peak loads, which are mainly controlled by the fiber strength, were well estimated.

Once the model was validated, it was used to examine the stress fields at intermediate stages. Results showed that the impact event was sufficiently slow to allow global plate bending. Perforation was controlled not only by the out-of-plane stresses generated at the top layers, but also by the in-plane tensile stresses arising at the bottom layers as the plate bends. The higher failure strain of the glass fibers located at the bottom ensures higher energy absorption during bending, and explains the differences between the GF and CF configurations.

Examination of the in-plane transverse and shear stress fields also revealed significant differences between specimens. Figures 7.22 and 7.23 compare the evolution of matrix cracking on both faces during a 94 J impact at $t_1 = 2.9$ ms and $t_2 = 6.3$ ms, revealing that matrix cracking was more extensive in the GF configuration. Note that some elements of the bottom layer of GF were deleted because the fiber tensile strength was exceeded during bending, whereas elements at the top were deleted because of crushing. The model perfectly captures that GF was almost perforated at t_2, which is in agreement with experimental results.
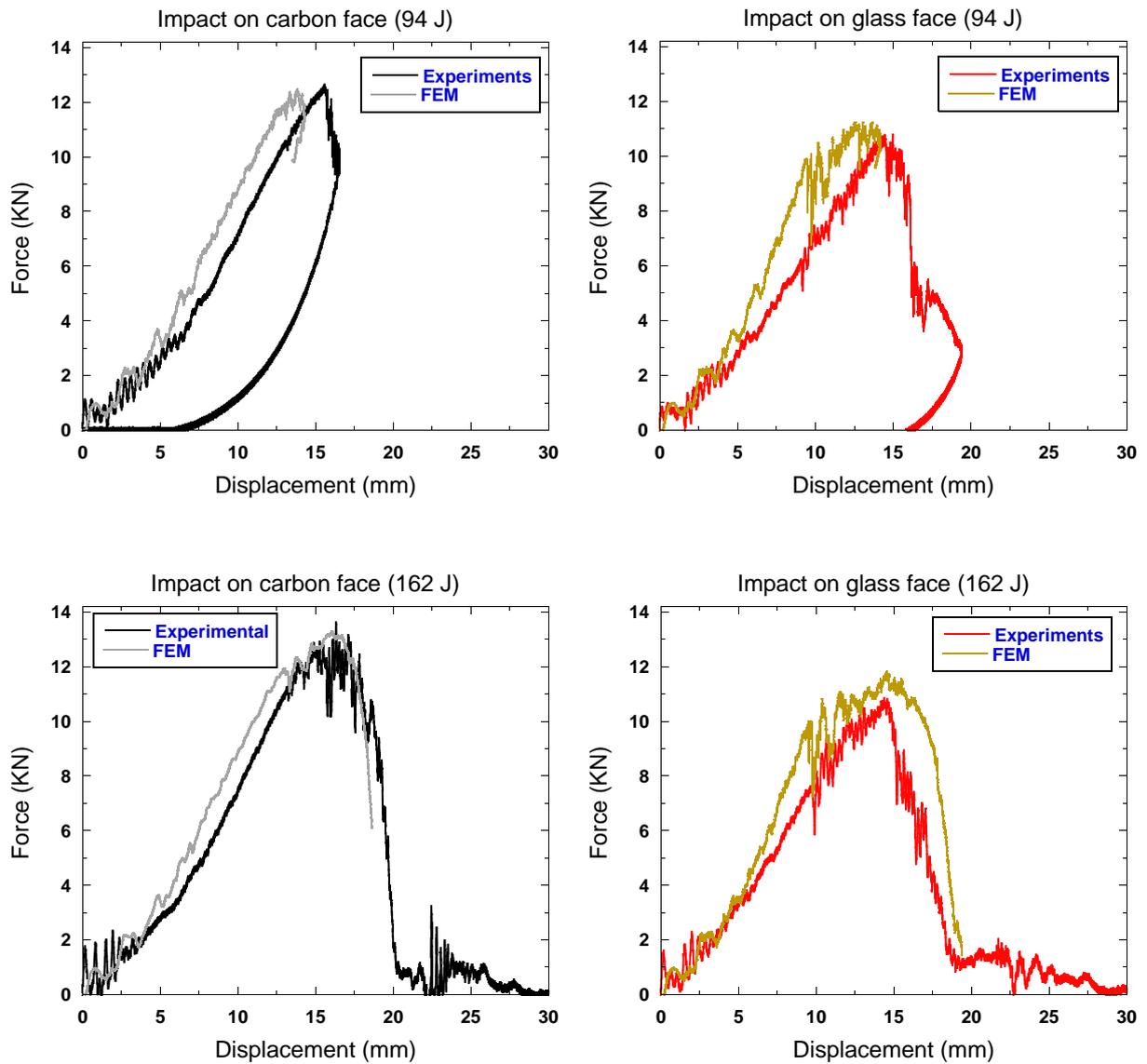
Figure 7.21: Load-displacement curves corresponding to low velocity impacts without penetration (top) and with penetration (bottom). Comparison between numerical and experimental results.
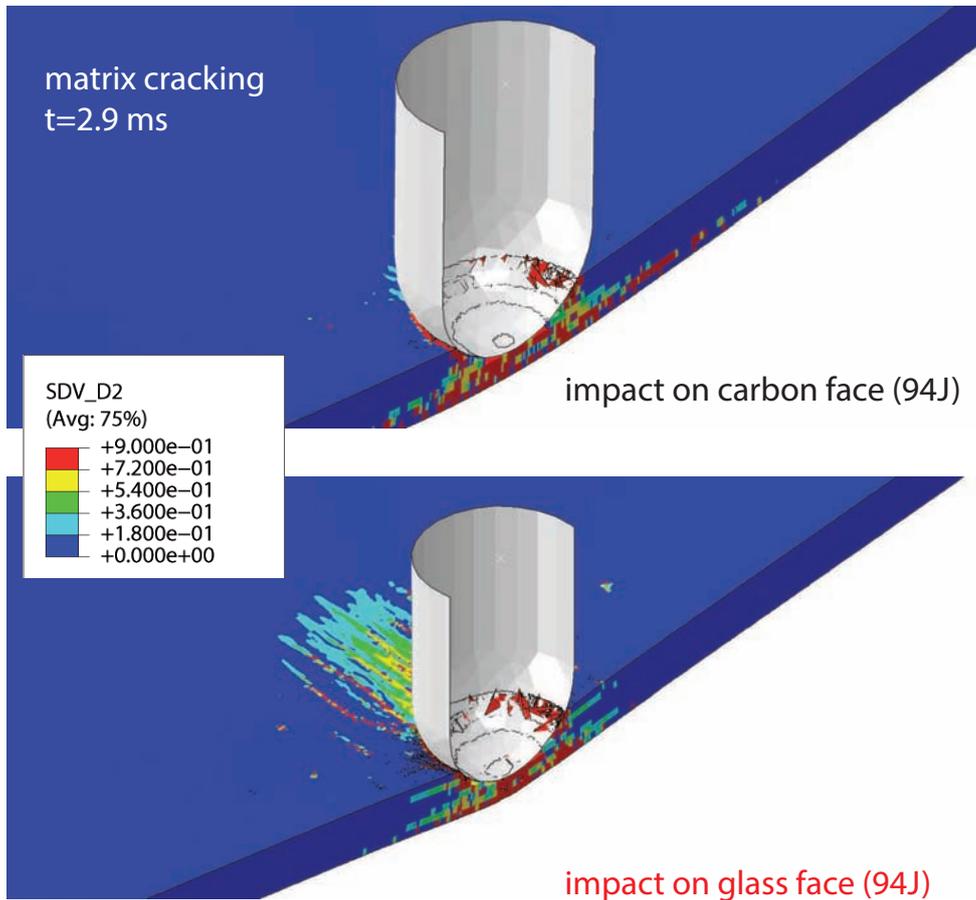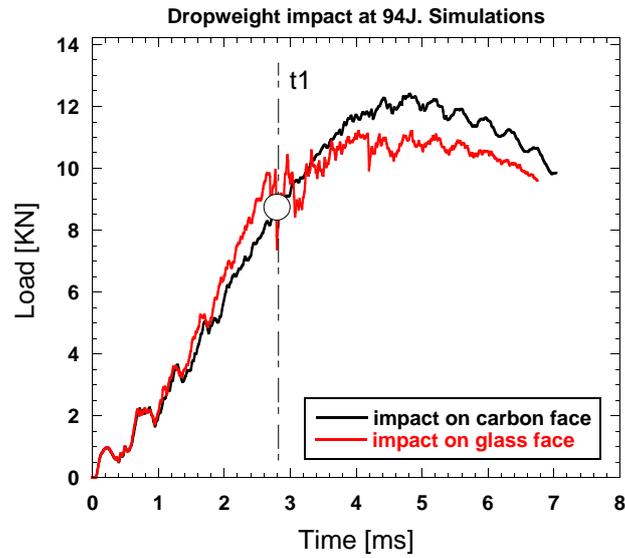
Figure 7.22: Simulation of dropweight impact of 94 J on carbon (top) and glass (bottom) faces at time $t_1 = 2.9$ ms. Contour plots indicate the damage level for matrix cracking.
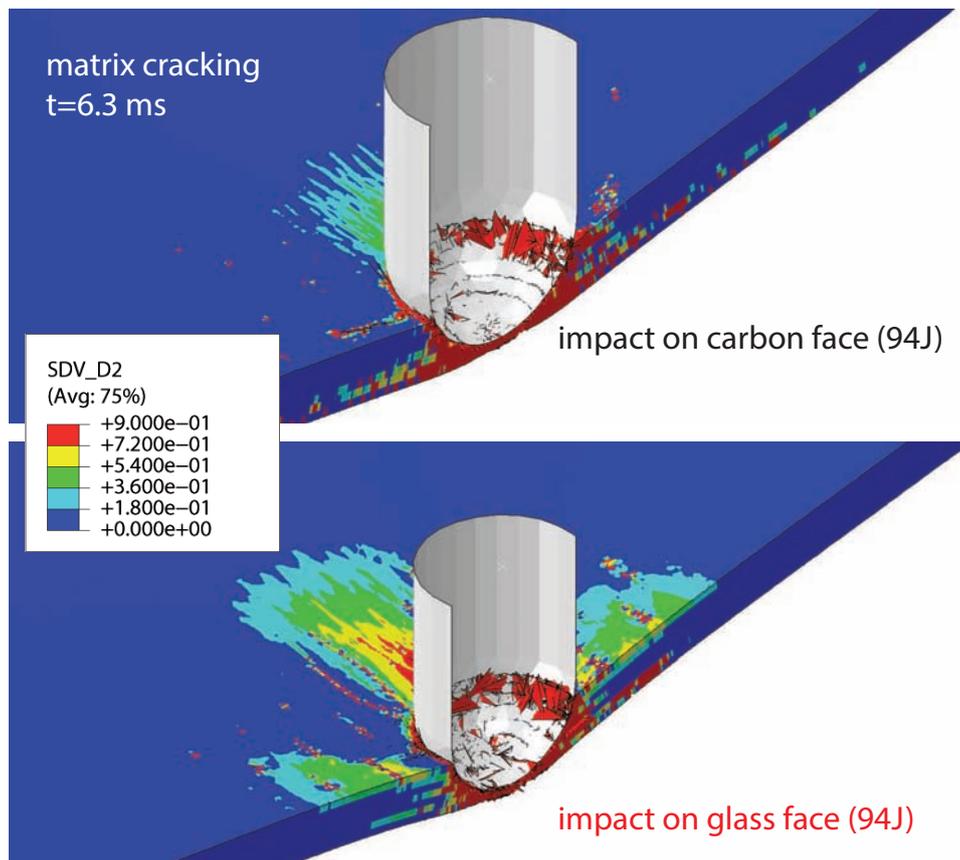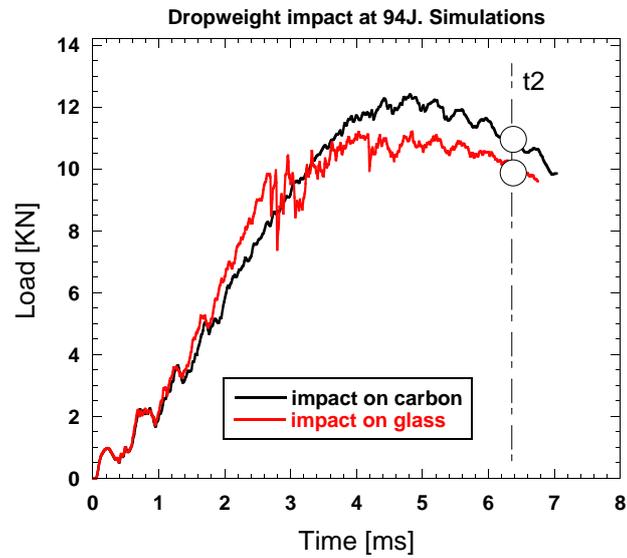
Figure 7.23: Simulation of drop-weight impact of 94 J on carbon (top) and glass (bottom) faces at time $t_2 = 6.3$ ms. Contour plots indicate the damage level corresponding to matrix cracking.

Likewise, in-plane shear stress fields were different in the CF and GF configurations. As shown in Figure 7.24, in-plane shear cracking of specimens impacted at 94 J in the GF configuration affected the whole thickness. The contour plot of the impacted layer was more uniform in the GF configuration due to the higher deformability of the glass fibers.

Finally, Figure 7.25 shows that the 162 J impact energy caused perforation, regardless of the the orientation of the laminate. This in agreement with experimental results. The vertical displacement of the impactor was higher on the GF configuration (Figures 7.21 and 7.25). Perforation was accompanied by considerable matrix cracking, particularly in the GF configuration.

It is worth noting that the influence of the erosion criteria on the mechanical response of the laminate is remarkable. For instance, when the eroding criteria was defined in terms of the damage variables d_1 (fiber breakage) and either d_2 (transverse matrix cracking) or d_6 (in-plane shear cracking), the response became excessively compliant. This can be explained by the ability of the composites to withstand further loading after matrix cracking. Likewise, when d_1 is the only damage variable included in the erosion criteria, the response becomes too stiff and the impactor was unable to penetrate the laminate, which ends up failing only by bending.
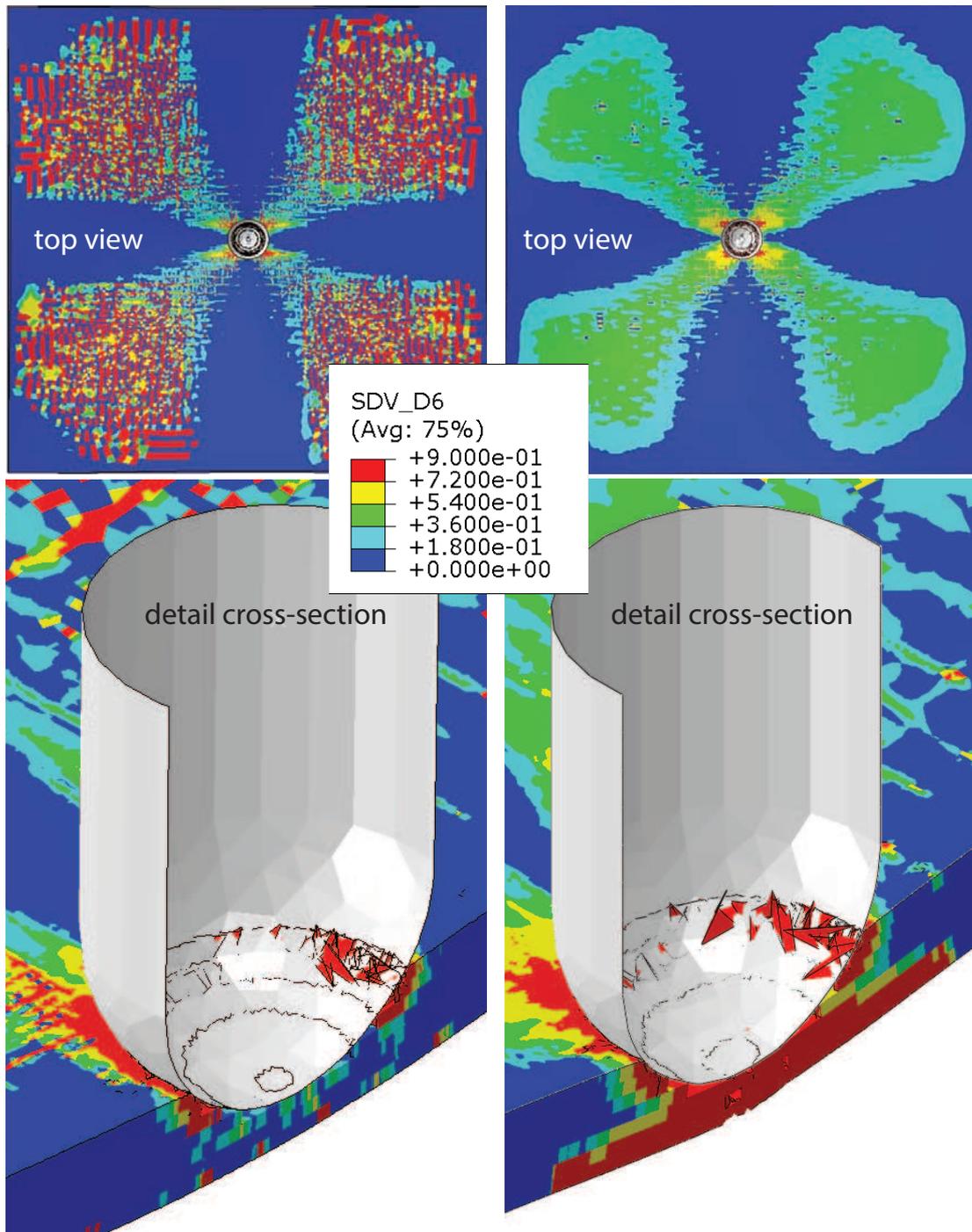
Figure 7.24: Simulation of drop-weight impact of 94 J on carbon (left) and glass (right) faces. Contour plots indicate the damage level corresponding to in-plane shear cracking at $t_1 = 2.9$ ms. Details of the impacted region are shown at the bottom.
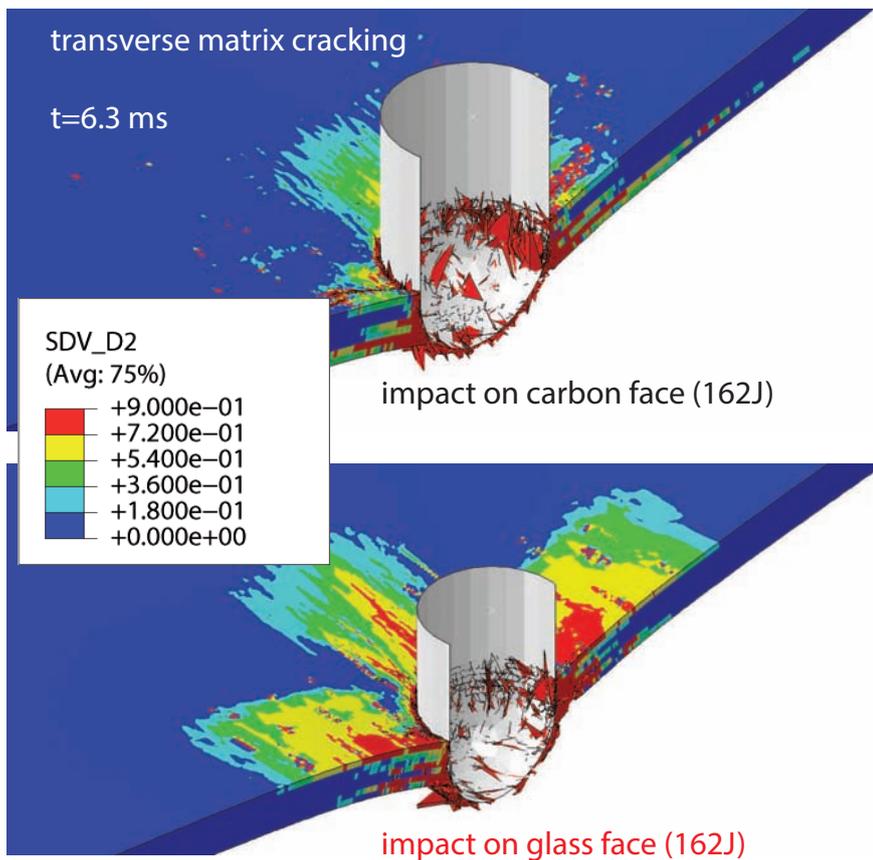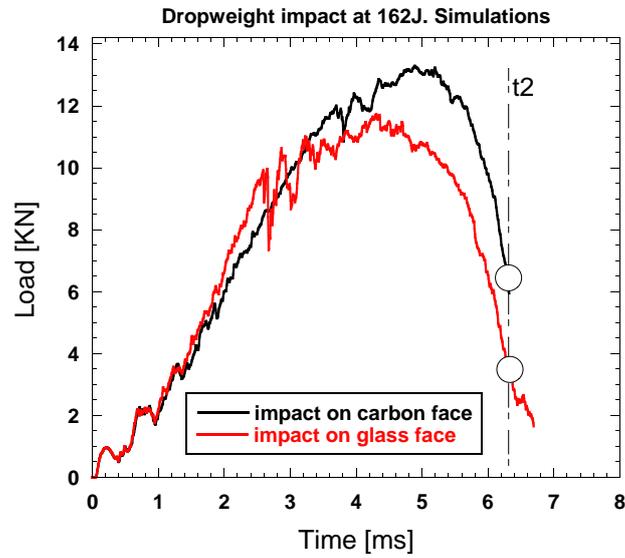
Figure 7.25: Simulation of drop-weight impact of 162 J on carbon and glass faces. Contour plots indicate the matrix damage level corresponding to matrix cracking at $t_2 = 6.35$ ms.
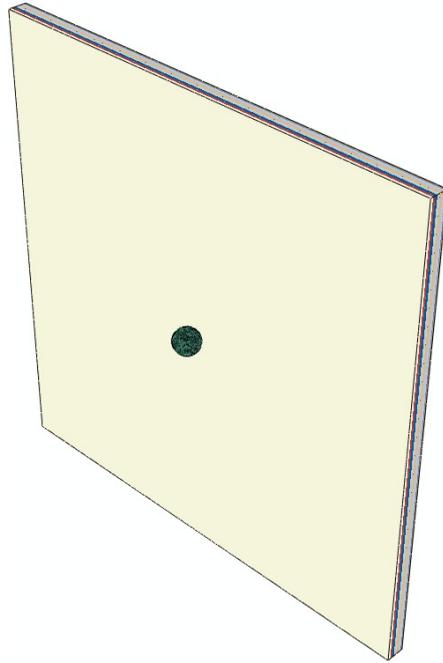
Figure 7.26: High velocity finite element model

7.3.2 High velocity: 2D approach

High velocity impact tests were simulated using a similar approach to the one described above. Only the following differences apply:

- The size of the target was smaller (100×100 mm^2) to replicate the size of the real coupon (Figure 7.26).

- Ballistic impacts are not influenced by the boundary conditions, so the target was not supported nor constrained in any direction.

- The projectile was not modeled as a rigid body, but as an elastic steel sphere discretized with solid elements with reduced integration (C3D8R). The elastic properties of the steel were $E = 210$ GPa and $\nu = 0.3$. This allows to account for possible stress wave interactions while not increasing significantly the computational cost.

- The number of elements of the model was approximately 270 000, and the duration of the simulations was t=0.08 ms. Computational cost was more than 100 times lower than that of drop-weight test simulations.

Table 7.5: Ballistic limits of the hybrid 3D woven composite measured as an average of the critical velocities V_0. Comparison between experimental and numerical results with two crushing strengths Z_c.

Ballistic limit (m/s)	Experimental	FEM	
		Zc=400 MPa	Zc=600 MPa
Impact on carbon face	359	352	409
Impact on glass face	326	343	413

Numerical results

The residual velocity of the projectile was computed for each impact velocity. Critical velocities V_0 and the ballistic limit V_{50} were determined from the simulations according to the procedure described in section 7.2.2. Results revealed the ability of the numerical model to reproduce the residual velocities measured experimentally, as well as to capture the experimental differences between the CF and the GF configurations in terms of the ballistic limit for the baseline configuration (crushing strength $Z_c = 400$ MPa). As shown in Figure 7.27, the ballistic limit was slightly underestimated by the numerical model in the GF configuration and overestimated in the CF configuration, but correlation was good in both cases.

The influence of the crushing strength on the ballistic limit was determined by comparing the response of the baseline material ($Z_c = 400$ MPa) with another material in which the crushing strength was increased up to $Z_c = 600$ MPa. Results revealed that the role played by crushing on the fem model is critical (Table 7.5). As Z_c increases, the ballistic limit clearly increases (Figure 7.28).

Further examination of the stress fields around the impact region revealed that local bending was not properly captured by the numerical model (Figure 7.29). The mechanical response was mainly controlled by crushing in the simulations. This is not in agreement with experimental observations, where local bending of the rear layers played an important role (Figures 7.11 and 7.18). Moreover, the model was unable to account for the effect of the z-yarns, so another modeling strategy was suggested.
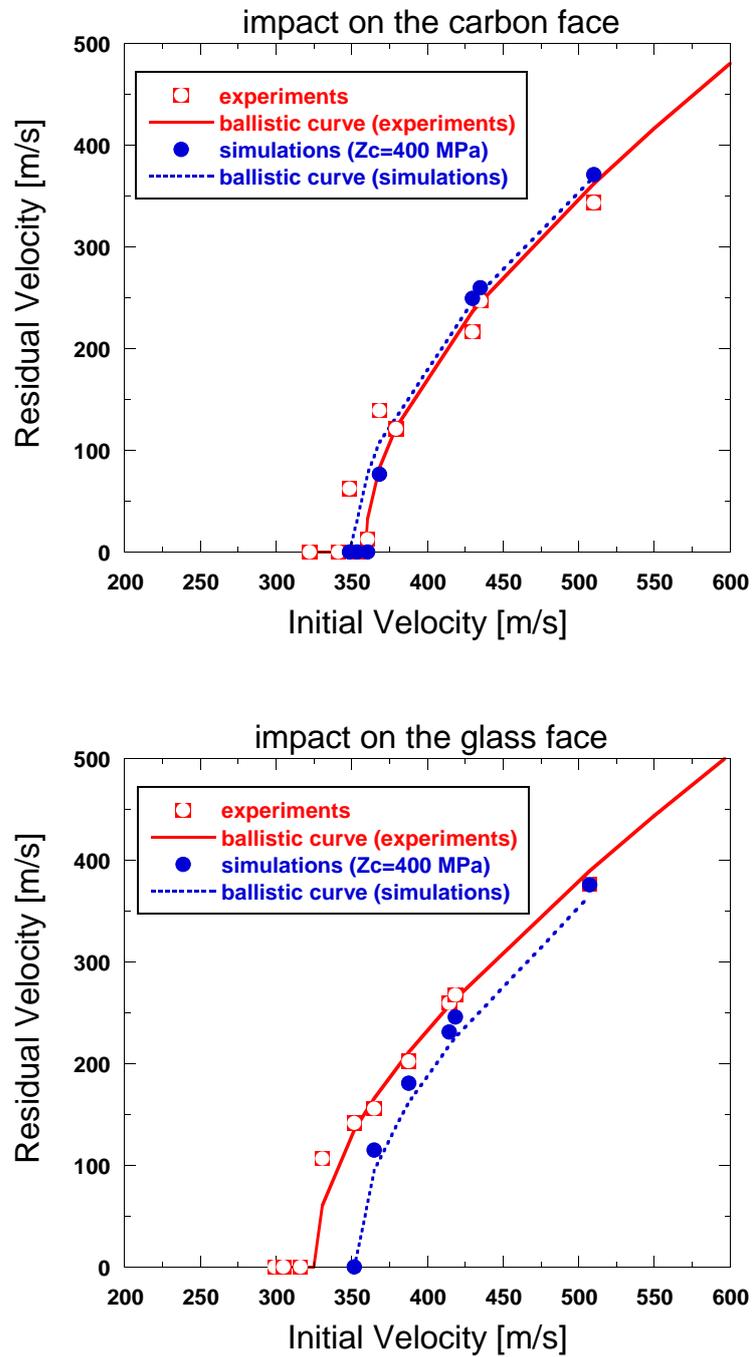
Figure 7.27: Comparison between experimental and numerical ballistic curves of the hybrid 3D woven composite. Impact on the carbon face (top) and impact on the glass face (bottom). Z_c=400 MPa.
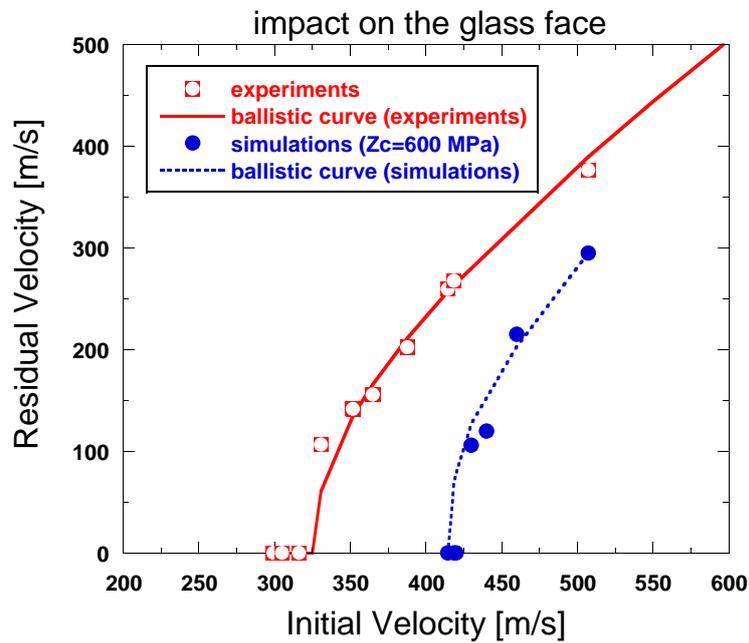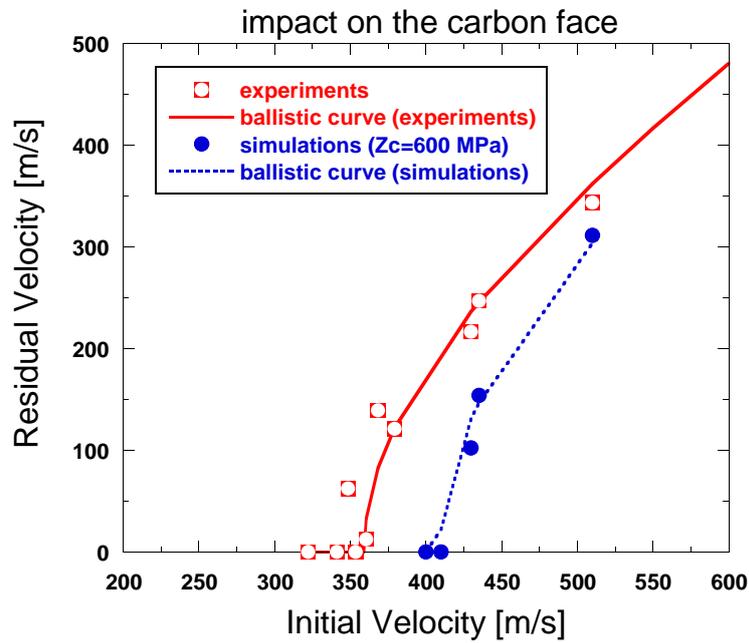
Figure 7.28: Comparison between experimental and numerical ballistic curves of the hybrid 3D woven composite modeled using a 2D approach. Impact on the carbon face (top) and impact on the glass face (bottom). Z_c=600 MPa.
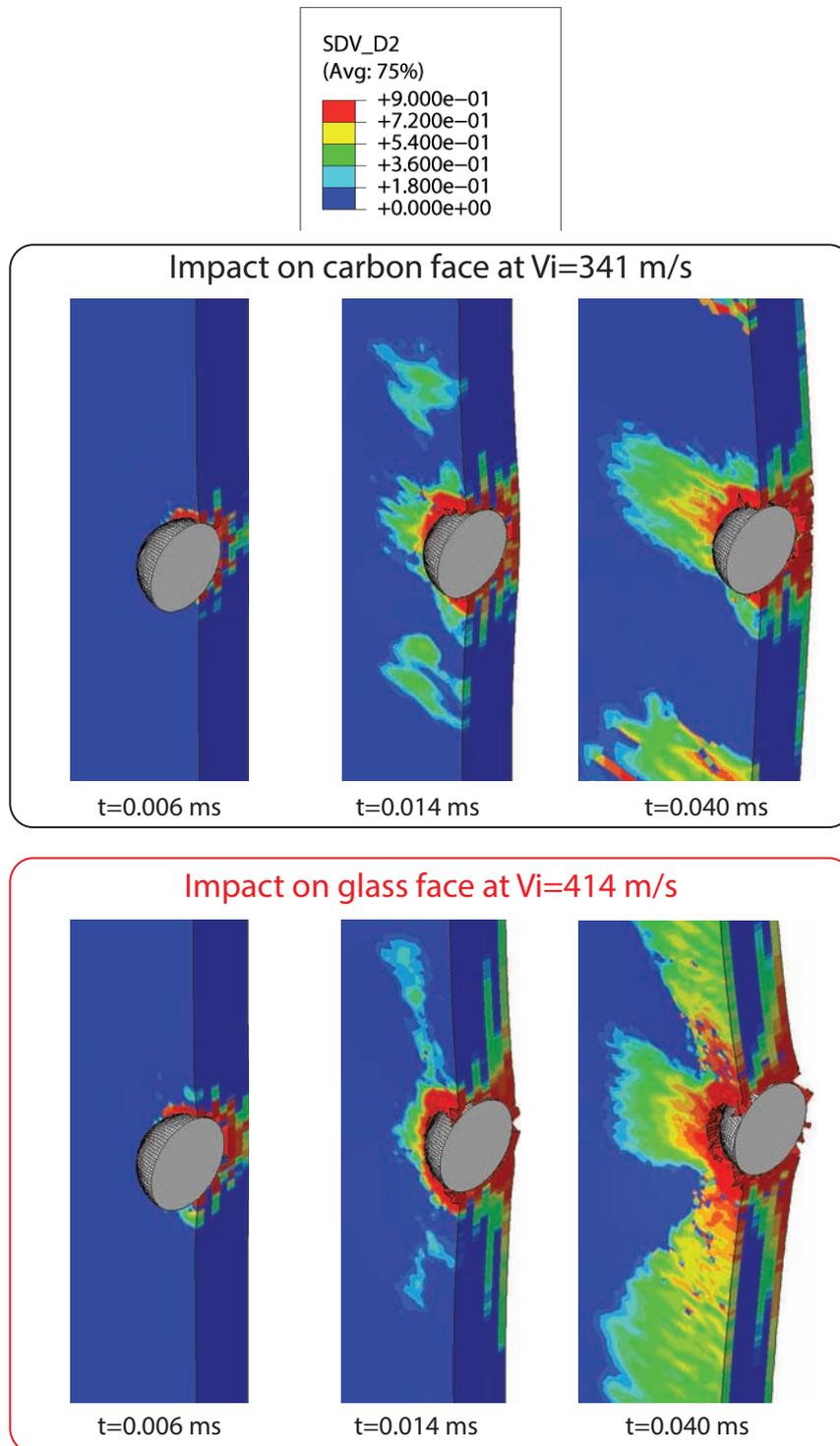
Figure 7.29: Cross section of the numerical model for the high velocity impact tests. Contour plots indicate the damage level corresponding to matrix cracking. V_i=341 m/s on the CF face (top) and V_i=414 m/s on the glass face (bottom).

7.3.3   High velocity: 2.5D approach

Embedded element technique

The finite element models described so far provide a good estimation of the low velocity and high velocity global impact response of 3D woven composites at a reasonably low computational cost. However, such models are unable to account for the influence of the z-yarns nor to capture local bending effects under ballistic impacts, so a new model strategy is presented here.

The modelization of composites with complex geometries has been traditionally afforded by creating unit cells and defining simple loading states in which periodic boundary conditions are applicable, Melro *et al.* (2012), Barbero *et al.* (2005a), Barbero *et al.* (2005b), Buchanan *et al.* (2010), Pankow *et al.* (2012). However, composites subjected to impact loading undergo complex stress states, which invalid the assumption of periodicity. Moreover, the tortuosity of the geometry requires very fine meshes at the resin pockets, increasing the computational cost. To overcome this problem, several mesh superposition techniques in which the components can be meshed separately have been suggested. Examples include the Binary Model, Cox *et al.* (1994a) and McGlockton *et al.* (2003), the Domain Superposition Technique suggested by Jiang (2013) or the multi-element digital chain technique proposed by Mahadik & Hallett (2010). Some of these techniques have been applied to model textiles with 3D reinforcement, giving an accurate account of the global stiffness, but these approaches usually require in-house codes or complex models, which limits their widespread use in industry.

More recently, Tabatabaei *et al.* (2014) has successfully applied the *embedded element technique* to predict the elastic properties and the damage patterns in a wide range of composites, such as 5-harness satin composites. The technique consists on superimposing two independent meshes, from now on *embedded* and *host*, and establishing a kinematic relationship between them. When a node of an embedded element lies within a host element, the translational degrees of freedom of the embedded node are constrained to the interpolated values of the corresponding degrees of freedom of the host element, Simulia (2010). Whether an embedded node lies within a host element or not depends on the size of the region of influence defined by the user. The process is illustrated in Figure 7.30. The main advantage of this technique is that nodes from the host and the embedded
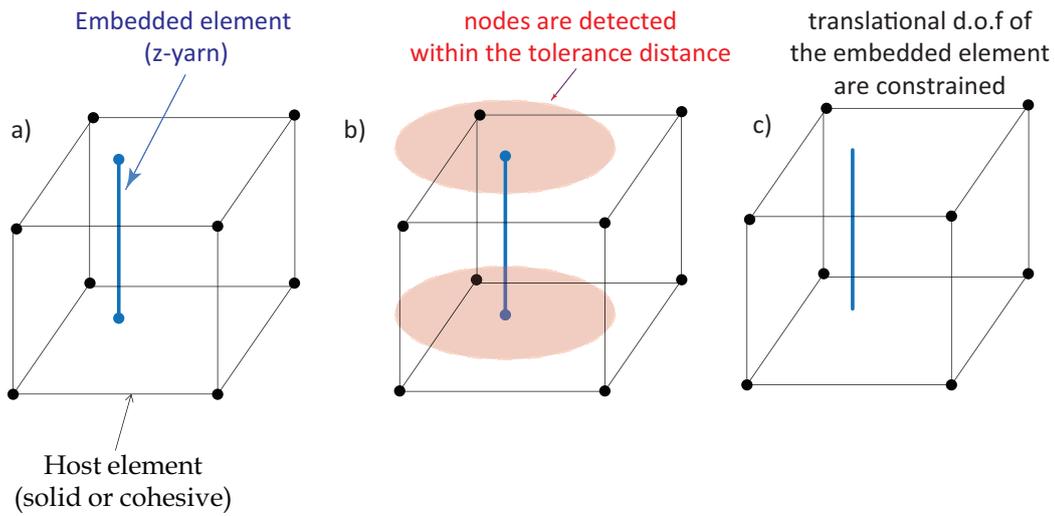
Figure 7.30: Schematic of the embedded element technique. a) Z-yarns are embedded within the solid element. b) A region of influence is defined around the embedded node. c) If a node belonging to the host element is detected, degrees of freedom of the embedded node are automatically constrained.

elements are not necessarily coincident, so it is possible to use non-conforming meshes. Furthermore, the technique is simple and is available in the commercial finite element code Abaqus Explicit.

To the author's knowledge, the embedded element technique has not been applied to impact problems. Hence, a 2.5D modeling approach based on the embedded element technique was developed to simulate the high velocity impact response of the hybrid 3D woven composite.

The host mesh is composed by solid and cohesive elements. Each ply is discretized with solid elements according to the same strategy followed in 7.3.2, whereas three-dimensional cohesive elements (COH3D8) are inserted between plies to account for delamination. The solid and the cohesive elements share the nodes. The thickness of the cohesive elements (8.75 μm) is considered to be representative of the resin rich region between adjacent plies. In addition, z-yarns are modeled as truss linear elements[6] (T3D2) running in zig-zag configuration. Truss elements are embedded within the host mesh by using the embedded element technique, so nodes of the host and the embedded elements are not necessarily

---

[6]Truss elements can only transmit axial forces.

Table 7.6: Interply properties in the hybrid 3D woven fem model

Parameter	Value
Normal interface Strength, N (MPa)	53
Shear interface Strength, S (MPa)	104
Mode I fracture toughness, G_{Ic} (KJ/m^2)	0.3
Mode II fracture toughness, G_{IIc} (KJ/m^2)	0.8
Benzeggah-Kenane parameter, η	1.75

Table 7.7: Z-yarn properties in the model

Parameter	Value
Density (Kg/m^3)	1500
Elastic Modulus (GPa)	47
Poisson's ratio	0.275
Fracture stress (GPa)	0.55
Normal fracture (GPa)	0
Strain	0.04
Shear retention factor	1
Shear fracture strain	0.002

coincident, Figure 7.31. The section of the z-yarns corresponds to the values measured experimentally (S_{z-yarn} = 1.028 mm^2). A python script was written to automatically generate the mesh.

The constitutive model of the solid elements is the same as in the 2D approach. Cohesive elements follow a traction-separation in which damage initiation is controlled by a quadratic strength-based damage criteria and damage evolves according to the fracture energy as detailed in Appendix C. The material behavior of the z-yarns was brittle in tension followed by a softening law and linear elastic in compression. This constitutive model is designated as *brittle cracking* in Abaqus/Explicit and is aimed to applications in which the behavior is dominated by tensile cracking. All the constitutive models are detailed in Appendix C.

The properties of the cohesive elements and the z-yarns are presented in Tables 7.6 and 7.7.
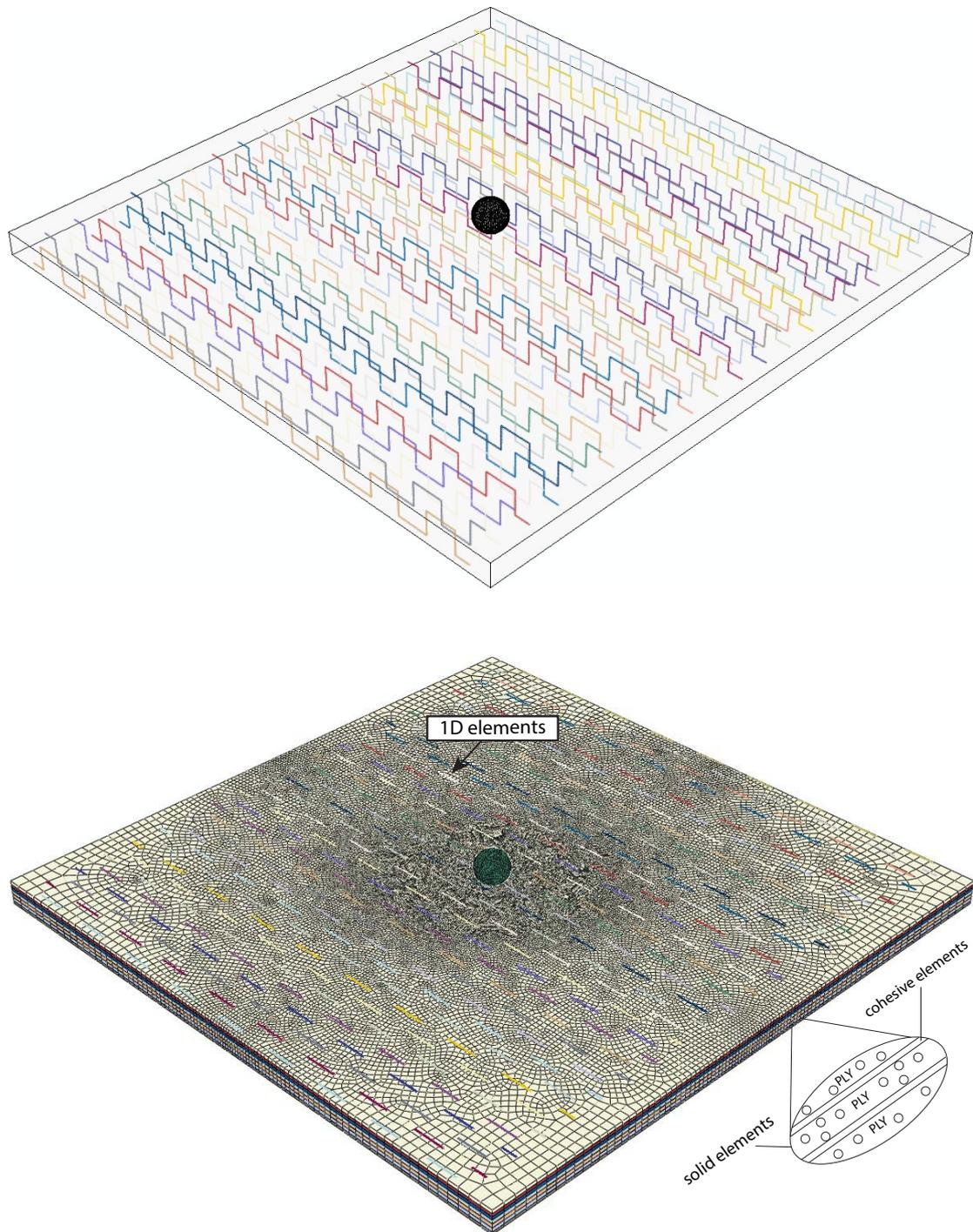
Figure 7.31: Finite element model of the high velocity impact test. The 2.5D modeling approach includes z-yarns (top) embedded in solid plies containing cohesive elements (bottom).

167

Table 7.8: Ballistic limits of the hybrid 3D woven composite measured as an average of the critical velocities V_0. Comparison between experimental and numerical results obtained from the 2.5D modeling approach.

Ballistic limit (m/s)	Experimental	FEM
Impact on carbon face	359	373
Impact on glass face	326	358

Numerical results

The presence of the cohesive elements reduced the ballistic limit of the numerical model, so this was compensated by increasing the crushing strength Z_c from 400 MPa to 600 MPa. This modification led to a good correlation between the experimental and numerical ballistic curves, especially in the case of the CF configuration, Figure 7.32. As shown in Table 7.8, the model was able to capture the differences between the ballistic limits of the CF and the GF configurations with an error below 10%.

Regarding the failure modes, this approach provided a more realistic insight in the damage patterns than the 2D approach. Crushing in the first layers was accompanied by local bending, which gives rise to membrane stresses at the bottom layers. When the velocity of the projectile is sufficiently high, the tensile strength of the layer is exceeded and the projectile perforates the hybrid 3D woven composite, Figure 7.33; otherwise, the projectile rebounds, Figure 7.34.

One of the main advantages of this modeling strategy is that the influence of the z-yarn can be also evaluated. A set of numerical models was generated without z-yarns. As shown in Figure 7.35, z-yarns arrest the propagation of delamination mainly at the bottom layers. This is also depicted in the Figure 7.36, which indicates that the area delaminated is smaller in the presence of the z-yarns.

The main disadvantage of the insertion of cohesive elements is the significant increase in the computational cost. The cohesive elements not only increase the total number of elements, but more importantly, reduce the stable time Δt. This can be mitigated by increasing the density of the cohesive elements, which in turn reduces the sound speed of the material, but only in those cases in which the kinetic energy is not heavily influenced.
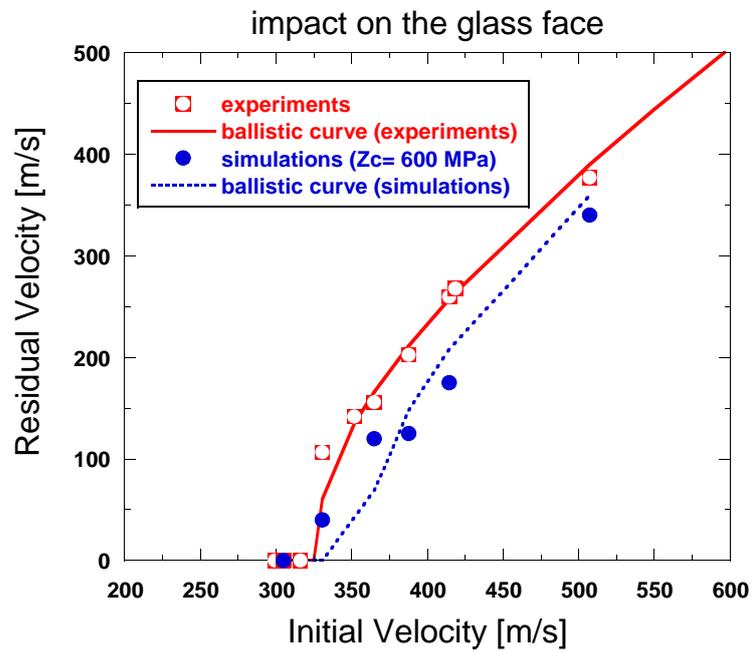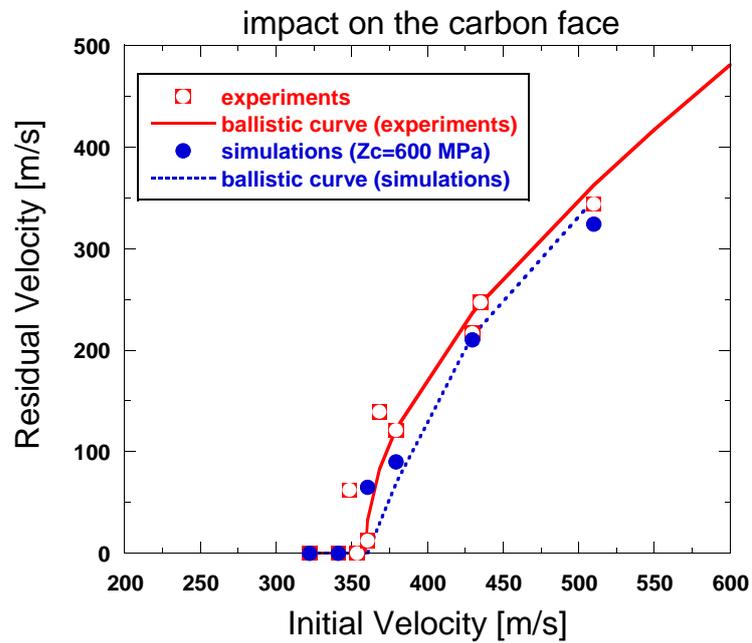
Figure 7.32: Comparison between experimental and numerical ballistic curves of the hybrid 3D woven composite obtained with a 2.5D modeling approach. Impact on the carbon face (top) and impact on the glass face (bottom).
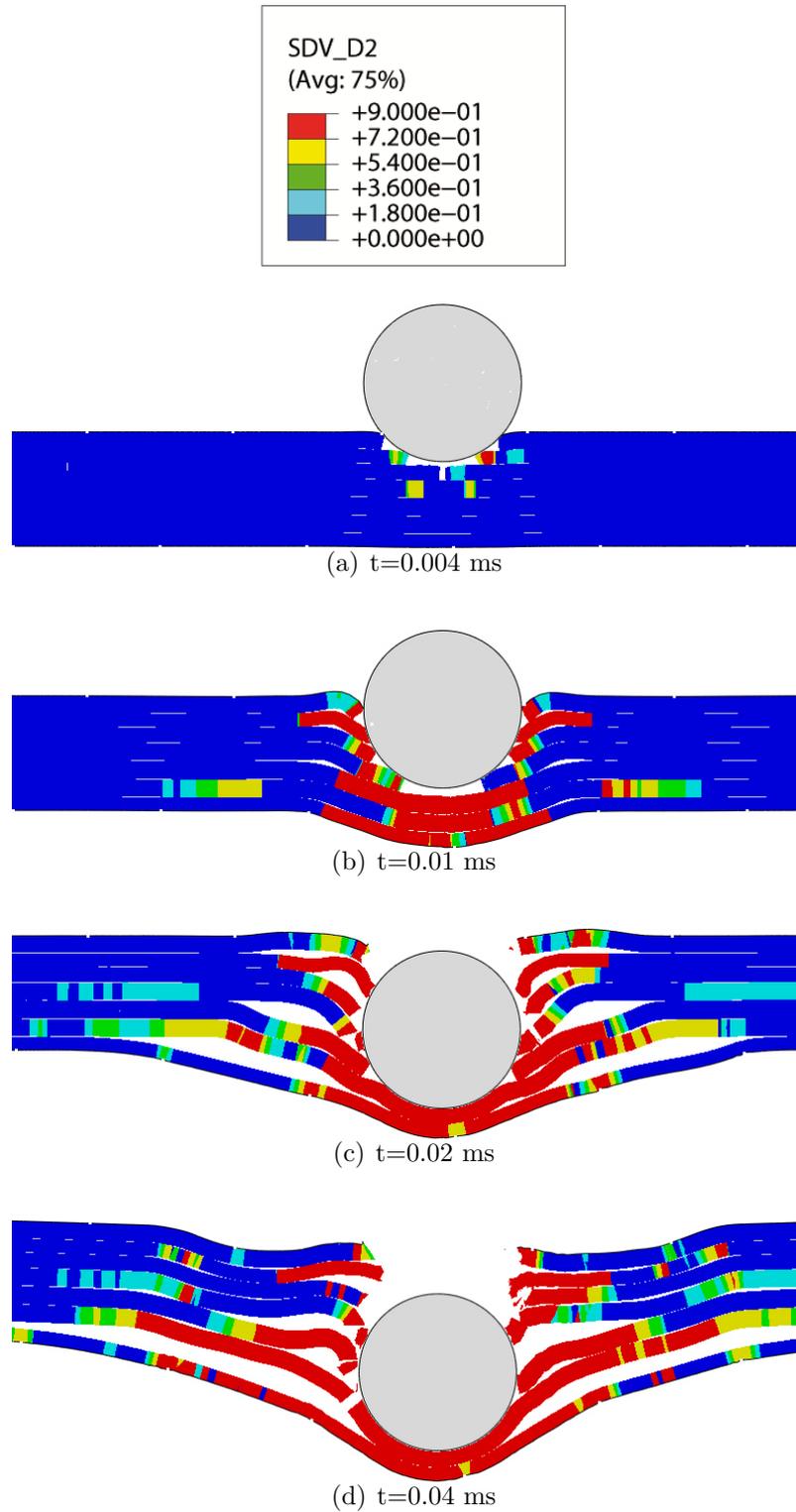
Figure 7.33: Sequence of impact events during a high velocity impact on the carbon face at V_i=341 m/s. The numerical model includes z-yarns and cohesive elements. Contour plots indicate the damage level corresponding to matrix cracking.
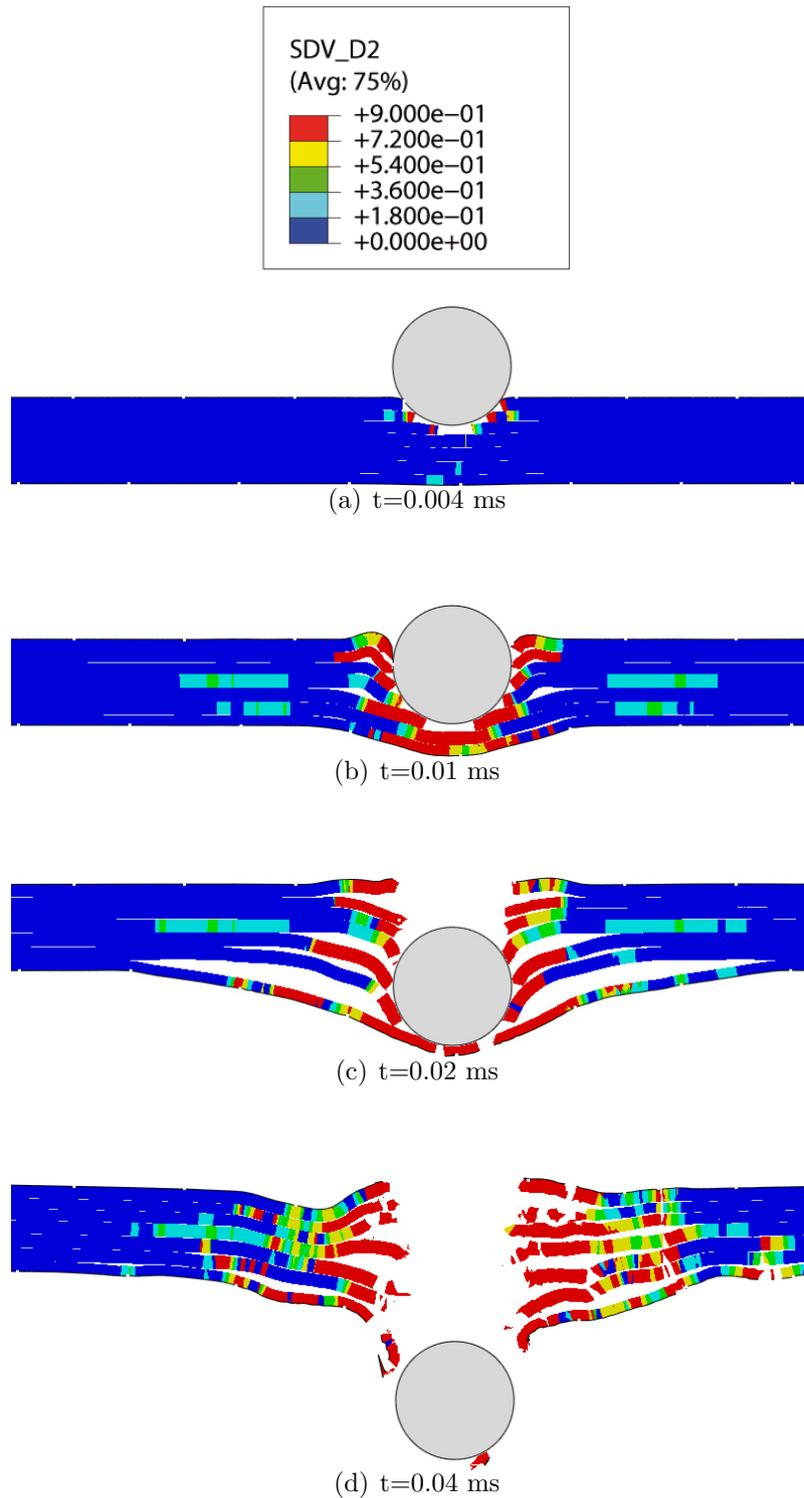
Figure 7.34: Sequence of impact events during a high velocity impact on the glass face at V_i=414 m/s. The numerical model includes z-yarns and cohesive elements. Contour plots indicate the evolution of the damage variable corresponding to matrix cracking.
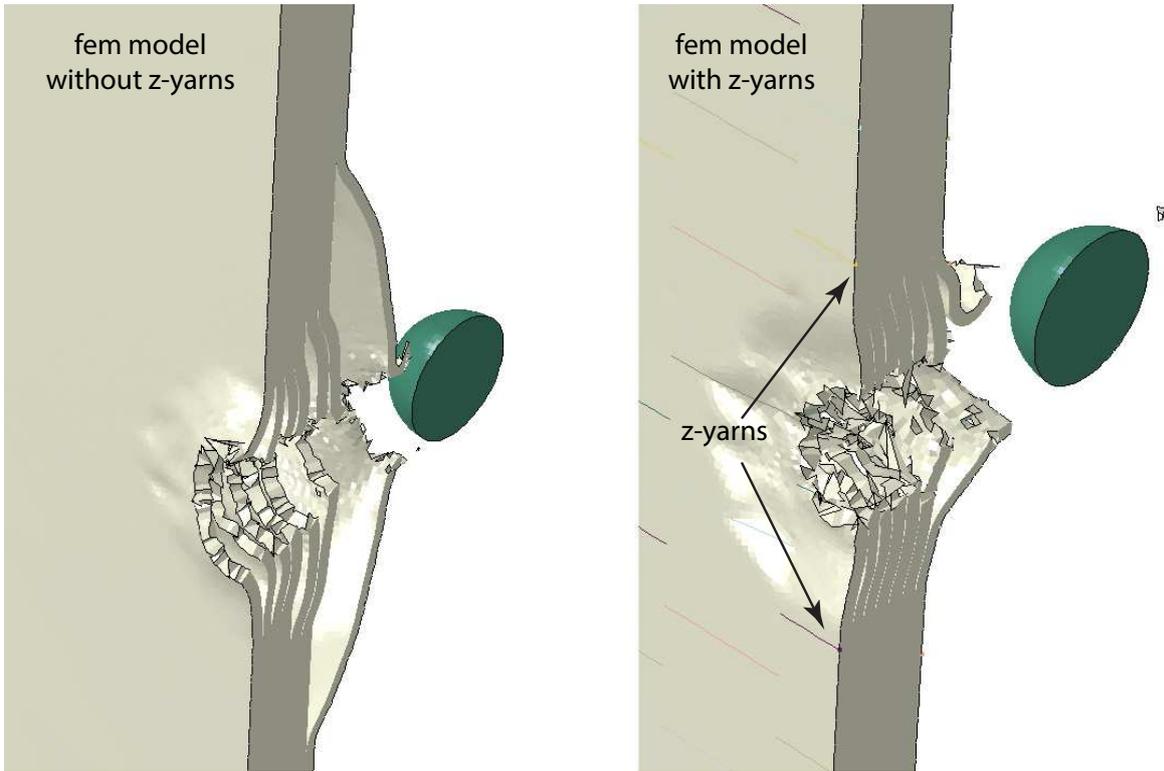
Figure 7.35: High velocity impact models at V_i=510 m/s without z-yarns (left) and with z-yarns (right).

(a)　　　　　　　　　　　　　　　　　(b)
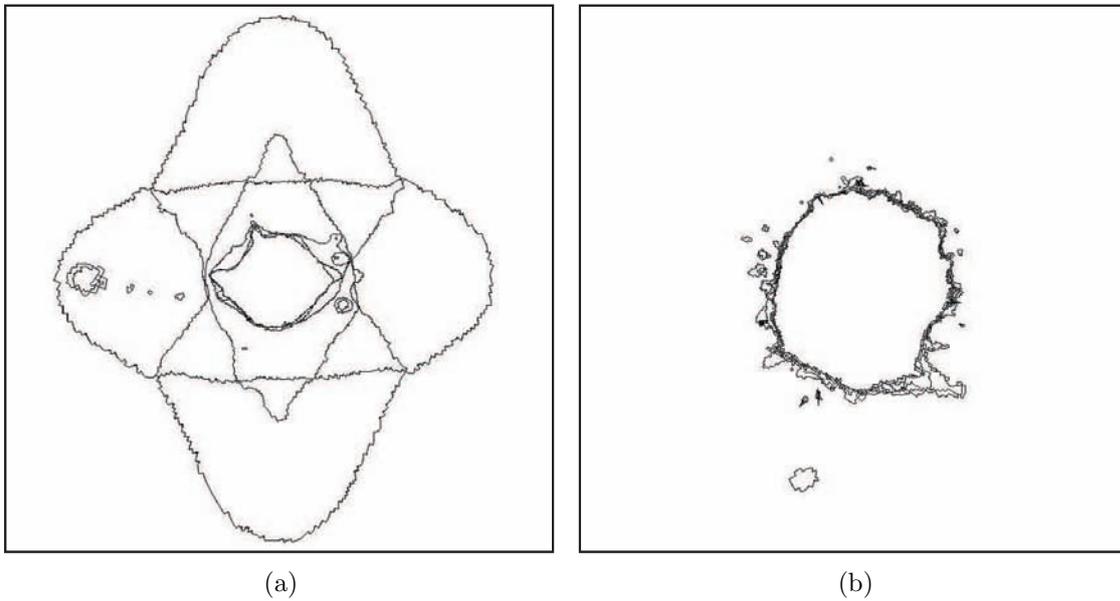
Figure 7.36: Total projected delaminated area in specimens impacted on the carbon face at 360 m/s (a) without z-yarns and with z-yarns (b).

7.4   Concluding remarks

The hybrid 3D woven composite exhibited higher energy absorption capability when damage was less localized and bending had a greater influence on the response of the laminate. This explains not only the effect of hybridization, but also the higher energy absorption capability of the material at low velocity. Bending implies tensile failure rather than shear, which releases more energy and involves a higher number of fibers contributing to dissipate energy.

Low velocity and high velocity impacts can be successfully simulated by using a mesomechanical approach in which each ply is modeled with solid elements. However, this approach does not properly capture the local bending that takes place during ballistic impacts. This problem can be overcome by adding truss and cohesive elements within the framework of an embedded element technique, which enables also to account for the influence of the z-yarns.

CHAPTER 8

Conclusions and Future work

8.1 Conclusions

The purpose of this dissertation was to analyze the role of hybridization and the presence of the z-yarns on the mechanical response of FRPs under quasi-static and impact loading. To this end, experimental tests, numerical simulations, analytical models and an extensive damage inspection campaign were carried out. The main conclusions can be summarized as follows:

- Hybrid 3D woven composites exhibit a very ductile behavior, high energy absorption capability, notch-insensitiveness as well as an outstanding damage tolerance compared to conventional unidirectional laminates. This is due to the complex architecture of the material, which enhances energy dissipation during deformation by means of the activation of multiple failure mechanisms.

- The in-plane tensile and compressive properties of the composite are poorer than those of unidirectional laminates, due to the crimping and the stress concentrations induced by the z-yarns.

- Z-yarns enhance the load-bearing capability after the peak load because they hold layers together and ensure a load transfer between broken and unbroken yarns.

175

- The impact response of the hybrid 3D woven composite depends upon the orientation; the composite presents a higher energy absorption capability and ballistic limit when the load is applied on the carbon face and glass fibers are located at the rear surface. This is due to the higher failure strain of the glass fibers.

- Damage inspection and numerical simulations revealed that bending is a major source of energy absorption during impact. Global bending and local bending were observed in low velocity and high velocity impact tests, respectively.

- Despite of the complexity of the 3D preform and the multiple failure mechanisms involved during the damage process, the mechanical response of the 3D orthogonal woven composites can be modeled using the same strategy used for unidirectional laminates, by accounting for the knock-down factors in the in-plane properties and considering a higher fracture toughness. The mechanical response of the material is still controlled by the stiffness, the strength and the fracture toughness of the plies.

- A new modeling strategy has been developed to simulate the mechanical response of 3D woven orthogonal composites. Intraply damage is formulated within the framework of continuum damage mechanics, whereas cohesive elements are combined with the embedded element technique to account for the interply damage. The procedure is relatively simple, computationally efficient and reproduces reasonably well the impact tests, though it is quite sensitive to the eroding criteria.

8.2 Future work

- This thesis studies the mechanical behavior of a hybrid 3D woven composite under multiple loading cases. However, intraply and interlaminar fracture toughness could not be measured experimentally. These material properties would provide critical information to feed numerical and analytical models.

- The role played by the z-yarns on the mechanical behavior of this composite material was mainly inferred from the analysis of the failure mechanisms. A direct comparison between specimens with and without z-yarns was only established in the case of short-beam tests. This comparison could be further extended to those cases in which the z-yarns are particularly critical, such as impact or compression after impact tests.

- The strain-rate effects were neglected in the numerical models. However, the mechanical response of the material during ballistic impacts can be rate-dependent, so simulations would be more realistic if this effect was included in the constitutive model.

- Numerical tools are particulary useful for design purposes. Since the numerical model of the hybrid 3D woven composite has already been validated, it can be used to optimize other parameters, such as layer thickness, stacking sequence, fiber properties and fiber content.

Appendix A

Laminate Properties

The elastic constants of the carbon and the glass plies can be estimated from the elastic constants and the volume fractions of the constituents according to C.C.Chamis (1984):

$$
\begin{aligned}
E_1 &= V_f E_{f1} + (1 - V_f) E_m \\
E_2 &= \frac{E_m}{1 - \sqrt{V_f}\,(1 - E_m/E_{f2})} \\
G_{12} &= \frac{G_m}{1 - \sqrt{V_f}\,(1 - G_m/G_f)} \\
\nu_{12} &= V_f \nu_f + (1 - V_f) \nu_m
\end{aligned}
\tag{A.1}
$$

where E and G stand for the elastic and the shear moduli, respectively, and ν for the Poisson's ratio. The subindexes f and m refer to fiber and matrix, whereas 1 and 2 refer to the longitudinal and transverse directions with respect to the fiber axis, respectively (Figure A.1). The elastic constants of the constituents (Table A.1) were obtained from multiple sources, namely AS4C Hextow and Agy S2-glass data sheets, Tsai & Daniel (1999), Bogdanovich *et al.* (2009) and Gay *et al.* (2003), whereas the global volume fraction ($V_f = 0.47$) was calculated from the areal density of the dry preform and the corresponding composite. The properties of the hybrid layer were calculated by weighting the properties of the glass and carbon fibers based on the carbon / glass ratio (63 /37).
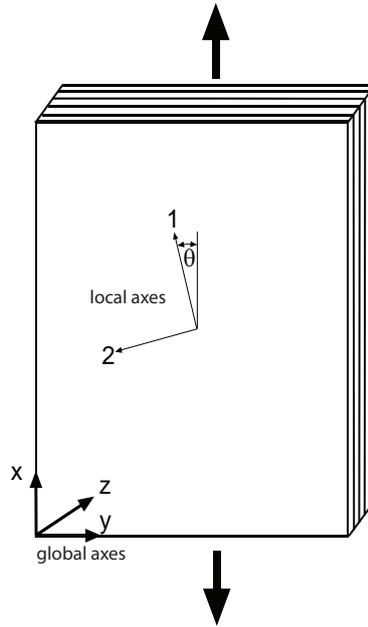
Figure A.1: Schematic ply and laminate orientation. $\theta = 0°$ for the warp yarns and $\theta = 90°$ for the fill yarns.

Table A.1: Fiber and matrix properties.

	Elastic Moduli		Shear Modulus	Poisson's ratio
	E_{f1}(GPa)	E_{f2}(GPa)	G_{f1}, G_m(GPa)	ν_{f1}, ν_m
Glass fiber	86.9	86.9	17.0	0.25
Carbon fiber	231.0	8.0	27.3	0.30
Matrix	2.9	2.9	1.1	0.35

Table A.2: Ply elastic properties (Chamis' rule, C.C.Chamis (1984))

	Elastic Moduli (GPa)			Poisson's ratio		Shear Moduli (GPa)	
	E_1	E_2	E_3	ν_{12}	$\nu_{13} = \nu_{23}$	G_{12}	$G_{13} = G_{23}$
Glass layers	42.3	8.6	7.5	0.31	0.41	3.8	1.91
Carbon layers	110.1	5.2	7.5	0.32	0.42	4.2	1.95
Hybrid layer	85.1	6.4	7.5	0.32	0.42	4.1	1.93

The resulting elastic constants of the ply constants are presented in Table A.2. These values can be used with the thickness of each ply (Table 2.1) to compute each ply stiffness matrix, as well as the A (extensional), B (coupling) and D (bending) matrices of the laminate by using the classical laminate theory.

Fill		**Warp**	

$$Q_{layer1}^{\text{glass}}(\text{GPa}) = \begin{pmatrix} 8.76 & 2.65 & 0 \\ 2.65 & 43.20 & 0 \\ 0 & 0 & 1.91 \end{pmatrix} \qquad Q_{layer2}^{\text{glass}}(\text{GPa}) = \begin{pmatrix} 43.20 & 2.65 & 0 \\ 2.65 & 8.76 & 0 \\ 0 & 0 & 1.91 \end{pmatrix}$$

$$Q_{layer3}^{\text{glass}}(\text{GPa}) = \begin{pmatrix} 8.76 & 2.65 & 0 \\ 2.65 & 43.20 & 0 \\ 0 & 0 & 1.91 \end{pmatrix} \qquad Q_{layer4}^{\text{glass}}(\text{GPa}) = \begin{pmatrix} 43.20 & 2.65 & 0 \\ 2.65 & 8.76 & 0 \\ 0 & 0 & 1.91 \end{pmatrix}$$

$$Q_{layer5}^{\text{carbon/glass}}(\text{GPa}) = \begin{pmatrix} 6.48 & 2.06 & 0 \\ 2.06 & 85.74 & 0 \\ 0 & 0 & 1.94 \end{pmatrix} \qquad Q_{layer6}^{\text{carbon}}(\text{GPa}) = \begin{pmatrix} 110.70 & 1.69 & 0 \\ 1.69 & 5.18 & 0 \\ 0 & 0 & 1.95 \end{pmatrix}$$

$$Q_{layer7}^{\text{carbon}}(\text{GPa}) = \begin{pmatrix} 5.18 & 1.69 & 0 \\ 1.69 & 110.70 & 0 \\ 0 & 0 & 1.95 \end{pmatrix}$$

Laminate matrices

$$A(\text{Pa} \cdot \text{m}) = \begin{pmatrix} 1.24 \cdot 10^8 & 9.28 \cdot 10^6 & 0 \\ 9.28 \cdot 10^6 & 1.75 \cdot 10^8 & 0 \\ 0 & 0 & 7.74 \cdot 10^7 \end{pmatrix} \qquad B(\text{Pa} \cdot \text{m}^2) = \begin{pmatrix} 28563 & -1746 & 0 \\ -1746 & 87373 & 0 \\ 0 & 0 & 70.67 \end{pmatrix}$$

$$D(\text{Pa} \cdot \text{m}^3) = \begin{pmatrix} 141.631 & 11.826 & 0 \\ 11.826 & 304.169 & 0 \\ 0 & 0 & 10.418 \end{pmatrix}$$

Finite Fracture Mechanics Model

This appendix describes the procedure for calculating the critical stress intensity factor $\mathcal{K}_{\mathcal{I}c}$ as well as the critical energy release rate G_c of the laminate from the ply properties, and notched and unnotched strengths. More details can be found in Camanho *et al.* (2012).

The application of the Finite Fracture Model requires solving the following set of equations:

$$\begin{cases} \frac{1}{l} \int_R^{R+l} \sigma_y(x,0)dx = X_T^L \\ \frac{1}{l} \int_R^{R+l} \mathcal{K}_I^2(a)da = \mathcal{K}_{Ic}^2 \end{cases} \tag{B.1}$$

where the stress intensity factor $\mathcal{K}_I$ can be expressed as a function of the length of the crack a, the remote stress σ^∞ and two geometrical factors F_h and F_w, according to:

$$\mathcal{K}_\mathcal{I} = \sigma^\infty F_h F_w \sqrt{\pi a} \tag{B.2}$$

with

$$F_h = \sqrt{1 - \frac{R}{d} f_n}, \quad F_w = \sqrt{\sec\left(\frac{\pi R}{W}\right) \sec\left(\frac{\pi a}{W}\right)} \tag{B.3}$$

and

$$f_n = 1 + 0.358\lambda + 1.425\lambda^2 - 1.578\lambda^3 + 2.156\lambda^4 \quad \text{and} \quad \lambda = \frac{R}{a} \tag{B.4}$$

The stress distribution along the x-axis at the center of the plate $\sigma_y(x,0)$ can be expressed as a function of the remote stress σ^∞ and the stress concentration factor of an infinite plate K_T^∞, which in turn depends on the components A_{ij} of the extension matrix of the laminate. A geometrical correction factor R_k has to be included in the case of finite width plates. Thus

$$\sigma_y(x,0) = R_k \frac{\sigma^\infty}{2}[2 + \xi^2 + 3\xi^4 - (K_T^\infty - 3)(5\xi^6 - 7\xi^8)] \tag{B.5}$$

where

$$R_k = \frac{K_T}{K_T^\infty} = \left\{ \frac{3(1 - 2R/W)}{2 + (1 - 2R/W)^3} + \frac{1}{2}\left(M\frac{2R}{W}\right)^6 (K_T^\infty - 3)\left[1 - \left(1 - M\frac{2R}{W}\right)^2\right] \right\}^{-1} \tag{B.6}$$

and

$$M^2 = \frac{\sqrt{1 - 8\left[\frac{3(1-2R/W)}{2+(1-2R/W)^3} - 1\right]} - 1}{2(2R/W)^2} \quad \text{being} \quad \xi = \frac{R}{x} \tag{B.7}$$

Mathematical computations lead to the following non-linear equation, which can be solved numerically in l:

$$\frac{4l\pi \int_R^{R+l} (F_h F_w)^2 a\, da}{R_k^2 \left\{ \int_R^{R+l} [2 + \xi^2 + 3\xi^4 - (K_T^\infty - 3)(5\xi^6 - 7\xi^8)]dx \right\}} = \left(\frac{\mathcal{K}_{Ic}}{X_T^L}\right)^2 \tag{B.8}$$

$\mathcal{K}_{Ic}$ can be readily determined by substituting l in eq. B.1, since σ^∞ was obtained from the experiments. Once the critical stress intensity factor of the laminate is known, the FFM model can be applied again to estimate the notched strength for different hole diameters.

Finally, for modelling purposes, it is useful to calculate the critical energy release rate G_c from the critical stress intensity factor making use of the Linear Elastic Fracture Mechanics:

184

$$G_c = \frac{\mathcal{K}_{Ic}^2}{E^*} \tag{B.9}$$

where E^* is a function of the effective properties of the laminate, Erçin *et al.* (2013):

$$E^* = \frac{\sqrt{2E_y E_x}}{\sqrt{\sqrt{\frac{E_y}{E_x}} + \frac{E_y}{2G_{xy}} - \nu_{xy}}} \tag{B.10}$$

APPENDIX C

Constitutive Models

C.1 Intraply damage

C.1.1 Fundamentals of continuum damage mechanics

The constitutive model of each ply in the finite element model is formulated within the framework of Continuum Damage Mechanics (CDM) for anisotropic solids. CDM is a local approach to fracture, Doghri (2000), in which the deterioration of the material properties due to the progressive damage is introduced into the constitutive equations by an internal damage variable d

$$d = \frac{A - \bar{A}}{A} \tag{C.1}$$

where $\bar{A}$ is the actual area contributing to the load carrying capacity of the material after the onset of damage and A is the nominal area.

Continuum damage models do not account for individual cracks, but smear their effect over a region of the material by degrading the stiffness and strength of the cracked material, Canal *et al.* (2012b).

In the case of a linear and isotropic solid, the mechanical response can be expressed mathematically as a function of the scalar d as
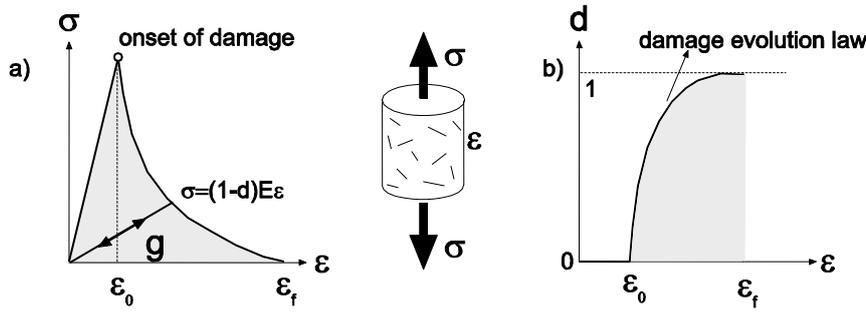
Figure C.1: a) Stress-strain curve of a material under uniaxial loading according to Continuum Damage Mechanics. g is the volumetric fracture energy (energy per unite volume) which is equal to the area under the σ–ε curve. b) Evolution of the damage variable d with strain.

$$\sigma = [1 - d(\varepsilon)]E\varepsilon \tag{C.2}$$

where E is the elastic modulus of the undamaged material. The response of the material is initially elastic up to a strain $\varepsilon_0(d = 0)$ at which damage starts and complete fracture occurs at $\varepsilon_f(d = 1)$, Fig. C.1. The damage variable controls the evolution of damage and may depend on any internal variable (such as stress, strain, elastic energy, etc.), Llorca et al. (2011). The area under the stress-strain curve g is the energy spent during failure per unit of volume and can be computed by integrating the stress-strain curve along the loading path as

$$g = \int_0^{\varepsilon_f} \sigma(\varepsilon)d\varepsilon \tag{C.3}$$

This approach has been applied to simulate the intraply damage of unidirectional composites, Maimí et al. (2007a). Damage is introduced into the constitutive equations by modifying the elastic compliance matrix of the composite material with the damage tensor $d_1, d_2, d_3, d_4, d_5, d_6$[1], which controls the evolution of damage during an arbitrary loading path, eq. C.4.

---

[1]Note that in the case of isotropic materials, the damage variable d was a scalar.
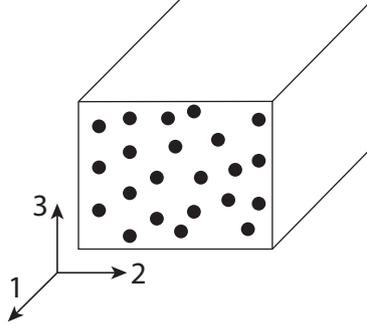
Figure C.2: *Local axis (1-2-3) in the material orientation.*

$$
\begin{bmatrix} \varepsilon_1 \\ \varepsilon_2 \\ \varepsilon_3 \\ \gamma_{13} \\ \gamma_{23} \\ \gamma_{12} \end{bmatrix} = \begin{bmatrix} \frac{1}{(1-d_1)E_1} & -\frac{\nu_{12}}{E_1} & -\frac{\nu_{13}}{E_1} & 0 & 0 & 0 \\ -\frac{\nu_{12}}{E_1} & \frac{1}{(1-d_2)E_2} & -\frac{\nu_{23}}{E_2} & 0 & 0 & 0 \\ -\frac{\nu_{13}}{E_1} & -\frac{\nu_{23}}{E_2} & \frac{1}{(1-d_3)E_3} & 0 & 0 & 0 \\ 0 & 0 & 0 & \frac{1}{(1-d_4)G_{13}} & 0 & 0 \\ 0 & 0 & 0 & 0 & \frac{1}{(1-d_5)G_{23}} & 0 \\ 0 & 0 & 0 & 0 & 0 & \frac{1}{(1-d_6)G_{12}} \end{bmatrix} \begin{bmatrix} \sigma_1 \\ \sigma_2 \\ \sigma_3 \\ \tau_{13} \\ \tau_{23} \\ \tau_{12} \end{bmatrix}
\tag{C.4}
$$

The terms E_1, E_2, E_3, ν_{12}, ν_{13}, ν_{23}, G_{12}, G_{13}, G_{23} are the nine independent elastic constants which determine the behavior of the undamaged orthotropic material in the local axis material orientation, figure C.2.

C.1.2   Computational implementation

Intralaminar damage was modeled by means of a continuum damage model based on a simple maximum stress criterion. It was implemented into Abaqus Explicit via material subroutine (VUMAT) according to the procedure described by Maimí *et al.* (2007b). The compliance matrix of the orthotropic material is modified with the damage variables d_1, d_2, d_3, d_4, d_5 and d_6, which control the evolution of damage during an arbitrary loading path. In this case, only four of them, d_1, d_2, d_3 and d_6, are considered active in the model.

Damage initiation

The maximum stress failure criterion was selected to trigger and control the damage evolution variables. Six failure functions, ϕ_{1+}, ϕ_{1-}, ϕ_{2+}, ϕ_{2-}, ϕ_6 and ϕ_{3-} are defined:

$$\text{\textit{longitudinal tension}:} \quad F_{1+} = \phi_{1+} - r_{1+} = \frac{E_1}{X_T}\varepsilon_1 - r_{1+} \tag{C.5a}$$

$$\text{\textit{longitudinal compression}:} \quad F_{1+} = \phi_{1+} - r_{1+} = \frac{E_1}{X_C}\varepsilon_1 - r_{1-} \tag{C.5b}$$

$$\text{\textit{transverse tension}:} \quad F_{1-} = \phi_{1-} - r_{1-} = \frac{E_1}{X_C}\varepsilon_1 - r_{1-} \tag{C.5c}$$

$$\text{\textit{transverse compression}:} \quad F_{2-} = \phi_{2-} - r_{2-} = \frac{E_2}{Y_C}\varepsilon_2 - r_{2-} \tag{C.5d}$$

$$\text{\textit{in-plane shear}:} \quad F_6 = \phi_6 - r_6 = \frac{|S_{12}|}{S_L} - r_6 \tag{C.5e}$$

$$\text{\textit{out-of-plane compression}:} \quad F_{3-} = \phi_{3-} - r_{3-} = \frac{|E_3|}{Z_C}\varepsilon_3 - r_{3-} \tag{C.5f}$$

where X_T is the longitudinal tensile strength; X_C the longitudinal compressive strength; Y_T the transverse tensile strength; Y_C the in-plane transverse compressive strength; Z_C the out-of-plane compressive strength and S_L the in-plane shear strength, Fig. C.3.

Damage evolution

The damage thresholds r_{1+}, r_{1-}, r_{2+}, r_{2-}, r_6 and r_{3-} are the internal variables which define the level of elastic strains that can be attained before the accumulation of additional damage, Maimí *et al.* (2008). They dictate the evolution of the damage surfaces ϕ_{1+}, ϕ_{1-}, ϕ_{2+}, ϕ_{2-}, ϕ_6 and ϕ_{3-} and can be determined at any material point through the consistency condition:

$$\dot{F}_M = \dot{\phi}_M - \dot{r}_M = 0 \tag{C.6}$$

Equation C.6 means that if damage occurs during a time interval, the solution should always remain on the damaged surface during all the time, Doghri (2000). The algorithm
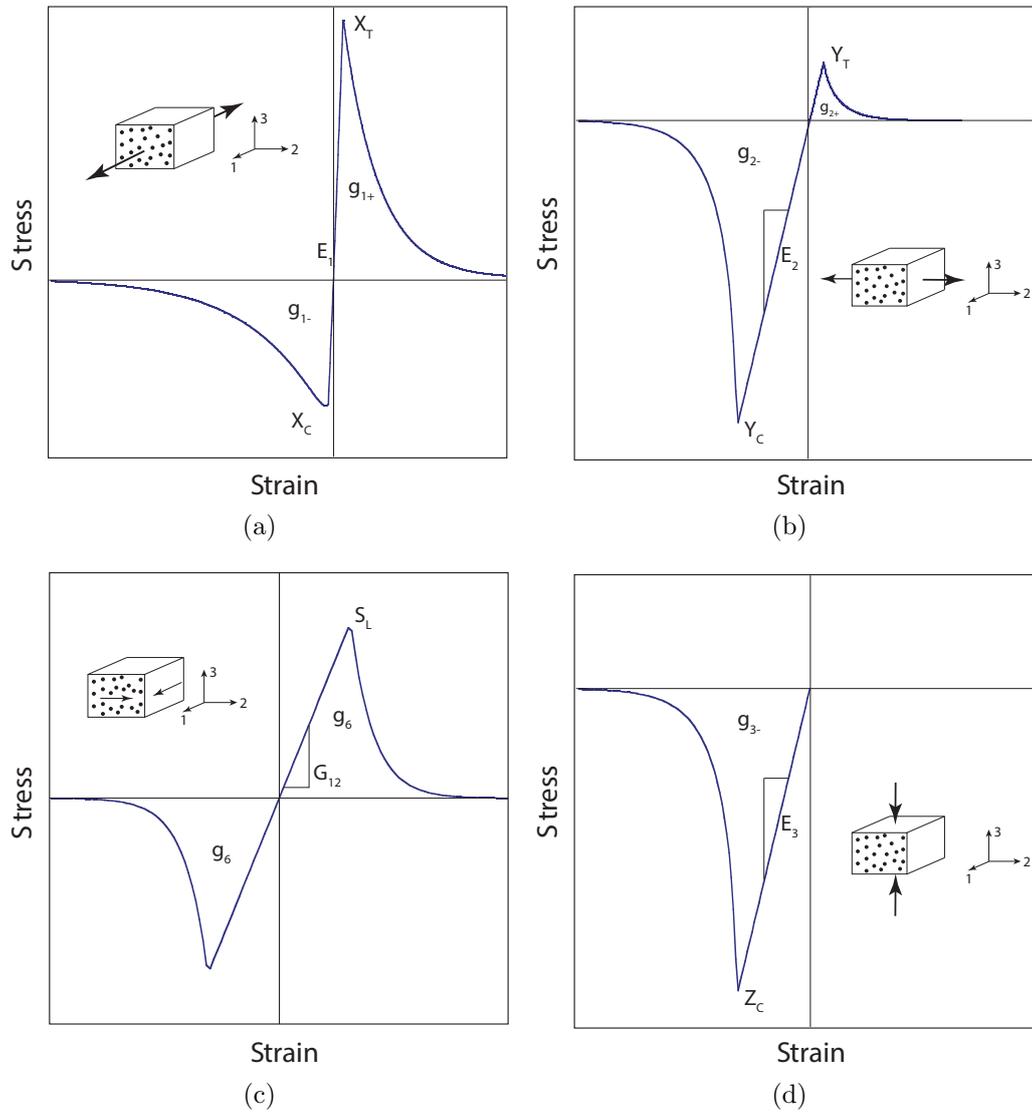
Figure C.3: Stress-strain curves in the (a) longitudinal direction, (b) transverse direction, (c) in-plane shear and (d) out-of-plane directions. The stiffness, strength and fracture energy is indicated for each case.
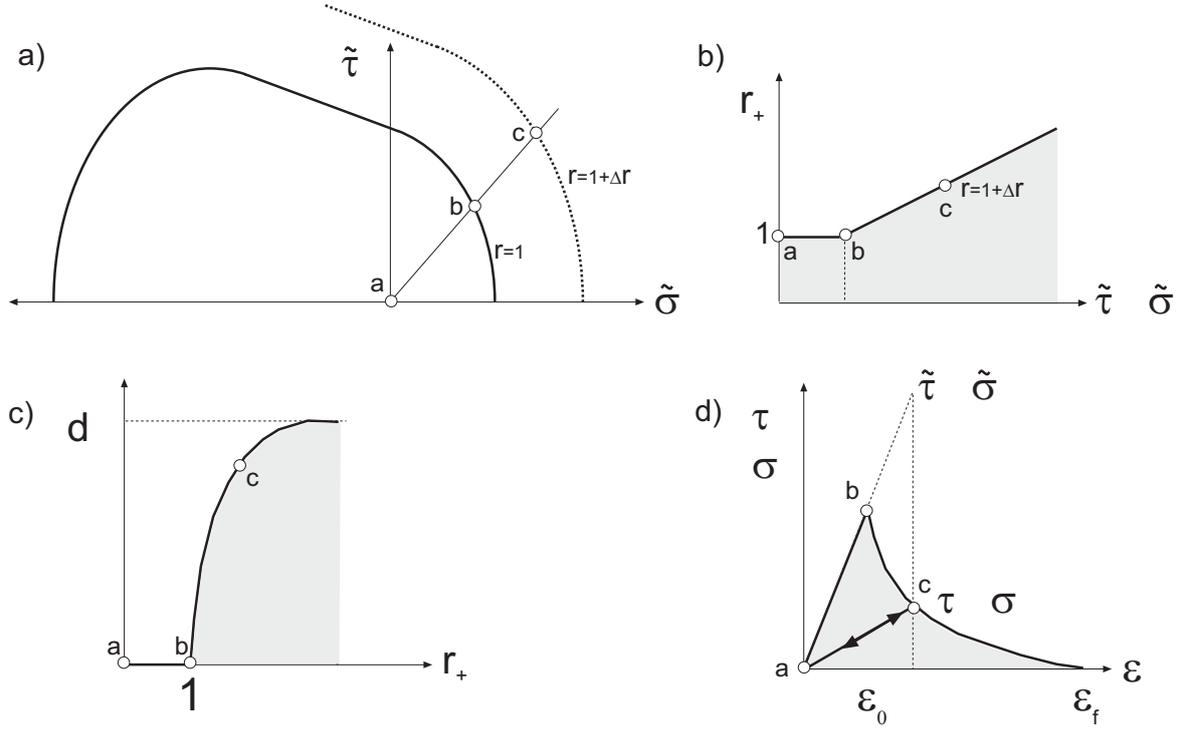
Figure C.4: Determination of the damage evolution. Points a, b and c represent the initial zero load point, the onset of failure and one damaged state, respectively. a) The load increases up to the onset of failure at the point b. Additional strain increments lead to larger nominal stresses (computed using the undamaged state). b) Increments of the damage thresholds are computed from equations C.5. c) Increments of the damage thresholds are used to compute the damage variables from equations C.8. Finally, the updated damage variables are used to compute the effective stresses according to the constitutive equation in the damaged state, equation C.4.

is illustrated in Fig. C.4. Mathematically, the evolution of the threshold values r_M is expressed by the Kuhn-Tucker conditions to ensure that damage variables increase monotonically, Maimí *et al.* (2007a):

$$\dot{r}_M \geq 0, \quad F_M \leq 0, \quad \dot{r}_M F_M = 0 \tag{C.7}$$

The damage thresholds r_M are set to 1 when no damage is present in the material.

Crack band model

The maximum values of the damage thresholds of the failure functions under tensile and compressive loads are stored to be used in tensile modes to take into account the effect of previous damage in compression. Then, the damage variables can be computed as functions of the damage thresholds:

$$d_M = 1 - \frac{1}{r_M} exp\left[A_M\left(1 - r_M\right)\right] \tag{C.8}$$

where M represents the damage mechanisms (1+, 1-, 2+, 2-, 6 and 3-). The coefficients A_{1+}, A_{1-}, A_{2+}, A_{2-}, A_6 and A_{3-} are softening parameters used to ensure mesh objectivity of the model. This method, known as the crack band model, allows the regularization of the finite element problem and the alleviation of mesh dependency problems commonly observed in continuum models with softening, Bažant & Oh (1983). They are obtained from the definition of the volumetric fracture energy g_M and the fracture toughness of the composite material G_M under the different failure modes according to

$$g_M = \frac{G_M}{l_{ch}} \tag{C.9}$$

$$A_M = \frac{2l_{ch}X_M^2}{2E_M G_M - l_{ch}X_M^2}$$

where l_{ch} is the characteristic length of the finite element used in the simulations.

C.2 Interply damage

The progressive interface fracture upon loading can be taken into account through the cohesive crack model at the interface between dissimilar materials (Figure C.5), Segurado & LLorca (2004). This approach assumes a cohesive constitutive equation based on a traction-separation law for the interface damage which relates the displacement jump δ across the interface with the traction vector t acting on it:
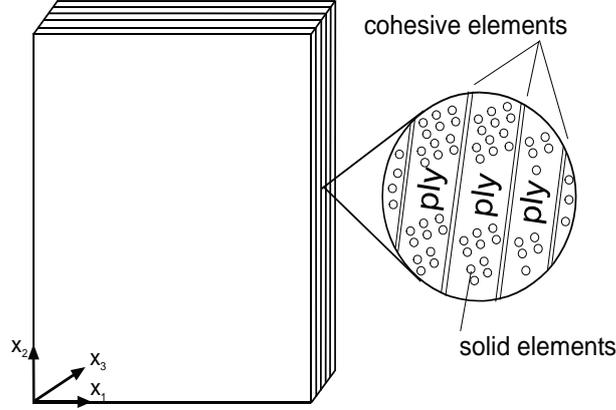
Figure C.5: Schematic laminate with cohesive elements inserted between plies.

$$t_i = K\delta_i, \quad i = n, s, t \tag{C.10}$$

where n stands for the normal direction and s, t for the two shear directions. K is the penalty stiffness, which should be large enough to ensure a stiff connection between two neighboring layers before delamination initiation, Turon *et al.* (2007), but not excessively high to avoid numerical problems. In this case, K was calculated according to the procedure suggested by Turon *et al.* (2007) as

$$K_1 = \frac{E_2}{e_{\text{cohesive}}}, \quad \text{and} \quad K_2 = K_3 = \frac{G_{12}}{e_{\text{cohesive}}} \tag{C.11}$$

A stress based damage initiation is considered, following a quadratic interaction criteria between normal and shear stresses acting on the interface:

$$\left(\frac{t_n}{N}\right)^2 + \left(\frac{t_s}{S}\right)^2 + \left(\frac{t_t}{S}\right)^2 = 1 \tag{C.12}$$

where t_n, t_s and t_t are the normal and shear elastic stresses acting on the interface, and N and S the normal and shear strengths.

The interface strength parameters have been set to $N = Y_T$ and $S = S_{12}$ as reasonable values in the absence of more detailed measurements. This approach sets the strength of
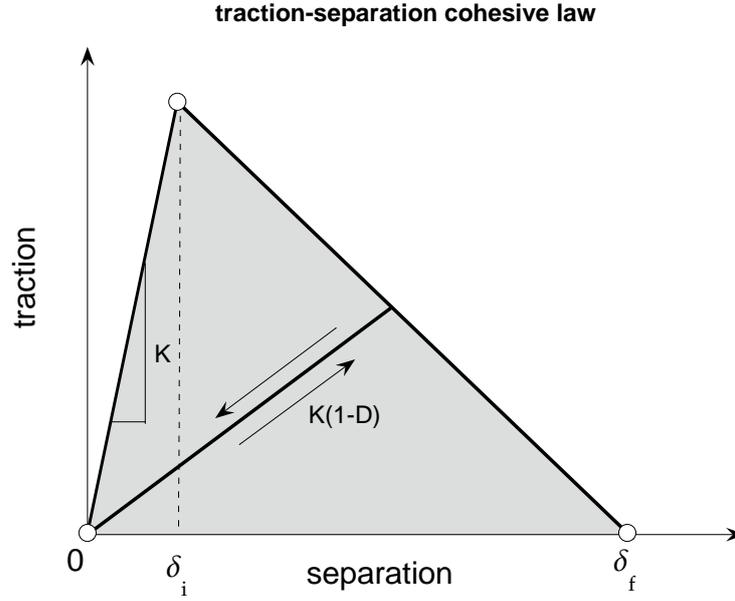
Figure C.6: Cohesive constitutive law

the interface at the same level of the strength of the ply material and can be considered an upper bound of the interface resistance. Once the stress failure criterion is fulfilled, the damage evolves depending on the mix mode ratio and the fracture energy of the interface according to expression suggested by Benzeggagh & Kenane (1996):

$$
G_{Ic} + (G_{IIc} - G_{Ic}) \left\{ \frac{G_{IIc}}{G_I + G_{II}} \right\}^{\eta} = G_C \tag{C.13}
$$

where G_I and G_{II} are the energy release rates in modes I and II, respectively; G_{Ic} and G_{IIc} the interface toughnesses, and η corresponds to the BK parameter controlling the interface mix mode behaviour, Table 7.6. This parameter should be fitted to experimental data of fracture toughness measurements under different mixed mode ratios, but typical values for carbon/epoxy composites range from 1.5 to 2.3 depending on the ductility of the matrix, Benzeggagh & Kenane (1996). It should be noticed that in this cohesive model, the energy necessary to create new free surfaces corresponds to the area under the traction-separation curve, Figure C.6.

C.3   Z-yarns

The mechanical behavior of the z-yarns was simulated using a constitutive model available in Abaqus Explicit. The model, named Brittle Cracking, is aimed to applications in which the behavior is dominated by tensile cracking and captures the effect of cracking and damage on stresses and stiffness. A length scale, typically in the form of a characteristic length, is introduced to regularize the smeared continuum models and attenuate the sensitivity of the results to mesh density, Simulia (2010).

The initial response of the undamaged material is modeled as isotropic and linear elastic up to the onset of cracking, which takes place when the maximum principal stress exceeds the material tensile strength. The damaged material becomes orthotropic, with cracks normal to the maximum principal stress, and follows a softening law.

The model is mathematically formulated by a set of equations expressed in rate form in which the total mechanical strain rate $d\varepsilon$ is decomposed into an elastic component corresponding to the undamaged state $d\varepsilon^{\mathrm{el}}$, and the cracking strain rate $d\varepsilon^{\mathrm{ck}}$:

$$d\varepsilon = d\varepsilon^{\mathrm{el}} + d\varepsilon^{\mathrm{ck}} \tag{C.14}$$

The global strain vector ε_i is written in a local coordinate system aligned with the crack directions by using the transformation matrix T:

$$\{\varepsilon\} = [T]\{e\}$$

where e_i is the local strain vector.

Likewise, the transformation between local t and global σ stresses reads

$$\{t\} = [T]^T\{\sigma\}$$

The relation between the local stresses and the cracking strains at the crack interfaces is written as

$$dt = D^{\mathrm{ck}}de^{\mathrm{ck}}$$

where D^{ck} is a cracking matrix that depends on the state of the existing cracks.

The rate of stress in global coordinates can be expressed as a function of the total strain and the cracking strain as

$$d\sigma = D^{\text{el}}(d\varepsilon - Tde^{\text{ck}})$$

where D^{el} is the isotropic linear elasticity matrix.

Operating, the cracking strain de^{ck} expressed in local coordinates reads

$$de^{\text{ck}} = (D^{\text{ck}} + T^T D^{\text{el}} T)^{-1} T^T D^{\text{el}} d\varepsilon$$

Finally, the rate constitutive equations are expressed as

$$d\sigma = [D^{\text{el}} - D^{\text{el}} T (D^{\text{ck}} + T^T D^{\text{el}} T)^{-1} T^T D^{\text{el}}] d\varepsilon$$

where σ and ε are the stress and strain expressed in global coordinates; D^{el} and D^{ck} stand for the isotropic linear elasticity matrix and the cracking matrix that depends on the state of the existing cracks.

The postcracked behavior is calculated from the tensile stress and the corresponding crack opening displacement:

$$G_f^I = \int \sigma_t^I du_n$$

Bibliography

ABRATE S. (1998). *Impact on Composite Structures*. Cambridge University Press.

AITM 1-0008 (2004). Determination of plain, open hole, filled hole compression strength. Airbus Test Method.

ANDERSON JR. C., WILBECK J., WESTINE P., LINDHOLM U. & WENZEL A. (2003). *A Short Course on Penetration Mechanics*. Southwest Research Institute, San Antonio, US.

ARTEIRO A., CATALANOTTI G., XAVIER J. & CAMANHO P. (2013a). Notched response of non-crimp fabric thin-ply laminates. *Composites Science and Technology*, **79**, 97–114.

ARTEIRO A., CATALANOTTI G., XAVIER J. & CAMANHO P. (2013b). Notched response of non-crimp fabric thin-ply laminates: Analysis methods. *Composites Science and Technology*, **88**, 165–171.

ASHBY M.F. (2005). *Materials selection in mechanical design*. Elsevier.

ASTM 3410 (1995). Standard Test Method for Compressive Properties of Polymer Matrix Composite Materials with Unsupported Gage Section by Shear Loading.

ASTM D2344/D2344M (1999). Standard test method for short-beam strength of polymer matrix composite materials and their laminates.

ASTM D3039 (2000). Standard Test Method for Tensile Properties of Polymer Matrix Composite Materials.

ASTM D3518 (2001). Standard Test Method for In-Plane Shear Response of Polymer Matrix Composite Materials by Tensile Test of a $\pm 45°$ Laminate.

ASTM D4018 (1999). Standard Test Methods for Properties of Continuous Filament Carbon and Graphite Fiber Tows.

ASTM D5379 (2001). Standard test method for in-plane shear properties of composite materials by the V-notched beam method.

ASTM D5766 (1995). Standard Test Method for open-hole Tensile Strength of Polymer Matrix Composite Laminates.

ASTM D7078 (1995). Standard test method for shear properties of composite materials by the V-notched rail shear method.

ASTM D7136/D7136M (1995). Standard Test Method for Measuring the Damage Resistance of a Fiber-Reinforced Polymer Matrix Composite to a Drop-Weight Impact Event.

ASTM D7137/D7137M (2005). Standard Test Method for Compressive Residual Strength Properties of Damaged Polymer Matrix Composite Plates.

AVESTON J. & KELLY A. (2013). First Cracking Strain and Strength of Hybrid Composites and Laminates. *Philosofical Transactions of the Royal Society of London. Series A, Mathematical and Physical Sciences*, **294**, 519–534.

BARBERO E., LONETTI P. & SIKKIL K. (2005a). Finite element continuum damage modeling of plain weave reinforced composites. *Composites Part B: Engineering*, **37**, 137–147.

BARBERO E.J., DAMIANI T.M. & TROVILLION J. (2005b). Micromechanics of fabric reinforced composites with periodic microstructure. *International Journal of Solids and Structures*, **42**, 2489–2504.

BAŽANT P.J., Z P (1998). *Fracture and size effect in concrete and other quasibrittle materials*. CRC Press.

BAŽANT Z. & OH B. (1983). Crack band theory for fracture of concrete. *Materials and Structures*, **16**, 155–177.

BENZEGGAGH M.L. & KENANE M. (1996). Measurement of mixed-mode delamination fracture toughness of unidirectional glass/epoxy composites with mixed-mode bending apparatus. *Composites Science and Technology*, **56**, 439–449.

Bibo G.A., Hogg I.J. & Kempb M. (1997). Mechanical characterisation of glass- and carbon-fiber-reinforced composites made with non-crimp fabrics. *Composites Science and Technology*, **3538**, 1221–1241.

Bogdanovich A.E. (2007). Advancements in manufacturing and applications of 3D woven preforms and composites. In *Proceedings of 16th International Conference on Composite Materials*, Kyoto, Japan.

Bogdanovich A.E., Mungalov D., Lomov S.V., Ivanov D.S. & Verpoest I. (2009). A combined theoretical and experimental study of progressive failure of non-crimp 3D orthogonal weave composite. In *Proceedings of 17th International Conference on Composite Materials*.

Bogdanovich A.E., Karahan M., Lomov S.V. & Verpoest I. (2013). Quasi-static tensile behavior and damage of carbon/epoxy composite reinforced with 3D non-crimp orthogonal woven fabric. *Composites Science and Technology*, **62**, 14–31.

Böhm R., Gude M. & Hufenbach W. (2011). A phenomenologically based damage model for 2D and 3D-textile composites with non-crimp reinforcement. *Materials and Design*, **32**, 2532–2544.

Buchanan S., Grigorash A., Archer E., McIlhagger A., Quinn J. & Stewart G. (2010). Analytical elastic stiffness model for 3D woven orthogonal interlock composites. *Composites Science and Technology*, **70**, 1597–1604.

Budiansky B. & Fleck N.A. (1993). Compressive failure of fibre composites. *Journal of the Mechanics and Physics of Solids*, **41**, 183–211.

Camanho P. & Catalanotti G. (2011). On the relation between the mode I fracture toughness of a composite laminate and that of a 0° ply: Analytical model and experimental validation. *Engineering Fracture Mechanics*, **78**, 2535–2546.

Camanho P., Erçin G., Catalanotti G., Mahdi S. & Linde P. (2012). A finite fracture mechanics model for the prediction of the open-hole strength of composite laminates. *Composites Part A: Applied Science and Manufacturing*, **43**, 1219–1225.

Canal L.P., González C., Molina-Aldareguía J., Segurado J. & LLorca J. (2012a). Application of digital image correlation at the microscale in fiber-reinforced composites. *Composites Part A: Applied Science and Manufacturing*, **43**, 1630 – 1638.

Canal L.P., González C., Segurado J. & LLorca J. (2012b). Intraply fracture of fiber-reinforced composites: Microscopic mechanisms and modeling. *Composites Science and Technology*, **72**, 1223 – 1232.

Carrara P., Ferretti D., Freddi F. & Rosati G. (2011). Shear tests of carbon fiber plates bonded to concrete with control of snap-back. *Engineering Fracture Mechanics*, **78**, 2663–2678.

Carvelli V., Pazmino J., Lomov S.V. & Verpoest I. (2012). Deformability of a non-crimp 3D orthogonal weave E-glass composite reinforcement. *Composites Science and Technology*, **73**, 9–18.

C.C.Chamis (1984). Simplified Composite Micromechanical Equations for Strength, Fracture Toughness, Impact Resistance and Environmental Effects. Tech. rep., Lewis Research Center, Cleveland.

Chang P., a.P. Mouritz & Cox B. (2006). Properties and failure mechanisms of z-pinned laminates in monotonic and cyclic tension. *Composites Part A: Applied Science and Manufacturing*, **37**, 1501–1513.

Courant R., Friedrichs K. & Lewy H. (1967). On the partial difference equations of mathematical physics. *IBM Journal*, **100**, 32–74.

Cox B.N. (1996). On the tensile composites failure of 3D woven. *Composites Part A*, **27A**, 447–458.

Cox B.N., Carter W.C. & Fleck N.A. (1994a). A binary model of textile composites-I. Formulation. *Acta Metallurgica et Materialia*, **42**, 3463–3479.

Cox B.N., Dadkhah M.S., Morris W.L. & Flintoff J.G. (1994b). Failure mechanisms of 3D woven composites in tension, compression, and bending. *Acta Metallurgica et Materialia*, **42**, 3967–3984.

DAI G. & JR L.M. (2014). Fatigue of hybrid glass / carbon composites: 3D computational studies. *Composites Science andD Technology*, **94**, 71–79.

DAVIES G.A.O., ZHANG X., ZHOU G. & WATSON S. (1994). Numerical modelling of impact damage. *Composites*, **25**, 342–350.

DÁVILA C.G., CAMANHO P.P. & ROSE C.A. (2005). Failure Criteria for FRP Laminates. *Journal of Composite Materials*, **39**, 323–345.

DESPLENTERE F., LOMOV S.V., WOERDEMAN D.L., VERPOEST I., WEVERS M. & BOGDANOVICH A. (2005). Micro-CT characterization of variability in 3D textile architecture. *Composites Science and Technology*, **65**, 1920–1930.

DOGHRI I. (2000). *Mechanics of deformable solids. Linear and nonlinear, analytical and computational aspects*. Springer, Berlin.

DONG C., RANAWEERA-JAYAWARDENA H.A. & DAVIES I.J. (2012). Flexural properties of hybrid composites reinforced by S-2 glass and T700S carbon fibres. *Composites Part B: Engineering*, **43**, 573–581.

DRACH A., DRACH B. & TSUKROV I. (2014). Advances in Engineering Software Processing of fiber architecture data for finite element modeling of 3D woven composites. *Advances in Engineering Software*, **72**, 18–27.

DUGDALE D. (1960). Yielding of steel sheets containing slits. *Journal of the Mechanics and Physics of Solids*, **8**, 100–104.

EDGREN F., SOUTIS C. & ASP L.E. (2008). Damage tolerance analysis of NCF composite sandwich panels. *Composites Science and Technology*, **68**, 2635–2645.

ENFEDAQUE A., MOLINA-ALDAREGUÍA J.M., GÁLVEZ F., GONZÁLEZ C. & LLORCA J. (2010). Effect of Glass Fiber Hybridization on the Behavior Under Impact of Woven Carbon Fiber/Epoxy Laminates. *Journal of Composite Materials*, **44**, 3051–3068.

ERÇIN G., CAMANHO P., XAVIER J., CATALANOTTI G., MAHDI S. & LINDE P. (2013). Size effects on the tensile and compressive failure of notched composite laminates. *Composite Structures*, **96**, 736–744.

Ferreira L.M., Graciani E. & París F. (2014). Modelling the waviness of the fibres in non-crimp fabric composites using 3D finite element models with straight tows. *Composite Structures*, **107**, 79–87.

Fleck N.A. (1997). Compressive Failure of Fiber Composites. *Advances in applied mechanics*, **33**, 43–117.

Gama B.A. & Gillespie J.W. (2011). Finite element modeling of impact, damage evolution and penetration of thick-section composites. *International Journal of Impact Engineering*, **38**, 181–197.

Gay D., Hoa S.V. & Tsai S.W. (2003). *Composite Materials, Design and Applications*. CRC Press.

Gerlach R., Siviour C.R., Wiegand J. & Petrinic N. (2012). In-plane and through-thickness properties, failure modes, damage and delamination in 3D woven carbon fibre composites subjected to impact loading. *Composites Science and Technology*, **72**, 397–411.

González E.V., Maimí P., Camanho P.P., Lopes C.S. & Blanco N. (2011). Effects of ply clustering in laminated composite plates under low-velocity impact loading. *Composites Science and Technology*, **71**, 805–817.

González E.V., Maimí P., Aja J.R.S.D., Cruz P. & Camanho P.P. (2014). Effects of interply hybridization on the damage resistance and tolerance of composite laminates. **108**, 319–331.

Grogan J., Tekalur S.A., Shukla A., Bogdanovich A. & Coffelt R.A. (2007). Ballistic resistance of 2D and 3D woven sandwich composites. *Journal of Sandwich Structures and Materials*, **9**, 283–302.

Gu B., Luo Y., Qiu Y., Lv L. & Sun B. (2007). Transverse impact behavior and energy absorption of three-dimensional orthogonal hybrid woven composites. *Composite Structures*, **81**, 202–209.

Gu H. & Zhili Z. (2002). Tensile behavior of 3D woven composites by using different fabric structures. *Materials and Design*, **23**, 671–674.

HANOMSILP C. & HOGG P.J. (2003). Penetration impact resistance of hybrid composites based on commingled yarn fabrics. *Composites Science and Technology*, **63**, 467–482.

HAQUE M.H., UPADHYAYA P., ROY S., WARE T., VOIT W. & LU H. (2014). The changes in flexural properties and microstructures of carbon fiber bismaleimide composite after exposure to a high temperature. *Composite Structure*, **108**, 57–64.

HERMAN G. (1980). *Reconstruction from projections: The fundamentals of computerized tomography*. Academic, New York.

HERNÁNDEZ S., SKET F., GONZÁLEZ C. & LLORCA J. (2013). Optimization of curing cycle in carbon fiber-reinforced laminates: Void distribution and mechanical properties. *Composites Science and Technology*, **85**, 73–82.

HODGE A., NETTLES A. & JACKSON J. (2011). Comparison of Open-Hole Compression Strength and Compression After Impact Strength on Carbon Fiber/Epoxy Laminates for the Ares I Composite. *NASA/TM-2011-216460*.

HOSUR M., ADBULAH M. & JEELANI S. (2005). Studies of the low-velocity impact response of woven hybrid composites. *Composites and Structures*, **67**, 253–262.

HOU J. (2008). *3-D fibrous assemblies*. CRC Press.

IRVING P.E. & CARTIE D.D.R. (2002). Effect of resin and fibre properties on impact and compression after impact performance of CFRP. *Composites Part A: Applied Science and Manufacturing*, **33**, 483–493.

IVANOV D.S., LOMOV S.V., BOGDANOVICH A.E., KARAHAN M. & VERPOEST I. (2009). A comparative study of tensile properties of non-crimp 3D orthogonal weave and multi-layer plain weave E-glass composites. Part 2: Comprehensive experimental results. *Composites Part A: Applied Science and Manufacturing*, **40**, 1144–1157.

JELF P.M. & FLECK N.A. (1992). Compression Failure Mechanisms in Unidirectional Composites. *Journal of Composite Materials*, **26**, 2706–2726.

JIANG W.G. (2013). Implementation of domain superposition technique for the nonlinear analysis of composite materials. *Journal of Composite Materials*, **47**, 243–249.

JOHNSON A.F. & DAVID M. (2010). Failure mechanisms in energy-absorbing composite structures. *Philosophical Magazine*, **90**, 4245–4261.

JR L.M. & DAI G. (2013). Hybrid carbon / glass fiber composites: Micromechanical analysis of structure-damage resistance relationships. *Computational Materials Science*.

KAK A. & SLANEY M. (1987). *Principles of computerized tomographic imaging*. IEEE Press.

KUO W.S., KO T.H. & CHEN C.P. (2007). Effect of weaving processes on compressive behavior of 3D woven composites. *Composites Part A: Applied Science and Manufacturing*, **38**, 555–565.

LEE L., RUDOV-CLARK S., A.P MOURITZ, BANNISTER M. & HERSZBERG I. (2002). Effect of weaving damage on the tensile properties of three-dimensional woven composites. *Composite Structures*, **57**, 405–413.

LLORCA J., GONZÁLEZ C., MOLINA-ALDAREGUÍA J.M., SEGURADO J., SELTZER R., SKET F., RODRÍGUEZ M., SÁDABA S., MUÑOZ R. & CANAL L.P. (2011). Multiscale modeling of composite materials: a roadmap towards virtual testing. *Advanced materials*, **23**, 5130–47.

LOMOV S.V., BOGDANOVICH A.E., IVANOV D.S., MUNGALOV D., KARAHAN M. & VERPOEST I. (2009). A comparative study of tensile properties of non-crimp 3D orthogonal weave and multi-layer plain weave E-glass composites. Part 1: Materials, methods and principal results. *Composites Part A: Applied Science and Manufacturing*, **40**, 1134–1143.

LOPES C.S., CAMANHO P.P., GÜRDAL Z., MAIMÍ P. & GONZÁLEZ E.V. (2009a). Low-velocity impact damage on dispersed stacking sequence laminates. Part II: Numerical simulations. *Composites Science and Technology*, **69**, 937–947.

LOPES C.S., SERESTA O., COQUET Y., GÜRDAL Z., CAMANHO P.P. & THUIS B. (2009b). Low-velocity impact damage on dispersed stacking sequence laminates. Part I: Experiments. *Composites Science and Technology*, **69**, 926–936.

MAHADIK Y. & HALLETT S.R. (2010). Finite element modelling of tow geometry in 3D woven fabrics. *Composites Part A*, **41**, 1192–1200.

MAHADIK Y. & HALLETT S.R. (2011). Effect of fabric compaction and yarn waviness on 3D woven composite compressive properties. *Composites Part A: Applied Science and Manufacturing*, **42**, 1592–1600.

MAHMOOD A., WANG X. & ZHOU C. (2013). Generic stiffness model for 3D woven orthogonal hybrid composites. *Aerospace Science and Technology*, **31**, 42–52.

MAIMÍ P., CAMANHO P., MAYUGO J. & DÁVILA C. (2007a). A continuum damage model for composite laminates: Part I - Constitutive model. *Mechanics of Materials*, **39**, 897–908.

MAIMÍ P., CAMANHO P., MAYUGO J. & DÁVILA C. (2007b). A continuum damage model for composite laminates: Part II - Computational implementation and validation. *Mechanics of Materials*, **39**, 909–919.

MAIMÍ P., MAYUGO J. & CAMANHO P. (2008). A Three-dimensional Damage Model for Transversely Isotropic Composite Laminates. *Journal of Composite Materials*, **42**, 2717–2745.

MANSOUR H. MOHAMED R. & MAHMOUD M. SALAMA C. (2001). High speed three-dimensional weaving method and machine. *Patent No.: US 6,315,007 B1*.

MARSTON C., GABBITAS B. & ADAMS J. (1997). Measurement of stress concentration around fibre breaks in carbon-fibre/epoxy-resin composite tows. *Composites Science and Technology*, **51**, 913–923.

MAZUMDAR S.K. (2002). *Composites Manufacturing. Materials, Product and Process Engineering*. CRC press.

MCGLOCKTON M.A., COX B.N. & MCMEEKING R.M. (2003). A Binary Model of textile composites: III high failure strain and work of fracture in 3D weaves. *Journal of the Mechanics and Physics of Solids*, **51**, 1573–1600.

MELRO A., CAMANHO P., ANDRADE PIRES F. & PINHO S. (2012). Numerical simulation of the non-linear deformation of 5-harness satin weaves. *Computational Materials Science*, **61**, 116–126.

MORTENSEN A. (2006). *Concise Encyclopedia of Composite Materials, 2nd Edition*. Elsevier.

MOURITZ A., BANNISTER M., FALZON P. & LEONG K. (1999a). Review of applications for advanced three-dimensional fibre textile composites. *Composites Part A: Applied Science and Manufacturing*, **30**, 1445–1461.

MOURITZ A.P., BAINI C. & HERSZBERG I. (1999b). Mode I interlaminar fracture toughness properties of advanced textile fibreglass composites. *Composites Part A: Applied Science and Manufacturing*, **30**, 859–870.

MUÑOZ R., DELGADO S., LÓPEZ-ROMANO B., WANG Y. & LLORCA J. (2014). Modeling Lightning Impact Thermo-Mechanical Damage on Composite Materials. *Applied Composite Materials*, **21**, 149–164.

NAIK N., RAMSIMHA R., ARYA H., PRABHU S. & SHAMARAO N. (2001). Impact response and damage tolerance characteristics of glass-carbon/epoxy hybrid composite plates. *Composites: Part B*, **32**, 565–574.

PADAKI N V D.D.L., ALAGISURAMY R (2010). *Multilyaer Woven Fabrics: Impregnation Behavior and Impact Properties*. Lambert academic publishing.

PANKOW M., SALVI A., WAAS A., YEN C. & GHIORSE S. (2011). Resistance to delamination of 3D woven textile composites evaluated using End Notch Flexure (ENF) tests: Experimental results. *Composites Part A: Applied Science and Manufacturing*, **42**, 1463–1476.

PANKOW M., WAAS A.M., YEN C.F. & GHIORSE S. (2012). Modeling the response, strength and degradation of 3D woven composites subjected to high rate loading. *Composite Structures*, **94**, 1590–1604.

PASCAULT J.P., SAUTEREAU H., VERDU J. & J W.R.J. (2002). *Thermosetting polymers*. Marcel Dekker.

PINHO S., ROBINSON P. & IANNUCCI L. (2006). Fracture toughness of the tensile and compressive fibre failure modes in laminated composites. *Composites Science and Technology*, **66**, 2069–2079.

208

Pinho S.T., Dávila C.G., Camanho P.P., Iannucci L. & Robinson P. (2005). Failure Models and Criteria for FRP Under In-Plane or Three-Dimensional Stress States Including Shear Non-Linearity. *NASA/TM-2005-213530*.

Potluri P., Hogg P., Arshad M., Jetavat D. & Jamshidi P. (2012). Influence of Fibre Architecture on Impact Damage Tolerance in 3D Woven Composites. *Applied Composite Materials*, **19**, 799–812.

Rao M., Nilakantan G., Keefe M., Powers B. & Bogetti T. (2009). Global/Local Modeling of Ballistic Impact onto Woven Fabrics. *Journal of Composite Materials*, **43**, 445–467.

Reid S.R. & Zhou G. (2000). *Impact Behavior of fibre-reinforced composite materials and structures*. Woodhead Publishing Ltd.

Rhymer J., Kim H. & Roach D. (2012). The damage resistance of quasi-isotropic carbon/epoxy composite tape laminates impacted by high velocity ice. *Composites Part A: Applied Science and Manufacturing*, **43**, 1134–1144.

Ridruejo A., González C. & LLorca J. (2011). Micromechanisms of deformation and fracture of polypropylene nonwoven fabrics. *International Journal of Solids and Structures*, **48**, 153 – 162.

Rosen B.W. (1965). Mechanics of composite strengthening. *American Society for Metals*, 37–75.

Rudov-clark S. (2007). *Experimental investigation of the tensile properties and failure mechanisms of three-dimensional woven composites*. Ph.D. thesis, RMIT University.

Rudov-Clark S., Mouritz a.P., Lee L. & Bannister M.K. (2003). Fibre damage in the manufacture of advanced three-dimensional woven composites. *Composites Part A: Applied Science and Manufacturing*, **34**, 963–970.

Sayer M. & Bektas N.B. (2010). An experimental investigation on the impact behavior of hybrid composite plates. **92**, 1256–1262.

Schoeppner G. & Abrate S. (2000). Delamination threshold loads for low velocity impact on composite laminates. *Composites Part A: Applied Science and Manufacturing*, **31**, 903–915.

Schultheisz C.R. & Waas A.M. (1996). Compressive failure of composites, part I: Testing and micromechanical theories. *Progress in Aerospace Sciences*, **32**, 1–42.

Segurado J. & LLorca J. (2004). A new three-dimensional interface finite element to simulate fracture in composites. *International Journal of Solids and Structures*, **41**, 2977–2993.

Seltzer R., González C., Muñoz R., LLorca J. & Blanco-Varela T. (2013). X-ray microtomography analysis of the damage micromechanisms in 3D woven composites under low-velocity impact. *Composites Part A: Applied Science and Manufacturing*, **45**, 49–60.

Sevkat E., Liaw B., Delale F. & Raju B.B. (2009). Drop-weight impact of plain-woven hybrid glass-graphite/toughened epoxy composites. *Composites Part A: Applied Science and Manufacturing*, **40**, 1090–1110.

Sevkat E., Liaw B. & Delale F. (2013). Drop-weight impact response of hybrid composites impacted by impactor of various geometries. *Materials and Design*, **52**, 67–77.

Simulia. *Abaqus 6.10 User's manual*.

Sket F., Enfedaque A., Alton C., González C., Molina-Aldareguia J. & Llorca J. (2014). Automatic quantification of matrix cracking and fiber rotation by X-ray computed tomography in shear-deformed carbon fiber-reinforced laminates. *Composites Science and Technology*, **90**, 129–138.

Soutis C. (2013). Compressive strength of composite laminates with an open hole: Effect of ply blocking. *Journal of Composite Materials*, **47**, 2503–2512.

Soutis C. & Curtis P. (2000). A method for predicting the fracture toughness of CFRP laminates failing by fire microbuckling. *Composites Part A*, **31(7)**, 733–740.

Sridharan S., ed. (2008). *Delamination behaviour of composites*. CRC press.

Stig F. & Hallström S. (2012). Spatial modelling of 3D-woven textiles. *Composite Structures*, **94**, 1495–1502.

Stig F. & Hallström S. (2013). Influence of crimp on 3D-woven fibre reinforced composites. *Composite Structures*, **95**, 114–122.

Tabatabaei S.A., Lomov S.V. & Verpoest I. (2014). Assessment of embedded element technique in meso-FE modelling of fibre reinforced composites. *Composite Structures*, **107**, 436–446.

Tabiei A. & Nilakantan G. (2008). Ballistic Impact of Dry Woven Fabric Composites: A Review. *Applied Mechanics Reviews*, **61**, 010801.

Tanzawa Y., Watanabe N. & Ishikawa T. (1999). Interlaminar fracture toughness of 3-D orthogonal interlocked fabric composites. *Composites Science and Technology*, **59**, 1261–1270.

Tarnopol Y.M., Kulakov V.L. & Aranautov A.K. (2000). Measurements of shear characteristics of textile composites. **76**, 115–123.

Tong L., Mouritz A.P. & Bannister M.K. (2012). *3D Fibre Reinforced Polymer Composites*. Elsevier.

Totry E., González C. & LLorca J. (2008). Failure locus of fiber-reinforced composites under transverse compression and out-of-plane shear. *Composites Science and Technology*, **68**, 829–839.

Totry E., Molina-Aldareguía J.M., González C. & LLorca J. (2010). Effect of fiber, matrix and interface properties on the in-plane shear deformation of carbon-fiber reinforced composites. *Composites Science and Technology*, **70**, 970–980.

Tsai C.L. & Daniel I.M. (1999). Determination of shear modulus of single fibers. *Experimental Mechanics*, **39**, 284–286.

Tsu-Wei C. (1992). *Microstructural design of fiber composites*. Cambridge University Press.

Turon A., Dávila C., Camanho P. & Costa J. (2007). An engineering solution for mesh size effects in the simulation of delamination using cohesive zone models. *Engineering Fracture Mechanics*, **74**, 1665–1682.

Van Paepegem W., De Baere I. & Degrieck J. (2006). Modelling the nonlinear shear stress-strain response of glass fibre-reinforced composites. Part I: Experimental results. *Composites Science and Technology*, **66**, 1455–1464.

Walter T., Subhash G., Sankar B. & Yen C. (2010). Monotonic and cyclic short beam shear response of 3D woven composites. *Composites Science and Technology*, **70**, 2190–2197.

Whitney J.M. & Nuismer R.J. (1974). Stress Fracture Criteria for Laminated Composites Containing Stress Concentrations. *Journal of Composite Materials*, **8**, 253–265.

Wisnom M. (1995). The effect of fibre rotation in 45° tension tests on measured shear properties. *Composites*, **26**, 25–32.

Yudhanto A., Watanabe N., Iwahori Y. & Hoshi H. (2013). Compression properties and damage mechanisms of stitched carbon/epoxy composites. *Composites Science and Technology*, **86**, 52–60.

Yushanov S.P., Bogdanovich A.E. & Mohamed M.H. (1999). Manufacturing and Property Analysis of a Novel Class of 3-D Woven Composites. *Journal of Thermoplastic Composite Materials*, **12**, 70–82.

Zeng X., Brown L.P., Endruweit A., Matveev M. & Long A.C. (2014). Composites : Part A Geometrical modelling of 3D woven reinforcements for polymer composites: Prediction of fabric permeability and composite mechanical properties. *Composites Part A*, **56**, 150–160.